Winter 2010

Analysis of Wake Vortices of a Medium Range Twin-Propeller Military Cargo Aircraft Using Statistically Designed Experiments

Burhan Sahin
Old Dominion University

Recommended Citation

Sahin, Burhan. "Analysis of Wake Vortices of a Medium Range Twin-Propeller Military Cargo Aircraft Using Statistically Designed Experiments" (2010). Doctor of Philosophy (PhD), Dissertation, Mechanical & Aerospace Engineering, Old Dominion University, DOI: 10.25777/v2xw-k765
https://digitalcommons.odu.edu/mae_etds/87

ANALYSIS OF WAKE VORTICES OF A MEDIUM RANGE TWIN-PROPELLER MILITARY CARGO AIRCRAFT USING STATISTICALLY DESIGNED EXPERIMENTS

by

Burhan Sahin
B.S. August 1992, Turkish Air Force Academy
M.S. July 1998, Middle East Technical University

A Dissertation Submitted to the Faculty of
Old Dominion University in Partial Fulfillment of the
Requirement for the Degree of

DOCTOR OF PHILOSOPHY

AEROSPACE ENGINEERING

OLD DOMINION UNIVERSITY
December 2010

Approved by:

Colin P. Britcher (Director)

Oktay Baysal (Member)

Resit Unal (Member)

Drew Landman (Member)

M. Fevzi Unal (Member)

ABSTRACT

ANALYSIS OF WAKE VORTICES OF A MEDIUM RANGE TWIN-PROPELLER MILITARY CARGO AIRCRAFT USING STATISTICALLY DESIGNED EXPERIMENTS

Burhan Sahin
Old Dominion University, 2010
Director: Dr. Colin P. Britcher

ABSTRACT

An experimental study was initiated to analyze the trajectories of the streamwise vortices behind the wing tip and flap of a medium range and propeller driven twin-engine military cargo aircraft. The model used for the experimental study was a generic, high wing and half model of a propeller driven aircraft and mounted within Old Dominion University's Low Speed Wind Tunnel where the wind tunnel flow speed was set to constant value of 9 m/sec. The main purpose of the study was to reach regression models for the motion and vorticity strength of both vortices under varying factors such as angle of attack, flap angle, propeller pitch angle and downstream distance. Velocity measurements of the flow fields were accomplished using both Particle Image Velocimetry (PIV) and Hotwire Anemometry (HWA) to yield average velocities, turbulence levels, vorticity strengths and Reynolds shear stresses in the wake of the model. The results of measurements showed that the vertical motions, horizontal motions, and vorticity strengths of both vortices as well as the shortest distance between both vortices depend on the aforementioned factors and the interactions of some factors. It can be concluded that propeller pitch angle mainly affects the behaviors of the vortices as much as angle of attack to the extent that their second order terms take place in some of the regression models.

Dedicated to my wife, Nihan, and our son, Yigit Sergen.

ACKNOWLEDGMENTS

I am heartily thankful to my advisor, Dr. Colin P. Britcher, whose encouragement, and support from the initial to the final level enabled me to accomplish this study. Without his guidance and persistent help this dissertation would not have been possible. I would like to express the deepest appreciation to Dr. Drew Landman for his endless help, guidance, and encouragement during the courses about design and analysis of experiments.

I would like to show my gratitude to Dr. Oktay Baysal, Colonel Sefer Kurnaz, and Dr. Osman Akan for their contributions to initiate the collaboration between Old Dominion University and Turkish Air Force which gives us the opportunity to accomplish Ph.D. study at Old Dominion University.

I owe my deepest gratitude to Dr. M. Fevzi Unal and Dr. Resit Unal for their valuable guidance and for the insights they shared. I would also like to thank to my friends and colleagues Major Arif Arin, 1st Lt. Hasan Ozgur Yavas, Dr. Bayram Celik, Murat Barisik, Can Sabuncu, Stargel Doane, and Mau-Kuo Chen for their friendship and technical support. I would also like to acknowledge Kevin Colvin, Tom Galloway, Thurman Gardner, and Lars Linberg from Batten's Model Shop for helping me build the experimental model and set-up.

Last but not the least, I would like to offer my deepest regards to my wife, Nihan, and our son, Yigit Sergen, for their continuous love and support.

NOMENCLATURE

Variables

AOA	Angle of Attack
c	Wing Chord Length
C_l	Lift Coefficient
C_d	Drag Coefficient
C_P	Power Coefficient
C_T	Thrust Coefficient
D	Drag
df	Degree of Freedom
D_P	Propeller Diameter
D_v	Induced Drag (or Vortex Drag)
e_{ij}	Residual of *j*th Observation in *i*th Treatment
J	Advance Ratio
L	Lift
n	Rotational Speed of Propeller
n_c	Replicate at Center Point
P	Power
p	Probability
p	Pitch Angle of Propeller
Q	Torque
R_m	Sensor Resistance
Re	Reynolds Number
r	Vortex Core Radius
se	Standar Error
T	Thrust
U	Flow Velocity in x Direction
u_a	Axial Velocity
V	Flow Velocity in y Direction
V	Variance
V_A	Airdrop Speed
v_θ	Tangential Velocity

$\hat{y}_{ij}$	Predicted Response
y_{ij}	Observed Response
W	Flow velocity in z direction
w	Propeller-Induced Velocity
w	Angular Velocity of Propeller
U_∞	Flow Freestream velocity

Greek Symbols

α	Angle of Attack
α_e	Effective Angle of Attack
α_i	Induced Angle of Attack
α_0	Zero-Lift Angle
α_S	Significance level
β	Propeller Pitch Angle
σ	Standard Deviation
σ_x	Axial Turbulence Intensity
δ	Flap Deflection Angle
ρ	Density of Air
Γ	Circulation
ε_{ij}	Random Error Component
ε	Downwash Angle
ω	Streamwise Vorticity

Acronyms

2FI	Two Factor Interaction
AAR	Air-to-Air Refueling
ANOVA	Analysis of Variance
CC	Constant Current
CCD	Charge-Coupled device
CCD	Central-Composite Design
CFD	Computational Fluid Dynamics
CT	Constant Temperature
CTA	Constant Temperature Anemometry

CV	Constant Voltage
DAQ	Data Acquisition
DOE	Design of Experiments
FAA	Federal Aviation Administration
FCD	Face-Centered Design
FVX	Vertical Motion of Flap Vortex
FVY	Horizontal Motion of Flap Vortex
FVVS	Flap Vortex Vorticity Strength
HVAD	High-Velocity Airdrop
HWA	Hotwire Anemometry
ICAO	International Civil Aviation Organization
IFR	Instrumented Flight Rules
IFR	In-Flight Refueling
LDV	Laser Doppler Velocimetry
LFST	Langley Full Scale Tunnel
LVAD	Low-Velocity Airdrop
MS	Mean Square
NATO	North Atlantic Treaty Organization
ODU	Old Dominion University
PIV	Particle Image Velocimetry
PRESS	Prediction Error Sum of Squares
RANS	Reynolds Averaged Navier-Stokes
RPM	Revolution per Minute
RSM	Response Surface Methodology
SDBV	Shortest Distance Between Vortices
SS	Sum of Squares
WTVX	Vertical Motion of Wing Tip Vortex
WTVY	Horizontal Motion of Wing Tip Vortex
WTVVS	Wing Tip Vortex Vorticity Strength

TABLE OF CONTENTS

Page

LIST OF TABLES

Table Page

LIST OF FIGURES

1 INTRODUCTION

1.1 Transport Aircraft Wakes

The circulating motion of the fluid swirling rapidly around a center is called a "vortex". A vortex line is considered to lie in the core of a vortex and every particle in the vortex circulates around this vortex line.

A wing generates aerodynamic lift by creating a region of relatively higher air pressure below and lower air pressure above. Air is forced to flow from high to low pressure and tends to migrate toward the top of the wing in a circular fashion creating a vortex (see Figure 1.1) unless a winglet (see Figure 1.2) is placed at the wing tip to hinder the swirling motion of the air.

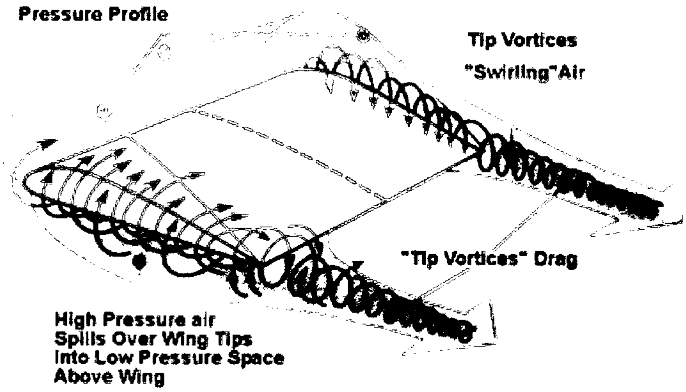

Figure 1.1: Wing Tip Vortices (www.centennialofflight.gov)

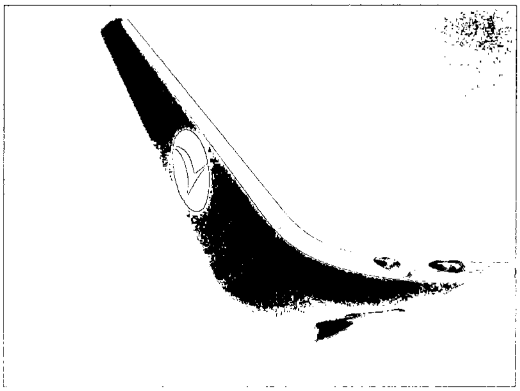

Figure 1.2: Winglet of a Transport Aircraft

The fluid pressure is lowest in the center of a vortex and rises progressively with distance from the center. Sometimes the core of the vortex is visible in the air due to the fact that water vapor in the low pressure core condenses, as seen in Figure 1.3.

Figure 1.3: Wing Tip Vortices During Take-Off

The wake flow behind a transport aircraft can be well described by near and far-field characteristics. Just behind the trailing edge of the wing (near field) a strong downward motion (downwash) dominates whereas a weaker upward motion (upwash) is observed in regions beyond both wing tips (see Figure 1.4). The far-field is defined as the region where the wake resembles an ideal vortex pair, with slow decay over time or distance downstream due to the impact of the atmospheric turbulence and viscosity on the vortices.

Trailing vortices have become a major research area since the 1950's but the flow characteristics and hazards of the transport aircraft wakes have been studied particularly since wide body and heavy transport aircraft (i.e. Boeing 747s) were put into service in the 1970's. The main goal of the research was to understand the hazards of heavy aircraft wakes when medium or small aircraft follow closely and to maintain a safe separation between two aircraft during take-off and landing. The control of aircraft wake vortices by some constructive methods (i.e. flap setting, active or passive control devices, jets) is the main goal of some studies. The shortened aircraft separations and reduction of time delays between consecutive take-offs and landings and increasing the airport capacities are benefits of these studies for the air transportation industry. Another issue to be dealt with is the induced drag (that can exceed 50% of the total drag) caused by the wing tip vortices.

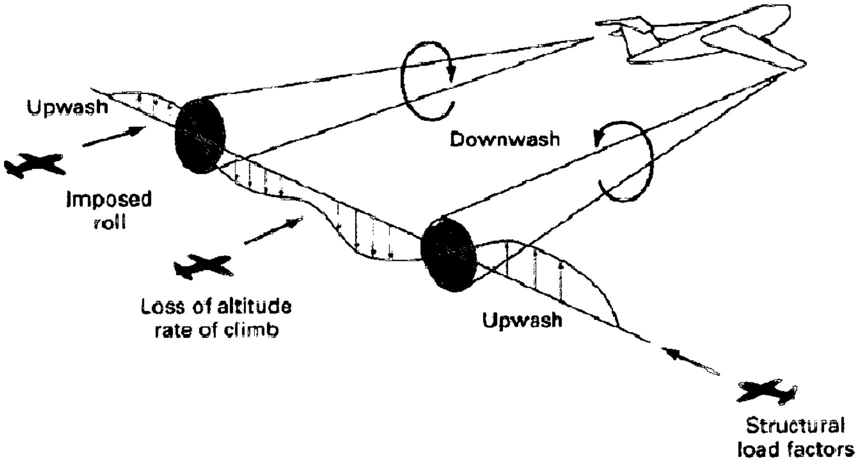

Figure 1.4: Hazards of Wake Vortices (Babie and Nelson, 2004)

The preferred experimental tool for the study of the near and extended near field (down to the order of 10 wing spans), is a wind tunnel with 5-hole pressure probes, Hotwire Anemometry, Laser Doppler Anemometry (LDA), and Particle Image Velocimetry (PIV) instrumentation to survey the mean field and instantaneous fields. Studies have shown that Computational Fluid Dynamics (CFD) calculations from a plane close behind the trailing edge to the near and extended near field agree well with the observations of the mean field. For mid- to far-field investigations, large catapult facilities and water towing tanks are being used for experimental research. Recently conducted smoke-visualization and PIV measurements in the catapult facilities, as well as very recent PIV measurements in water-tanks, yielded encouraging results for the data reproducibility and for wake characteristics due to configuration changes. It is well understood that once established and validated, CFD tools can predict the far-field wake characteristics in a given environment from the near-field data.

1.2 Motivations for the Current Study

Wake turbulence is one of the main reasons for capacity problems in the air-transportation industry. The lift force exerted on aircraft wings produces vortices which are long lasting in their wakes (Figure 1.5). Especially during an aircraft's critical landing phase, these can endanger any aircraft following close behind.

Figure 1.5: Wing Wake of a Military Cargo Aircraft

The Federal Aviation Administration (FAA) of the USA and the International Civil Aviation Organization (ICAO) divided aircraft into three weight classes and established safe separations in the terminal area for each combination of these classes as shown in Table 1.1. The separations are based on the maximum take-off weights of leader and follower aircraft and must be observed when the airport operates under Instrumented Flight Rules (IFR).

The hazardous effects of vortices and turbulent wakes limit airport capacity and a safe separation between two consecutive aircraft during take-off and landing should be maintained to comply with both civilian and military aviation regulations. Larger separations between aircraft are critical for commercial air transportation industry economics whereas scheduling of the air operations is being limited for military aviation.

Leader aircraft **(Max take-off weight)**	**Follower aircraft**	**Separation (nautical miles)**	**Time delay (seconds) (Approach speed 70 m/sec)**
Heavy (≥136,000 kg)	Heavy	4	106
Heavy	Medium	5	132
Heavy	Light	6	159
Medium (< 36,000 kg)	Light	5	132
For all other combinations, the minimum radar separation of 3 NM (79 sec) or 2.5 NM (66 sec) applies.			

Table 1.1: ICAO Aircraft Separation Distances to Avoid Wake Vortex Encounter (Gerz et al., 2002)

Wake hazard is of great concern for Air Force operations such as air-refueling and air-drop operations. The factors that create hazards should be well understood and controlled in order to sustain safe operations. Air-refueling operations are mainly undertaken by long-range multi jet-engine aircraft, such as the KC-135 as shown in Figure 1.6. Military aircraft with propellers are also being widely used by many countries for air-drop, and air-refueling operations as shown in Figures 1.7 and 1.8 (see Appendix A for more details). The wake hazards created by a wide-bodied and heavy aircraft are different compared to medium-range twin-engine (propeller driven) aircraft. The scope of the dissertation study was to understand the wake profile of this second category of aircraft.

During air-drop operations, parachutists or logistic supplies are discharged from the aircraft and as soon as they leave the aircraft (typically cruising at around 140 knots), they interact with the swirling effects of the aircraft's wake vortices. Besides the wing tip and flap vortices, swirling airflows are also observed in the wake of the propellers which are thought to interact with the nearest vortices (such as flap vortices) in the extended near-field wake.

During air-refueling operations, the aircraft in the wake of a tanker aircraft with propellers is under the influence of the vortices and propeller wake. As a consequence, understanding the wake characteristics of a propeller military cargo aircraft is important since the wake can be manipulated in order to maintain safe operations.

Figure 1.6: Air-Refueling Operation Performed by Turkish Air Force KC-135 Aircraft

Figure 1.7: Air-Drop Operations

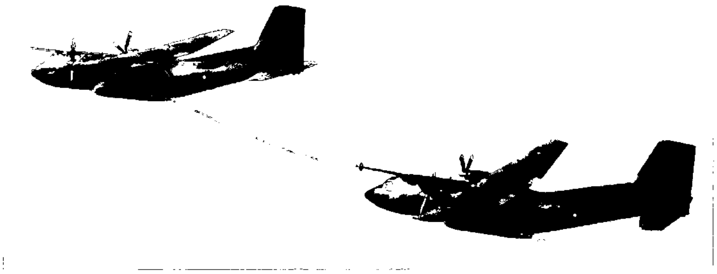

Figure 1.8: Air-Refueling Operations by Medium Range Twin-Engine Military Cargo Aircraft

The wake flow can be controllable to a certain extent by manipulating the factors as desired, but this does not mean that the wake hazards necessarily diminish. This study showed that the vortices of both wing tip and flap are physically approaching each other even in the near field of the wake and the trajectories of both vortices are aligned as if to create a spiral shape, and indicate the tendency towards merging. It was expected that these two vortices would merge in the medium range of the wake so as to create a single vortex in the far-field.

The results of this study also showed that the propellers of medium range twin-engine aircraft are influencing the flow characteristics above and below the wing to such an extent that both wing tip and flap vortex parameters are changing according to propeller settings. During air operations, the propellers should therefore be set in order to maintain the flight requirements as well as to reduce wake hazards.

Understanding the near field behavior of the vortices (both wing tip, flap and propeller vortices) of a propeller military cargo aircraft during air-drop and air-refueling operations is the main goal of the current study and a statistical experiment design was used to develop a model for the behaviors of the vortices.

2 PREVIOUS RESEARCH

2.1 Tip Vortices

In the case of a wing with nearly elliptic loading, a discrete vortex forms just inboard of the tip and as the vortex moves downstream, it rolls up more and more of the wing wake until its circulation is nominally equal to that of the wing on the centerline. The flow in the near-field rollup region is therefore important in providing a possible means of controlling the far-field vortex.

There have been several experimental studies of the fully developed vortex downstream of the wingtip, including parametric studies where various tip shapes and devices were used to alter or manipulate the tip vortices. It is concluded that tip shape can substantially affect the way the vorticity in the tip vortex is concentrated. Some landmark studies in this area are the flight experiments performed by McCormick et al. (1968). The eddy viscosity analysis of Hoffman and Joubert (1963) is one of few analytic studies of turbulent trailing vortex. They predicted a logarithmic radial variation of circulation near the edge of the vortex core. Batchelor (1964) and Moore and Saffman (1973) investigated fully rolled-up laminar trailing vortices and concluded that trailing vortices are normally turbulent. Other experimental work was performed by Chigier and Corsiglia (1972) on the flow over the tip and in the rollup region which showed a characteristic surface-pressure suction peak near the tip, denoting the approximate location of the tip vortex as it develops on the top surface of the wing.

Westphal and Mehta (1989) made turbulence measurements downstream of an oscillating vortex and compared them with results for a stationary vortex. They found that $\hat{v}$ (where $\hat{u}, \hat{v}, \hat{w}$ are the x, y, and z components of rms velocity) increased by a factor of 2 and that contours of the Reynolds shear stresses were altered considerably for a meandering vortex.

Green and Acosta (1991) obtained measurements with double-pulsed holography on a rectangular planform wing with rounded tip at a Reynolds number based on a chord of about 7×10^5. At a 10-degree angle of attack, the averaged axial velocity in the core of the vortex was 1.6 times the freestream velocity and the mean pressure drop from the freestream to the core was about 3.3 times the freestream dynamic pressure.

Bandyopadhyay et al. (1990) investigated the turbulence structure in a trailing vortex and concluded that, for their range of test conditions, the Rossby number (axial velocity defect/maximum tangential velocity) was the controlling parameter for the turbulence structure and not the vortex Reynolds number (circulation/viscosity). They also concluded that the inner core is not, as suggested previously, a region of solid-body rotation that does not interact with the outer vortex region but rather is a relaminarizing region where patches of turbulent fluid are intermittently brought in from the outer region. McAlister and Takahashi (1991) used Laser Doppler Velocimetry (LDV) to measure the mean velocity field of a meandering trailing vortex. They observed a slow periodic spanwise oscillation of the vortex (fc/U_∞ on the order of 0.01, where "f" is the oscillation frequency, "c" is the wing chord, and U_∞ is the freestream velocity) and used conditional sampling methods to extract the "true" flow field. Devenport et al. (1995) obtained turbulence and mean field measurements from $x/c=5.0$ to 30.0 behind a rectangular NACA0012 wing by using seven-hole and four-wire probes. High turbulent stress measured in the core region was attributed primarily to meandering of their vortex. They found the meandering amplitudes increased approximately linearly with downstream distance and decreased with angle-of-attack.

Computational studies were done by Dacles-Mariani et al. (1995) in conjunction with an experimental study that showed that it is possible to predict the mean flow of the tip-vortex near field rather well by using a Reynolds-Averaged Navier-Stokes (RANS) code; however, the turbulence modeling used was not as accurate as desired.

Spalart (1998) presented the formation, motion, persistence of trailing vortices and also examined the predictability of the vortices, the durability of multiple vortex pairs as well as the various atmospheric and ground-related factors. Rossow (1999) presented an overview of research on the vortices generated by lifting surfaces of subsonic transport aircraft. The primary purpose of the research was to find a way to reduce the hazard potential of lift-generated vortices created by subsonic aircraft in the vicinity of airports during landing and takeoff operations. The information presented in the research points out the characteristics of lift-generated vortices related to the aerodynamic shapes that produce them, and that various arrangements of surfaces can be used to produce quite different vortex structures. Huenecke (2002) examined the vortex characteristics of transport type aircraft from formation to decay. Data were obtained by using near realistic generic half and full models in wind tunnels and a towing tank. The techniques employed allowed the complete lifetime of a wake to be assessed from formation to decay. Babie and Nelson (2004) performed an experiment to study the interaction of a wake consisting of four vortices. They used the helium-bubble visualization technique in an atmospheric boundary layer wind tunnel. They investigated interactions of vortices and how a wake consisting of four vortices can be made unstable to promote a rapid decay. Paoli and Garnier (2005) presented a survey about interaction between exhaust jets and trailing vortices in the near field of an aircraft wake. Emphasis was placed on the effects of the jet on the wake vortex dynamics and the effects of the wake on the exhaust dispersion, as well as their potential microphysical and chemical transformations. Allen and Breitsamter (2009) presented an experimental investigation on the wake vortex formation and evolutions of a four vortex system of a generic model in the near field and extended near field using hotwire anemometry in a wind tunnel. The model used consisted of a wing plus tailplane configuration with the wing producing positive lift and the tailplane negative lift. The model set up was chosen to create a most promising four vortex system.

2.1.1 Circulation of the Tip Vortex

The circulation of a vortex at different radial locations is computed by using the equation $\mathit{\Gamma} = \sum_i \overline{v_\iota .} \Delta \overline{l_\iota}$ where $\overline{v}_\iota$ and $\overline{l}_\iota$ are the velocity and the length of each segment along the contour, respectively. The studies of Shekarriz et al. (1993) showed that a vortex reaches 85% of its maximum measured strength at the trailing edge and further downstream of the wing, and the overall circulation remains constant within the measurement error. These observations are consistent with the studies reporting that roll-up of the tip vortex begins at the leading edge of the wing. Dependence of circulation on Reynolds number (Re=3.6×10^4, 7.2×10^4, and 2.2×10^5) and incidence angle (α=5 and 10 degrees) was also examined (see Figure 2.1). The slope of the circulation curves increases with Reynolds number within the core of the vortex. Outside the core, the increase is significantly slower and more uniform at Re=2.2x10^5. Higher levels of turbulence and mixing may be an explanation for this trend. At this Reynolds number, the tip vortex also contains fewer secondary structures, probably due to higher levels of shear stresses. When the incidence angle is increased to 10 degrees, the core vorticity does not show the same trend with an increasing Reynolds number. It was determined that the apparent inconsistency was a result of fluctuations in the circulation profile and overall strength of the vortex. These fluctuations tend to increase with the incidence angle and, as a result, are more significant at 10 than at 5 degrees, and decrease along with the Reynolds number.

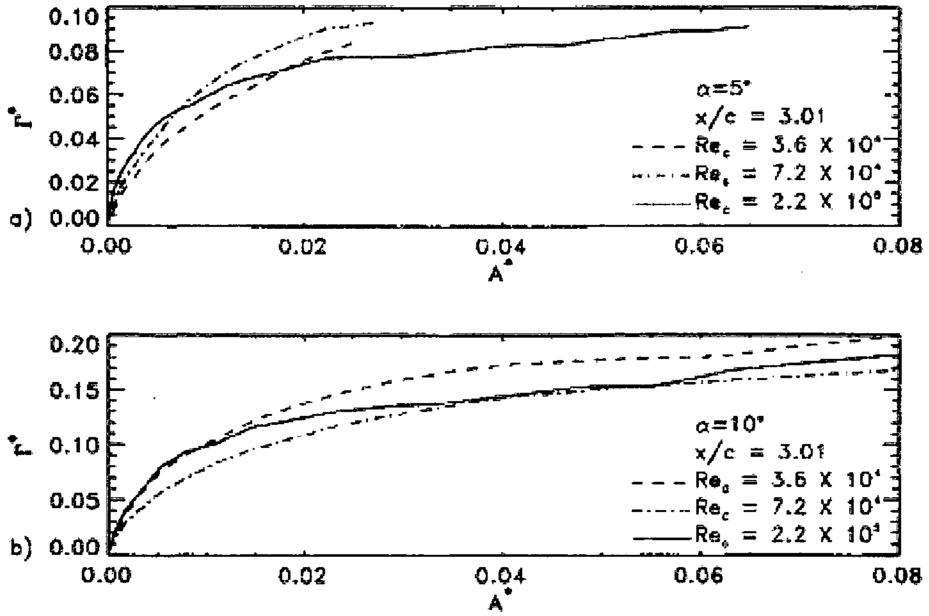

Figure 2.1: Mean Circulation Distribution at Different Reynolds Numbers for a.) α=5 Degrees b.) α=10 Degrees (Shekarriz et al., 1993)

2.1.2 Velocities

2.1.2.1 Tangential Velocity

V_θ is the dominating velocity in the vicinity of the vortex core and vorticity can be estimated by computing $\frac{1}{r}\left[\frac{\partial(rV_\theta)}{\partial r}\right]$. Within the enclosed contours located in the annular area surrounding the core, where V_θ is almost constant, the vorticity is approximately equal to V_θ/r.

Studies by Shekarriz et al. (1993) showed that traces of similar secondary structures, all of them rotating in the same direction as the tip vortex, are evident in all of the contour plots. When the Reynolds number and incidence angle are increased (2.2×10^5 and 10 degrees respectively), the flow structure around the core becomes considerably more symmetric and the presence of secondary vortices is much less evident. Another fact is the lack of symmetry in the velocity field as shown in Figure 2.2. It is evident that the velocity is higher on the suction side, sometimes by as much as 40%.

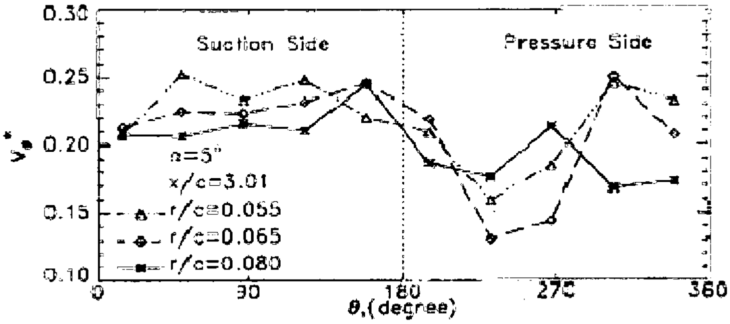

Figure 2.2: Circumference Distribution of the Instantaneous Tangential Velocity at α=5 Degrees and Re_c=7.2×10^4 ($v_\theta^* = v_\theta/U_\infty$) (Shekarriz et al., 1993)

When the distributions of normalized average tangential velocity $\overline{v_\theta^*} = \Gamma/(2\pi r U_\infty)$ are analyzed, the peak average tangential velocity $\overline{v_{\theta_{max}}^*}$ increases with the incidence angle from 22% at 5 degrees to 34% at 10 degrees (see Figure 2.3). The overall strength of the tip vortex at the same Re_c is proportional to α. Note also that the values of $\overline{v_{\theta_{max}}^*}$ vary by as much as 20% from section to section, primarily due to entrainment and migration of secondary structures.

The core size r_l/c defined as the radius at which $\overline{v_\theta^*}$ is maximum, is 0.05 and 0.04 at 5- and 10-degree incidences, respectively. Furthermore, the axial changes in r_l/c are quite small. In fact, the only noticeable change in core size occurs due to narrowing of the body.

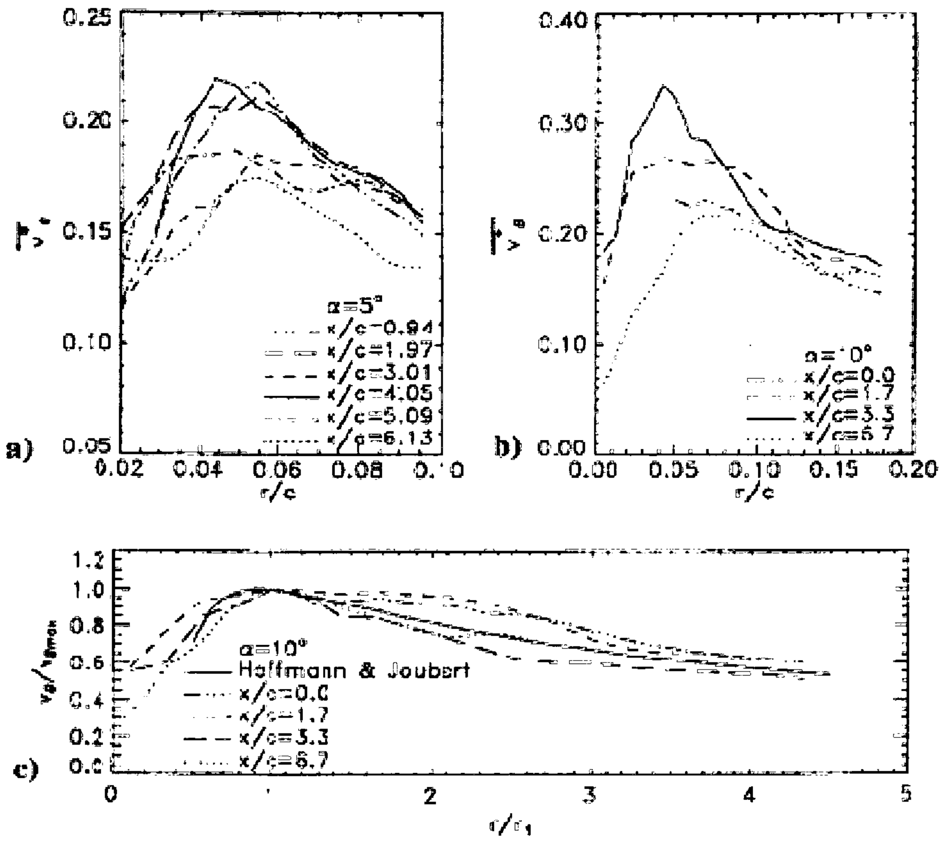

Figure 2.3: Circumferentially Averaged Tangential Velocity ($\overline{v_\theta^*} = \Gamma/2\pi r U\infty$) at a.) α=5 Degrees, Re$_c$=7.2x10^4 ; b.) α=10 Degrees, Re$_c$=2.2x10^5 and c.) Normalized Tangential Velocity Distribution at Re$_c$=2.2x10^5 (Shekarriz et al., 1993)

2.1.2.2 Axial Velocity

Shekarriz et al. (1993) analyzed the axial velocity distribution within tip vortices and along the span in the wake of a wing as shown in Figure 2.4 (the axial velocities are scaled with U_∞ and denoted by u*), and concluded that:

a. At the inboard side of the vortex (y/S<0.8), the visualized plane is located within the wake of the wing, u* is only about 88%,

b. Within the spanwise range (0.82<y/S<0.98), namely in the vicinity of the vortex core, the velocity deficit is even larger (u*<0.65). The size of this range is almost the same diameter as the vortex core,

c. Further outboard, the axial velocity quickly recovers to the freestream velocity ($u^* \rightarrow 1$).

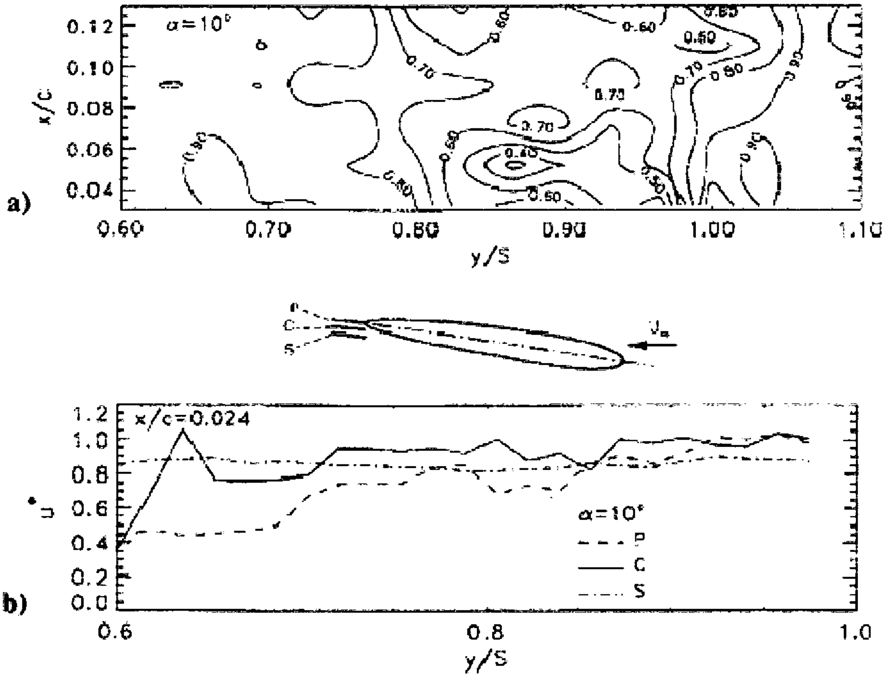

Figure 2.4: Axial Velocity ; a.) Contour Map of the Dimensionless Axial Velocity ($u^*=u/U_\infty$) within and in the Vicinity of a Tip Vortex at α=10 Degrees and $Re_c=7.4\times10^4$ and b.) Dependence of Axial Velocity on z, α=10 Degrees and $Re_c=2.2\times10^5$ (Shekarriz et al., 1993)

The axial flow was visualized in three planes (plane located at suction (S) and pressure (P) sides of wing and plane crossing the vortex center (C)) as shown in Figure 2.4.b. The variations of axial velocities in the z-direction are given below:

a. Consistent with its location relative to the surface (boundary layer) of the wing, the axial velocity in the P section is considerably lower for most of the wing span.
b. The velocity in the S section remains almost constant and unaffected by the presence of the vortex.

Dependence of the axial velocity on Re_c and α is shown in Figure 2.5:

a. For $Re_c<10^5$, the deficit in velocity appears to increase with an increasing α and a decreasing Re_c. These results are consistent with the observations in the lateral planes.

b. The only mechanism affecting the axial velocity is the momentum deficit within the boundary layer. For a laminar flow, one would expect a larger deficit when the boundary layer is thicker, namely at a lower Re_c or a higher incidence angle.

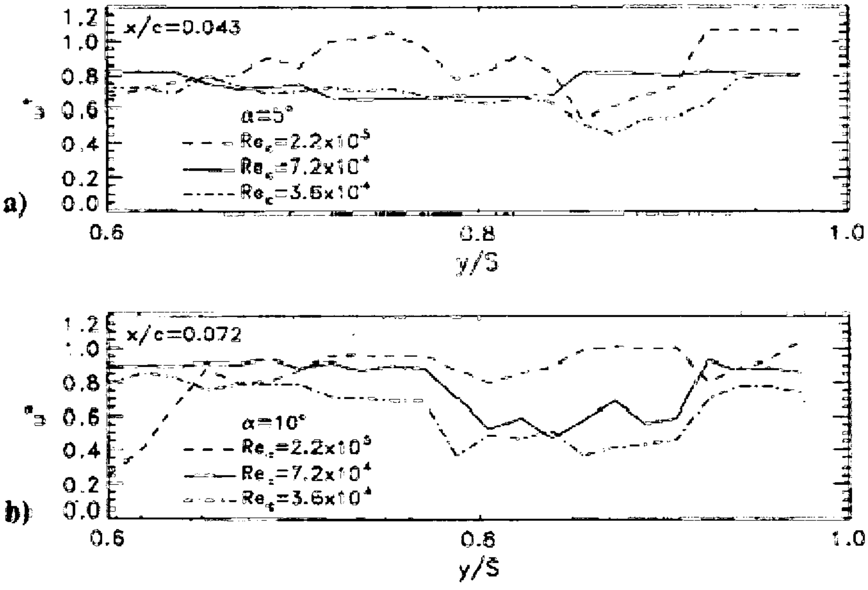

Figure 2.5: Dependence of Axial Velocity on Reynolds Number at a.) α=5 Degrees and b.) α=10 Degrees (Shekarriz et al., 1993)

The two primary mechanisms that affect the axial velocity in the core of a tip vortex are given as:

a. Momentum deficit caused by the boundary layer on the wing: radial diffusion of the tangential momentum results in an increase in the core pressure and a reduction in the axial velocity. This phenomenon is typically observed within a vortex that is decaying, expanding or subjected to breakdown.

b. Axial variation of the core tangential velocity: it gives rise to an axial pressure gradient and in turn to a change in the axial velocity. During the vortex rollup, the tangential velocity increases with x/c, creating a negative axial pressure gradient and consequently, an increase in the axial velocity.

The normalized crossflow and axial velocities in the wing tip vortex were studied by Chow et al. (1997) and the contours are shown in Figure 2.6.

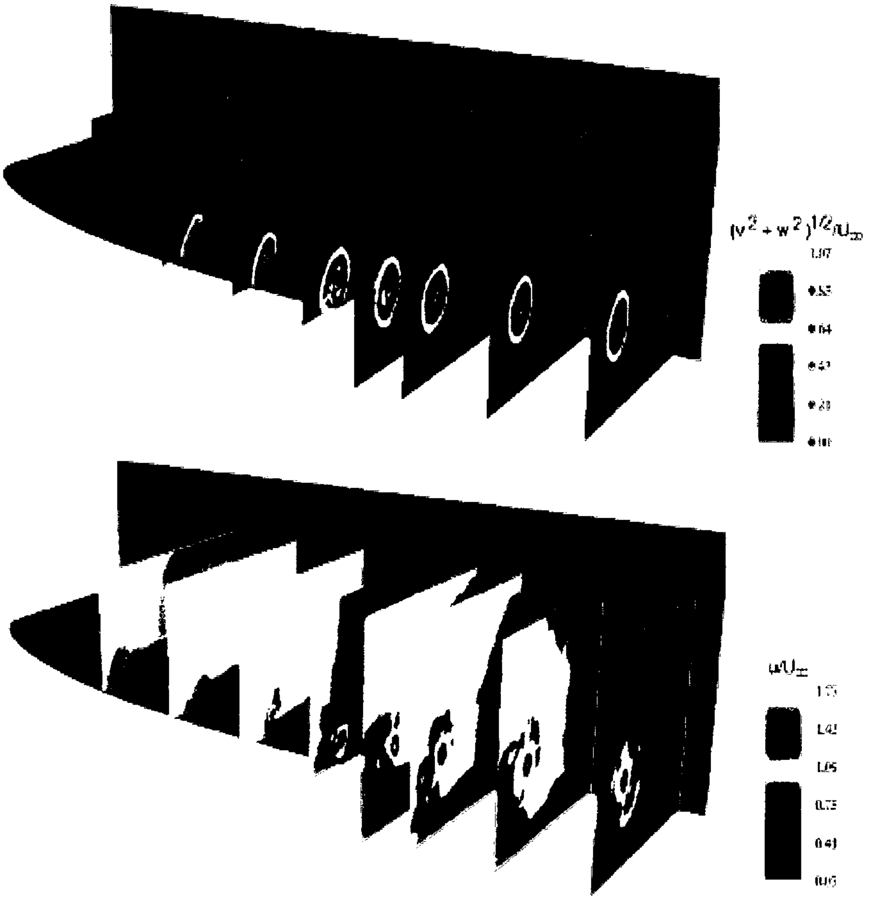

Figure 2.6: Normalized Crossflow and Axial Velocity Contours (Chow et al., 1997)

2.2 Flap Vortices

An airfoil with a displaced trailing-edge flap becomes a new airfoil with a different camber. Further, the downward deflected trailing-edge shifts the zero-lift angle, α_0, negatively and increases the values of the lift, nose-down pitching moment and maximum lift coefficient. Since flaps seldom extend close to the wing tip, the change in local circulation at the outboard end of the flap causes a trailing vortex in addition to the normal wing tip vortex.

In a study by Birch and Lee (2005) a full span flap was analyzed in order to characterize the effects of a trailing-edge flap on the near-field behavior of a tip vortex (up to two chord lengths downstream of the trailing edge) by using a miniature seven-hole pressure probe and cross-hotwire probe in the wake a rectangular, square-tipped wing which has a NACA0015 type airfoil (see Figure 2.7).

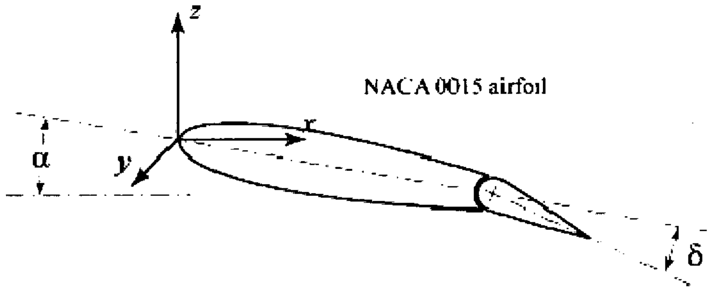

Figure 2.7: Schematic of an Airfoil Model (Birch and Lee, 2005)

Similar to the case of a baseline airfoil (no flap deflection or δ=0 degree), the presence and rollup of the swirling secondary flows or vortices over onto the upper surface of the tip of the wing was apparent for a flapped airfoil (α=10 degrees and for δ=10, 15 and 20 degrees) but with the strength increasing with flap angle.

Note that, for a displaced flap, there was a presence of multiple vortices immediately downstream of the trailing edge as shown in Figure 2.8:

a. Vortex "A" is the main vortex generated by the main body of the airfoil,
b. Vortex "B" is the shear layer vortex generated as a result of the rollup of the shear layers separated from the forward part of the airfoil of same rotation and approximately same strength and diameter (secondary vortex),
c. Vortex "C" is the flap vortex originated from the rollup of shear layers separating from displaced flap with a higher core vorticity as a result of high concentration of circulation at the flap.

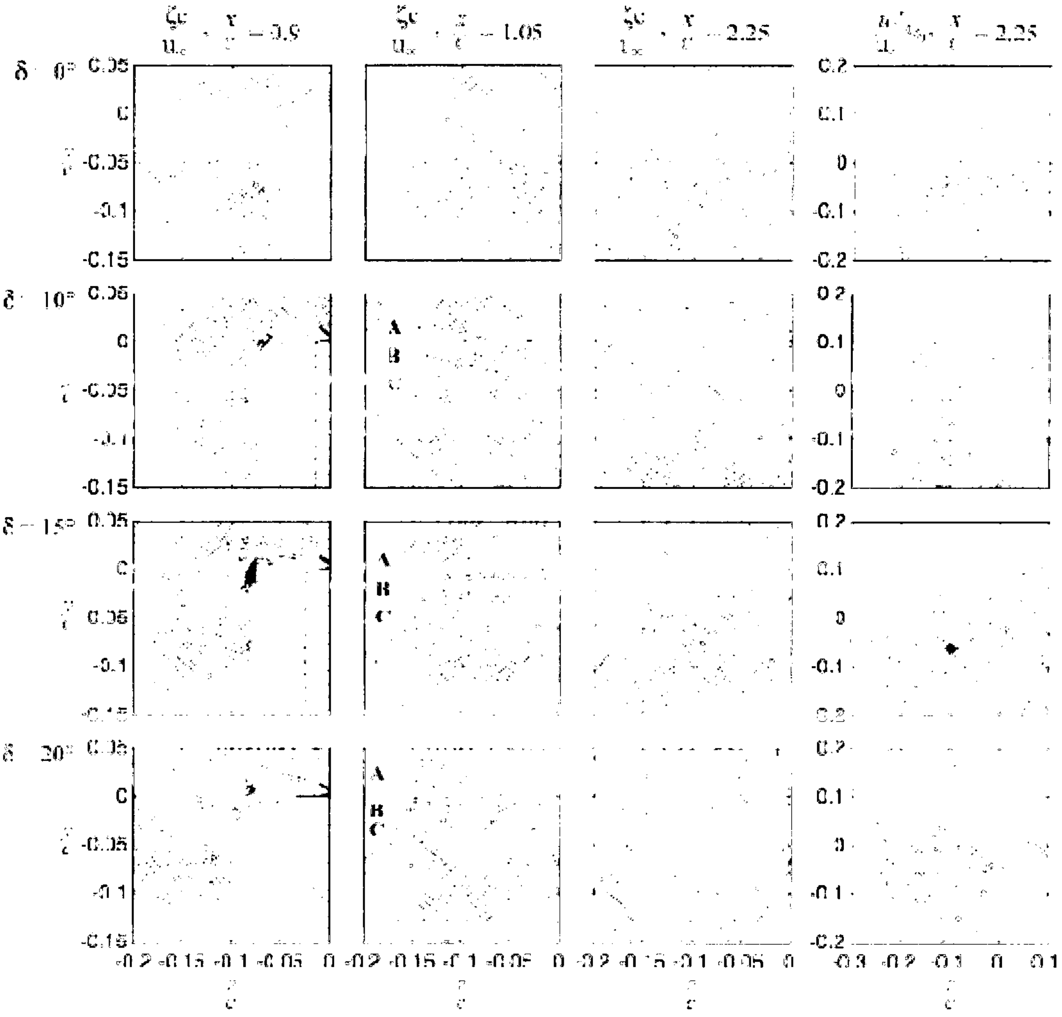

Figure 2.8: Contours of Streamwise Vorticity and Fluctuating Axial Velocity for α=10 Degrees, Numerical Values Denote $\zeta c/U_\infty$ or u'_a/u_∞ Levels (Burch and Lee, 2005)

The displaced flap, which produced a more concentrated vortex but of similar diameter (compared to those of baseline airfoil) had a larger radial gradient in circulation strength, as shown in Figure 2.9.

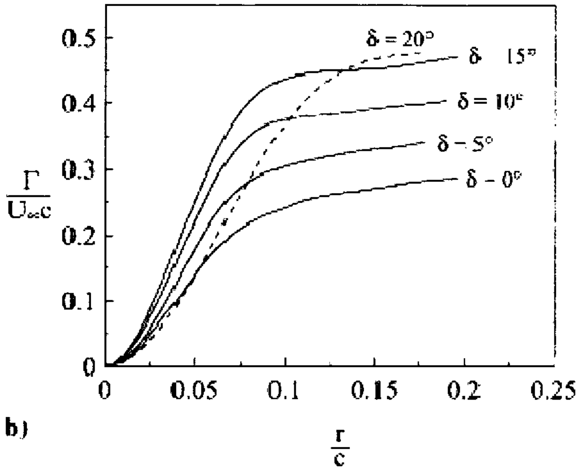

Figure 2.9: Radial Distribution of Circulation at x/c=2.25 for α=10 Degrees 1-inner core, 2-buffer region, 3-logarithmic region, 4-outer region (Burch and Lee, 2005)

The scaling of the circulation parameter (Γ/Γ_c) by the vortex core radius (r/r_c) collapses the data of displaced flaps (except for δ=20 degree) to a single linear curve, as shown in Figure 2.10.

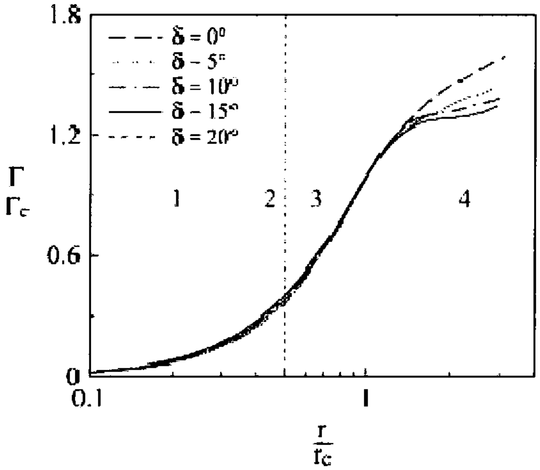

Figure 2.10: Radial Distribution of Circulation at x/c=2.25 for α=10 Degrees 1-inner core, 2-buffer region, 3-logarithmic region, 4-outer region (Burch and Lee, 2005)

The swirl-induced pressure drop along the vortex axis immediately behind the wing was strong enough to accelerate fluid from the wing tip area in the downstream direction and therefore generated a larger axial velocity. The jetlike core with high axial velocity increased progressively with flap angle.

For $\delta \leq 15$ degrees, the displaced flap rendered a remarkable increase in the peak values of $v_{\theta,max}$ (tangential velocity), ω_{max} (streamwise vorticity), $u_{a,c}$ (the core axial velocity). The core radius r_c (estimated by determining the distance from the point of $v_{\theta,max}$ to the vortex center) remains basically the same compared to that of a baseline airfoil. For $\delta=20$ degrees, a significant increase in r_c was observed. A decrease in of $v_{\theta,max}$, ω_{max} , and $u_{a,c}$ was observed which suggests that the flow was largely separated from the upper airfoil surface.

Another study presented by Schell et al. (2000) showed the results of an experimental investigation of a wake-vortex structure behind a flapped rectangular wing for one flap setting, with means of alleviation also examined. The purpose of this investigation was to study the main features of lift generated vortices in order to find ways to alleviate hazardous wake vortex encounters for following airplanes. The wake structure at different flap settings was investigated by measuring the velocity field at different positions in the near field behind the wing. The measurements were performed by means of 3-D hotwire anemometry, as shown in Figure 2.11.

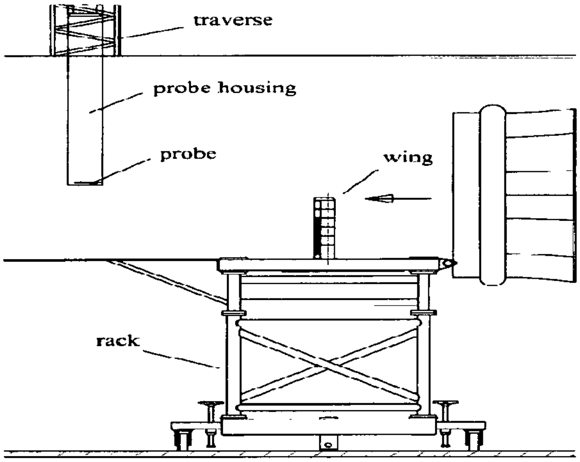

Figure 2.11: Experimental Set Up for Measuring the Flap Vortex (Schell et al, 2000)

Another study by Greenblatt et al. (2009) presented an experimental study which was conducted to assess the applicability of limited-span Gurney flaps for altering the flap edge vortex characteristics as shown in Figure 2.12. Data acquisition included PIV measurements downstream of the flap edge, six-component load measurements, and surface pressure measurement on the main element and in the flap-edge region. They found that the Gurney flaps produced significant variation of the vortex centroids, up to 5.3% of the semi-span (13.1% of chord), with corresponding small changes to lift and drag coefficients. The study involved the testing of static Gurney flaps which were mounted at the trailing edge and flap edge, in which different flap heights and fractions of flap span were evaluated.

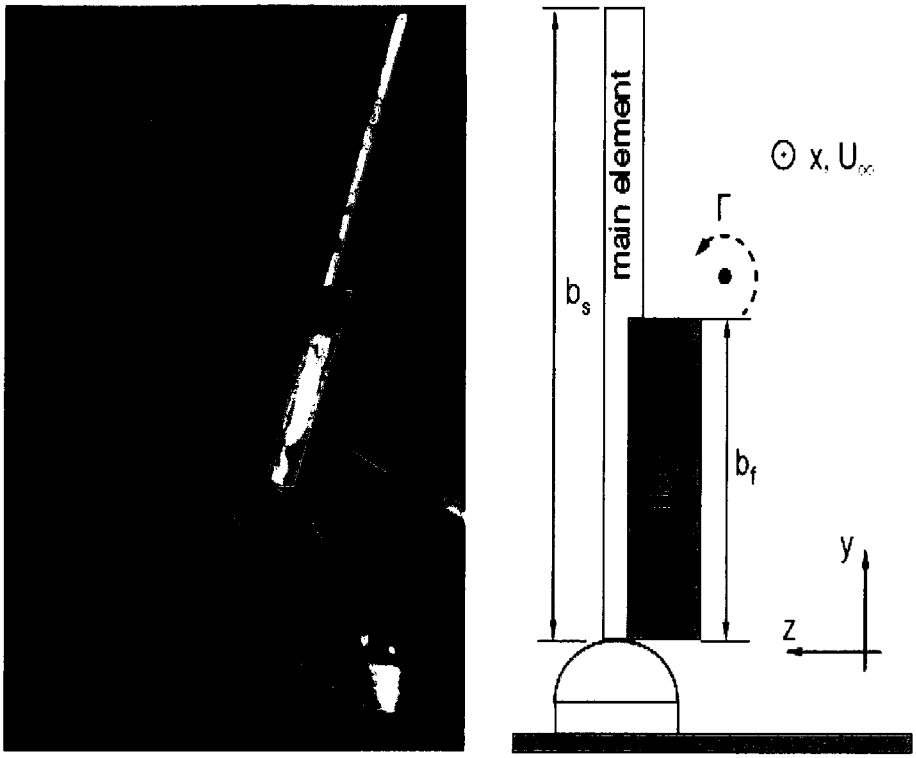

Figure 2.12: Experimental Set Up for Altering the Flap Edge Vortex Characteristics (Greenblatt et al., 2009)

2.3 Propeller Wakes

Laser Doppler Velocimetry (LDV) is a non-intrusive technique for measurement of flow direction with a high spatial resolution and good frequency response. The employment of LDV techniques by Landgerebe & Johnson (1974), Biggers & Orloff (1975), and Serafini et al. (1981) in the aeronautical field and by Min (1978) and Kobayashy (1981) in the naval area, have been a turning point for characterizing the actual shape of the propeller wake. Cenedese (1985), and Jessup (1989) performed LDV investigations in order to better understand the phenomena associated with turbulent diffusion and viscous dissipation. In the available literature, works specifically aimed at the description of the propeller wake from its formation at the trailing edge up to the final breakdown of the vortices are rare. Some guidelines on this subject can also found in the works of Min (1978), Cenedese (1985), and Hoshino (1987) based on LDV applications.

Most current computational codes for propeller analysis adopted potential flow representations and simplified wake models. Jessup (1989) included the viscous aspects of the turbulence effects accounted for in the Reynolds Averaged Navier-Stokes (RANS) methods and of accurate models of the trailing vortex sheets.

Westmoreland et al. (2008) presented a CFD solution for a propeller flow field. They conducted a basic investigation using propeller-spinner geometry to validate their results with experimental data, then made full simulations for a full aircraft model. They explained the effects of the propeller flow field on vehicle aerodynamics and stability using CFD. An example flow field is shown in Figure 2.13.

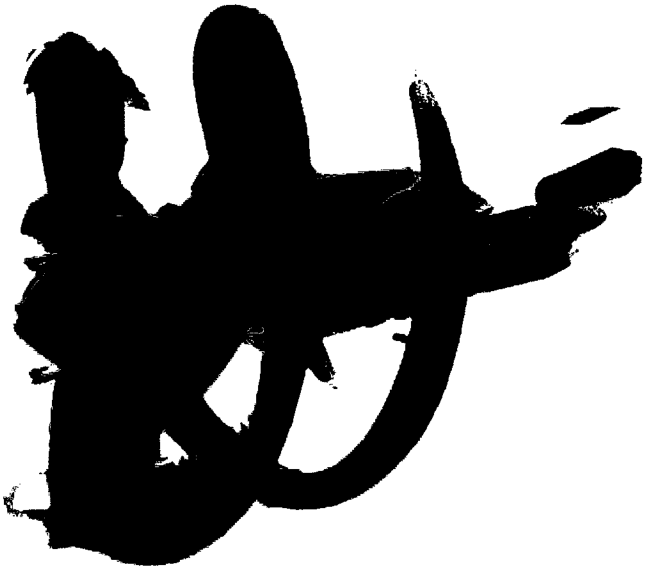

Figure 2.13: Flow Field of Propeller Obtained by CFD (Westmoreland et al., 2008)

2.3.1 Propeller Wake Analysis

In a study by Stella and Guj (1999) some angular variations of the phase-averaged mean axial velocity in the first measurement disk are shown in Figure 2.14:

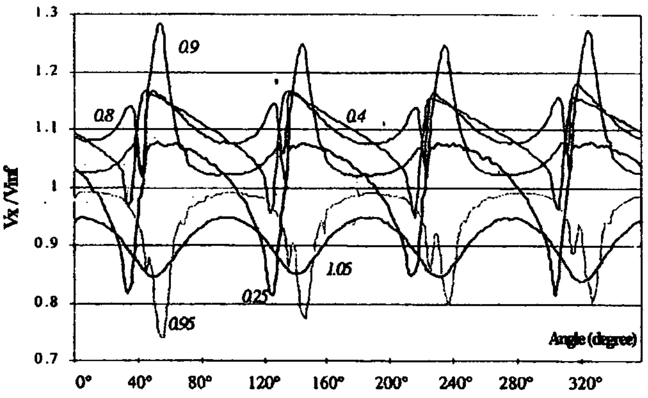

Figure 2.14: Angular Variation of Mean Axial Velocity V_x Nondimensionalized by Incoming Flow Velocity V_∞ at X/R=0.2 (Stella and Guj, 1999)

The velocity is periodical, although a lack of a perfect similarity among the four velocity profiles is observed. The discrepancies (lower than 10%) occur in the velocity peaks and decays associated, respectively, with the passage of the tip vortex and the blade wake.

2.3.2 Turbulent Wake

Stella et al. (2000) showed that the maximum value of the axial turbulence intensity, σ_x/V_{inf}, at the trailing edge is about 20% in the tip vortex core. Along the blade wake, the highest axial fluctuations are measured at the root sections, where σ_x/V_{inf}=10-14%. The radial variation of the σ_x/V_{inf} has instead a minimum around r/R=0.7 as shown in Figure 2.15.

Figure 2.15: Turbulent Axial Velocity Distributions in the Near Wake (Stella et al., 2000)

2.3.3 Vortex Geometry

The V_x peak at r/R=0.9 is due to the presence of the tip vortex, which formed at the blade tip and moved inboard in the slipstream. Outside the propeller slipstream (r/R=0.95 and r/R=1.05), the V_x azimuthal variations show an opposite phase oscillation with respect to those inside (see Figure 2.14). In the root zone, deeper V_x defects are measured. This flow distribution in the inner radii is due to the increasing thickness of the blade sections toward the root. Flow visualizations confirm that the tip vortex convects over the blade suction side as soon as it formed at the tip.

It can be seen that from a geometrical point of view the downstream wake evolution is characterized by a progressive bending of the blade wake surfaces (see Figure 2.16). In the V_x distribution, the trajectory of the tip vortex causes an angular displacement with respect to the inner blade wake, which increases moving downstream. The turbulent wake instead preserves memory of the original shape of the propeller, where the σ_x contours show a continuous trace of the blade wake which ends into the tip vortex.

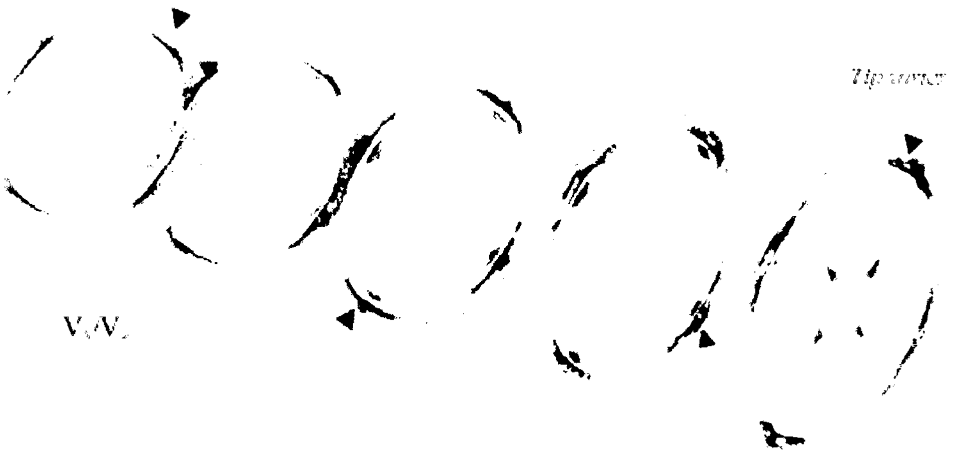

Figure 2.16: Mean Axial Velocity Distributions in the Near Wake (Stella et al., 2000)

The highest axial flow accelerations and the thinnest viscous wake velocity deficits along the blade span occur in the radial stations around r/R=0.77, where this blade section is consequently the most efficient radial point for thrust generation, as shown in Figure 2.16.

A quantitative description of the blade wake geometry in the near wake where the angular positions of the σ_x peaks in the five measurement planes for some radial stations is plotted in Figure 2.17. The slope of the locus represents the pitch angle of the wake. The almost linear variation of the traces means that the pitch is nearly constant during wake convection downstream. The comparison of these traces with the propeller (constant) pitch angle is evidence that the hydrodynamic pitch equals the geometrical one at around r/R=0.7.

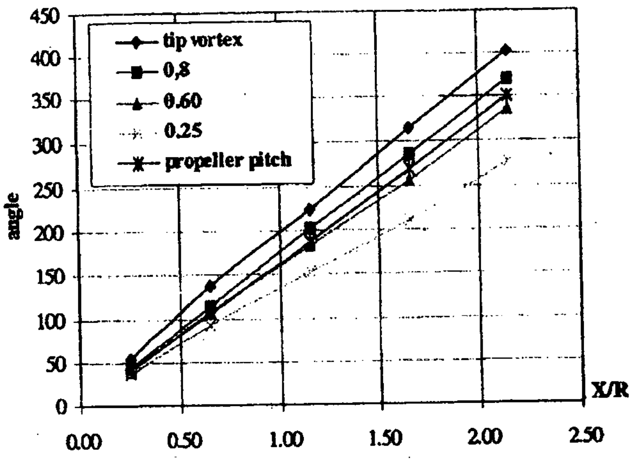

Figure 2.17:Traces of σ_x Peaks Locations for Various Radial Positions in Five Measurement Disks (Stella et al., 2000)

A second factor affecting wake geometry is the contraction of the slipstream, which is the result of the flow axial acceleration behind the propeller as shown in Figure 2.18. The experimental observations sustain the significance of the basic and simplified concept of a stream tube. Min (1978) used the radial location of the tip vortex for evaluating the radius of the slipstream of several propellers. It is characterized by a very high rate of contraction in the neighborhood of the propeller and is practically complete within the first diameter. The asymptotic radius of the contraction is r/R=0.82-0.83 which can also be verified by actuator disc theory (details of the actuator disc theory will be given in Chapter 4).

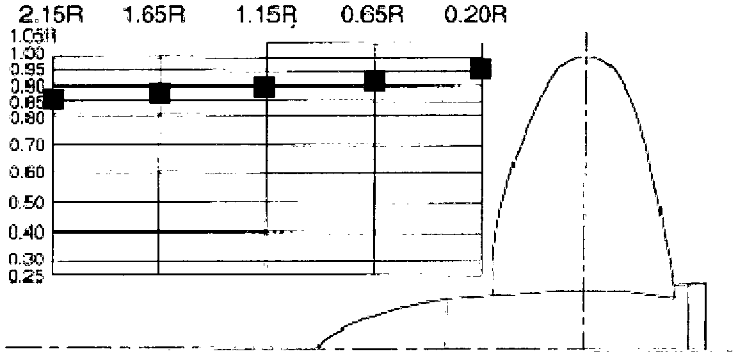

Figure 2.18: Contraction of Slipstream (Stella et al., 2000)

2.4 Combined Wakes

2.4.1 Wing/Flap/Jet Wake

Experimental studies were performed by Miake-Lye et al. (1993) to evaluate the effect of a jet on a trailing edge vortex. The interaction is mainly separated in two phases:

a. In the first phase (jet regime) the jet mixes with the ambient air while the vorticity sheet rolls-up around the tip vortex. During this regime the interaction between the jet and the vortex is minimal which has been the main assumption behind a number of simulations of the jet/vortex interaction as in Ferreira Gago et al. (2002) and Paoli et al. (2003,2004).
b. The second phase (interaction regime) is dominated by the entrainment of the jet into vortex.

Using a delta wing as vortex generator and with a jet blowing along the centerline, Wang et al. (2000) showed that the effect of the jet on the trajectory of the vortices is minimal whereas the jet was significantly influenced by the vortices. The jet lost its axisymmetric shape and was compressed vertically and elongated horizontally. In a further study by Wang and Zaman (2002), it was shown that the vortex induced flow results in the generation of vortices around the jet. The strength of these vortices is significant and leads to the deformation (stretching) of the jet. Secondary vortices have also been observed from the studies of Ferreira Gago et al. (2002), Paoli et al. (2003, 2004), forming at the periphery of the vortex due to the effect of the axial velocity of the jet, when the initial separation between the jet and vortex is large. In the studies of Ferreira Gago et al. (2002), these structures lose coherence further downstream without penetrating into core. Paoli et al. (2003) showed that when the jet is blowing very near the core and the jet-to-vortex velocity ratio is high, and the tip vortex diffuses rapidly but maintains its total circulation.

In a comparative numerical and experimental study by Huppertz et al. (2004), a number of jet-to-vortex distances were examined for two jet velocities. The jet was shown to have a small impact in the tangential velocity of the vortex for all jet-to-vortex distances and jet velocities whereas the distance between the jet and the vortex affected the axial vortex velocity significantly.

An experimental study by Margaris et al. (2008) on the single vortex and jet interaction showed that there is no visible interaction up to 0.25 spans downstream of the trailing edge, but the jet is seen to have been elongated and rotated due to the cross-flow velocity field around the vortex and the one end of the jet has been wrapped around the vortex at 1.74 spans downstream, as shown in Figure 2.19.

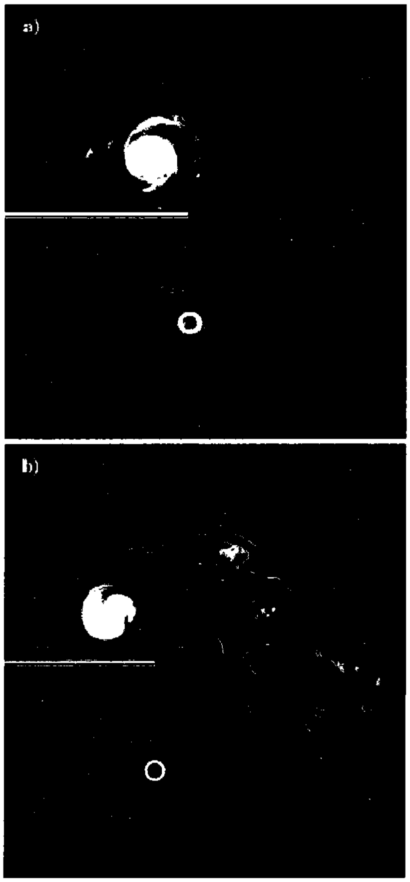

Figure 2.19: Instantaneous Flow Visualization Images (Water Tunnel) for Re_Γ=5500, h/dj=6.7, Uj/U∞=2.01 R=0.13 a.) x/b=0.35 b.) x/b=1.75 (Margaris et al., 2008)

It was also shown that when the jet is closer to the vortex it gets wrapped around the vortex faster and thus affects it more. Almost all of the jet structure is seen around the vortex core at 1.75 spans downstream of the trailing edge for (h/d_j=4.0) and also penetrates into the core of the vortex.

In the experimental study by Huppertz et al. (2006) on the jet and vortex interactions showed that engine jet modifies the stability properties of the wake flow depending on the engine position and operation mode, as shown in Figure 2.20. They suggested that for high lift configurations the preferable engine position is closer to the wingtip if the focus is on the stability properties of the vortex wake.

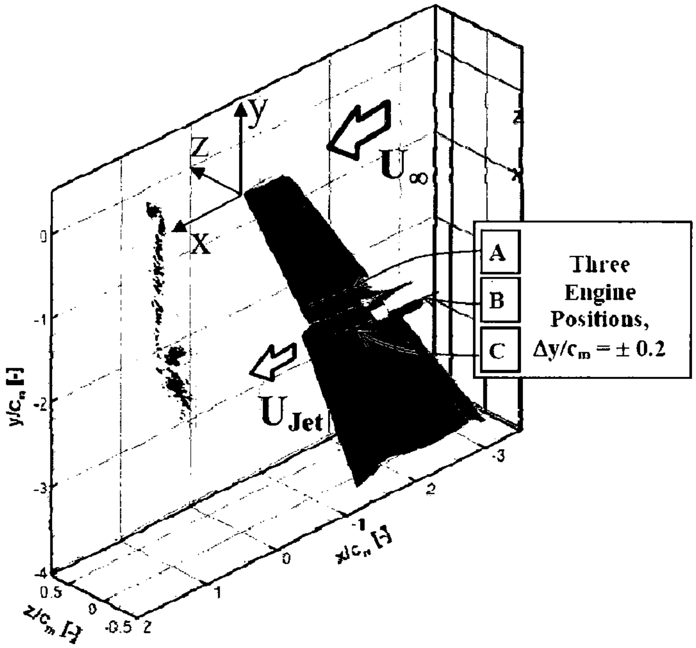

Figure 2.20: Sketch of Swept Wing Half Model and Spanwise Engine Positions (Huppertz et al., 2006)

2.4.2 Wing/Propeller Wake

Veldhuis and Rentema (1995) presented a flow field survey performed with a 5-hole pressure probe at one chord length behind a combination of a low aspect ratio semi-span wing model combined with a four-bladed tractor propeller, as shown in Figure 2.21. The survey revealed important qualitative and quantitative information on the propeller dominated interactive flow field, as shown in Figures 2.22-2.24. With the propeller running, the structure of the flow field changes radically and the strong total head rise occurs in the slipstream. There are remarkably strong spatial gradients in total pressure towards the slipstream boundary. The wake of the nacelle is completely embedded in the slipstream which is substantially distorted by the wing.

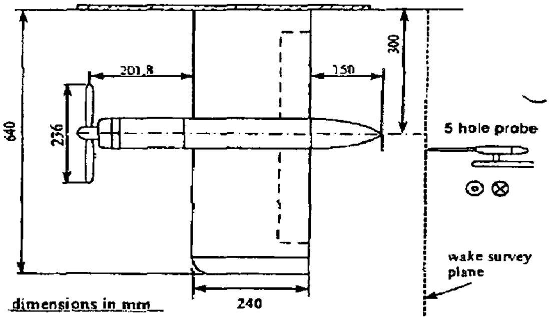

Figure 2.21: Layout of the Wind Tunnel Model With 5 Hole Probes (Veldhuis and Rentema, 1995)

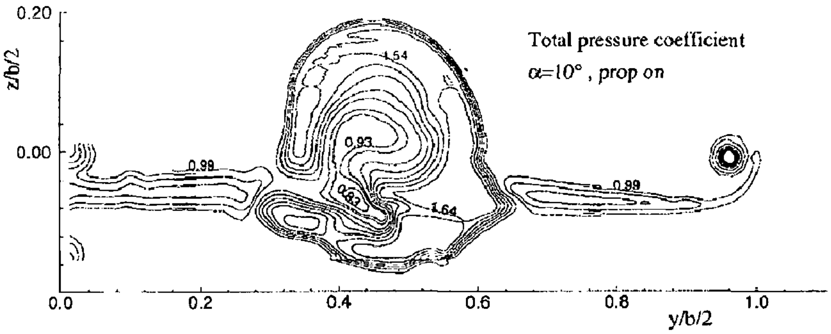

Figure 2.22: Total Pressure Coefficients at α =10 Degrees (Veldhuis and Rentema, 1995)

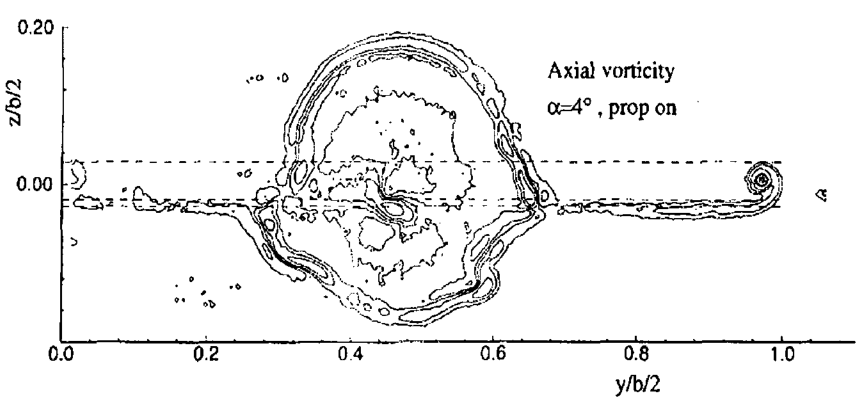

Figure 2.23: Axial Vorticity Contours at α=4 Degrees (Veldhuis and Rentema, 1995)

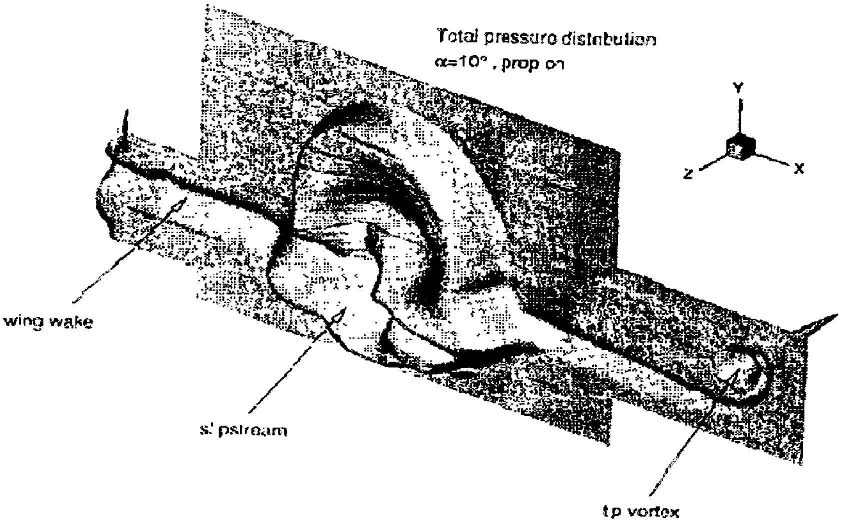

Figure 2.24: 3D View of Total Pressure Distribution at α=10 Degrees (Veldhuis and Rentema, 1995)

Chiaramonte et al. (1996) presented a survey investigating the interaction effects generated on a propeller/nacelle/half-wing configuration for different angles of attack. Determination of the instantaneous wake geometry distortion associated with different angles of attack, the influence of the distorted propeller slipstream on the load distribution along the half-wing span, and the reciprocal influence of the half-wing on the overall propeller performance were included in this survey. The wind-tunnel investigation was conducted by means of a series of overall force and moment measurements, unsteady local chordwise pressure distributions measured at different spanwise sections of the half wing, and wake flow measurements characterizing the vortex distortions and instantaneous aspects of the interaction. The results indicated that the propeller slipstream produces a significant increase in induced lift and drag coefficients along the half-wing span. However, at angle of attack, the propeller swirl influence appears to be reduced.

3 THEORY

The development of vortex theory for lifting airfoils and wings was a great step in aeronautics achieved by Lanchester and Prandtl (see Figure 3.1), due to the fact that previously all data had to be obtained from experimental work. Among others, their theory showed how two-dimensional airfoil data could be used to predict the aerodynamic characteristics of three-dimensional wings with different shapes and planforms, provided that the aspect ratio was fairly large and the assumptions of thin-aerofoil theory were met.

Figure 3.1: Ludwig Prandtl (left) and Frederick W. Lanchester (right)

3.1 The Vortex System

Lanchester's contribution was essentially replacing the actual wing with a theoretical vortex system and assuming that both impart similar motions to the surrounding air, and sustain equivalent lift force. The vortex system he proposed can be divided into three main parts:

a. The starting vortex,
b. The trailing vortex system, and
c. The bound vortex system.

Each of these may be treated separately but they are all components of a complete vortex system.

3.1.1 The Starting Vortex

When a wing is accelerated from rest, lift is not produced instantaneously. Since a stagnation point occurs on the rear upper surface (see Figure 3.2), the fluid is required to change direction suddenly at the sharp trailing edge, but as the velocity increases the fluid is unable to turn round the trailing edge to the stagnation point. Consequently, a vortex is developed just above the trailing edge, which convects downstream (see Figure 3.3). As the stagnation point moves towards the trailing edge, the lift increases progressively, and when the stagnation point reaches the sharp trailing edge a stable flow structure is established. A circulation equal to the strength of the starting vortex shed (but opposite in sign) around the wing stabilizes the stagnation point at the trailing edge.

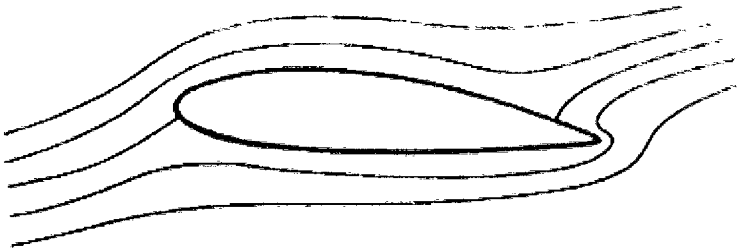

Figure 3.2: Streamlines of the Flow around an Airfoil with Zero Circulation, Stagnation Point on the Rear Upper Surface

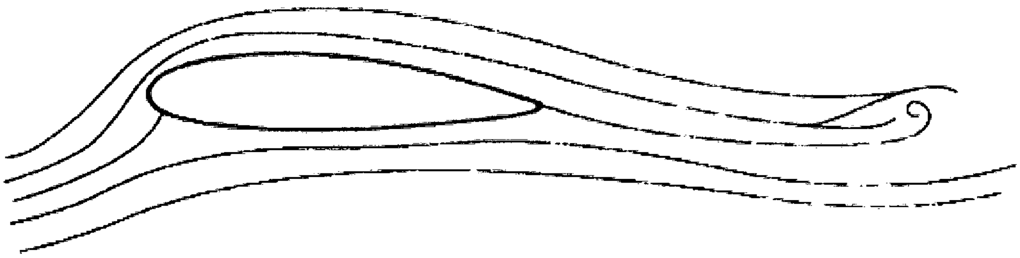

Figure 3.3: Streamlines of the Flow around an Airfoil with Full Circulation, and Stagnation Point at the Trailing Edge. The Initial Eddy is Left Way Behind.

3.1.2 The Trailing Vortex System

The vortex theorems revealed similar conclusions with the experimental studies such that vortices occur at the downstream of the lifting surfaces (see Figure 3.4). As the wing generates lift, the pressure on the upper surface of the wing is lower compared to the lower surface and the pressure beneath the wing may be greater than the surrounding atmosphere. Thus, the air over the upper surface tends to flow inwards (it moves from the tips towards the root), and similarly, air tends to flow outward below the wing. The air rolls up into a number of small streamwise vortices at the trailing edge due to the velocity differences along the span. These small vortices roll up to create two large separate vortices at both wing-tips. The strength of each of these two vortices is equal to the strength of the vortex representing the wing itself.

Figure 3.4: Trailing Vortices at Wing Tips and Flap Edges

3.1.3 The Bound Vortex System

The equivalent bound vortex system accurately simulates most of the properties, effects, disturbances, force systems, etc., of a real wing except for viscous effects. The bound vortex system is a hypothetical vortex arrangement that simulates the effects of a real wing, while both the starting vortex and the trailing system of vortices are physical entities that can be explored (viewed) when conditions are satisfied. For instance, very high velocities and low pressures exist at the core of the wing-tip vortices, and water vapor condenses as the air is drawn into the low-pressure flow field of the tip vortices which makes the vortices visible.

3.1.4 The Horseshoe Vortex

As steady flight proceeds, the starting vortex is left far behind and the trailing vortex asymptotes to infinity. What we have at hand is a horseshoe vortex (see Figure 3.5) which is made up of a bound vortex with trailing vortices at both wing tips. This vortex system satisfies all physical laws and replaces the physical wing.

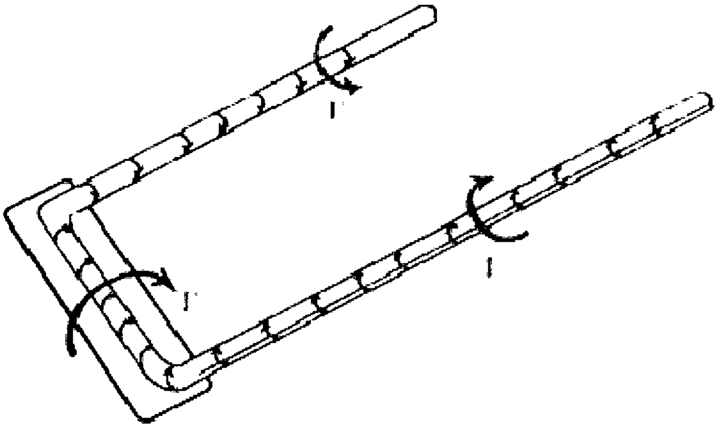

Figure 3.5: The Simplified Horseshoe Vortex

3.2 Three Dimensional Wing Theory

Before analyzing the three dimensional flow around a finite wing, a two dimensional analysis of flow around an infinite span wing can be performed. Aerodynamic analysis of subsonic flow around an unswept airfoil reveals that the flow is identical for each spanwise station and three dimensional effects cannot be observed. The lift is created due to the pressure differences between the lower and the upper surfaces of the wing, and the circulation (integrated along the chord length of the section) does not vary along the span. When the wing has finite span, the high-pressure air under the wing forces the air flow toward the upper surface of the wing at the wing tips and creates horizontal helical motions of air. At the wing tips, since the pressures acting on both top and bottom surfaces of the wing tend to equalize, the lift distribution decreases towards the tips. As a consequence, the chordwise and spanwise variation in the pressure differential between the lower and the upper surfaces of the wing may be integrated to give the resultant lift.

When analyzing the motion of air flowing around a finite span wing, it is observed that due to the spanwise pressure distribution, the air on the upper surface flows inboard towards the root, and the air beneath the wing will tend to flow outward towards the wing tips. With the addition of these inward and outward motions to the streamwise flow, the resultant flow around a wing of finite span becomes three dimensional. At the trailing edge of the wing where the flows from the upper surface and the lower surface join, the air rolls up into a number of streamwise vortices, distributed along the span, due to the difference in spanwise velocity components. At the trailing edge of the wing, these small vortices roll up into two large vortices just inboard of the wing tips (see Figure 3.6).

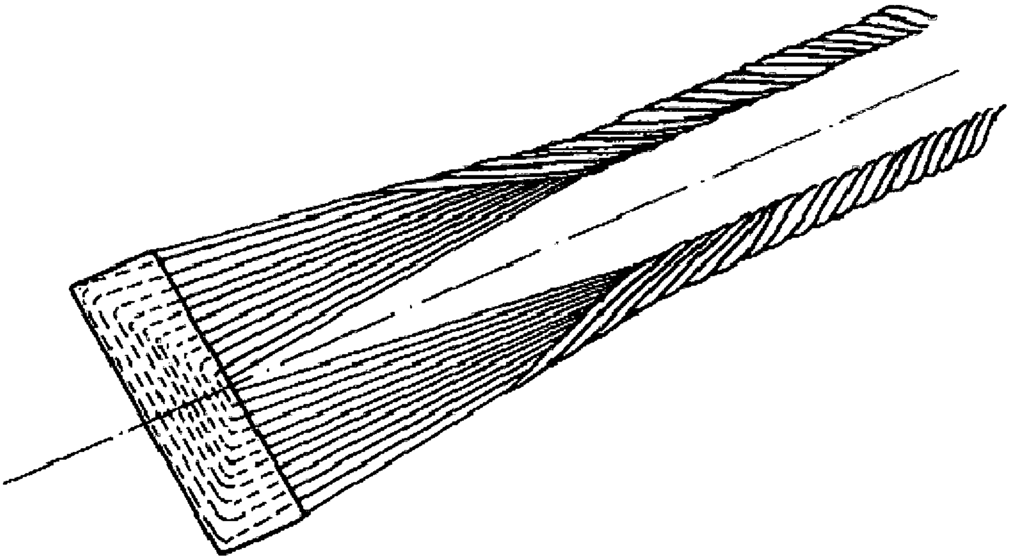

Figure 3.6: The Bound and Trailing Vortices

3.2.1 Lifting Line Theory for Unswept Wings

A theorem was proposed by Prandtl to estimate the aerodynamic characteristics of an unswept (or slightly swept) wing operating at relatively low angles of attack and which has an aspect ratio of 4.0 (or greater). This theorem was named as "Lifting Line Theory" and provides reasonable estimates of the lift and of the induced drag until boundary-layer effects become important. Prandtl and Tietjens (1957) hypothesized that each airfoil section of the wing acts as an isolated two-dimensional section, provided that the spanwise flow is not very high, and it is assumed that the lift acting on an incremental spanwise element of the wing is related to the local circulation ($\Gamma(y)$) through the Kutta-Joukowski theorem. The lift is related to the circulation through Kutta-Joukowski theorem as given in Equation 3.1:

$$l(y) = \rho_\infty U_\infty \Gamma(y) \qquad (3.1)$$

As mentioned before, the wing can be modeled by a large bundle of infinitesimal-strength filaments of vortices that lie along the quarter chord of the wing, and the sum of the strengths of all of the vortex filaments in the bundle is equivalent to $\Gamma(y)$. As the lift changes at some spanwise location (i.e., $\Delta l(y)$), the total strength of the bound-vortex system changes proportionally (i.e., $\Delta\Gamma(y)$), but the change $\Delta\Gamma(y)$ is represented in a model by having some of the filaments from the bundle turn 90° and continue in the streamwise direction (see Figure 3.7). As a consequence, the strength of the trailing vortex at any spanwise location is equal to the change in strength of the bound vortex system which depends on the spanwise variation in lift and, therefore, depends upon parameters such as wing planform, the airfoil sections that make up the wing, the geometric twist of the wing, etc.

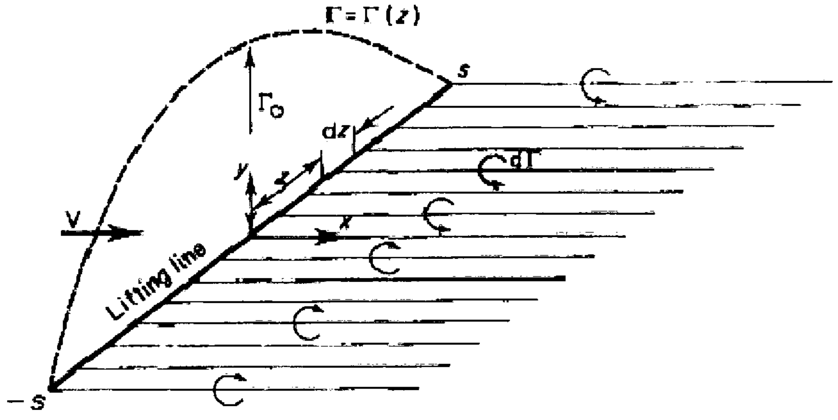

Figure 3.7: Prandtl's Lifting Line Model

3.2.2 Trailing Vortices and Downwash

Consider a semi-infinite vortex of strength ΔΓ trails from the segment Δy, as shown in Figure 3.8, with the assumption that each spanwise strip of the wing behaves as if the flow was locally two dimensional. The vortex at y induces a velocity at a general point y_1 equal to one-half the velocity that would be induced by an infinitely long vortex filament of the same strength (see Equation 3.2).

$$\delta w_{y1} = \frac{1}{2}\left[+\frac{d\Gamma}{dy}dy\frac{1}{2\pi(y-y_1)}\right] \qquad (3.2)$$

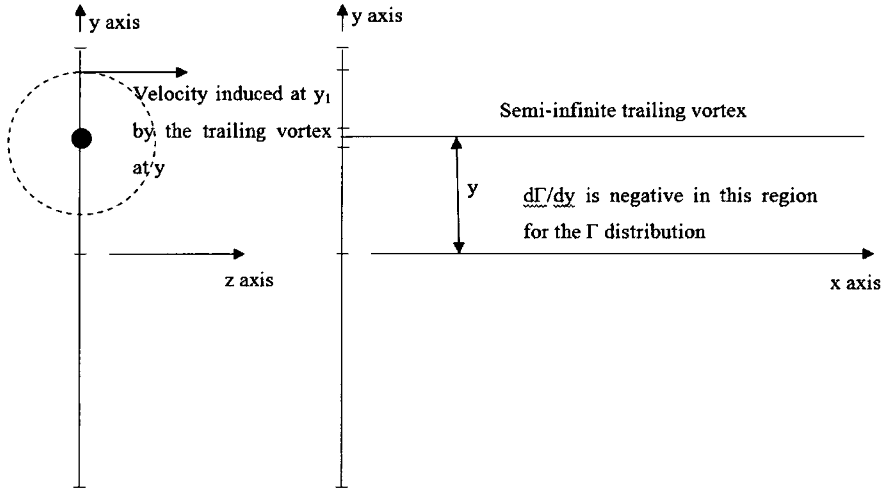

Figure 3.8: Induced Velocity at y_1

To calculate the resultant induced velocity at any point y_1 due to the cumulative effect of all the trailing vortices, the preceding expression should be integrated from the left wing tip to the right wing tip (see Equation 3.3):

$$w_{y1} = +\frac{1}{4\pi}\int_{-s}^{+s}\frac{d\Gamma/dy}{y-y_1}dy \qquad (3.3)$$

The resultant induced velocity at y_1 is, in general, in a downward direction and is called the "downwash", and the downwash angle, "ε" (see Figure 3.9) can be calculated as given in Equation 3.4:

$$\varepsilon = tan^{-1}\left(-\frac{w_{y1}}{U_\infty}\right) \approx -\frac{w_{y1}}{U_\infty} \quad (3.4)$$

The downwash has the effect of tilting the undisturbed air, so the effective angle of attack, "α_e" at the aerodynamic center (i.e. the quarter-chord) is calculated as given in Equation 3.5:

$$\alpha_e = \alpha - \varepsilon \qquad (3.5)$$

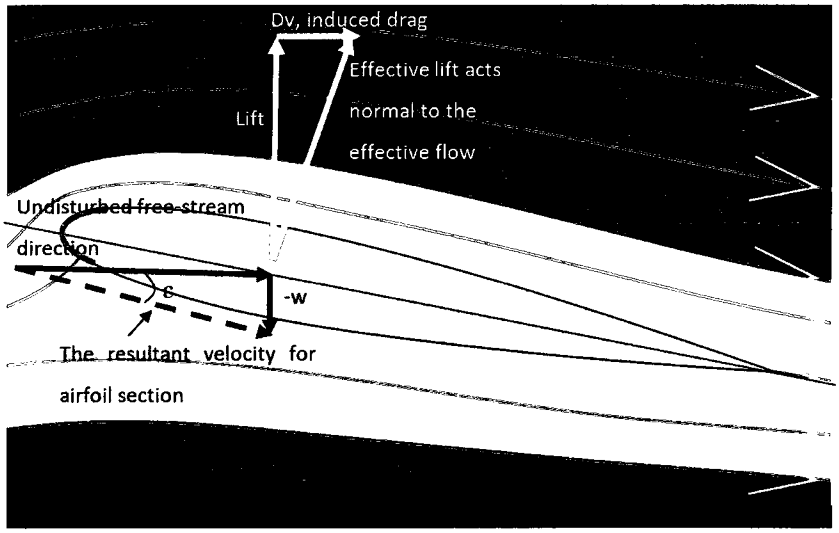

Figure 3.9: Induced Flow and Drag

Since the effective lift on the wing has a component of force parallel to the undisturbed free-stream air, additional drag force named "induced drag" or "vortex drag" occurs. Another consequence of the downwash is the less lift generated by three dimensional flow over a finite span wing compared to two dimensional flow over an infinite span airfoil.

The vortex drag can be calculated as given in Equation 3.6:

(3.6)

3.3 Propeller Analysis

3.3.1 Momentum Theory

The propeller can be thought to be an infinitely thin “actuator” disc and across the propeller the static pressure increases discontinuously. Taking into consideration the continuity of flow in and out of the cylindrical control surface (see Figure 3.10), the net flux can be written as:

(3.7)

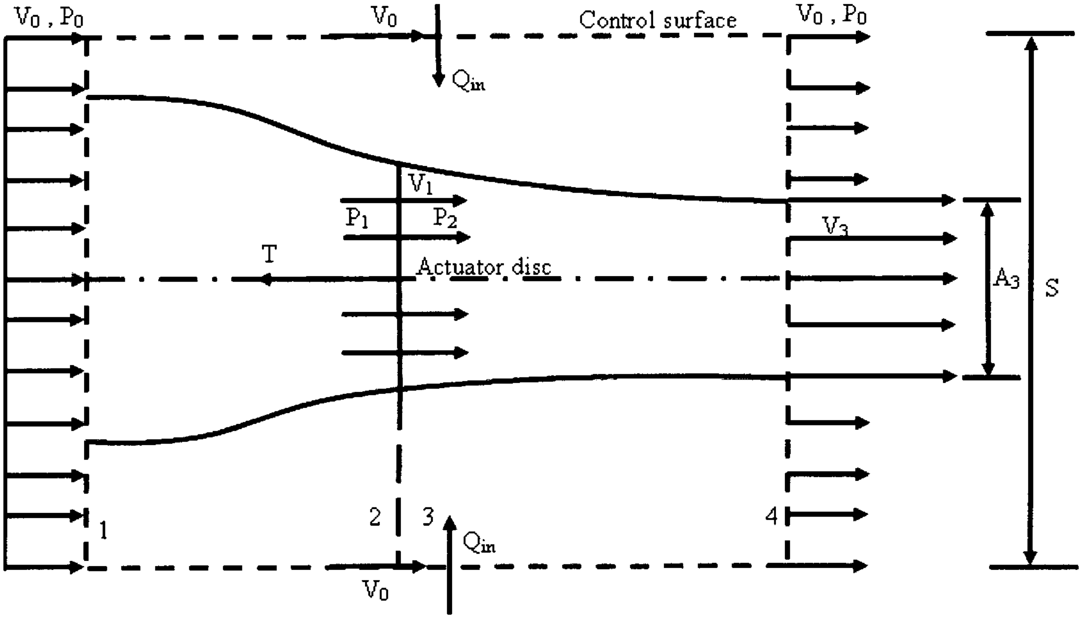

Figure 3.10: Idealized Flow Model for Application of Classical Momentum Theory

According to the momentum theory, thrust can be calculated in a simplified equation as given in Equation 3.8:

$$T = \rho A_3 V_3 (V_3 - V_0) \quad (3.8)$$

while another definition of the thrust, T, is the pressure difference across the actuator disc multiplied by the disc area, A (see Equation 3.9).

$$T = A(p_2 - p_1) \qquad (3.9)$$

Bernoulli's equation can be used to relate static pressures between inlet and actuator disc or between actuator disc and outlet, as given in Equation 3.10:

$$p_2 - p_1 = \frac{1}{2}\rho(V_3^2 - V_0^2) \qquad (3.10)$$

Noting the fact of continuity and combining the equations given the above results where the velocity through the propeller equals the average of the velocity far ahead and downstream of the propeller (see Equation 3.11):

$$V_1 = \frac{(V_3 + V_0)}{2} \qquad (3.11)$$

A new term induced velocity can be used hereafter to write the velocity relations in terms of propeller-induced velocity (*w*) as given in Equation 3.12.

$$V_3 = V_0 + 2w \quad (3.12)$$

where "*w*" is the propeller-induced velocity.

Thus the thrust can be rewritten using the term "propeller induced velocity" (see Equation 3.13).

$$T = 2\rho A(V_0 + w)w \quad (3.13)$$

The power added to the flow is given in Equation 3.14:

$$P = 2\rho Aw(V_0 + w)^2 \quad (3.14)$$

or in Equation 3.15 by applying the energy theorem:

$$P = T(V_0 + w) \qquad (3.15)$$

where the "TV_0" is the useful power and "Tw" is the induced power.

The induced velocity (w) can be obtained for both dynamic ($V_0 \neq 0$) and static cases ($V_0=0$) (see Equations 3.16 and 3.17):

For the dynamic case:

$$w = \frac{1}{2}\left[-V_0 + \sqrt{V_0^2 + \left(\frac{2T}{\rho A}\right)}\right] \quad (3.16)$$

For the static case:

$$w = \sqrt{\frac{T}{2\rho A}} \quad (3.17)$$

3.3.2 Blade-Element Theories

In order to predict the performance of an existing propeller, it is necessary to examine the aerodynamics of the blade in detail. Figure 3.11 presents the cross-section view of a three-bladed propeller that is rotating with an angular velocity of "w" rad/s and advancing through the air with velocity of V. The view of Figure 3.11 is along the blade and the section is moving to the right (due to rotation) and toward the top of the page as the propeller advances into the air.

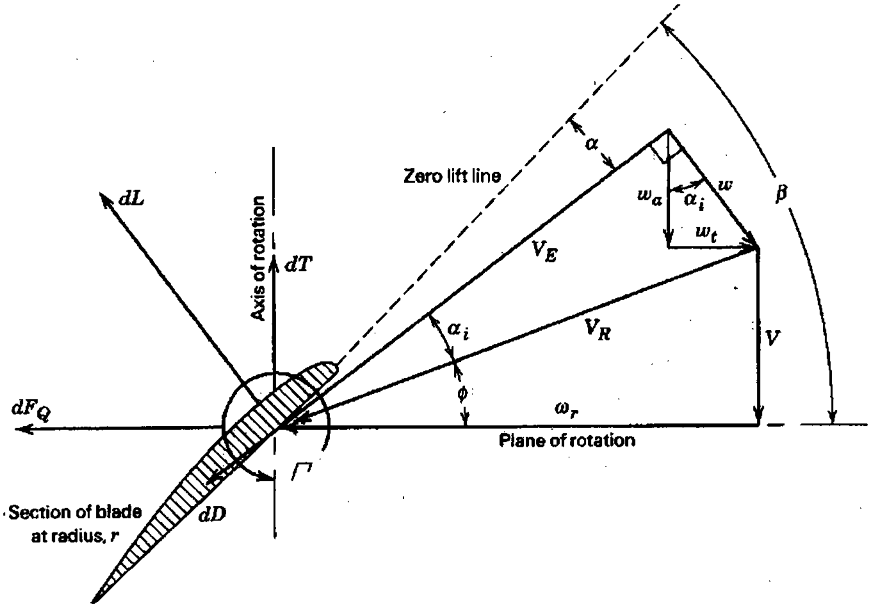

Figure 3.11: Propeller Cross-Section (Barnes, 1995)

The pitch angle, β, of the section is defined relative to the zero lift line of the airfoil section while propeller pitch angles are frequently tabulated with respect to the chord line or to a flat lower surface. The pitch of a propeller has reference to the corresponding quantity for the ordinary screw. If the propeller "screws" itself through the air without slipping, the distance it would move forward in one revolution is the pitch, "*p*" (see Equation 3.18):

$$p = 2\pi r(tan(\beta)) \qquad (3.18)$$

Propellers are sometimes categorized by their pitch-diameter ratios, as given in Equation 3.19:

$$\frac{p}{D} = \pi x(tan(\beta)) \qquad (3.19)$$

where x=r/R, the relative radius of the blade section.

A constant pitch propeller is the one whose pitch does not vary with radius. Thus for such a propeller, the pitch angle is given in Equation 3.20:

$$\beta = tan^{-1}\frac{p/D}{\pi x} \qquad (3.20)$$

3.3.3 Momentum-Blade Element Theory

The thrust, T, and torque, Q using the lift (L) and drag (D) contributions of one-blade element are given in Equations 3.21 and 3.22:

$$dT = dLcos(\phi + \alpha_i) - dDsin(\phi + \alpha_i) \qquad (3.21)$$

$$dQ = r[dLsin(\phi + \alpha_i) + dDcos(\phi + \alpha_i)] \quad (3.22)$$

where α_i is induced angle of attack resulting from the induced velocity, *w*. The differential lift (dL) and drag (dD) forces can be calculated, as given in Equations 3.23 and 3.24:

$$dL = \frac{1}{2}\rho V_E^2 cC_l dr \qquad (3.23)$$

$$dD = \frac{1}{2}\rho V_E^2 cC_d dr \qquad (3.24)$$

where C_l can be found from the Equation 3.25.

$$C_l = a(\beta - \phi - \alpha_i) \quad (3.25)$$

and section C_d is a function of the section C_l, Mach number and local Reynolds number. There is a dilemma that "α_i" is a function of "*w*" in order to get the blade loading but "*w*" depends on the blade loading. This problem is overcome by using momentum blade-element theory to reach a quadratic equation for α_i (see Equation 3.26) with the assumption that both α_i and drag-to-lift ratio is small:

$$\alpha_i^2 + \alpha_i\left(\frac{\lambda}{x} + \frac{\sigma a V_R}{8x^2 V_T}\right) - \frac{\sigma a V_R}{8x^2 V_T}(\beta - \phi) = 0 \quad (3.26)$$

where

$$\lambda = \frac{V}{\omega R}$$

$$V_R = V_T\sqrt{x^2 + \lambda^2}$$

$$\sigma = \frac{Bc}{\pi R}$$

$$\phi = tan^{-1}\frac{\lambda}{x}$$

$$V_T = \omega R$$

$$x = \frac{r}{R}$$

The induced angle of attack (α_i) can be solved as given in Equation 3.27 if the geometry, forward speed, and rotational speed of the propeller are given:

$$\alpha_i = \frac{1}{2}\left\{-\left(\frac{\lambda}{x} + \frac{\sigma a V_R}{8x^2 V_T}\right) + \left[\left(\frac{\lambda}{x} + \frac{\sigma a V_R}{8x^2 V_T}\right)^2 + \frac{\sigma a V_R}{2x^2 V_T}(\beta - \phi)\right]^{1/2}\right\} \quad (3.27)$$

The thrust and power of a propeller are normally expressed in terms of thrust coefficient "C_T", and power coefficient "C_P", as given Equations 3.28 and 3.29:

$$C_T = \frac{T}{\rho n^2 D_P^4} \qquad (3.28)$$

$$C_p = \frac{P}{\rho n^3 D_p^5} \qquad (3.29)$$

where "n" is rotational speed in revolutions per second and "D_P" is the propeller diameter. Another useful term is the "advance ratio (J)" (see Equation (3.30)), which can be defined as the ratio of the distance traveled forward per each rotation of the propeller. By using advance ratio the propeller diameter and RPM were decided to simulate realistic flow characteristics for test setup.

$$J = \frac{V}{nD} \quad (3.30)$$

4 EXPERIMENTAL WORK

4.1 Overview

To improve understanding of the wake flow characteristics with variation of several parameters, a realistic aircraft model was designed to be tested in the Old Dominion University (ODU) low-speed wind tunnel. In this Chapter, details of the model, facilities, experimental design, and regression model adequacy checking will be given in order as:

a. The design and characteristics of the model in Section 4.2,
b. The details of facilities and instrumentation in Section 4.3,
c. The experiment design in Section 4.4,
d. The regression model adequacy checking in Section 4.4.

Since the wing wake is symmetrical along the longitudinal axis of an aircraft, a half model was used to simulate the wake flow. A model of a generic commuter transport, used for wake hazard studies, was recovered from the Langley Full Scale Tunnel (LFST) as shown in Figure 4.1. The model was extensively modified to create a medium range twin-engine military cargo aircraft resembling a C-160, CN-235, or G-222, etc.

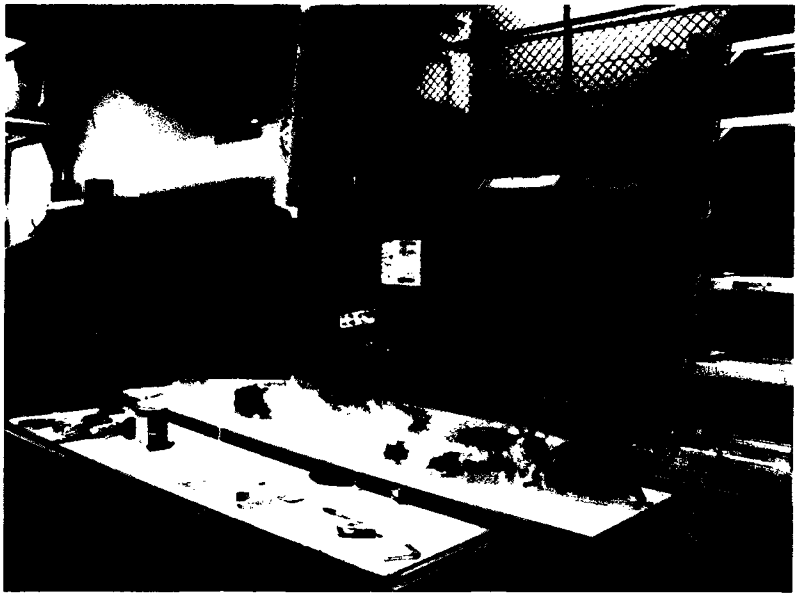

Figure 4.1: Model Under Construction

The instruments used to measure and analyze the wake flow were the Particle Image Velocimetry (PIV) and the Hotwire Anemometry (HWA) system.

Since medium range twin-engine military cargo aircraft typically have propellers as a propulsion system, an electric motor with a propeller installed on the shaft was used to create a propeller wake to interact with the wing tip and flap vortices.

The tests were conducted at the large test section of the ODU low-speed wind tunnel due to the dimensions of the model and to permit measurement of the wake flow with as much detail as possible. A two dimensional electro-mechanical traverse mechanism was used to make wake flow measurements with both PIV camera and hotwire probe.

4.2 Model

During the process of specifying the dimensions of the model, research was performed to analyze the medium range twin-engine military cargo aircraft being used by NATO member countries. CASA CN-235 and Transall C-160 are the two candidates that are in the inventories of the Turkish Air Force and Aeritalia G-222 is a third suitable candidate in this category of aircraft.

The overall specifications of the candidate aircraft used in the Turkish Air Force and the comparison with the model are shown in Table 4.1. Among many parameters to compare, some factors are particularly useful such as:

a. "J", advance ratio,
b. "C_p", power coefficient,
c. "C_t", thrust coefficient,
d. "β", Pitch angle of the propeller
e. Ratio of induced velocity to freestream velocity (static case),
f. Ratio of induced velocity to freestream velocity (dynamic case),
g. Ratio of propeller diameter to wing span.

SPECIFICATIONS	C-160	CN-235	G-222	MODEL
(D_P) Propeller diameter- m	5.50	3.66	4.88	0.36
(V_A) Airdrop Speed- m/sec	60.00	60.00	60.00	9.00
(n) Propeller revolution- RPS	20.00	23.07	20.00	43.26
(J) Advance ratio	**0.55**	**0.71**	**0.61**	**0.65**
(C_p) Power coefficient	**0.09**	**0.13**	**0.09**	**0.15**
(P) Engine power- Watt	4,485,000	1,305,000	2,535,000	84.61
(T) Engine thrust- N	30,043	10,116	17,167.50	3.67
(C_t) Thrust coefficient	**0.07**	**0.09**	**0.06**	**0.10**
(b) Wing span- m	40.00	25.81	28.70	2.30
(β) Propeller Pitch angle-degree	**9.85**	**12.75**	**11.07**	**11.69**
(W) Aircraft weight- N	480,690	161,865	274,680	-
Propeller number	2	2	2	2
Induced power (static) watt	682,548	200,422	332,291	14.23
Power added to flow- watt	2,031,869	667,199	1,127,942	41.54
1. Useful power- watt	1,802,587	606,993	1,030,050	36.66
2. Induced power- watt	229,282	60,205	97,892	4.88
Induced velocity (static) m/sec	22.72	19.81	19.36	3.88
Induced velocity (dynamic) m/sec	7.63	5.95	5.70	1.33
Induced velocity (static)/ freestream	**0.38**	**0.33**	**0.32**	**0.39**
Induced velocity (dynamic)/ freestream	**0.13**	**0.10**	**0.10**	**0.13**
Propeller Area- square meter	23.76	10.52	18.70	0.10
Ratio of Propeller diameter to Wing Span	**0.14**	**0.14**	**0.17**	**0.15**

Table 4.1 Overall Specifications of Medium Range Twin-Engine Military Cargo Aircraft and the Model

The geometry of the half model is illustrated in Figures 4.2 and 4.3.

Figure 4.2: Model (Side view)

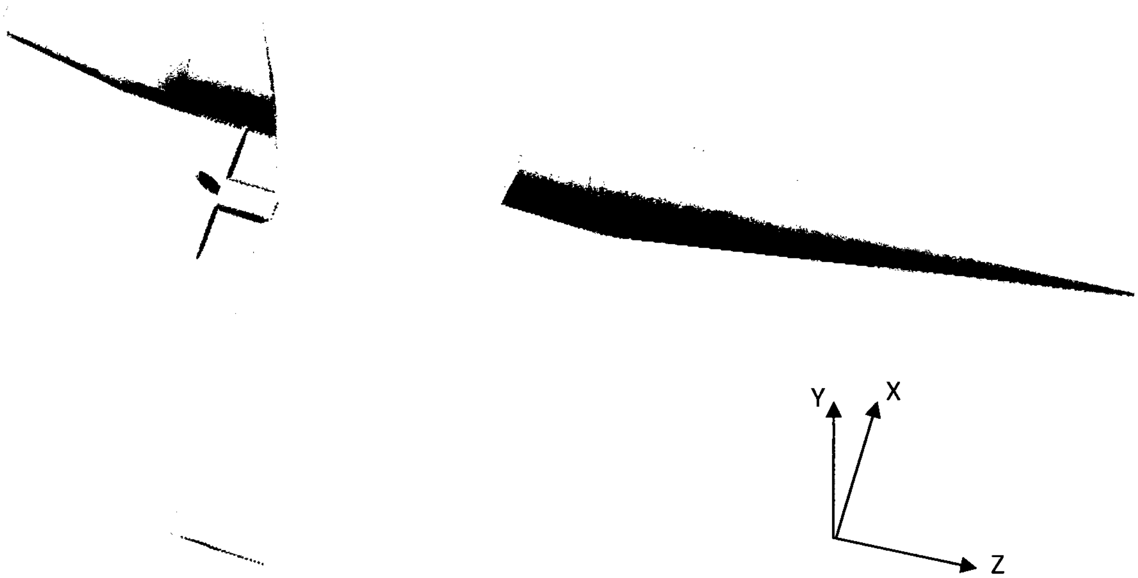

Figure 4.3: Model (Perspective view)

4.2.1 Fuselage and Wing Geometry

Instead of creating a new model, a model previously used at NASA Langley Research Center in the 1990's for free-flight wake vortex hazard tests was modified. When the entire model was brought to ODU, the wing layout was low and model fuselage is long to be used. First, the wing was relocated to the top of the fuselage as shown in Figure 4.4. Second, the fuselage was shortened to meet the requirements of the wind tunnel installation.

Figure 4.4: Wing Mounted to the Top of the Fuselage

Third, the full model was cut along the longitudinal axis to create a half model. The major dimensions of the model are given in Figure 4.5. Finally, the model was mounted on a ground board which is a flat plate, mounted a short distance above the test section floor (see Figure 4.6).

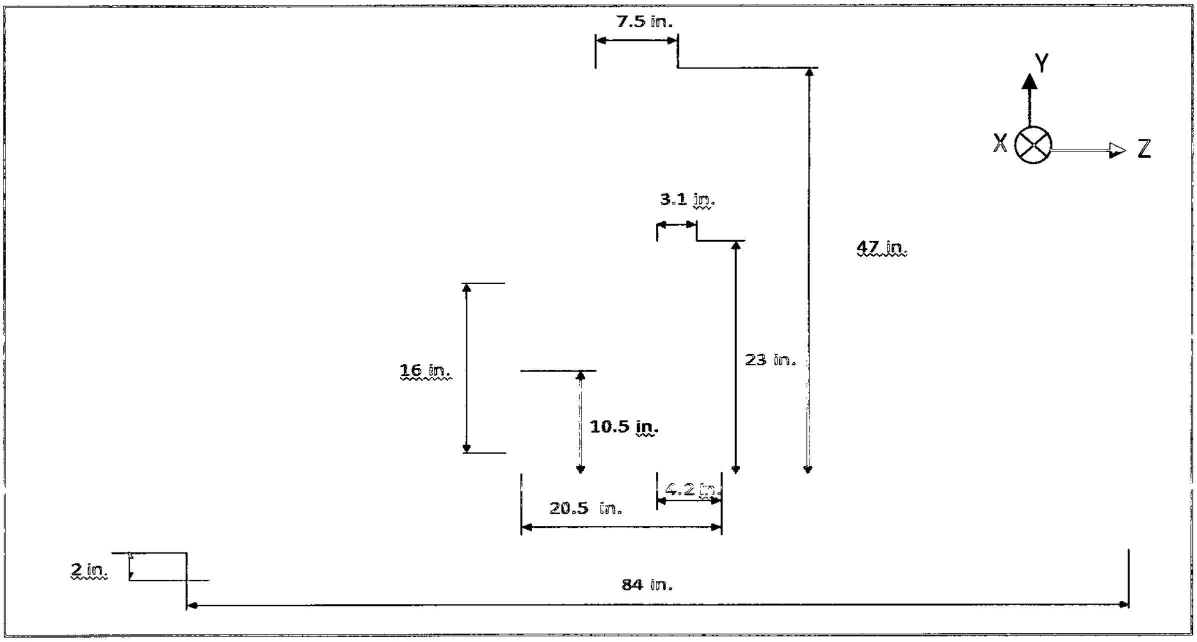

Figure 4.5: Dimensions of the Model

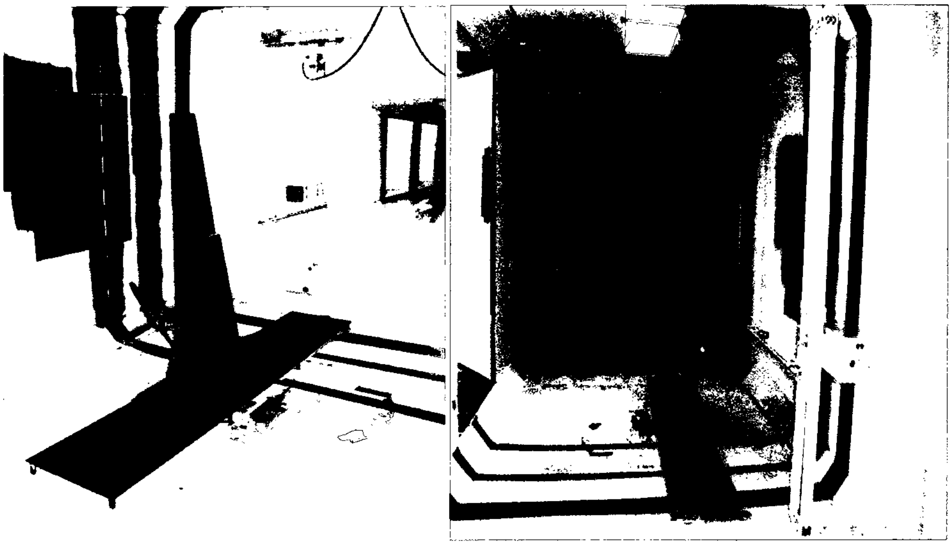

Figure 4.6: Model, Hotwire Probe and PIV Camera Located in the Test Section (left- view from upstream and right-view from downstream)

The airfoil used for the wing was the NASA NLF (1)-0416 and the geometry of the airfoil is shown in Figure 4.7:

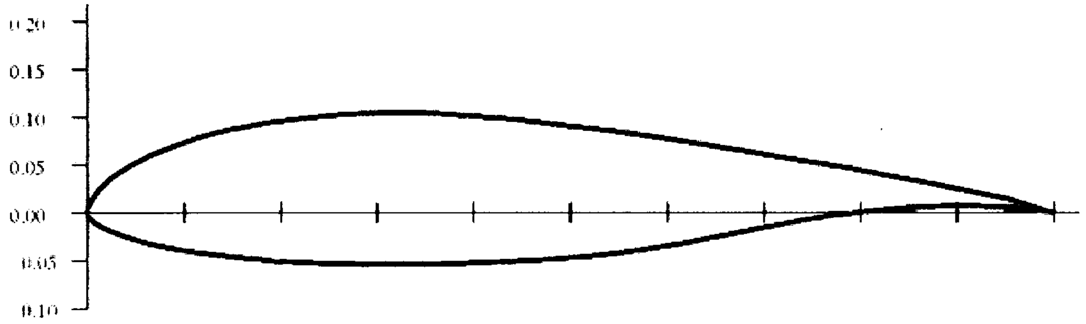

Figure 4.7: Airfoil Used for the Wing- NASA NLF (1)-0416 (Airfoil Investigation Database, http://www.worldofkrauss.com)

The aerodynamic characteristics of the NASA NLF (1)-0416 airfoil are given in Table 4.2, Figures 4.8 and 4.9:

Thickness	15.9%	C_L @ **Max L/D**	1.187
Camber	2.5%	**Max L/D angle**	5.5
Max C_L	1.528	**Stall angle**	14.0
Max C_L angle	13.5	**Zero lift angle**	-4.5
Max L/D	58.903		

Table 4.2: Aerodynamic Characteristics of NASA NLF (1)-0416 Airfoil (Airfoil Investigation Database, http://www.worldofkrauss.com)

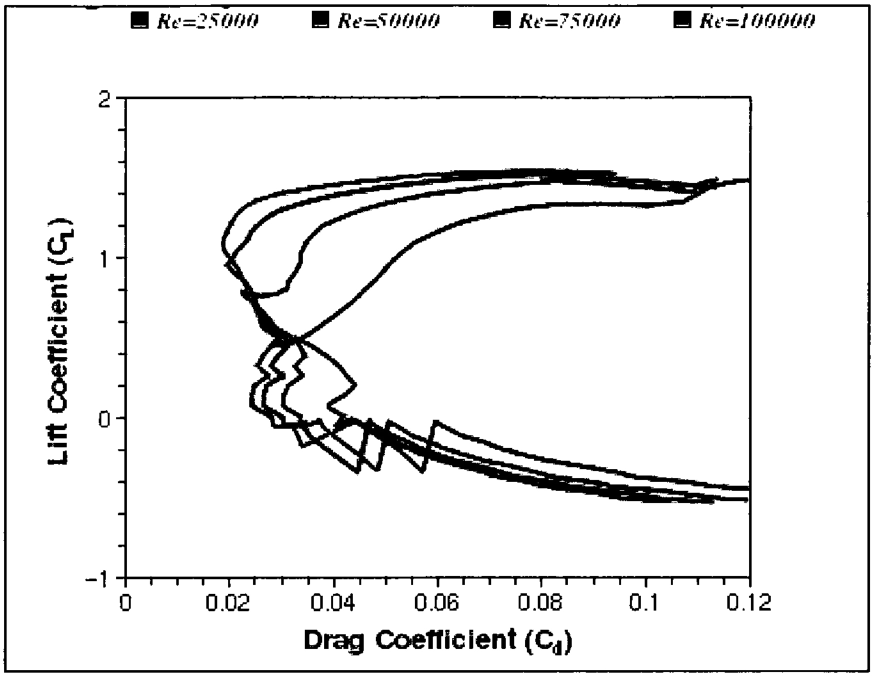

Figure 4.8: Drag Polar for NASA NLF (1)-0416 Airfoil

(Airfoil Investigation Database, http://www.worldofkrauss.com)

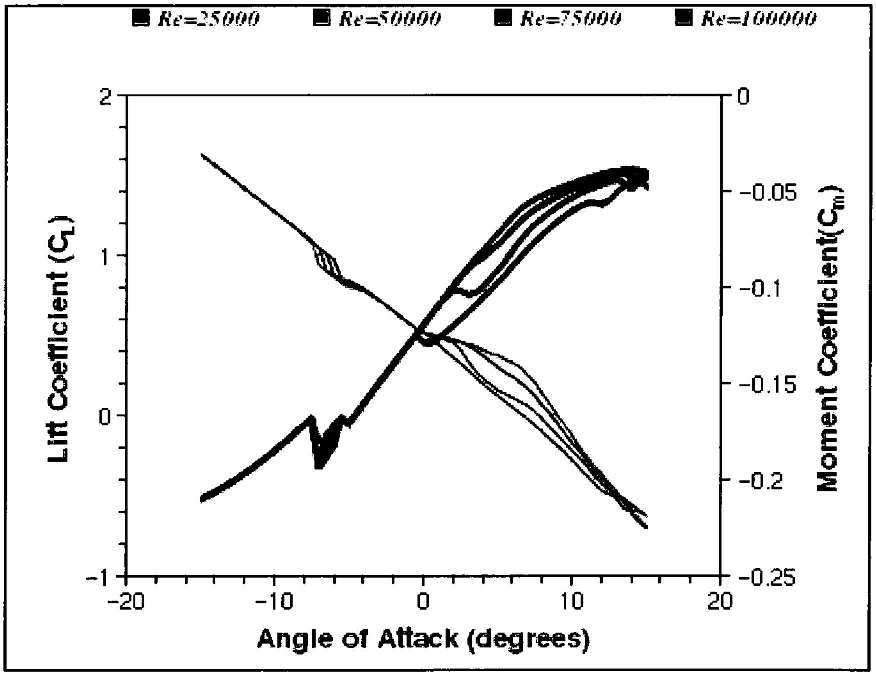

Figure 4.9: Lift and Momentum Coefficients for NASA NLF (1)-0416 Airfoil

(Airfoil Investigation Database, http://www.worldofkrauss.com)

To create a boundary layer on both fuselage and wing similar to a real flight case some precautions were taken. The model was mounted on a two inch raised flat plate in order to avoid interaction with the boundary layer of the wind tunnel. Thus the boundary layer on the fuselage starts on the nose of the model (the leading edge of the flat plate was sharp-edged to prevent flow separations at the leading edge of the plate). The flow was tripped to insure a turbulent boundary layer at the leading edge of the wing by adhering 0.04 inch size roughness elements at 5% of chord length back from the leading edge, as shown in Figure 4.10.

To change the Angle of Attack (AOA) of the model, the model was rotated around the vertical axis located at the quarter chord of the wing by means of a rotatable support. After the AOA was changed to the desired value, the model was secured during experimentation by screws in both the long front and rear support legs placed between the plate and the wind tunnel floor.

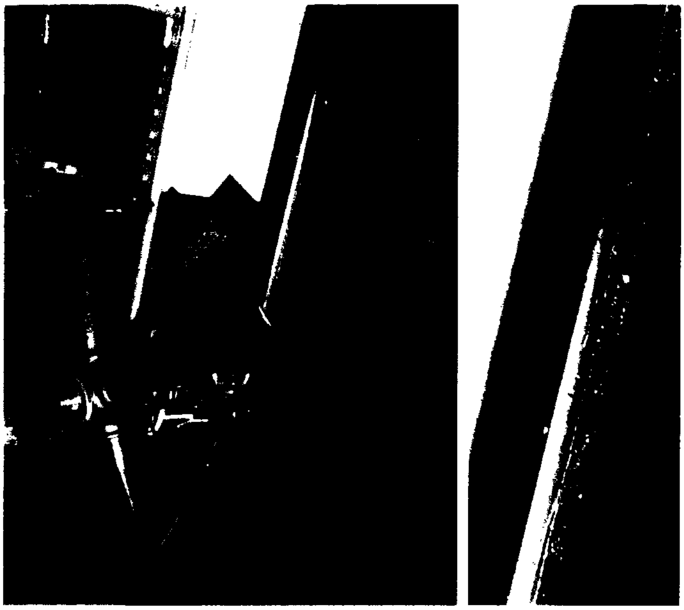

Figure 4.10: The Flow is Tripped by Adhering Roughness Elements on the Wing (Left); Magnified View of the Roughness Elements (right)

The flap extends spanwise from 11.5% inboard to the 54% outboard of the half wing span while the length of the trailing flap is 25% of the local chord length (see Figure 4.11). A mechanism was built to change the flap angle to three different values (i.e. 15°, 32.5 ° and

50°). The locations of the flap and the propeller axis were chosen such that the flap vortex was not in the wake of the propeller wake in order to observe the behavior of the flap vortex under differing conditions. The position of the flap and its dimensions were decided by comparing the geometry and locations of the real medium range twin-engine military cargo aircraft flaps.

Figure 4.11: Wing Flap (left-rear view and right-side view)

4.2.2 Propeller and Propulsion Simulation

Determination of the propeller diameter along with the pitch angle was performed by making comparisons with typical medium range twin-engine real military cargo aircraft (such as C-160, CN-235, and G-222) used for air-drop and air-refueling operations, as shown in Table 4.1. The specifications of the propeller were chosen as listed below:

a. The propeller is four bladed as mostly used by the real aircraft,
b. The diameter of the propeller is 16 inches,
c. 22° is the nominal pitch angle of the propeller, and
d. The RPM value is constant (2,000 RPM) throughout the experimentation.

The "J" (Advance Ratio) value of the propeller, and the ratio of the induced velocity to freestream velocity are the key parameters to establish the correct propeller operating conditions while the wing and body dimensions are the key parameters to establish the blade diameter.

The propeller used was procured from a supplier to the model aircraft market (SOLO Propellers). The blades of the propeller were machined from prime grade Eastern Maple, the blades were square tipped and the diameter of propeller was 16 inch. The hub was also supplied by SOLO Propellers, and the pitch angle of the propeller was adjusted by first turning the dial on the hub as shown in Figure 4.12 and then locking of the hub at the desired angle.

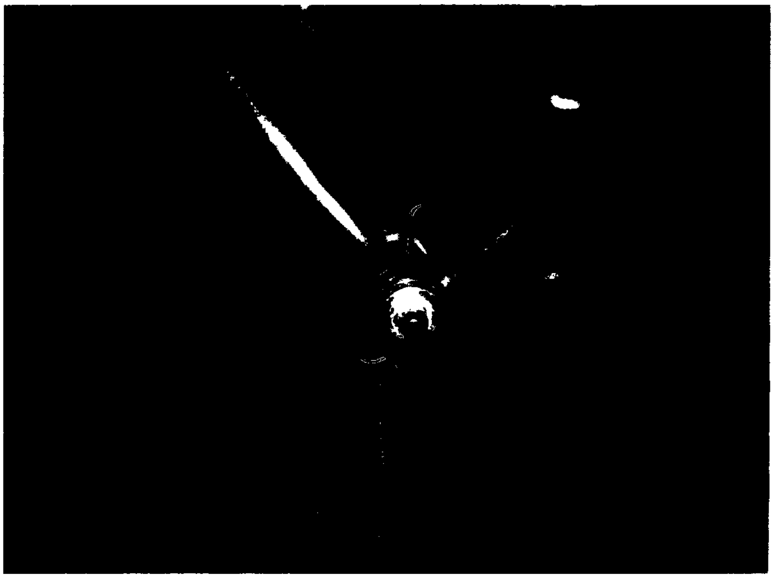

Figure 4.12: Propeller and Hub

The airfoil section used for the propeller blades is Clark Y and the geometry of the Clark Y airfoil is given in Figure 4.13.

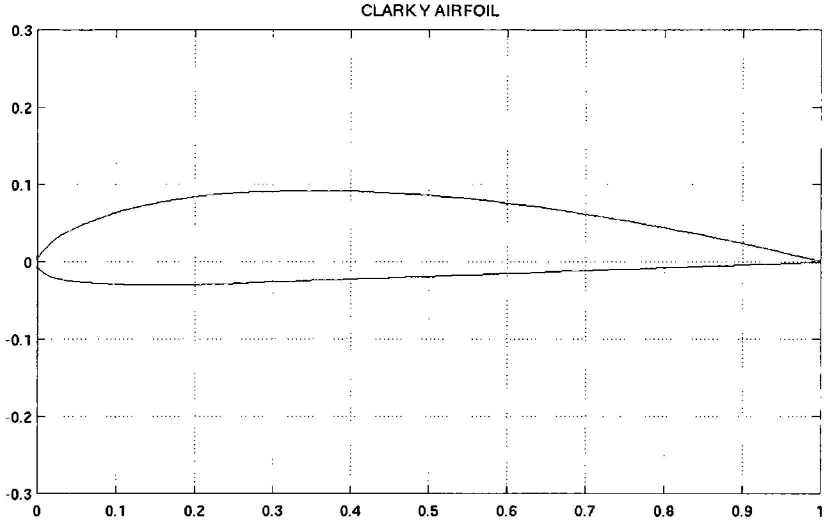

Figure 4.13: Geometry of Clark Y Airfoil
(http://www.aerospaceweb.org)

Since most small electric motors have very high rotation with moderate voltages values, an electric motor with gearbox was chosen in order to maintain constant rotational speed of 2,000 RPM. The motor is AXI 2826 GOLD LINE with a PG 4/33 gearbox as shown in Figure 4.14.

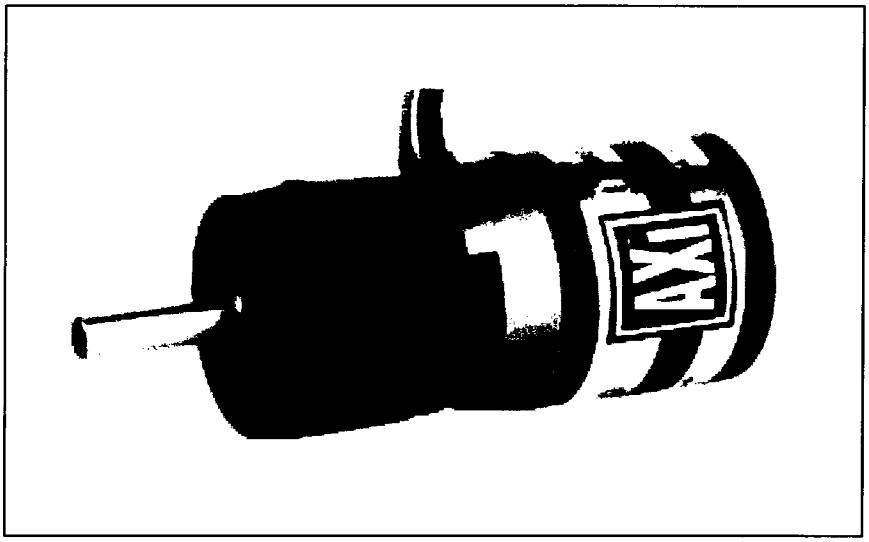

Figure 4.14: Motor and Gearbox
(Black colored front part is the gearbox)

Specifications for the AXI 2826 PG 4/33 motor are:

- RPM/V: 1130
- Max. Efficiency current: 25 - 37A (>75%)
- No load current/ 8V : 2.9 A
- Current capacity: 55A / 60s
- Internal resistance : 30 mohm
- Dimensions : 35 x 80 mm
- Shaft diameter : 6 mm
- Weight with cables : 255 g

4.3 Facility and Instrumentation

4.3.1 ODU Low-Speed Wind Tunnel

The ODU Low-Speed Wind Tunnel is an atmospheric pressure, closed return, fan-driven type, with two closed test sections. The dimensions of the large test section are 7x8x7 ft (HxWxL) and the dimensions of the small test section are 3x4x8 ft. The tunnel is powered by a 125 HP AC induction motor with a Westinghouse variable frequency drive. The sketch of the ODU Low-Speed Wind Tunnel is shown in Figure 4.15:

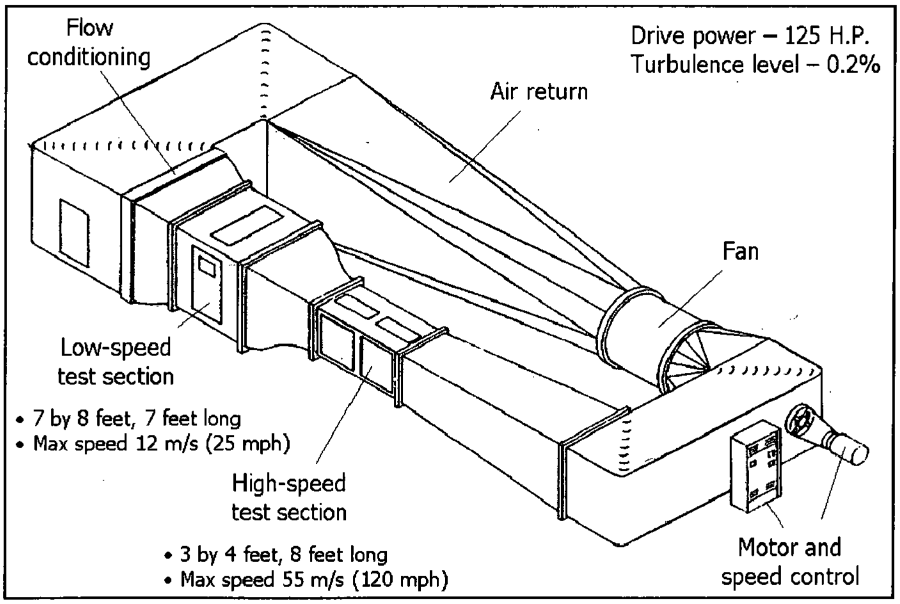

Figure 4.15: ODU Low-Speed Wind Tunnel

The speed range for the small section is 10 to 55 m/s whereas the maximum speed for the large test section is 12 m/s. The lower velocity is set by fan RPM stability and the upper is set by maximum drive power. The turbulence level of the empty test section is around 0.7%, slightly higher at lower speeds. There is no thermal control system for the wind tunnel, but it reaches steady-state below 70% speed. Flow quality in the large test section has been evaluated recently in a study by Doane (2010), showing that velocity uniformity is of the order of ±1.4%.

Since there is a converging part at the downstream region of the low speed test section (see Figure 4.16), the velocity within this region changes gradually. The measurements for these experiments are out of the region where the velocity increases significantly.

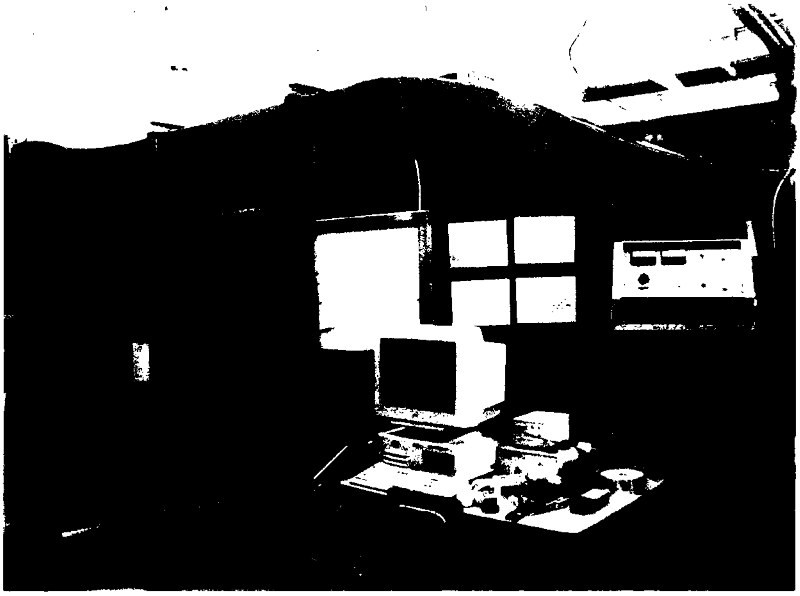

Figure 4.16: Low-Speed Test Section of ODU Wind Tunnel

A 2-axis (x and y axis, where the positive z axis is the air flow direction within the wind tunnel) computer controlled traverse mechanism was mounted to the upper wall of the wind tunnel in the downstream region of the low speed test section. Since the traverse mechanism is 2 axes, measurements for different longitudinal stations were performed by holding the probe with supports of different lengths. The 2-axis traverse mechanism is shown in Figure 4.17.

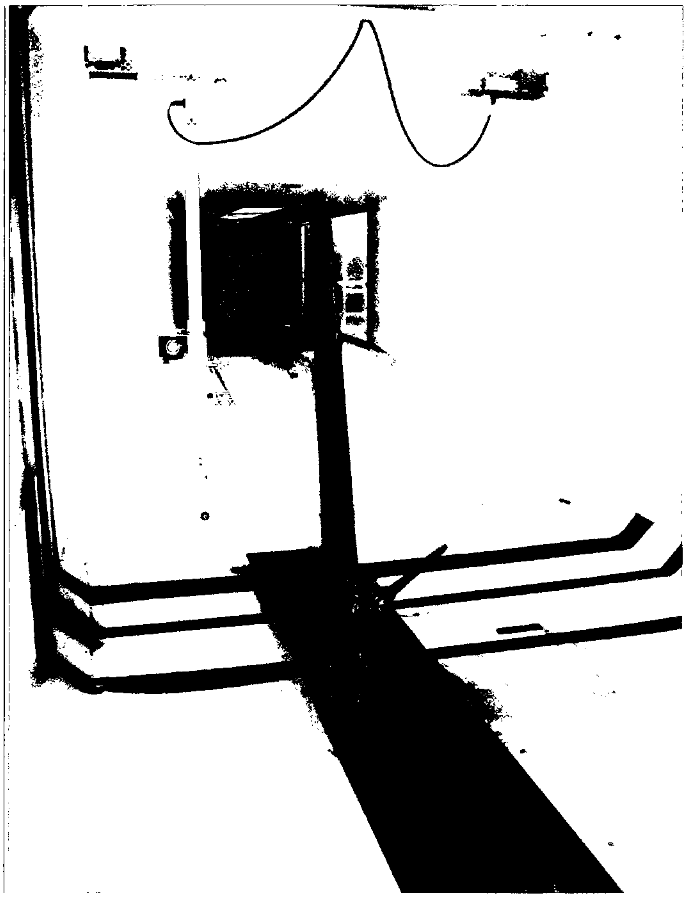

Figure 4.17: 2-Axis Traverse Mechanism

(View from upstream)

4.3.2 PIV System

The set-up of a Particle Image Velocimetry (PIV) system typically consists of several subsystems: the seeding system, light source (laser), optical system (digital camera), and PIV software (commercially available by companies such as TSI or DANTEC).

Raffel et al. (2007) summarized the PIV technique. As tracer particles are added to the flow for seeding, the seeding particles are then illuminated at least twice in a plane within a very short time interval, usually by means of a pulsed laser. The laser light scattered by the particles is recorded either on a single frame or on a sequence of frames by using a camera. The displacement of the particle images between the light pulses has to be determined from the camera captures by using software in a host computer. In order to handle the large amount of data, sophisticated post-processing is required.

Figure 4.18 illustrates a typical set-up for PIV in a wind tunnel. Small tracer particles are added to the flow for seeding. A plane of flow is illuminated twice by using a laser in which the time delays between the pulses depends on the mean flow velocity and the magnification at imaging. The tracer particles are assumed to move with the local flow velocity between the consecutive illuminations. The lights scattered by the tracer particles are recorded by using a lens either on a single or two separate frames of charge-coupled device (CCD) sensor and the output of the CCD sensor is stored in the memory of a computer.

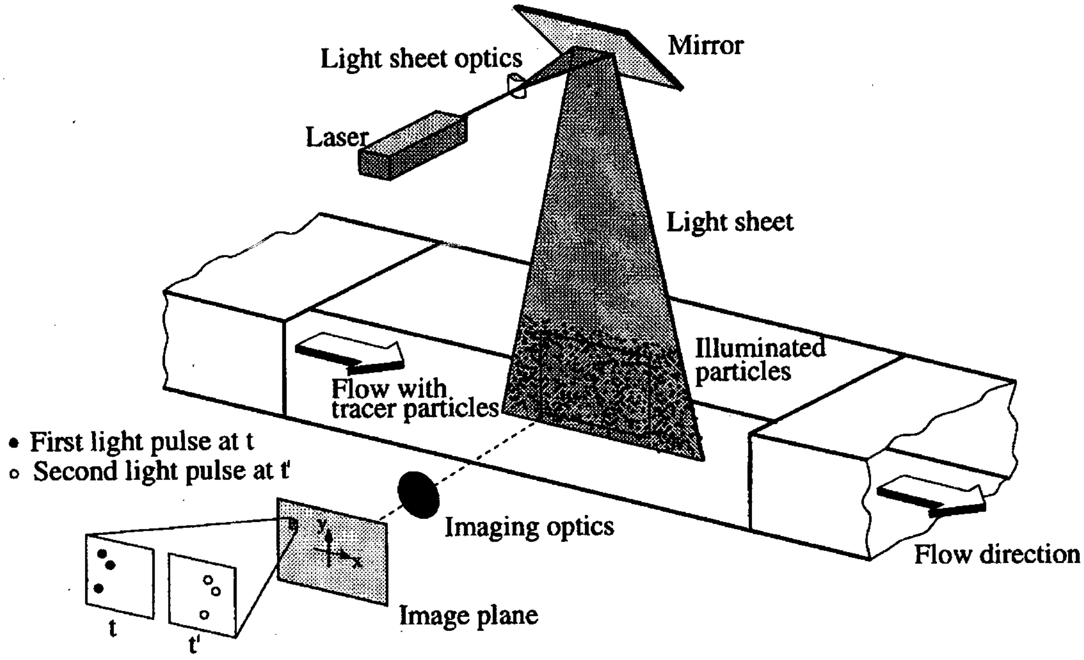

Figure 4.18: Experimental Arrangements for Particle Image Velocimetry in a Wind Tunnel (Raffel et al., 2007)

The evaluation of the digital PIV recordings is performed by dividing the PIV recordings into small subareas called "interrogation regions". The local displacement vector of the tracer particles is calculated by finding the distance traveled by the tracer particles between the first and second illuminations within each interrogation region by using statistical methods (auto- and cross- correlation). It is assumed that most of the tracer particles within an interrogation area have moved homogeneously between the two illuminations. The projection of the local flow velocity vector into the plane of the light sheet (two component velocity vector) is calculated from the mean distance traveled by the tracer particles and the time delay between the two illuminations.

Considering the flow domain size, the amount of data are actually considerable but the technology of computers allows for evaluating thousands of instantaneous velocity vectors within few seconds. If online monitoring of the flow is required, dedicated hardware processors are commercially available which perform evaluations of similar quality within fractions of a second.

4.3.2.1 PIV in Aerodynamics

In fluid mechanics, especially in unsteady flows, PIV allows the capture of whole velocity fields instantaneously which makes it unique compared to the other techniques. PIV makes it possible to obtain spatially resolved measurements of the instantaneous flow velocity field within a very short time. It also allows the detection of large and small scale spatial structures in the flow velocity field. In order to validate computational fluid dynamics applications, adequate experimental data are needed. If both numerical and experimental applications validate each other then it can be concluded that the physics of the problem has been modeled correctly. The experimental data of a flow field must possess high resolution in time and space in order to be able to compare them with high density numerical data fields. The PIV technique is an appropriate experimental tool for this task, especially if information about the instantaneous velocity field is required.

PIV systems used in wind tunnels are operated for velocities starting from 1 m/sec (for example in boundary layers) to 600 m/sec (in supersonic flows with shocks). The application of the PIV technique in large, industrial wind tunnels poses a number of special problems: large observation area, long distances between the observation area and the light source and the recording camera, restricted time for the measurement, and high operational costs of the wind tunnel.

4.3.2.2 PIV Measurements of the Dissertation Experiment

The specifications of the PIV measurements were adjusted in order to measure the planar (x and y axes components) velocity field in the wake of the aircraft model, such that the laser source illuminated the planar components of the velocity field and the camera captured images of illuminated smoke particles viewing from downstream.

The laser source was located at the side wall of the wind tunnel and used to illuminate the smoke injected air flow twice with a 0.50 μs delay, and the frequency of the measurements was set at 3.75 Hz. Due to the coverage limitations of the camera capture, the whole flow field was divided into subareas to make measurements. The limited camera coverage areas are shown as colored areas in Figure 4.19. To make successful measurements with PIV, the laser source was adjusted to coincide with the camera field of view.

The camera was located at downstream and installed to a 2-axis traverse mechanism (see Figures 4.19 and 4.20). The camera did not disturb any part of the wake since it was located sufficiently far downstream of the model. The total number of image pairs captured for each area was 250. The images were then analyzed with TSI Insight Version 5.0 software to recover velocity field. The velocity field data were then analyzed and data about turbulence and Reynolds stresses were derived by using Tecplot 360 with a TSI PIV plug-in.

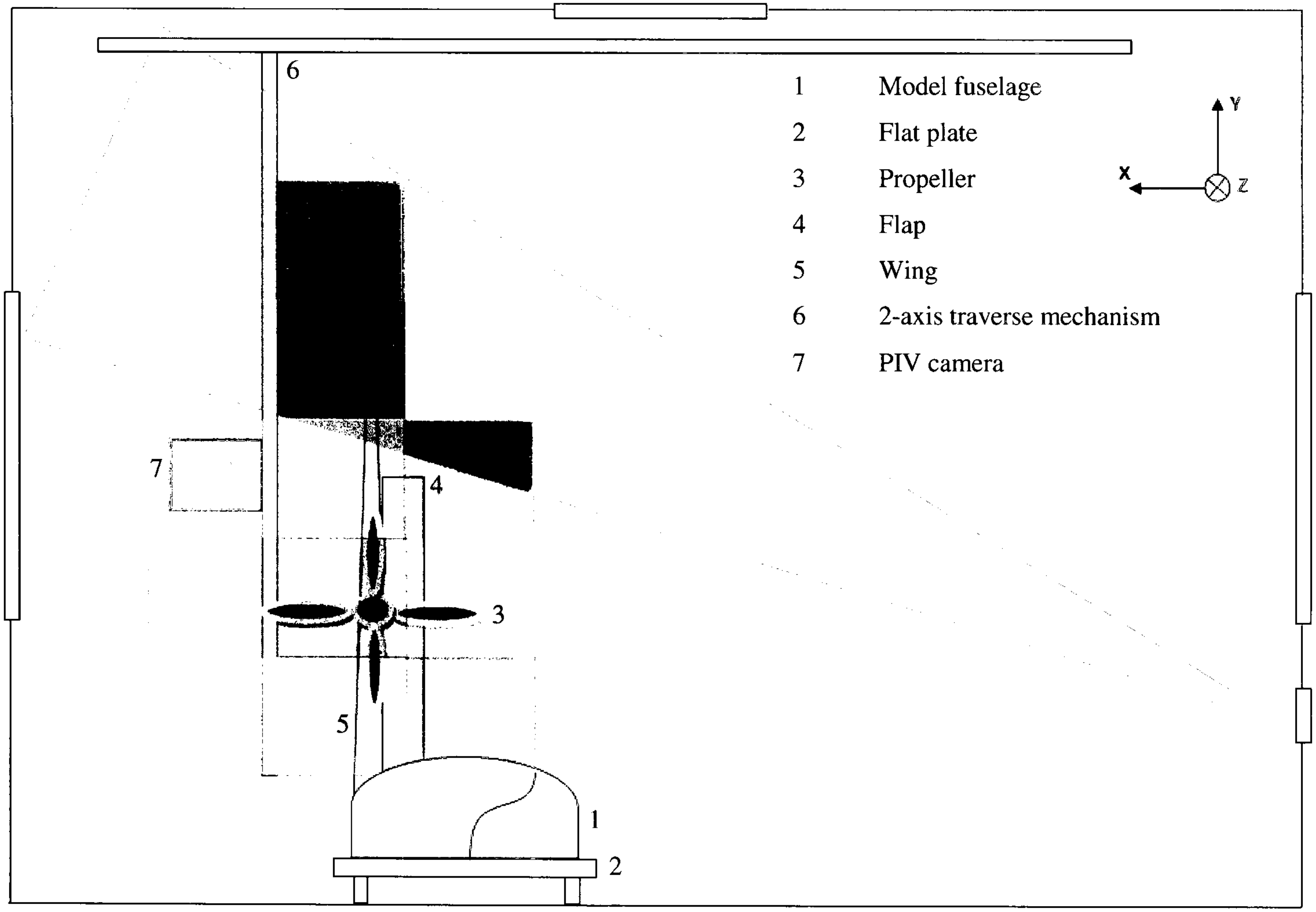

Figure 4.19: Experiment Layout for PIV Measurements (View from Upstream)

Figure 4.20: PIV Camera Located at the Downstream of the Model (Positive z Axis is along the Flow Direction)

4.3.3 Hotwire System

4.3.3.1 Hotwire Anemometry

Hotwire anemometry has been used extensively for many years as a research tool in fluid mechanics. Fundamentally, a hotwire makes use of the principle of heat transfer from a heated surface being dependent upon the flow conditions passing over it. Hotwire anemometers are used for measuring fluid velocity by sensing the changes in heat transfer from a small, electrically heated sensor exposed to the fluid motion. These changes in heat transfer are related to velocity, density, and the temperature of the fluid. Their small size and good frequency response makes them suitable for studying flow details, particularly in turbulent flow.

For anemometer measurements a TSI IFA-100 constant temperature hotwire anemometer was used (Figure 4.21). Voltage outputs were monitored via a National Instruments Data Acquisition (DAQ) card via LabView. Three custom written LabView programs were used for calibration, data acquisition, and data analysis (Figure 4.22). King's Law was used for calculating the velocity values from the voltage values measured by the anemometer. Detailed information about King's Law and calibration data can be found in Appendix B.

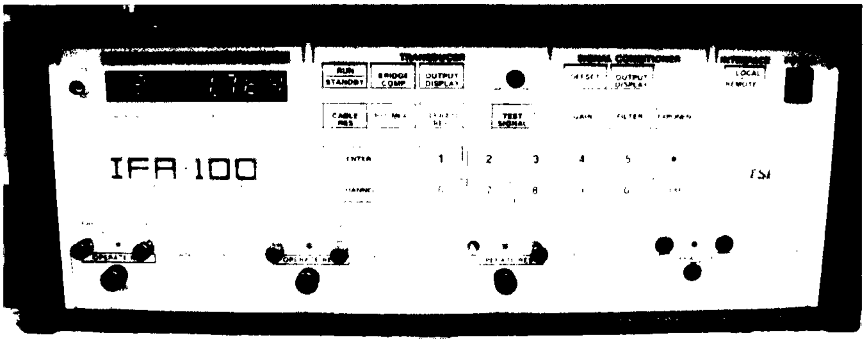

Figure 4.21: TSI IFA-100 Hotwire Anemometry System

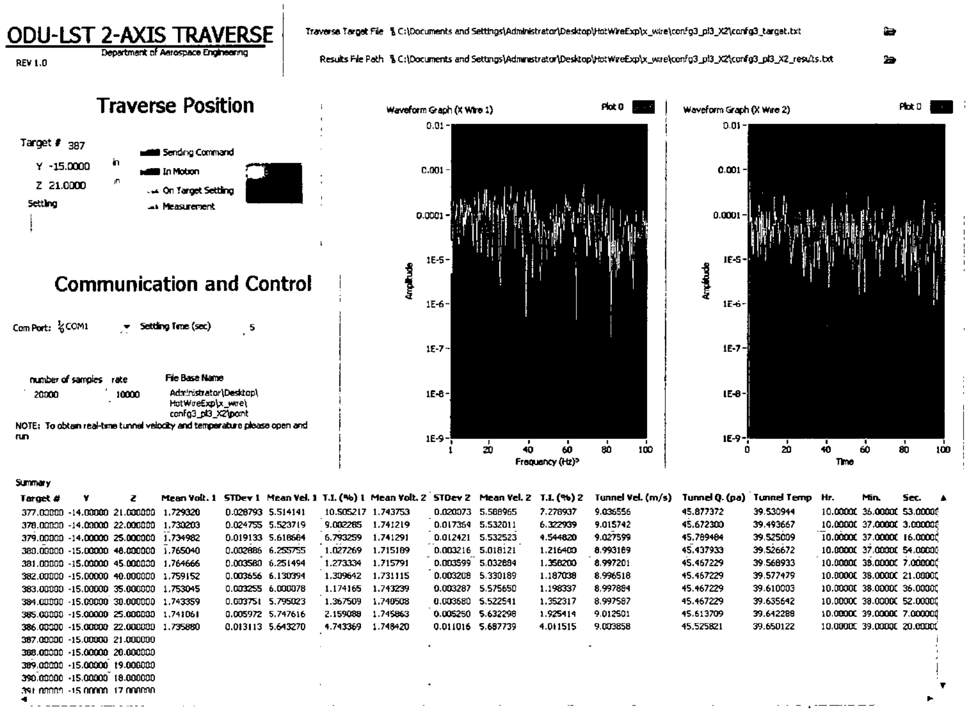

Traverse Target File C:\Documents and Settings\Administrator\Desktop\HotWireExp\x_wire\config3_pl3_X2\config3_target.txt

Results File Path C:\Documents and Settings\Administrator\Desktop\HotWireExp\x_wire\config3_pl3_X2\config3_pl3_X2_results.txt

Target # 387

Y -15.0000 in

Z 21.0000 in

Settling

Com Port: COM1

Setting Time (sec) 5

number of samples	rate	File Base Name
20000	10000	Administrator\Desktop\ HotWireExp\x_wire\ config3_pl3_X2\point

NOTE: To obtain real-time tunnel velocity and temperature please open and run

Summary

Target #	Y	Z	Mean Volt. 1	STDev 1	Mean Vel. 1	T.I. (%) 1	Mean Volt. 2	STDev 2	Mean Vel. 2	T.I. (%) 2	Tunnel Vel. (m/s)	Tunnel Q. (pa)	Tunnel Temp	Hr.	Min.	Sec.
377.00000	-14.00000	21.000000	1.729320	0.028793	5.514141	10.505217	1.743753	0.020073	5.588965	7.278937	9.036556	45.877372	39.530944	10.0000	36.0000	53.0000
378.00000	-14.00000	22.000000	1.730203	0.024755	5.523719	9.002285	1.741219	0.017364	5.532011	6.322939	9.015742	45.672300	39.493667	10.0000	37.0000	3.00000
379.00000	-14.00000	25.000000	1.734982	0.019133	5.618684	6.793259	1.741291	0.012421	5.532523	4.544820	9.027599	45.789484	39.525009	10.0000	37.0000	16.0000
380.00000	-15.00000	48.000000	1.765040	0.002886	6.255755	1.027269	1.715189	0.003216	5.018121	1.216400	8.993189	45.437933	39.526672	10.0000	37.0000	54.0000
381.00000	-15.00000	45.000000	1.764666	0.003580	6.251494	1.273334	1.715791	0.003599	5.032884	1.358200	8.997201	45.467229	39.568933	10.0000	38.0000	7.00000
382.00000	-15.00000	40.000000	1.759152	0.003656	6.130394	1.309642	1.731115	0.003208	5.330189	1.187038	8.996518	45.467229	39.577479	10.0000	38.0000	21.0000
383.00000	-15.00000	35.000000	1.753045	0.003255	6.000078	1.174165	1.743239	0.003287	5.575650	1.198337	8.997884	45.467229	39.610003	10.0000	38.0000	36.0000
384.00000	-15.00000	30.000000	1.743359	0.003751	5.795023	1.367509	1.740508	0.003680	5.522541	1.352317	8.997587	45.467229	39.635642	10.0000	38.0000	52.0000
385.00000	-15.00000	25.000000	1.741061	0.005972	5.747616	2.159088	1.745863	0.005250	5.632298	1.925414	9.012501	45.613709	39.642288	10.0000	39.0000	7.00000
386.00000	-15.00000	22.000000	1.735880	0.013113	5.643270	4.743369	1.748420	0.011016	5.687739	4.011515	9.003858	45.525821	39.650122	10.0000	39.0000	20.0000
387.00000	-15.00000	21.000000														
388.00000	-15.00000	20.000000														
389.00000	-15.00000	19.000000														
390.00000	-15.00000	18.000000														
391.00000	-15.00000	17.000000														

Figure 4.22: Front Panel of X-Wire Data Acquisition LabView Program

Measurements were made with X-wire sensors, specifically TSI Model 1241 End Flow "X" Probes, as shown in Figure 4.23.

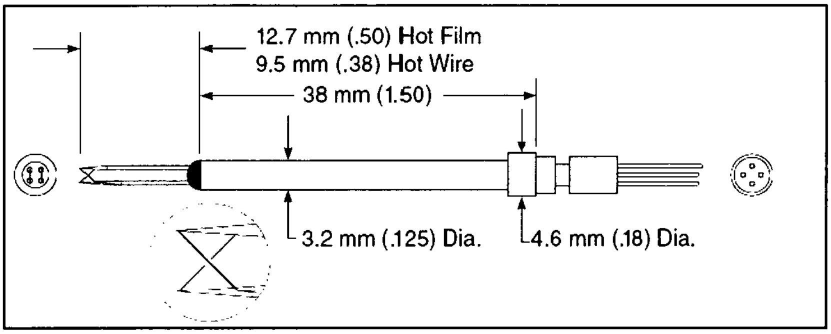

Figure 4.23: TSI X-Wire Probes

(http://www.tsi.com)

4.3.3.2 Data Acquisition and Software

After the X-wire probe was positioned at the desired to point, a delay of five seconds was applied so as to allow any vibration of the probe support to diminish. Then two seconds of data acquisition took place with a sample rate of 10,000 samples per second. The total number points to survey the 3D wake flow was 1080 and at each point 20,000 samples were acquired which is sufficiently high to resolve the expected turbulence levels at the wake.

The tunnel reference speed was acquired via a Honeywell precision pressure transducer, read through a serial port, while the test section temperatures were acquired via a Hewlett Packard 3497A Data Acquisition and Control Unit (Figure 4.24), and the monitoring of the thermocouple signals was taken from the HP3497A via a HP-IB interface. All acquired data were recorded and shown by a custom LabView program (Figure 4.25).

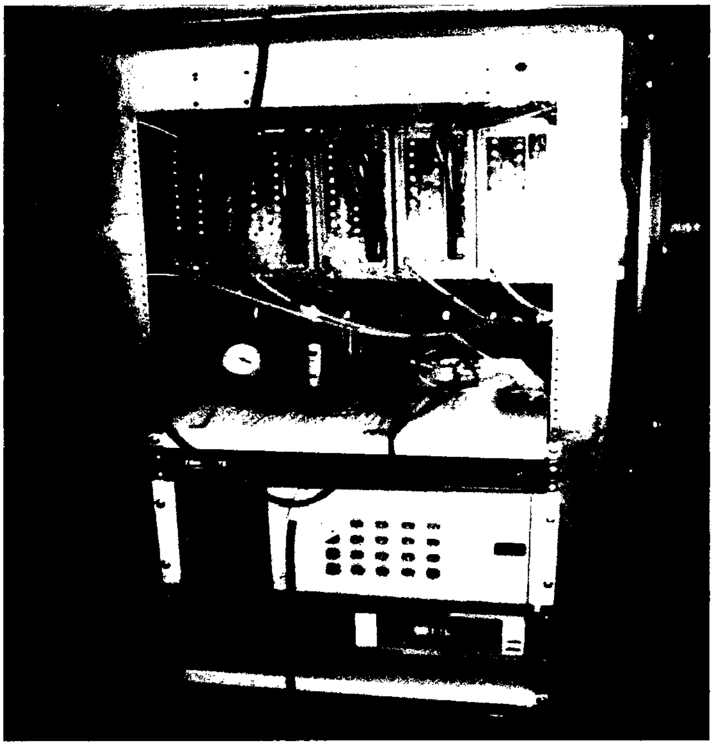

Figure 4.24: Hewlett Packard 3497A Data Acquisition and Control Unit

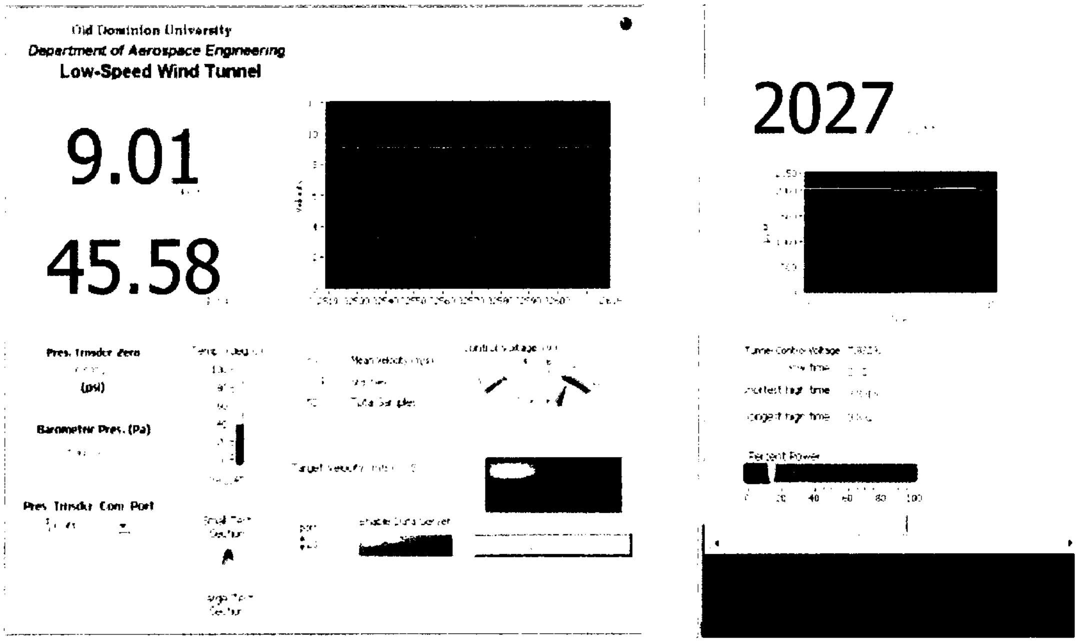

Figure 4.25: Front Panels of Wind Tunnel and Propeller Operating LabView Programs

4.4 Experimental Design

The main goal of the experiments is to gain an understanding of the evolution of both flap and wing tip vortices in the wake of a medium range twin-engine (propeller engine) military cargo aircraft by using both PIV and Hotwire Anemometry measurements in a statistically designed experiment. Since the vortex trajectories were expected to show smooth curvature, a quadratic model seemed appropriate. Therefore, a Central Composite Design (CCD) of experiment layout was planned. Due to restrictions on the feasible range of variation of the factors (i.e. AOA was limited between 0° and 10° in order not to create flow separations over the wing), the CCD for experimentation was chosen to be Face Centered Design (FCD) layout.

The experimental design for the dissertation study is presented for both coded and actual values in Table 4.3 and 4.4 respectively where the coded values are transformed from the actual values of variables using Equation 4.1.

$$Coded\ Value = \frac{Actual\ Value - \left(\frac{Actual\ Value_{Low} + Actual\ Value_{High}}{2}\right)}{\left(\frac{Actual\ Value_{High} - Actual\ Value_{Low}}{2}\right)} \qquad (4.1)$$

Throughout the dissertation study, the strength of tip vortices and flap vortices were changed by changing wing angle of attack and flap angle respectively as well as the pitch angle of the propeller to change the propeller disc loading (and thrust) in order to understand how each of the factors affect the behaviors of the streamwise vortices.

4.4.1 Background

4.4.1.1 Response Surface Methodology

Montgomery (2005) defined the Response Surface Methodology (RSM) as a collection of mathematical and statistical techniques useful for the modeling and analysis of problems in which a response of interest is influenced by several variables and the objective is to optimize this response.

In most RSM problems, the form of the relationship between the response and the independent input variables is unknown. Thus, the first step in RSM is to find a suitable approximation for the true functional relationship between the response and the set of independent input variables. Usually, a low-order polynomial in some region of the independent variables is employed. If the response is well modeled by a linear function of the independent variables, then the approximation function is a first-order model as given Equation 4.2:

$$y = \beta_0 + \beta_1 x_1 + \beta_2 x_2 \ldots\ldots + \beta_k x_k + \epsilon \qquad (4.2)$$

If there is curvature in the system, then a polynomial of higher degree must be used, such as the second-order model (see Equation 4.3):

$$y = \beta_0 + \sum_{i=1}^{k} \beta_i x_i + \sum_{i=1}^{k} \beta_{ii} x_i^2 + \sum\sum_{i<j} \beta_{ij} x_i\, x_j + \epsilon \qquad (4.3)$$

Montgomery (2005) suggested that it is unlikely that a polynomial model will be a reasonable approximation of the true functional relationship over the entire space of the independent variables, but for a relatively small region they usually work quite satisfactorily.

The method of least squares is used to estimate the parameters in the approximating polynomials and the response surface analysis is then performed using the fitted surface. If the fitted surface is an adequate approximation of the true response function, then analysis of the fitted surface will be approximately equivalent to analysis of the actual system.

4.4.1.2 Face-Centered Central Composite Design

The CCD was first introduced by Box and Wilson (1951) and is still one of the most popular second-order designs for experimentation. Generally, the number of experiments required for a CCD is given in Equation 4.4, where "2^k" relates to the factorial (or fractional factorial of resolution V) runs, denoted by "n_F", "2k" corresponds to axial runs, denoted by "n_a", and "n_c" is the number of center runs. CCDs for k=2 and k=3 are shown in Figure 4.26.

$$Number\ of\ expriments = 2^k + 2k + n_c \qquad (4.4)$$

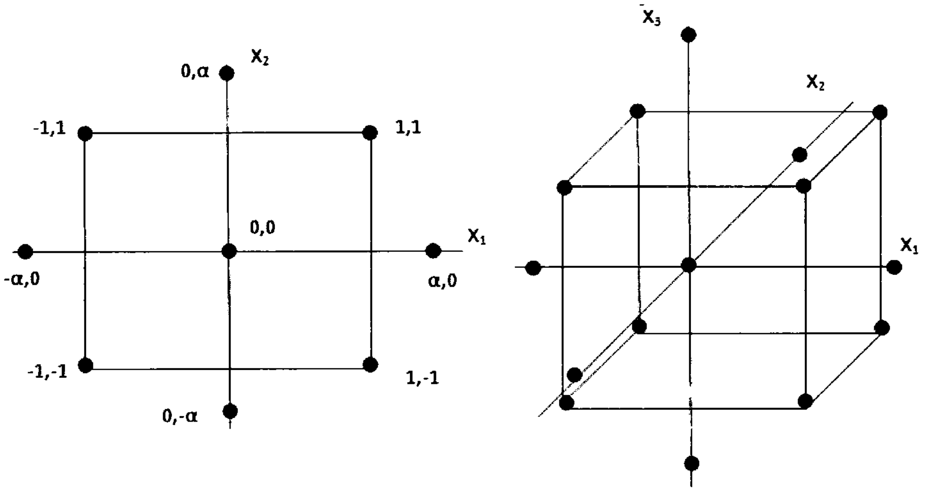

Figure 4.26: Central Composite Designs for k=2 and k=3 (Montgomery, 2005)

CCD is a very efficient design for fitting the second-order model. There are two parameters in the design that must be specified: the distance α of the axial runs from the design center and the number of center points n_c.

4.4.1.3 Rotatability of CCD

It is important for the second-order model to provide good predictions throughout the region of interest. One way to define "good" is to require that the model should have a reasonably consistent and stable variance of the predicted response at points of interest x. The variance of the predicted response at some point x is given Equation 4.5:

$$V[\hat{y}(x)] = \sigma^2 x'(X'X)^{-1}x \qquad (4.5)$$

where $X' = [X_1; X_2; X_3; X_{12}; X_{13}; X_{23}; X_1^2; X_2^2; X_3^2]$

Box and Hunter (1957) suggested that a second-order response surface design should be rotatable. This means that the $V[\hat{y}(x)]$ is the same at all points x that are at the same distance from the design center. That is, the variance of predicted response is constant on spheres. Figure 4.27 shows contours of constant $\sqrt{V[\hat{y}(x)]}$ for the second-order model fit. Notice that the contours of constant standard deviation of predicted response are concentric circles. A design with this property will leave the variance of $\hat{y}$ unchanged at a fixed radial distance from the design center.

Rotatability is a reasonable design objective for the selection of the optimum and is unknown prior to running the experiment; it makes sense to use a design that provides equal precision of estimation in all directions. A central composite design is made rotatable by the choice of α. The value of α for rotatability depends on the number of points in the factorial portion of the design: in fact, $\alpha=(n_F)^{1/4}$ yields a rotatable central composite design where n_F is the number of points used in the factorial portion of the design.

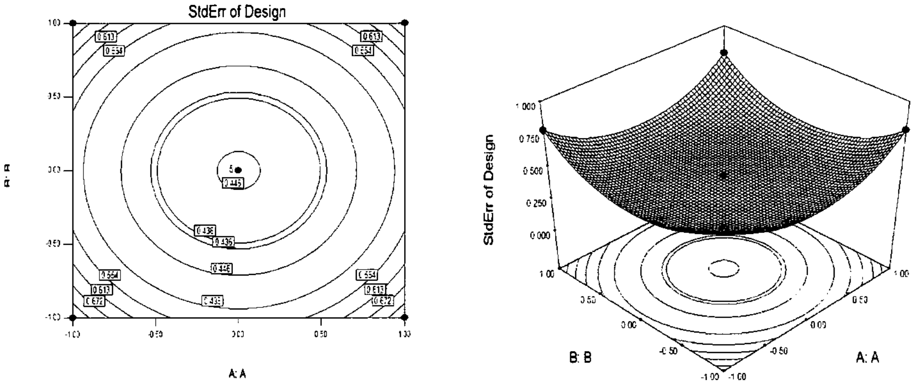

Figure 4.27: Contour Plots of Prediction of Standard Error for Rotatable Design (left-2D view and right-3D view)

4.4.1.4 Cuboidal Region of Interest

In many situations, the region of interest is cuboidal rather than spherical. In these cases, a useful variation of the central composite design is the face-centered design or the face-centered cubic, in which α=1. This design locates the axial points on the centers of the faces of the cube, as shown in Figure 4.28.

This variation of the central composite design is also useful because it requires only three levels of each factor where the levels of the factors are hard to change. However, note that face-centered designs are not rotatable.

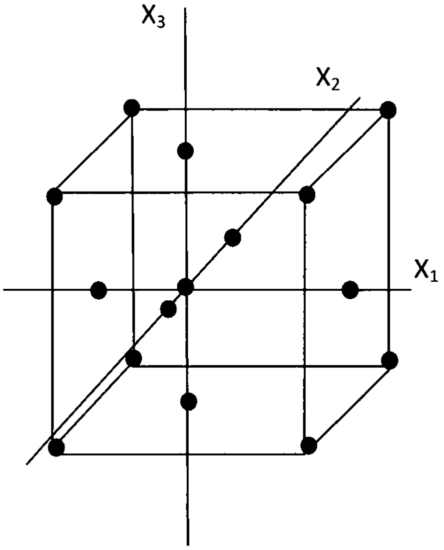

Figure 4.28: A Face-Centered Central Composite Design for k=3 (Montgomery, 2005)

The face-centered cube does not require as many center points as the spherical CCD for variance prediction stabilization. In practice, n_c=2 or 3 is sufficient to predict the variance throughout the experimental region but for reliable pure error estimations higher degrees of freedom are required. Figure 4.29 shows the contours of constant $\sqrt{V[\hat{y}(x)]}$ for the face-centered cube for k=3 with n_c=3 center points. Notice that the standard deviation of predicted response is reasonably uniform over a relatively large portion of the design space.

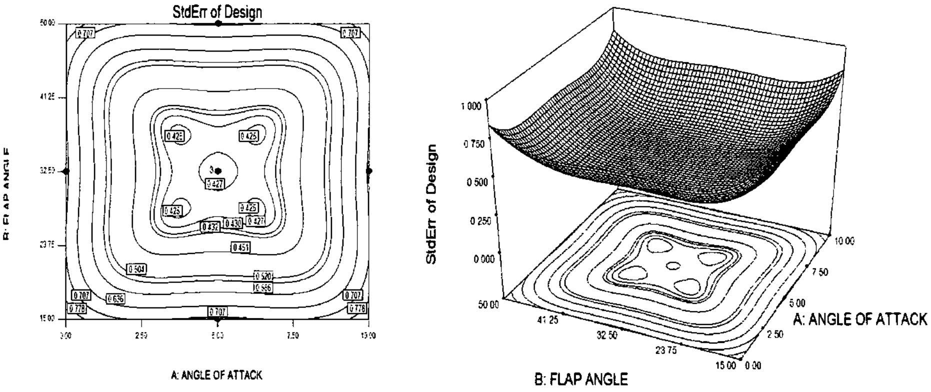

Figure 4.29: Contour Plots of Prediction of Standard Error for Non-Rotatable Design (left-2D view and right-3D view)

4.4.2 Factors and Responses

During the selection of the factors, the factors directly affecting the vortex strengths and locations were chosen such that the angle of attack and flap angle change the strengths and locations of the wing tip and flap vortices respectively. In addition to these factors, propeller pitch angle was chosen as a factor since it changes the propeller disc loading and thus changes the thrust. The evolution of the vortices in the downstream direction were also considered so the "downstream axis" was added to the factors (see Figure 4.30). It was expected to see a quadratic regression model including some of the two-factor interaction terms after the experiments were analyzed statistically. Briefly the factors are listed below:

a. Angle of attack,
b. Flap angle,
c. Propeller pitch angle, and
d. Downstream distance.

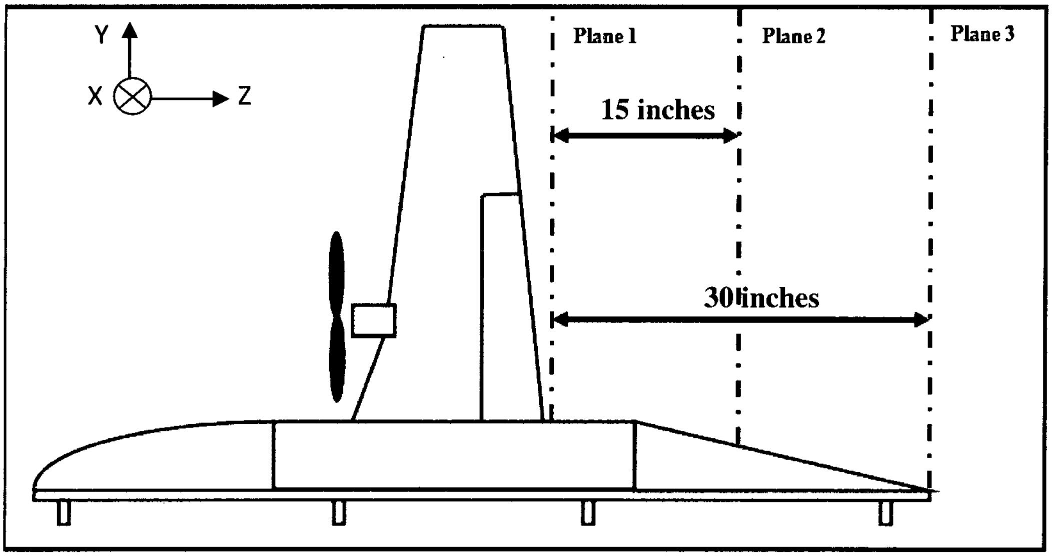

Figure 4.30: Downstream Stations where the Flow were Analyzed with respect to FCD Experiment Layout

In the literature survey, it was understood that the wing tip and/or flap vortices were analyzed in the experiments not having any propeller effect at the same setup. In these experiments, the behaviors of the vortices were analyzed while simulating an air-drop or air-refueling operation of a medium range twin-engine military cargo aircraft. Since the motions of the vortices are important with the complex wake of the propeller, the vertical and horizontal motions of the vortices were analyzed as well as the tendency of the vortices to merge. Other responses are the maximum vorticity levels in the core of the vortices. The responses to be evaluated through the FCD experimentation are given below:

a. The vertical motion (upward or downward) motion of the flap vortex,
b. The horizontal motion (inward or outward) motion of the flap vortex,
c. The vertical motion (upward or downward) motion of the wing tip vortex,
d. The horizontal motion (inward or outward) motion of the wing tip vortex,
e. The shortest distance between the wing tip and flap vortices (to understand whether the vortices are getting closer to merge or not)
f. The maximum vorticity in the core of the flap vortex, and
g. The maximum vorticity in the core of the wing tip vortex.

The four factor experiment layout is shown graphically in Figure 4.31. The four factors are given as defined previously:

a. X_1, Angle of attack,
b. X_2, Flap angle,
c. X_3, Propeller pitch angle, and
d. X_4, Downstream distance.

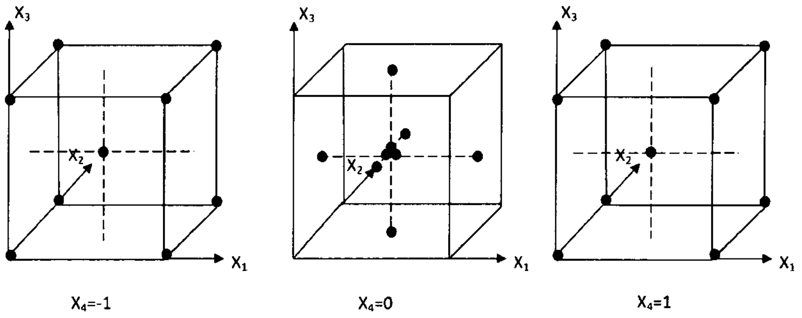

Figure 4.31: FCD Experiment Layout for Dissertation Experiment (k=4 factors) with n_C=3

Run Number	FACTORS					RESPONSES
	Angle of Attack	Flap Angle	Propeller Pitch Angle	Downstream Station		
1	-1	-1	-1	-1	FACTORIALS	
2	1	-1	-1	-1		
3	-1	1	-1	-1		
4	1	1	-1	-1		
5	-1	-1	1	-1		
6	1	-1	1	-1		
7	-1	1	1	-1		
8	1	1	1	-1		
9	-1	-1	-1	1		
10	1	-1	-1	1		
11	-1	1	-1	1		
12	1	1	-1	1		
13	-1	-1	1	1		
14	1	-1	1	1		
15	-1	1	1	1		
16	1	1	1	1		
17	-1	0	0	0	AXIALS	
18	1	0	0	0		
19	0	-1	0	0		
20	0	1	0	0		
21	0	0	-1	0		
22	0	0	1	0		
23	0	0	0	-1		
24	0	0	0	1		
25	0	0	0	0	CENTERS	
26	0	0	0	0		
27	0	0	0	0		

Table 4.3: Experiment Design in Standard Order (Coded)

Run Number	FACTORS					RESPONSES
	Angle of Attack	Flap Angle	Propeller Pitch Angle	Downstream Station		
1	0	15	19	0	FACTORIALS	
2	10	15	19	0		
3	0	50	19	0		
4	10	50	19	0		
5	0	15	25	0		
6	10	15	25	0		
7	0	50	25	0		
8	10	50	25	0		
9	0	15	19	60		
10	10	15	19	60		
11	0	50	19	60		
12	10	50	19	60		
13	0	15	25	60		
14	10	15	25	60		
15	0	50	25	60		
16	10	50	25	60		
17	0	32.5	22	30	AXIALS	
18	10	32.5	22	30		
19	5	15	22	30		
20	5	50	22	30		
21	5	32.5	19	30		
22	5	32.5	25	30		
23	5	32.5	22	0		
24	5	32.5	22	60		
25	5	32.5	22	30	CENTERS	
26	5	32.5	22	30		
27	5	32.5	22	30		

Table 4.4: Experiment Design in Standard Order (Actual)

4.4.3 Experimental Approach

In general, guidelines for formally designing experiments show that there are some basic stages of experimentation such as;

a. Recognition of and statement of the problem,
b. Selection of the response variable,
c. Choice of factors, levels, and ranges,
d. Choice of experimental design,
e. Performance of the experiment,
f. Statistical analysis of the data, and
g. Conclusions and recommendations.

Since the problem is to understand the trajectories of both wing tip and flap vortices with varying conditions the recognition of the problem was done accordingly such that these trajectories could be measured under varying conditions and analyzed statistically to obtain mathematical models relating the drivers and results of the vortex motions.

The literature survey revealed that the angle of attack highly influenced the wing tip vortex as the flap angle does for the flap vortex. Since the interaction of the propeller wake with the vortices is the main part of the study, propeller pitch angle was chosen to be the third factor to vary. The downstream distance was chosen as the fourth factor since the vortices evolve along the freestream flow direction and the dissertation study was to analyze whether or not any tendency of merging of the vortices and the propeller wake exists. The levels and ranges were chosen such that no flow separations exist around the model in order not to generate discontinuities at the responses.

FCD experimentation was chosen as the experiment design because within the near field wake region the trajectories of vortices are expected to be approximately quadratic and if the quadratic model was not sufficient when concluding the analyses of vortex trajectories then a higher order regression model would be recommended which would need a higher number of experimental runs in future work.

The experiments were performed by measuring the wake flow with both Particle Image Velocimetry (PIV) and Hotwire Anemometry (HWA) which gave the mean flow velocities, turbulence intensities, Reynolds stresses in the wake flow, and the vorticity magnitudes in the vortices.

The trajectories of the vortices along with their vorticity strengths were statistically analyzed using Design Expert Version 7.1.5. Meaningful regression models were expected to define the motions and properties of vortices with respect to the main physical parameters of the aircraft that can be varied during flight.

There are some basic principles for the proper execution of experiments such as randomization, replication, and blocking. Randomization is the most critical criteria since statistical methods require that errors are independently distributed which is realized by properly randomized experiments. Randomization is done by allocating the materials and the trial run orders in the experiment design in a random order. When properly randomized experiments are performed, the effects of extraneous factors are also averaged out. Replication is another important factor in properly designed experiments which means an independent repeat of each factor combination that allows the experimenter to obtain an estimate of the experimental error. For determination of whether or not the observed data are statistically different, this estimate of error is used as a basic unit of measurement. Besides, if the replication is used for the estimation of the true mean response for one of the factor levels, then replication allows a more precise estimate of the mean response. The third principle is blocking which is used to reduce or eliminate the variability transmitted from nuisance factors. Generally, a block can be defined as a set of relatively homogenous experimental conditions.

Throughout the experiments reported in this dissertation, most of the aforementioned principles were applied for the design and execution of the experiment but blocking could not be applied due to the fact that neither the experimenter nor the conditions (including the measurement systems and materials, etc.) in the experiments changed during the trial runs. Since randomization is the most critical principle for an experiment to observe independently distributed residuals, measurements of wake flow were done in a random order. Each response was obtained by the HWA and PIV measurements which acquired

20,000 HWA data for every location and 250 frames for each PIV subarea, respectively. These acquired data were averaged and the corresponding values were put in the response tables. Replication of the cases was not achieved for all cases except the case when all factors were at medium levels. Actually replication of all cases would support a superior analysis but due to limitations of wind tunnel usage and schedule, data from the experiment design with only one replicate of all cases (exceptional case was defined above) was acquired.

Throughout the measurements of velocity in the wake field by using the PIV system the wake was divided into subsections to acquire data. Similarly, a simultaneous measurement of the whole wake field was also not achieved using HWA since the single hotwire probe acquired data pointwise. This means that if all the instantaneous measurements belonging to different portions of the wake were combined to picture the whole wake flow field, it would not truly represent a complete flow since the measurements were performed at different times. Averaging is a method to understand the general aspects of the wake characteristics and was applied to view the resultant and planar velocity fields, as well as the turbulence and shear stress values.

As expected PIV is not capable of achieving high frequency measurements of the flow but its field of view permits the capture of instantaneous measurements over a larger region compared to HWA. Contrary to HWA measurements, PIV measurements centered especially on vortices enabled viewing of the wandering of vortices which contributes to the turbulence values of vortices and should be taken account of when turbulence intensity is of great concern.

During experimentation, the temperature in the wind tunnel changed due to frictional effects and since it needs two hours for testing each case an average of 20ºC of temperature rise was observed between start and finish. From the perspective of Design of Experiments, temperature is an uncontrollable factor that may change the responses.

4.5 Regression Model Adequacy Checking

Regression model adequacy checking requires that certain assumptions are satisfied, and the observations can be described, as given in Equation 4.6:

$$y_{ij} = \mu + \tau_i + \varepsilon_{ij} \qquad (4.6)$$

If the errors denoted by "ε_{ij}" are normally and independently distributed, while the variance is unknown with a mean value of zero, then the analysis of variance (ANOVA) can be applied to test the hypothesis that there is no difference in treatment means.

In reality, these assumptions are not practical and cannot be satisfied exactly and it is unwise to rely on ANOVA without confirmation of the validity of assumptions. Possible violations of these assumptions as well as the regression model adequacy can be checked with the residual analysis in which any residual can be defined as given in Equation 4.7 (residual of *j*th observation in *i*th treatment);

$$e_{ij} = y_{ij} - \hat{y}_{ij} \qquad (4.7)$$

where $\hat{y}_{ij}$ is predicted response (the equation below shows that any predicted response is just the corresponding treatment average) and y_{ij} is the observed response (see Equation 4.8):

$$\hat{y}_{ij} = \hat{\mu} + \hat{\tau}_i = \bar{y}_{..} + (\bar{y}_{i.} - \bar{y}_{..}) = \bar{y}_{i.} \quad (4.8)$$

If the results of ANOVA show that the model is adequate, then the residuals should be structureless, meaning that no obvious pattern is observed.

4.5.1 The Normality Assumption

A first check that should be applied for the residuals is the normality check by plotting a histogram of the residuals. If the errors are normally and independently distributed the distribution of residuals looks like a normal (Gaussian) distribution centered at zero. This is usually not valid for small samples of data and considerable fluctuations in the histogram can be observed. As a consequence, moderate departures from normality should not be taken as a serious violation of the assumptions. Larger deflections and deviations from normality should be considered as serious problems. If the error distribution is normal, the graph shows the residuals lying along a straight line in which more emphasis should be applied on the residuals located around center compared to the ones at extremes. If there is any tendency of bending towards outward of the straight line (bending down slightly on the left side and upward slightly on the right side), it implies that the tails of the error distribution are thinner compared to the tails of normal distribution which means that largest residuals are not as large as expected.

While checking the tendency of the residuals, another fact that should be checked is the presence of outliers which is the residual that is very much larger than others. Even one outlier can sometimes seriously distort ANOVA and it is certain that more of them cause more serious problems. The frequent reason why outliers happen is mainly the mistakes that occur during calculation or data acquisition processes. If these are not the cause for the presence of the outlier, special precautions should be taken for the experimental circumstances. If there is no explanation for the outlier then, at the worst case, the analyses can be performed with both cases; one with the outlier and one without.

Outliers can be detected with several formal statistical procedures but one simple check is given in Equation 4.9, derived from the standardized residuals;

$$d_{ij} = \frac{e_{ij}}{\sqrt{MS_E}} \qquad (4.9)$$

If the errors are normally and independently distributed with the mean error 0 ($N(0,\sigma^2)$), the standardized residual defined above should also be distributed normally with mean zero and unit variance. Then it can be concluded that 68% of the standardized residuals should be located within ±1 standard deviation, 95% of them should be within ±2 standard deviations, and all the standardized residuals should be located within ±3 standard deviations. The presence of any outlier can be proved if any value bigger than three standard deviations from zero is observed.

4.5.2 Plot of Residuals in Time Sequence

The residuals plotted in time order is another helpful graph for detecting the presence of correlation between the residuals. The plots of residuals grouped either in the positive or negative region indicate a correlation and the independence assumption of errors is violated. Actually, this is a serious problem and is hard to correct. If possible, precautions should be taken to prevent the correlation problem when the data are collected, for example proper randomization of the experiment should be done as an important precaution in obtaining independence.

Sometimes the independence problem occurs due to factors related to the experimenter such as the skill of the experimenter may change as the experiment progresses (long and difficult experiments may cause lack of attention and carelessness of the experimenter) and result in a change in the error variance over time.

4.5.3 Plot of Residuals versus Fitted Values

As mentioned before, if the regression model is calculated correctly and the assumptions (the errors normally and independently distributed with mean zero and unit variance) are satisfied, then no structure can be observed in residual plots, which means that they should be unrelated to other variables. To ensure the independence of residuals, another simple check can be applied by plotting the residuals versus the fitted values. In this plot also no obvious pattern should be observed in the case of assumptions being satisfied.

In worst-case scenarios, a defect on the plot as nonconstant variance is observed, and sometimes an increase in the variance of the observations can be observed, when the error or background noise in the experiment was directly linked to the observations. Then the residuals get larger as y_{ij} gets larger, and the plot of residuals versus predicted responses would look like a diverging funnel. Another case for nonconstant variance is the case when the data follow a skewed distribution in which the variance tends to be a function of the mean.

Usually a variance stabilizing transformation is applied to deal with nonconstant variance and then the ANOVA should be run again. It should be noted that the analysis and conclusions of ANOVA should be applied on the new transformed populations.

Choosing the transformation method is another challenging issue that much research has been devoted to the selection of an appropriate transformation. If experimenters know the distribution of the observations, this information can be used in choosing a transformation such that, if the observations follow the Poisson distribution, the square root transformation would be used, or if the data follow lognormal distribution, the logarithmic transformation would be superior. If no information about the theoretical distribution of the observation is known, then a transformation that equalizes the variance (regardless of the value of the mean) should be sought.

4.5.4 Box Cox Plot

In subsequent sections, analyses of residuals will take place including the Box Cox plot which is a tool to help determine the most appropriate power transformation to apply to response data. In general, data transformations can be described by the power function such that

$$\sigma = function(\mu^{\alpha}) \quad (4.10)$$

where "σ" is the standard deviation, "μ" is the mean and "α" is the power. λ denotes the value equal to (1-α) in all cases. If the standard deviation associated with an observation is proportional to the mean raised to the power, then transforming the observation by a 1-α (or λ) power gives a scale satisfying the equal variance requirement of the statistical model. Below some commonly used transformations are given:

$\lambda = -1$ inverse

$\lambda = 0$ natural log

$\lambda = 0.5$ square root

$\lambda = 1$ no transformation

In Box Cox plots, the lowest point in the plot represents the value of lambda (λ) that results in the minimum residual sum of squares in the transformed model. If the range of maximum to minimum response value is greater than 3 then improvement is the greatest whereas it should also be noted that the transformations of power law can only be performed on responses that are greater than zero, and in case of negative value responses, a constant "k" should be added to make all the responses positive.

5 RESULTS

In this chapter, the results of both PIV and Hotwire measurements will be given in the order given below:

a. Reynolds shear stress distributions of the first plane using PIV system measurements, and
b. Mean value of the resultant velocity field, turbulence intensities of the resultant velocity field, and z vorticity magnitude (planar velocity vectors plotted in the same graph) distribution in all three planes using Hotwire Anemometry measurements.

The velocities, Reynolds shear stress, and vorticity are calculated as given below.

$$Mean\ Resultant\ Velocity = \sqrt{U^2 + V^2 + W^2} \qquad (5.1)$$

$$Turbulence\ Intensities\ of\ Resultant\ Velocity = \frac{\sqrt{\overline{u'^2} + \overline{v'^2} + \overline{w'^2}}}{3} \frac{100}{U_\infty} \qquad (5.2)$$

$$Turbulence\ Intensities\ of\ PlanarVelocity = \frac{\sqrt{u'^2 + v'^2}}{2} \frac{100}{U_\infty} \qquad (5.3)$$

$$Reynolds\ Shear\ Stress = -\overline{u'v'} \qquad (5.4)$$

$$z\ vorticity = \frac{\partial v}{\partial x} - \frac{\partial u}{\partial y} \qquad (5.5)$$

Since the trajectories of the vortices were under consideration, first the vortex centers were determined by plotting the vorticity fields and finding the points where the vorticity magnitudes are the highest around both wing tip and flap outboard edge and then the motions of the centers of these vortices with respect to the trailing edge of the wing tip and flap were measured with varying factors, as given in Table 5.1.

CASE	FACTORS			
	Angle of Attack	**Flap Angle**	**Propeller Pitch Angle**	**Downstream Station**
1	0	50	19	0
2	0	50	25	0
3	0	15	19	0
4	0	15	25	0
5	10	50	19	0
6	10	50	25	0
7	10	15	19	0
8	10	15	25	0
9	5	32.5	22	0
10	10	32.5	22	30
11	0	32.5	22	30
12	5	32.5	19	30
13	5	32.5	25	30
14	5	15	22	30
15	5	50	22	30
16	5	32.5	22	30
17	5	32.5	22	30
18	5	32.5	22	30
19	5	32.5	22	60
20	5	50	19	60
21	5	50	25	60
22	5	15	19	60
23	5	15	25	60
24	10	50	19	60
25	10	50	25	60
26	10	15	19	60
27	10	15	25	60

Table 5.1: Factor Settings for Different Experiment Cases

5.1 PIV Survey and Reynolds Shear Stress

The wake field of a wing with a propeller mounted inboard was analyzed within this study using PIV for understanding the Reynolds shear stress distribution in the wake. Since PIV is a system which is not capable of measuring the flow velocities with a high frequency, some other parameters related to the velocity measurements (i.e. turbulence, Reynolds stress etc.) cannot be measured ideally, so the main purpose of using PIV in this study was to visualize the wake flow so as to understand the geometric extensions of the wake flow. Then, high frequency measurements using Hotwire Anemometry were performed in the second phase.

The studies by Westphal and Mehta (1988) showed the results of turbulence measurements made downstream of an oscillating (due to wandering) and a stationary tip vortex which revealed that the Reynolds shear stresses alter considerably for a wandering vortex. Another study by Stella et al. (2000) was performed to understand the wake of the propeller which stated that the blade wake turbulence produces Reynolds stress 2 orders of magnitude larger than the ones of the undisturbed flow. Within this study the Reynolds shear stress distributions in the wing (with a propeller mounted) wake for the first plane with varying factors such as angle of attack, flap angle, and propeller pitch angle were visualized using PIV. The results showed that increasing propeller pitch angle varied the Reynolds shear stress distribution in the propeller wake more compared to the effect of angle of attack on it. The shear stress in the tip vortex is less evident for most of the cases and for some cases such as high flap angle, the shear stress in the flap wake is more evident than the shear stress in the tip vortex (see Figures 5.1-5.9). Another effect that changes the shear stress distribution is the wing thickness since the higher levels of shear stress are observed in the thicker wing wake (toward wing root) compared to the wake toward the wing tip.

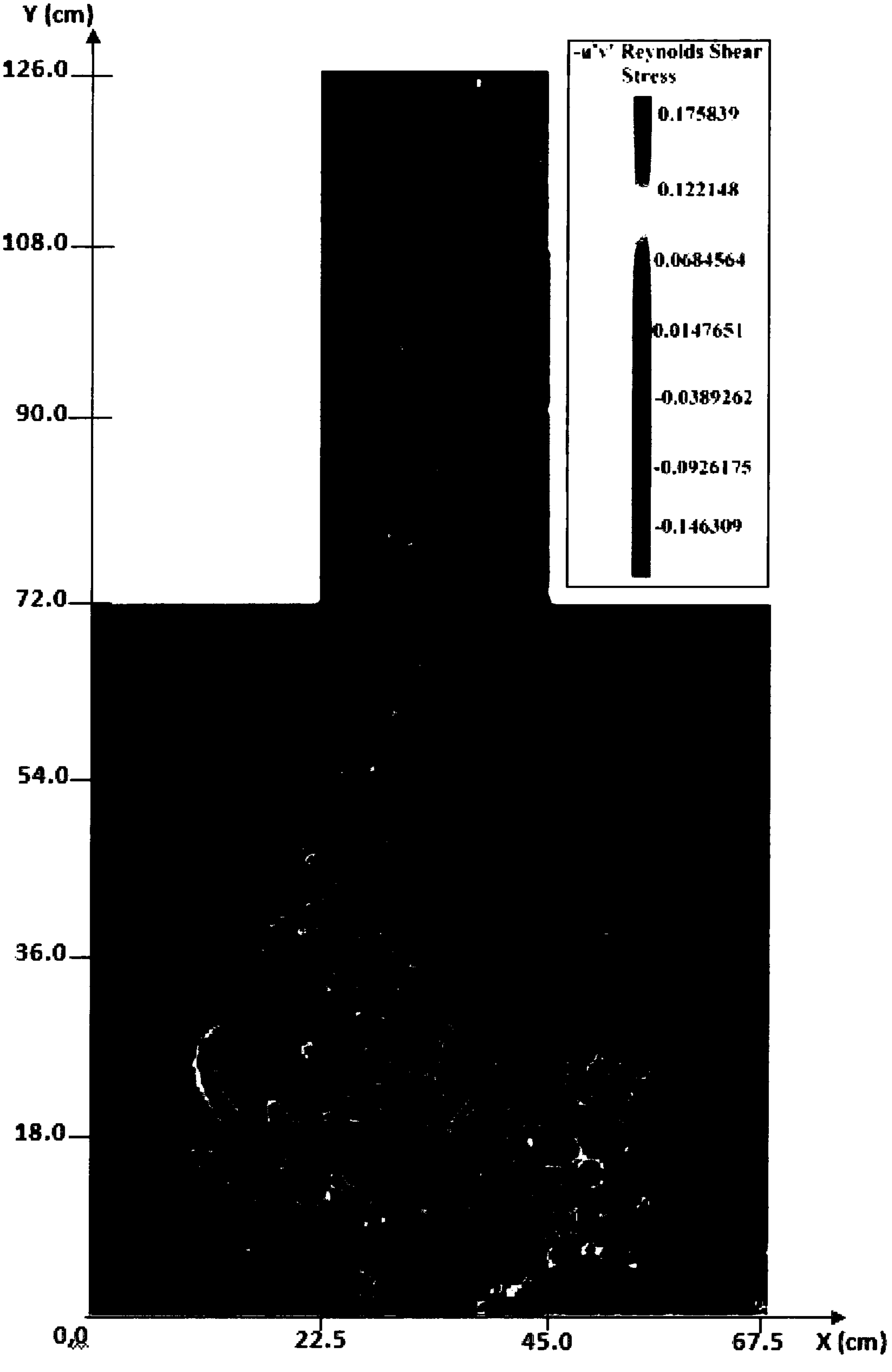

Figure 5.1: Reynolds Shear Stress using PIV Measurements (Case 1)

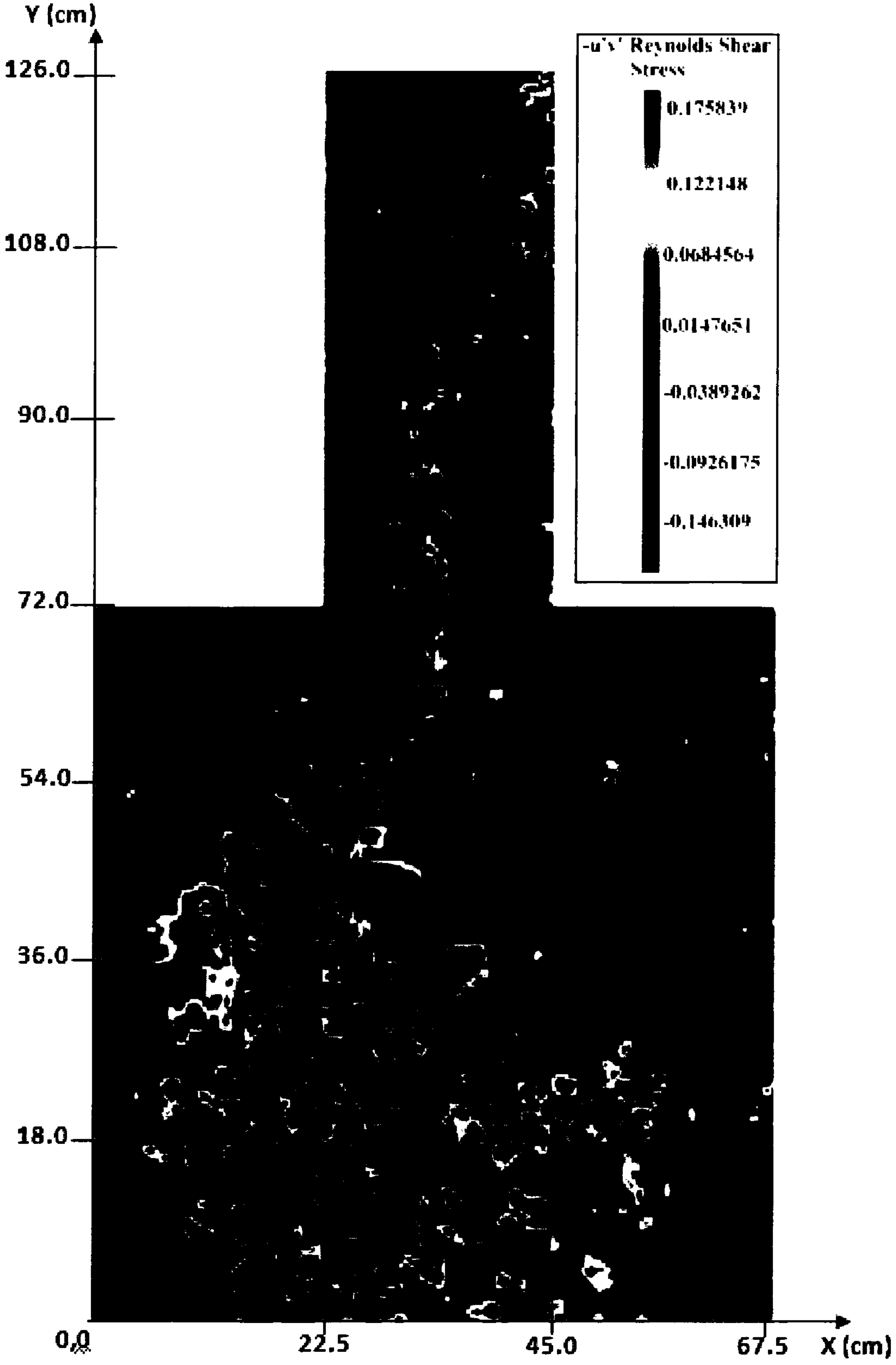

Figure 5.2: Reynolds Shear Stress using PIV Measurements (Case 2)

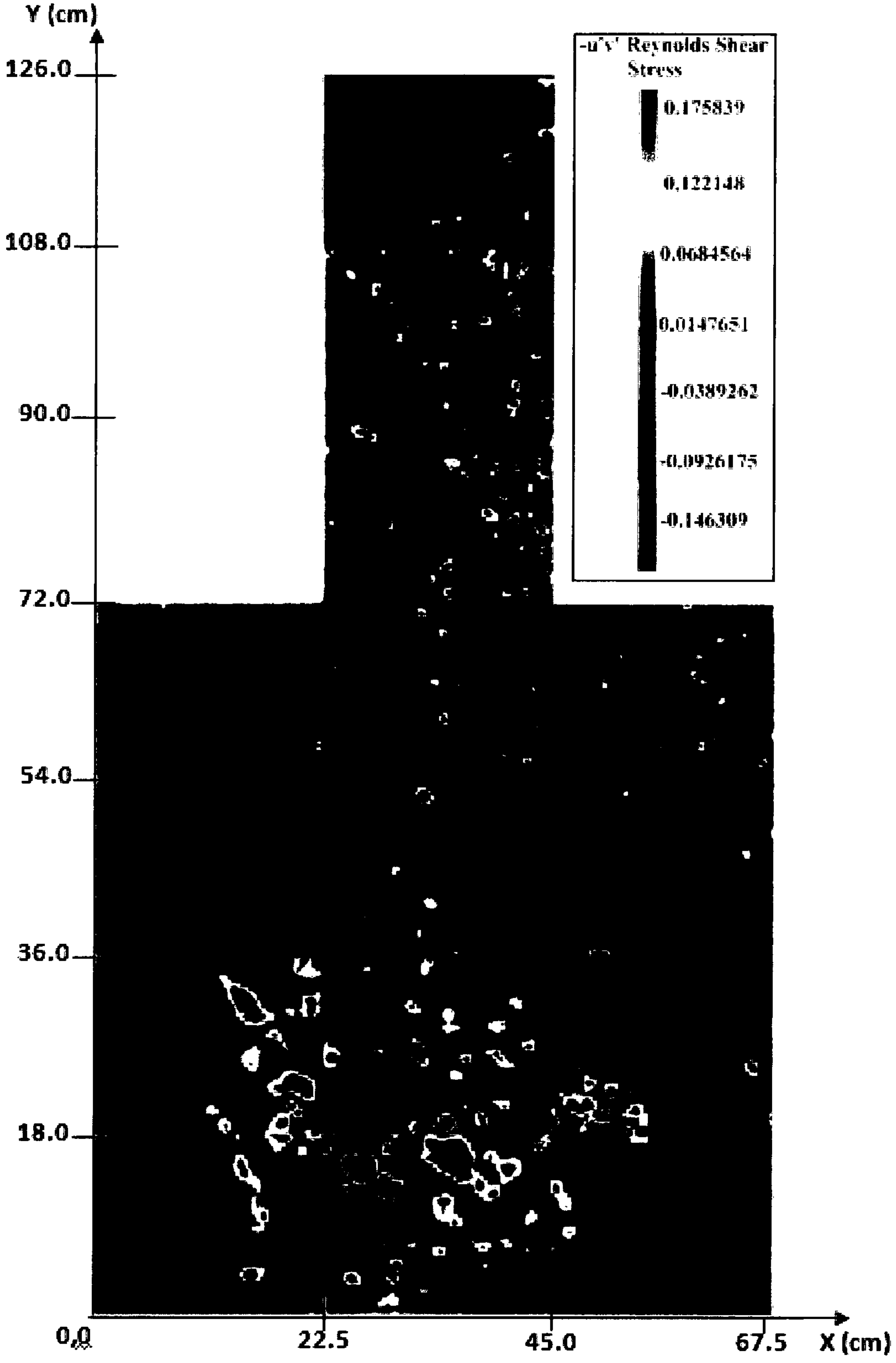

Figure 5.3: Reynolds Shear Stress using PIV Measurements (Case 3)

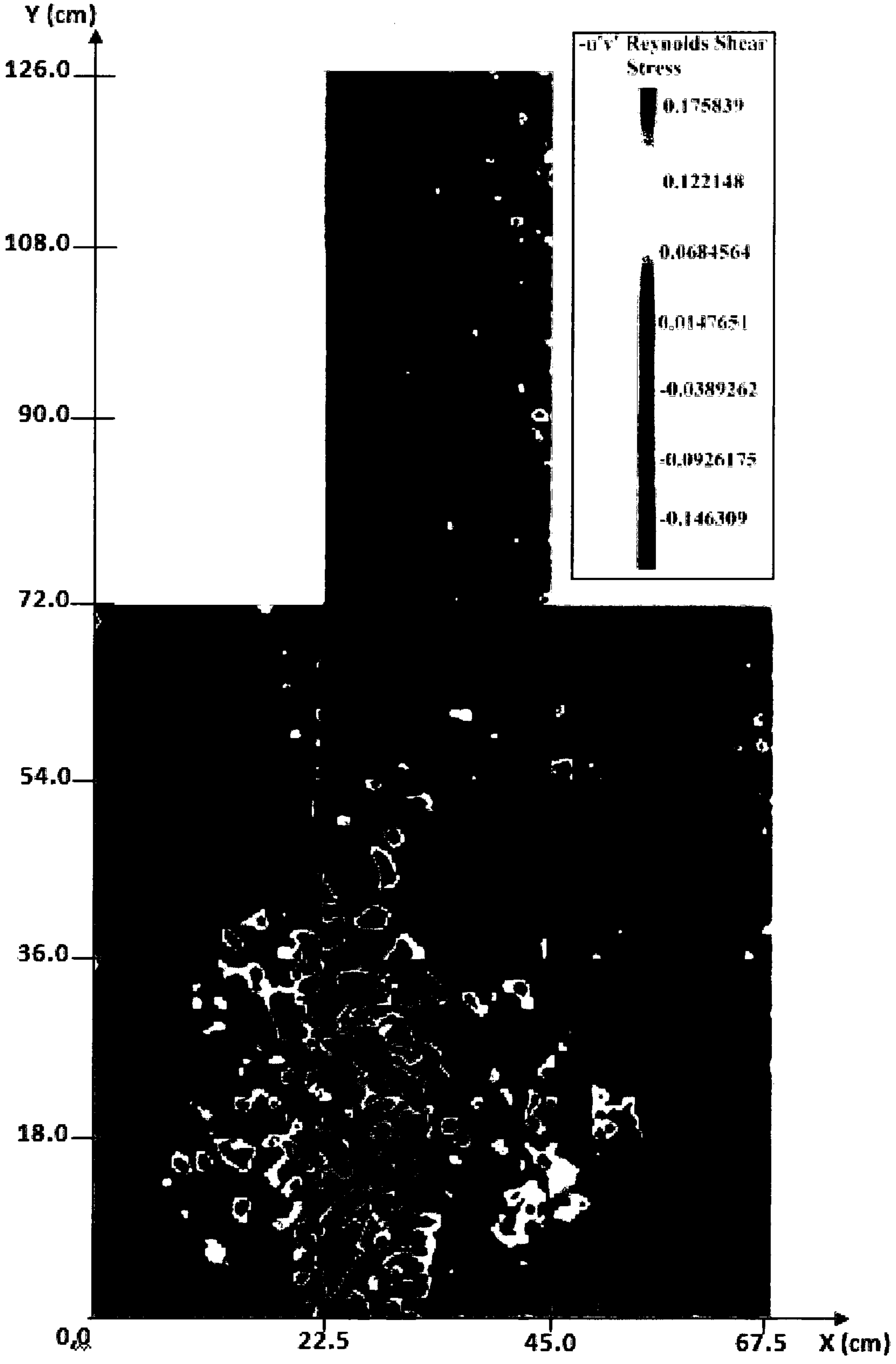

Figure 5.4: Reynolds Shear Stress using PIV Measurements (Case 4)

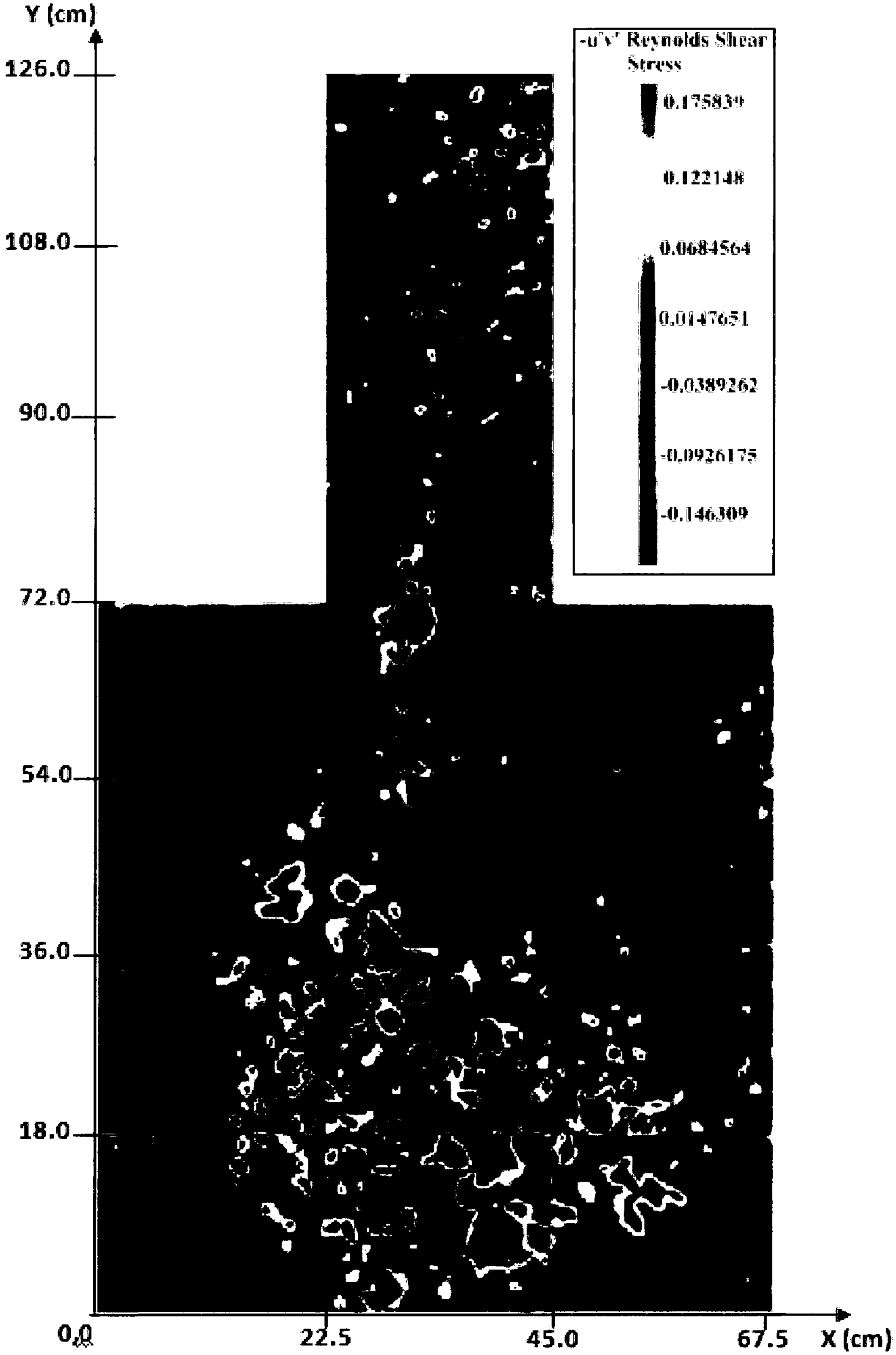

Figure 5.5: Reynolds Shear Stress using PIV Measurements (Case 5)

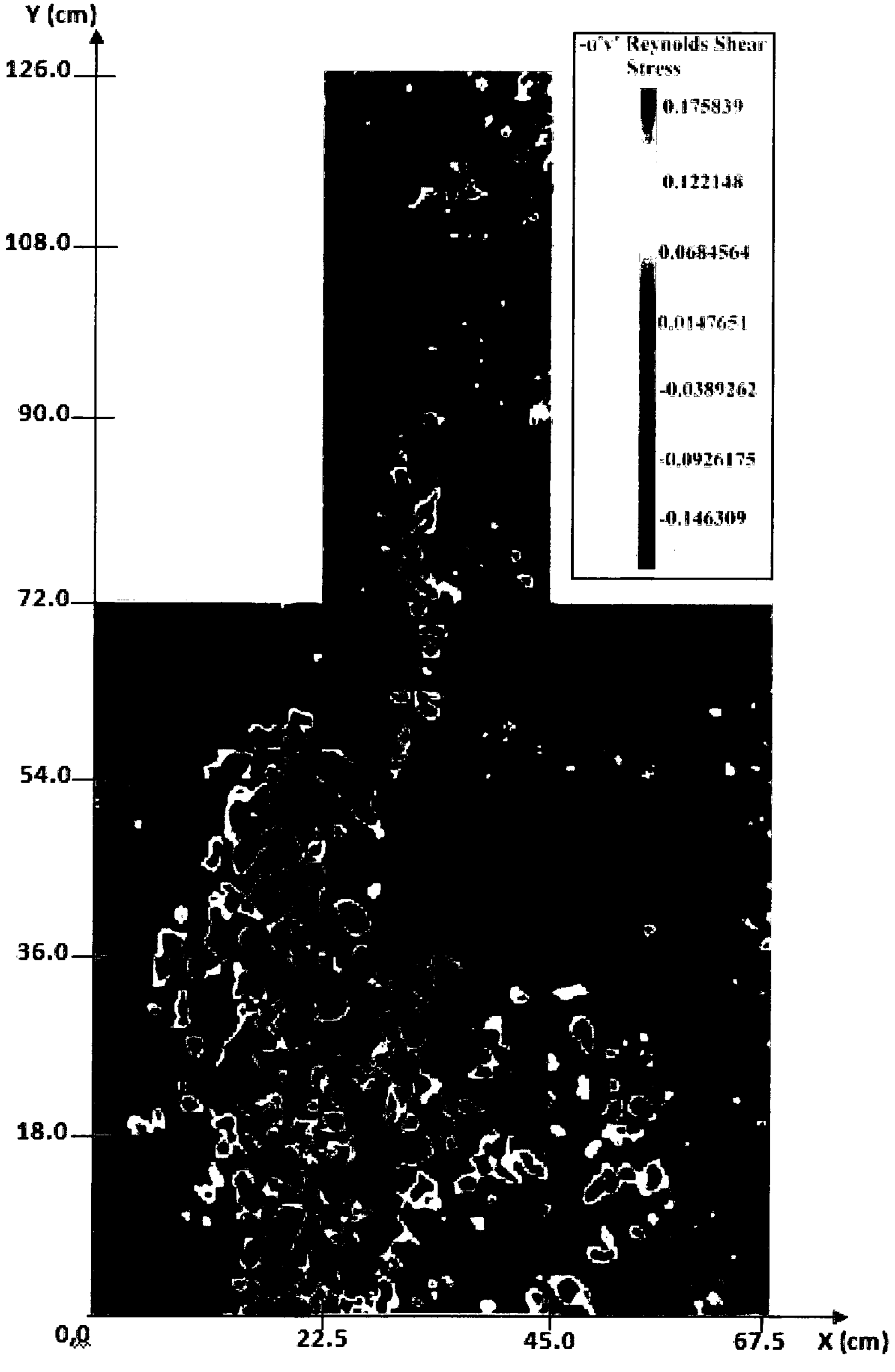

Figure 5.6: Reynolds Shear Stress using PIV Measurements (Case 6)

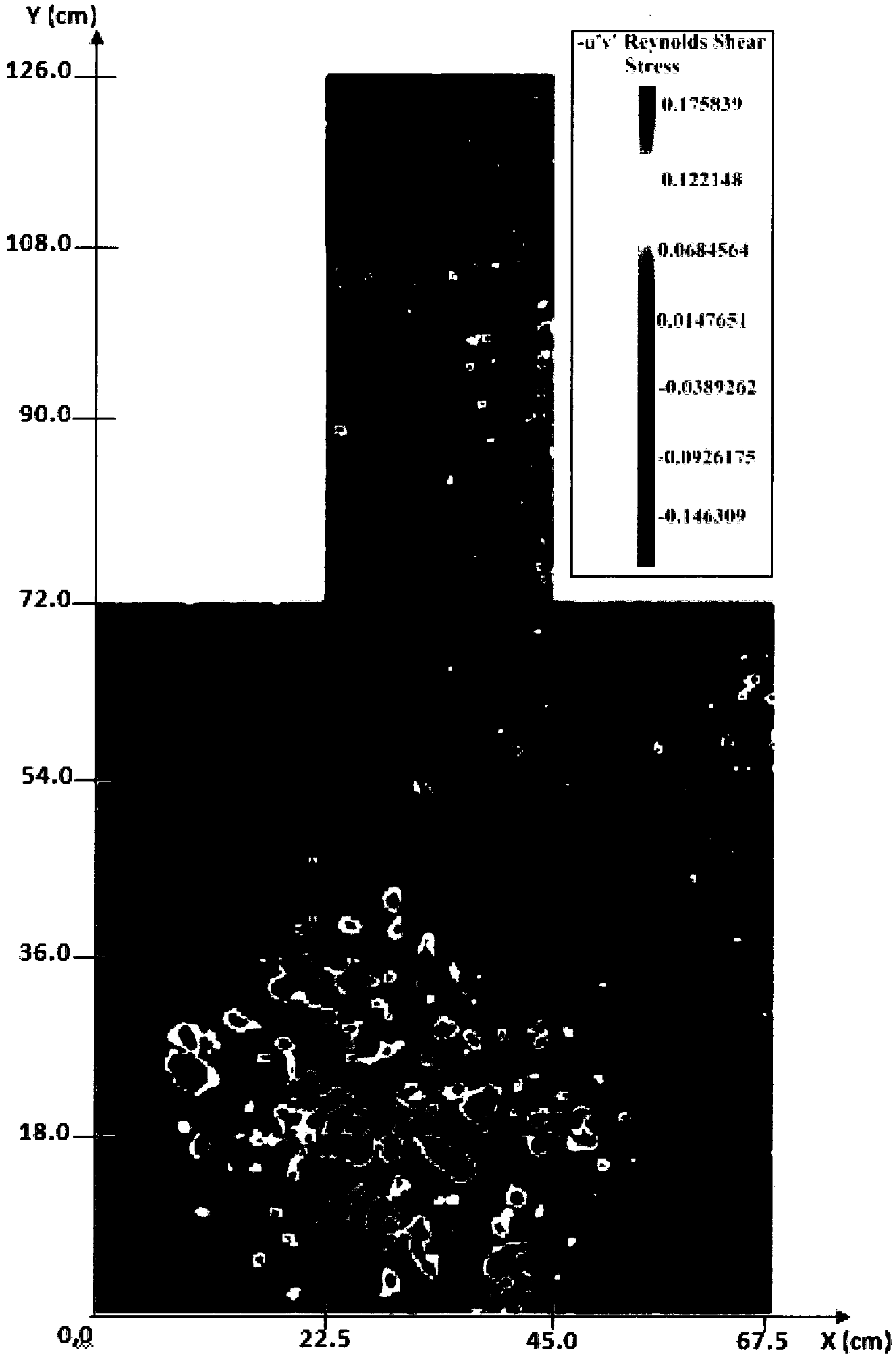

Figure 5.7: Reynolds Shear Stress using PIV Measurements (Case 7)

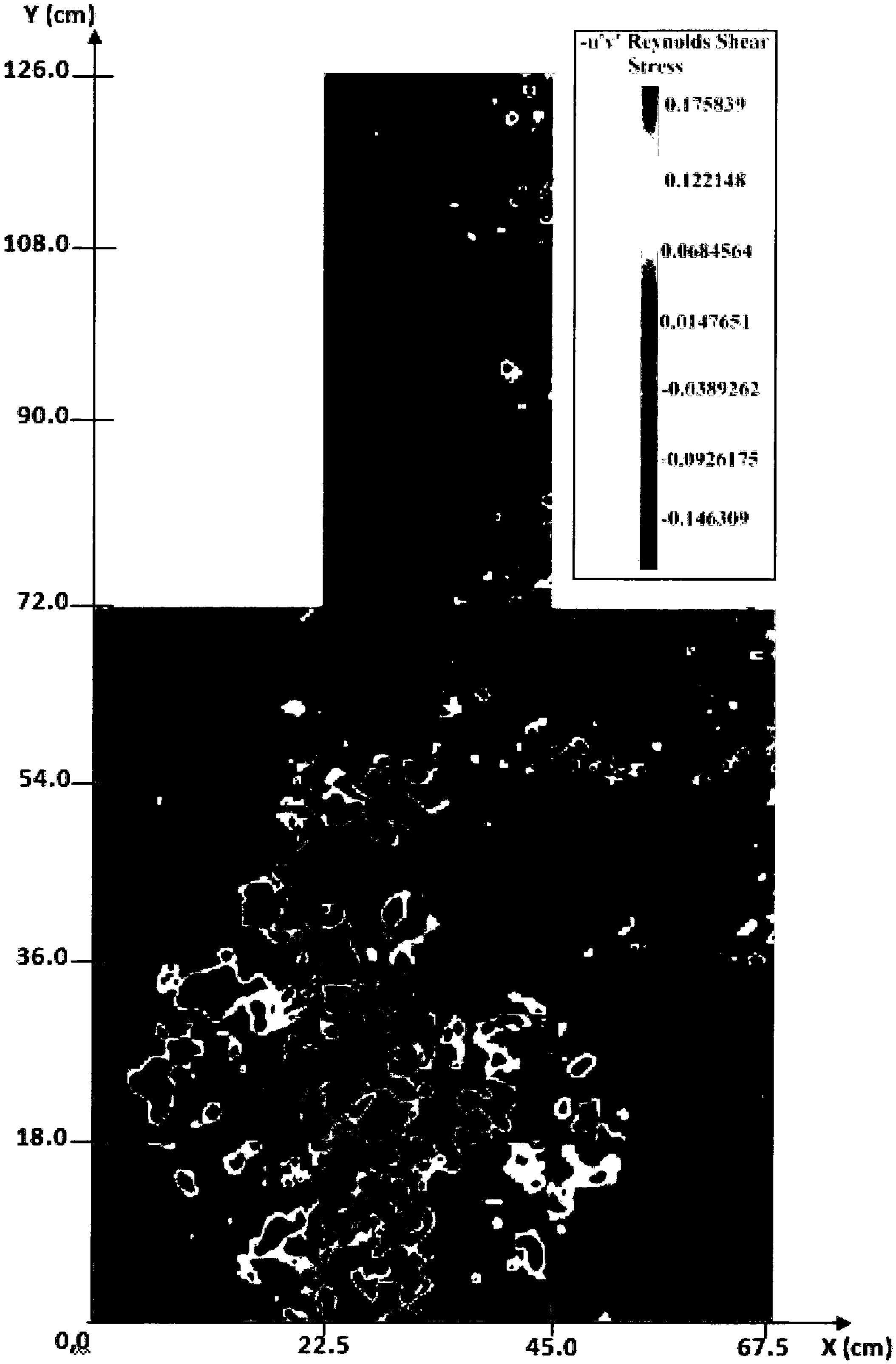

Figure 5.8: Reynolds Shear Stress using PIV Measurements (Case 8)

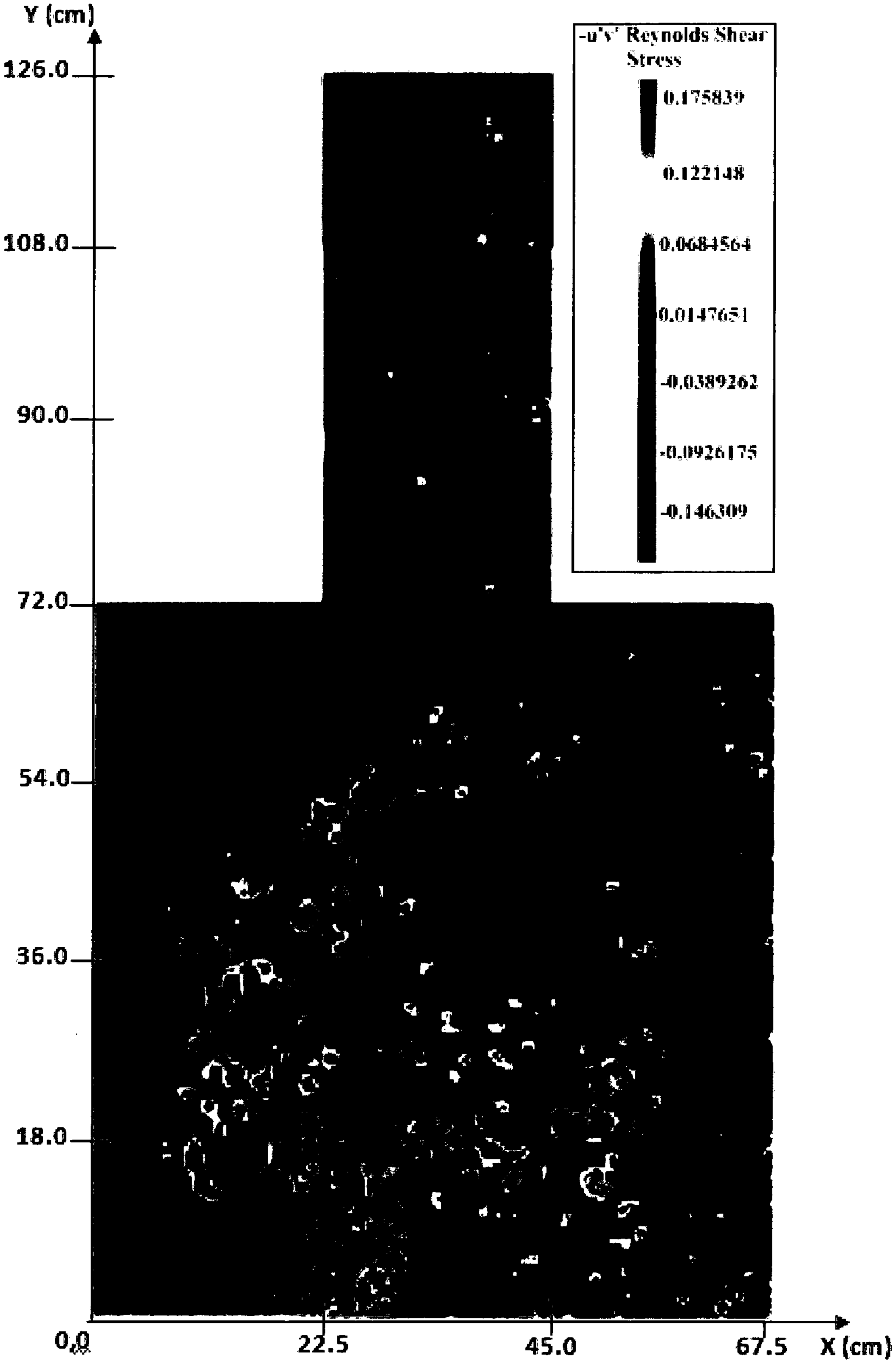

Figure 5.9: Reynolds Shear Stress using PIV Measurements (Case 9)

5.2 Hotwire Survey

Hotwire Anemometry measurements were performed in order to survey the three components of the velocity field and the turbulence intensity levels in three wake planes. Since all the components of the velocity distribution were obtained, the planar velocity field can be visualized by plotting vectors to show how the vortices occur at the wing tip and the outboard edge of the flap. The vorticity is one of the parameters used to locate the vortices in the wake so the z component of vorticity distribution was also plotted. In this section the graphics showing the distribution of resultant velocity, turbulence intensity and z vorticity magnitude are presented. In subsequent sections, some interpretations will be made about the flow field to show how the wake changes with different factor settings. It should be noted that the units along x and y axes are inches.

5.2.1 Mean Velocity Field

The mean velocity field shows the distribution of resultant velocity (or total velocity) under the conditions defined in Table 5.1. The first insights obtained from the graphics (see Figures 5.10-5.23) are the velocity differences below and above the wing (in the Figures, right hand side corresponds to the region above the wing). Since for the cases 1-4 the angle of attack is 0°, the velocity difference between the two regions (above and below) is not as obvious as in the cases 5-8 where the angle of attack is 10°.

Within the dissertation study, vortices must be observed in order to define their trajectories but for the cases 1-4 the wing tip vortex is not easily observable from the graphics showing the total velocity due to the small angle of attack. However the PIV results and vorticity distributions revealed the vortices occurring due to the curvature of the wing. The flap vortices are observed for all cases since the smallest deflection angle used for the experimentation was 15°. The total velocity in the wing tip vortices is sometimes up to 1.45 times the freestream velocity at 10° angle of attack whereas Green (1991) obtained the axial velocity as 1.6 times the freestream velocity by using a double-pulsed holography method on a rectangular wing at the same angle of attack.

The propeller wake is another important wake structure since merging of the propeller wake with the flap vortex significantly affects the flap vortex behavior. As the propeller pitch angle increases, the propeller wake shows greater induced velocity in its wake and close to the tip of the propeller individual propeller tip vortices are also observed. Since the propeller is located between the outboard and inboard edges of the flap, the propeller wake greatly influences the flow above and below the flap. For all cases, the propeller wake above the wing is deflected along the negative y axis and the propeller wake below the wing is deflected along the positive y axis since the propeller is rotating in a clockwise direction (viewed from downstream) and the helical wake interacts with the wing. The deflection of the shape with increasing distance downstream is also observable and the shape observed at first plane convects toward the flap vortex while proceeding downstream. The velocity deficit in the wing wake can also be viewed for all cases and as the downstream distance increases this deficit dissipates. The first nine cases showed the wing trailing edge clearly while the wing shape is not easily observable for the last nine cases (cases 19-27) due to the reduction of velocity deficit. The wing thickness is considerably higher at the wing root than the wing tip and the thickness distribution is linear for the model. Due to this fact, the velocity deficit towards the wing root is higher and wider. As the flap is deployed for all cases, there seems to be a shift between the outward and inboard wing wake regions. The extension of the wing wake with respect to the y axis is inclined towards the right side (note that this is observed from a downstream view) due to the dihedral angle of the wing.

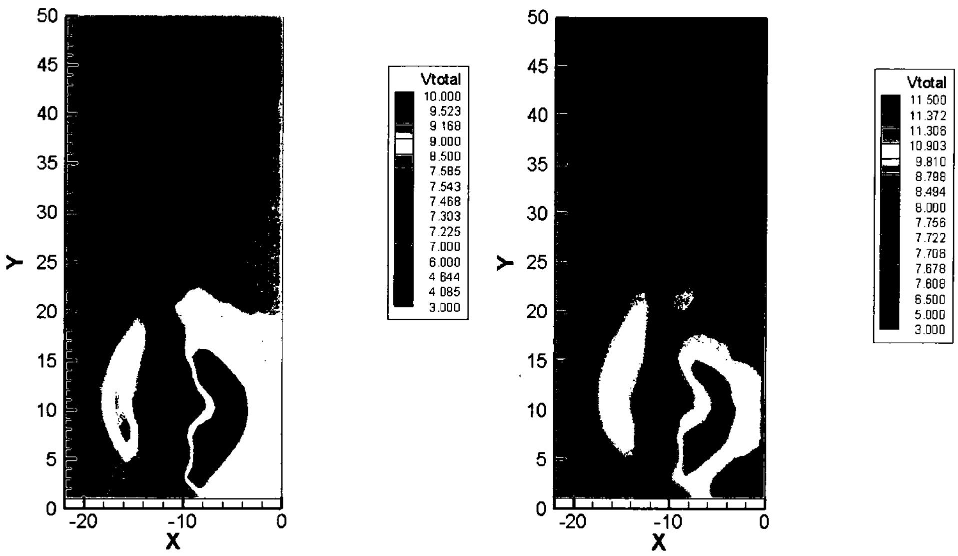

Figure 5.10: Mean Velocity Field (left-case 1 and right-case 2)

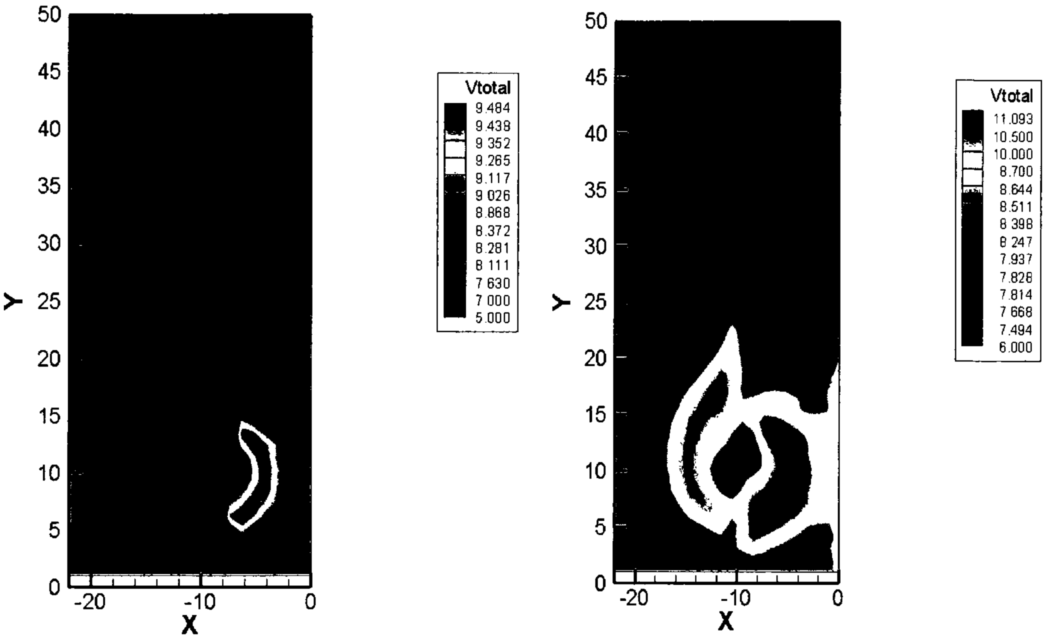

Figure 5.11: Mean Velocity Field (left-case 3 and right-case 4)

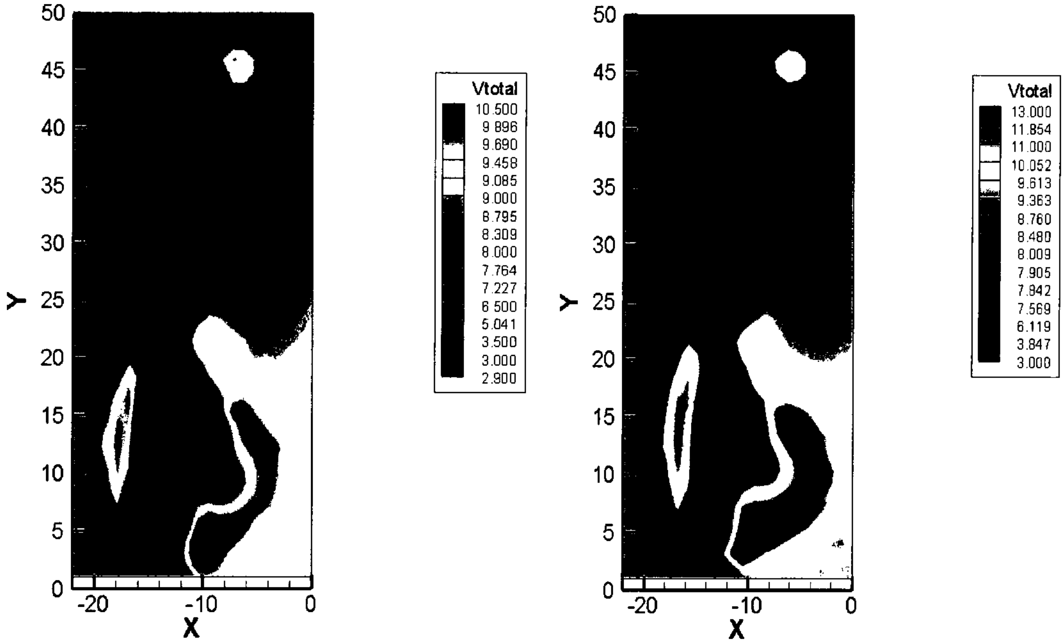

Figure 5.12: Mean Velocity Field (left-case 5 and right-case 6)

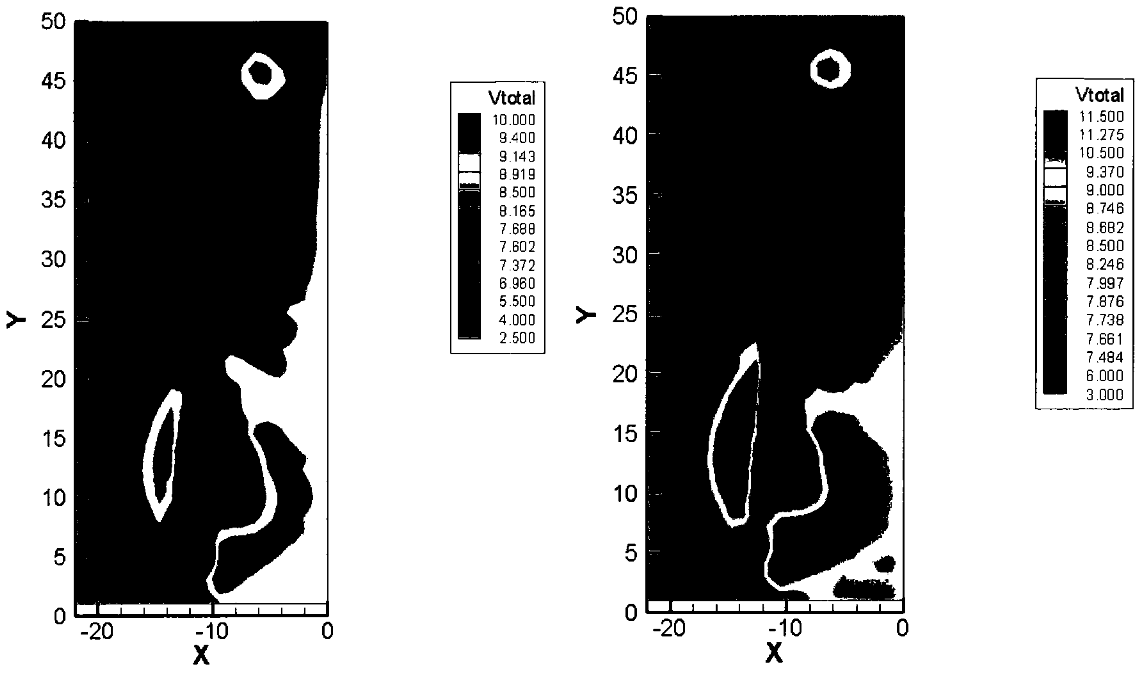

Figure 5.13: Mean Velocity Field (left-case 7 and right-case 8)

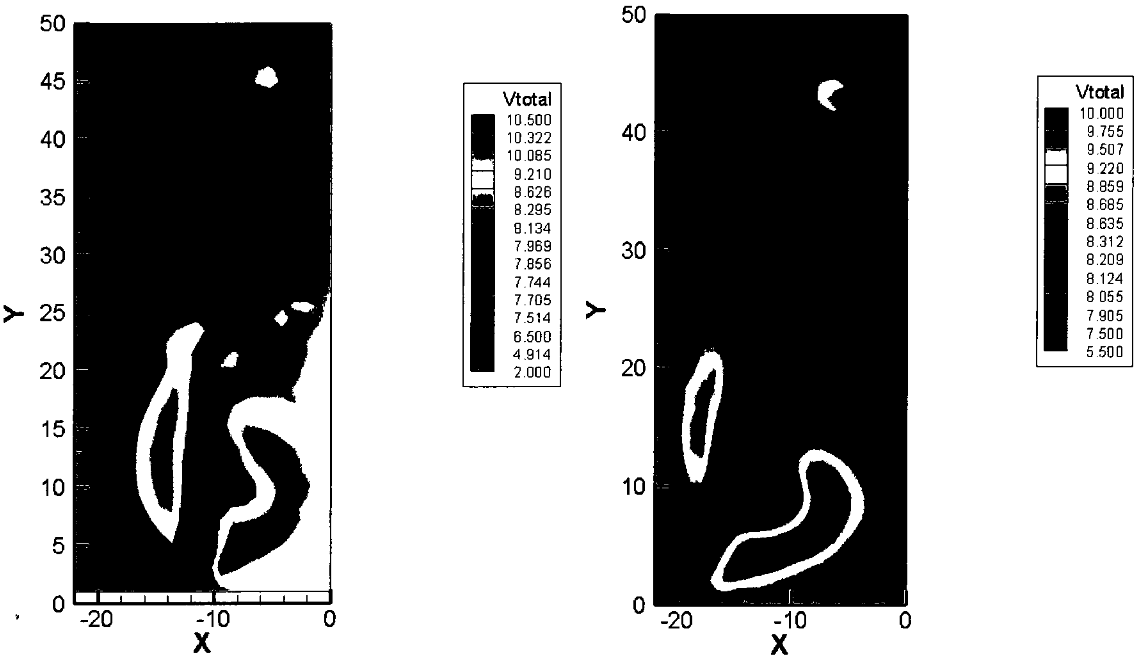

Figure 5.14: Mean Velocity Field (left-case 9 and right-case 10)

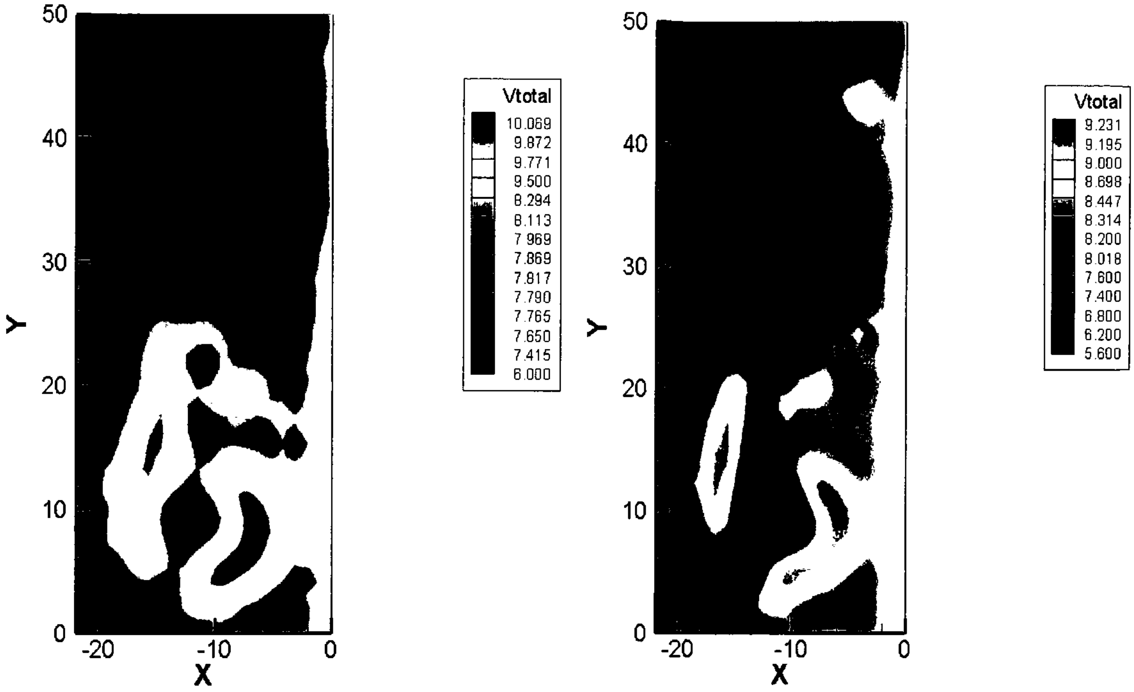

Figure 5.15: Mean Velocity Field (left-case 11 and right-case 12)

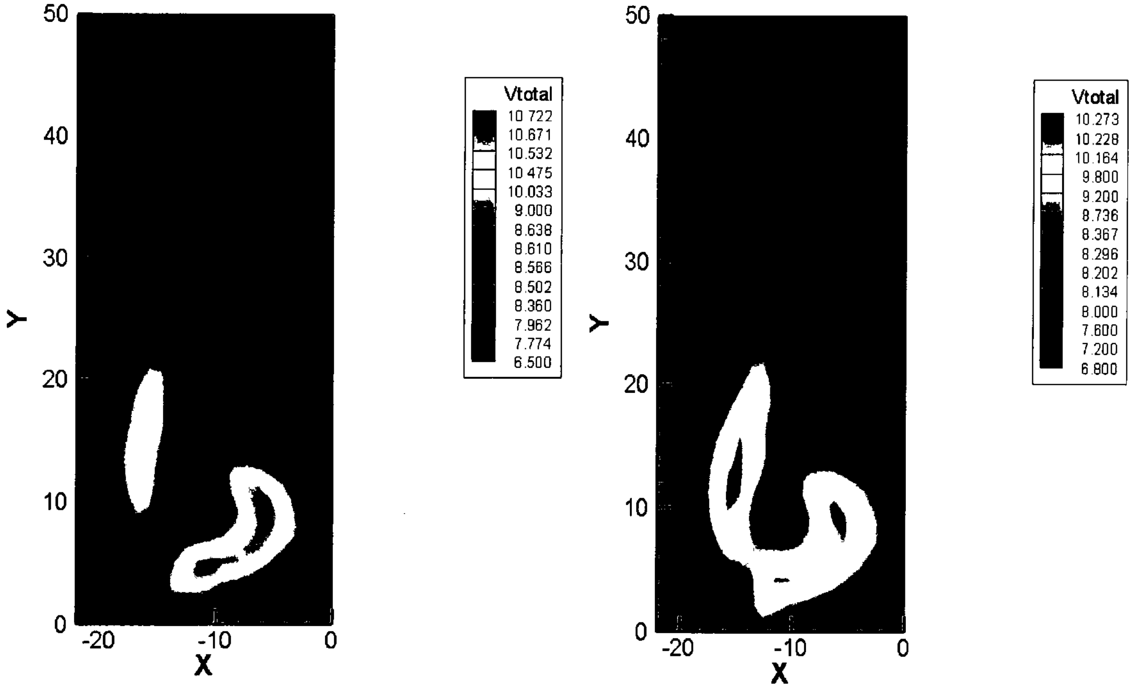

Figure 5.16: Mean Velocity Field (left-case 13 and right-case 14)

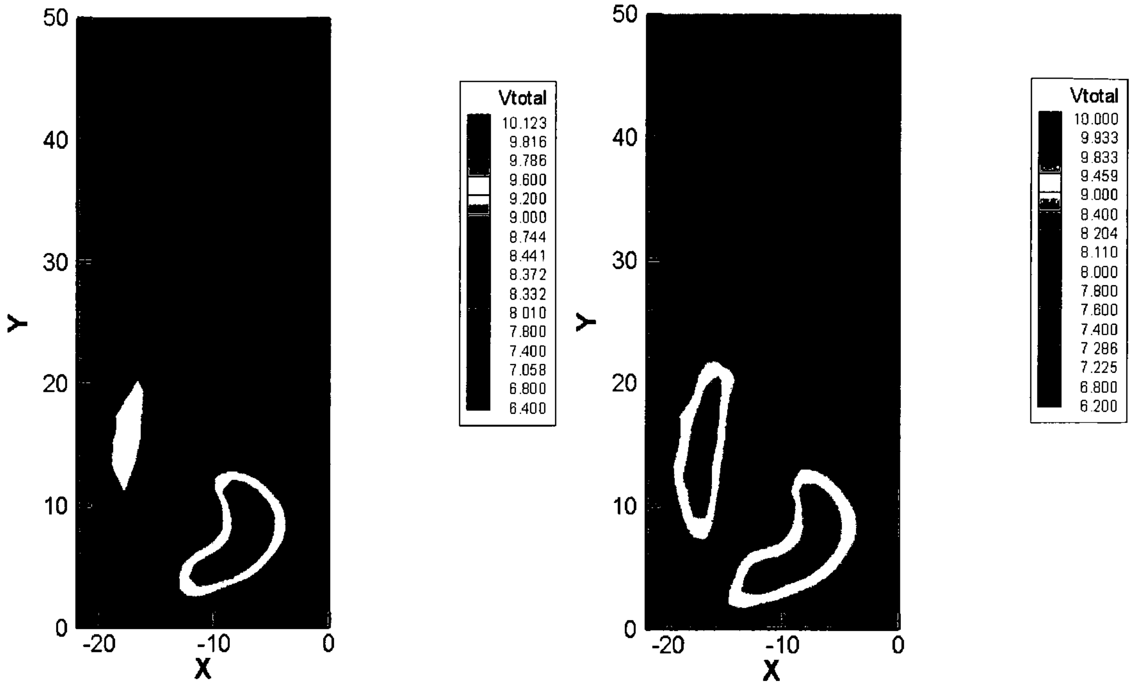

Figure 5.17: Mean Velocity Field (left-case 15 and right-case 16)

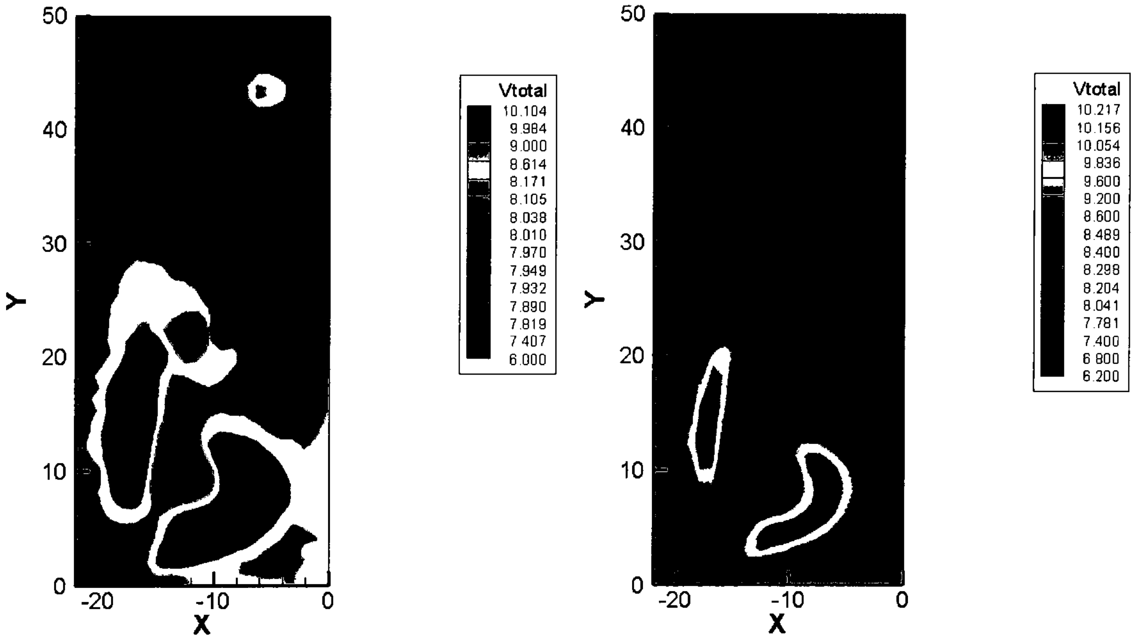

Figure 5.18: Mean Velocity Field (left-case 17 and right-case 18)

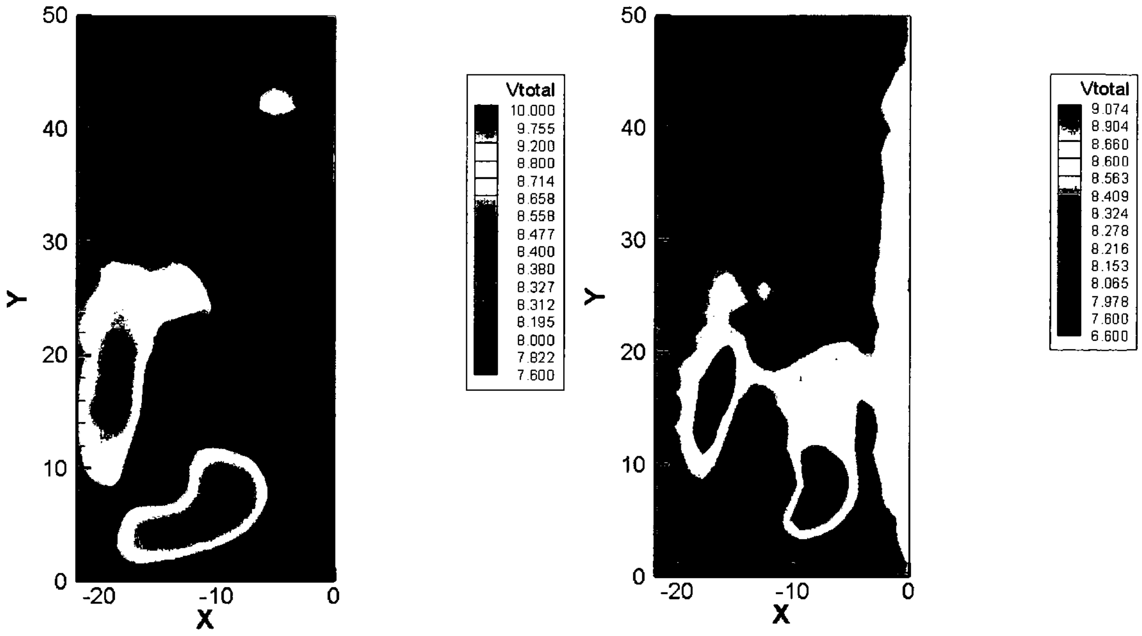

Figure 5.19: Mean Velocity Field (left-case 19 and right-case 20)

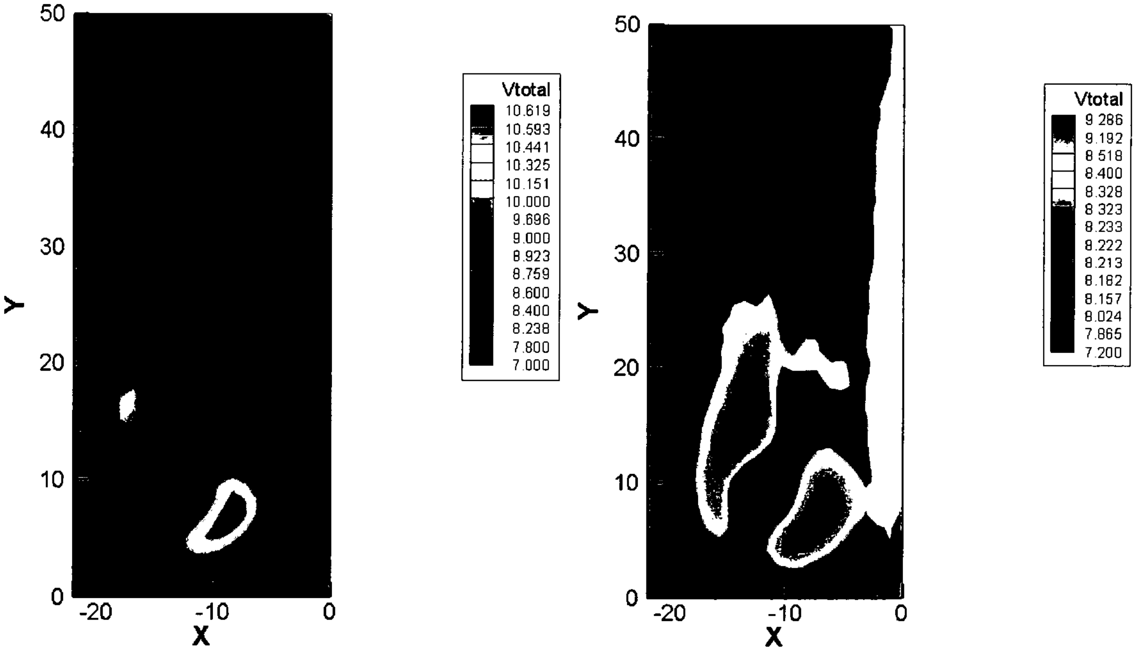

Figure 5.20: Mean Velocity Field (left-case 21 and right-case 22)

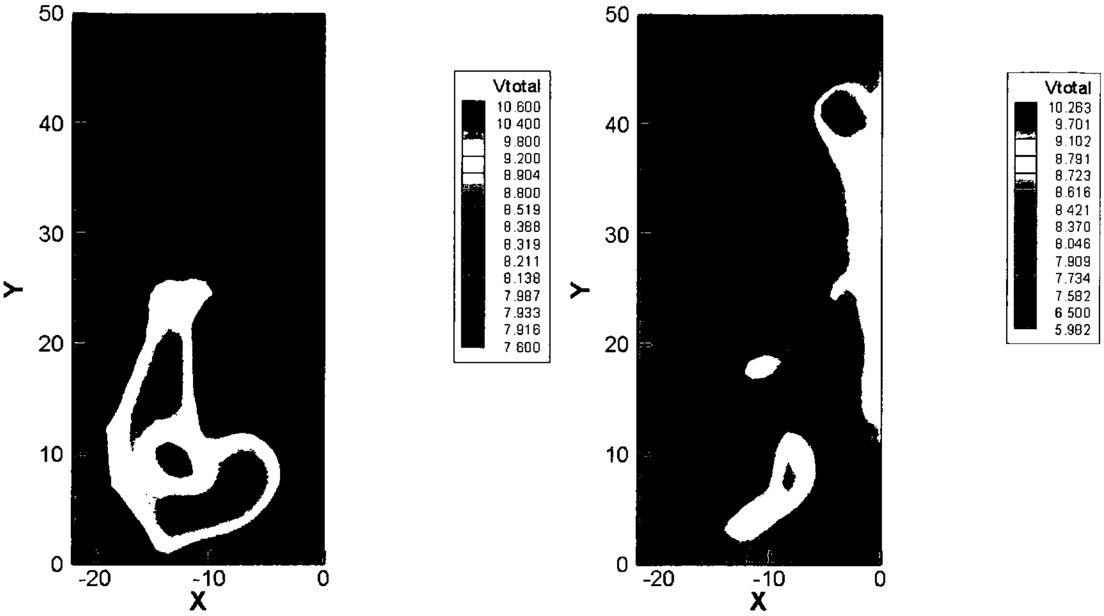

Figure 5.21: Mean Velocity Field (left-case 23 and right-case 24)

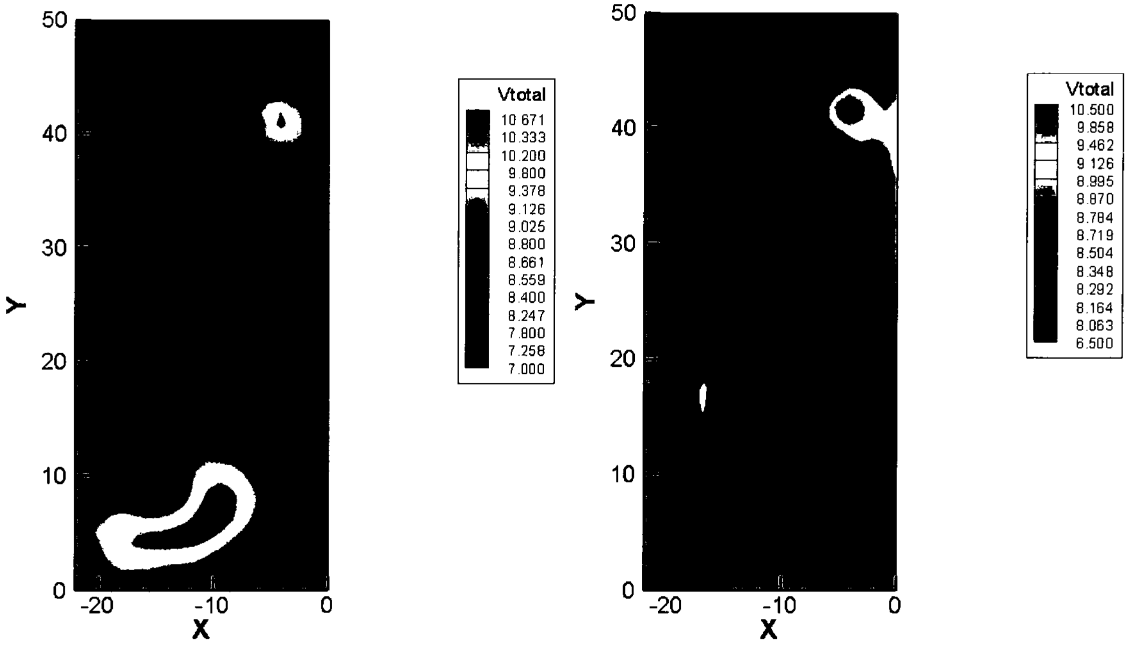

Figure 5.22: Mean Velocity Field (left-case 25 and right-case 26)

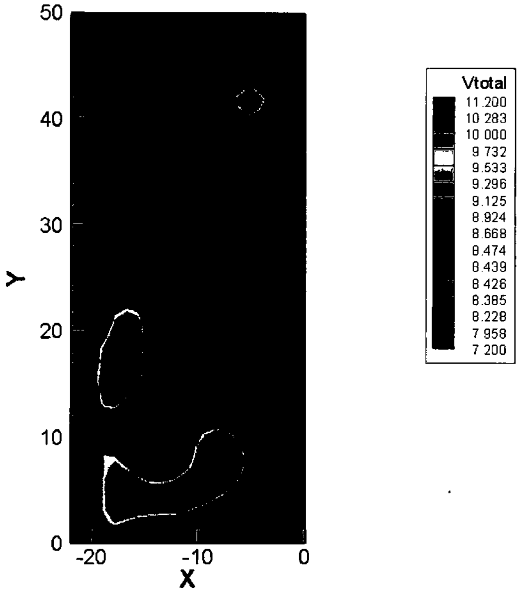

Figure 5.23: Mean Velocity Field (case 27)

5.2.2 Turbulence Intensities

Batchelor (1964) and Moore and Saffman (1973) concluded that fully rolled-up vortices at the wing tips are turbulent, and Figures 5.24-5.37 revealed that the vortices at both wing tip and flap have turbulent structures within them. Their evolutions are also observable with changing factor settings. The maximum turbulence intensities were observed around the propeller axis due to the thickness of both propeller blades (toward propeller shaft) and wing as well as the interaction effects of the propeller wake with the wing. The other easily observable structure is the wing tip vortex which is located uppermost in the graphics. The turbulence levels are higher in the core of the wing tip vortex compared to the ambient turbulence intensities as expected and can be attributed primarily to meandering of the vortex as stated in a study by Devenport (1995). It is observed that the turbulence intensities are increasing with angle of attack as the total velocity and the vorticity of the wing tip vortex also increase. This is also true for the flap vortex because as the flap angle increases these values also increase and make the flap vortex shape observable among other structures and the freestream flow.

Traces of similar secondary structures, all of them rotating in the same direction as the tip vortex are also evident for some cases although when the angle of attack of attack is increased these secondary vortices are less evident.

The wake of the wing and the merging of the propeller wake with the flap vortex are also observable from the turbulence intensity distributions. This merging makes the behavior of the flap vortex more complex compared to the wing tip due to the interaction effects.

The peak turbulence intensity is in the order of 25% of uniform velocity in the first plane while for the second and third planes this value reduces to approximately 20% and 15% respectively. As the downstream distance increases, the turbulence decays and the shape of the wake is distorted.

The trajectory of both the wing tip and flap vortices showed that wing tip vortex is travelling upward and inward while the flap vortex is mainly moving downward and inward. The downwash is the main effect on the downward motion of the flap vortex. The wing tip vortex is moving upward only within this near field region and is expected to move downward at larger downstream.

The shortest distance between two vortices indicates the tendency towards merging of two vortices either in extended near or medium range fields. It is observed that the vortices seem to be approaching each other with increasing angle of attack and the interaction of propeller pitch angle and downstream distance while the factors such as the flap angle, the propeller pitch angle, and the downstream distance are tending to increase the distance between two vortices.

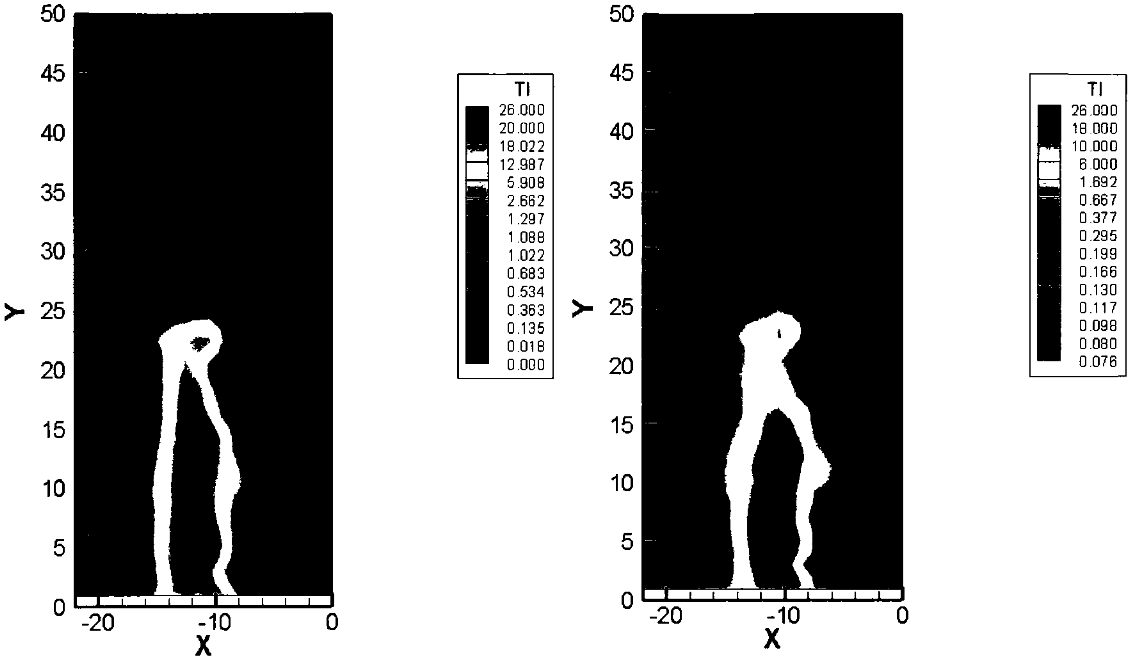

Figure 5.24: Turbulence Intensities (left-case 1 and right-case 2)

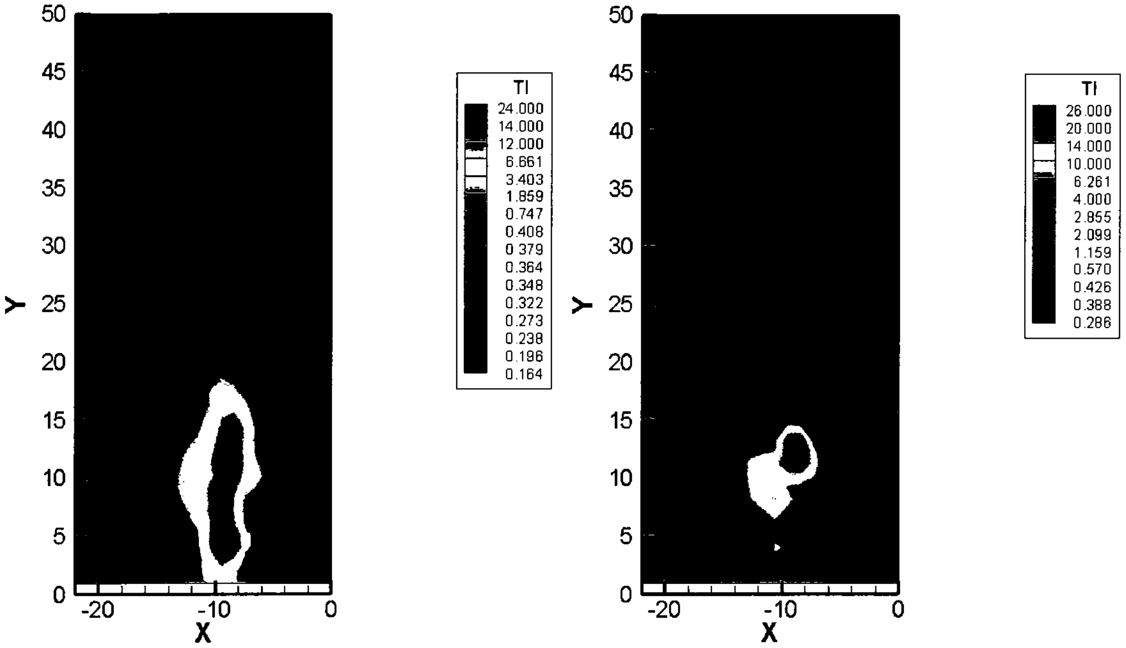

Figure 5.25: Turbulence Intensities (left-case 3 and right-case 4)

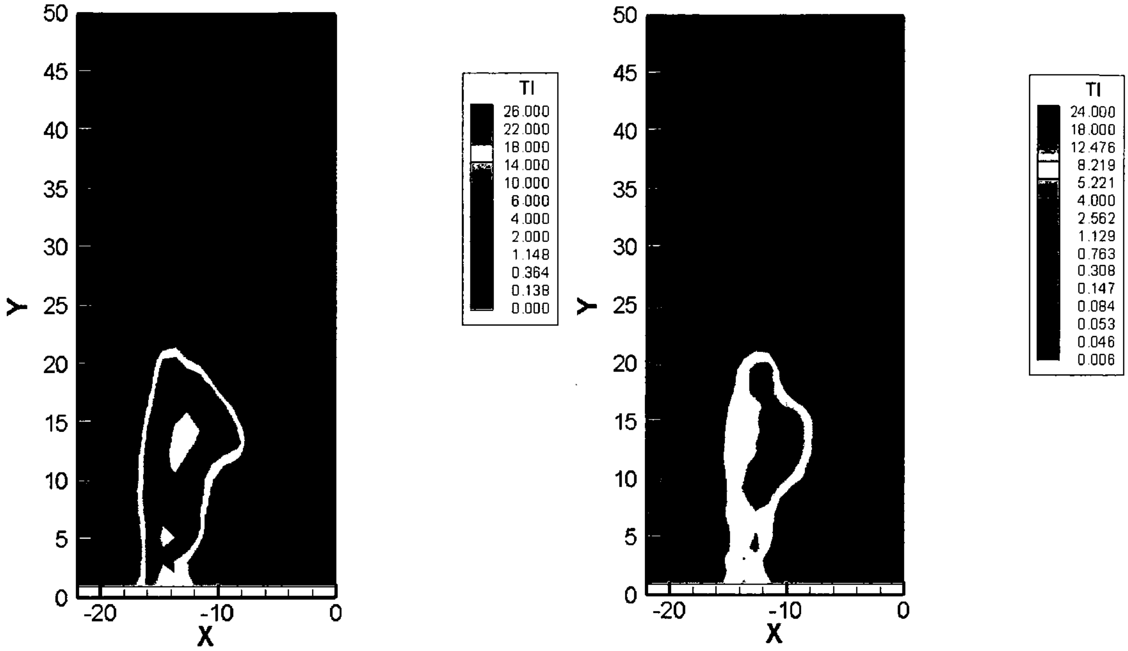

Figure 5.26: Turbulence Intensities (left-case 5 and right-case 6)

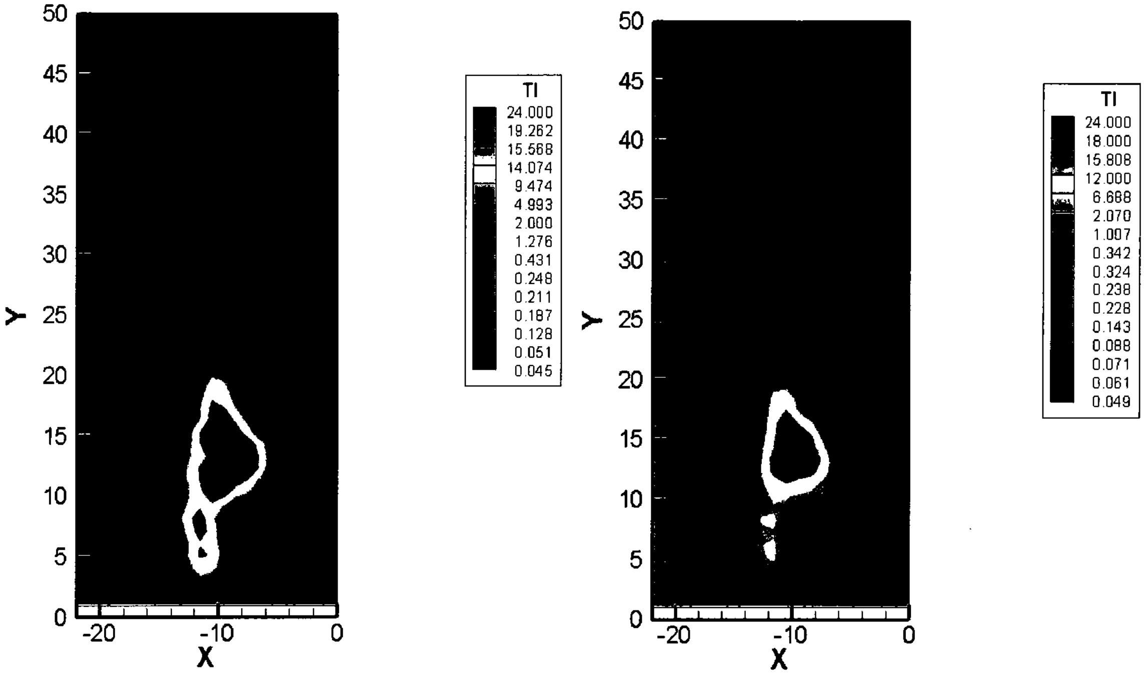

Figure 5.27: Turbulence Intensities (left-case 7 and right-case 8)

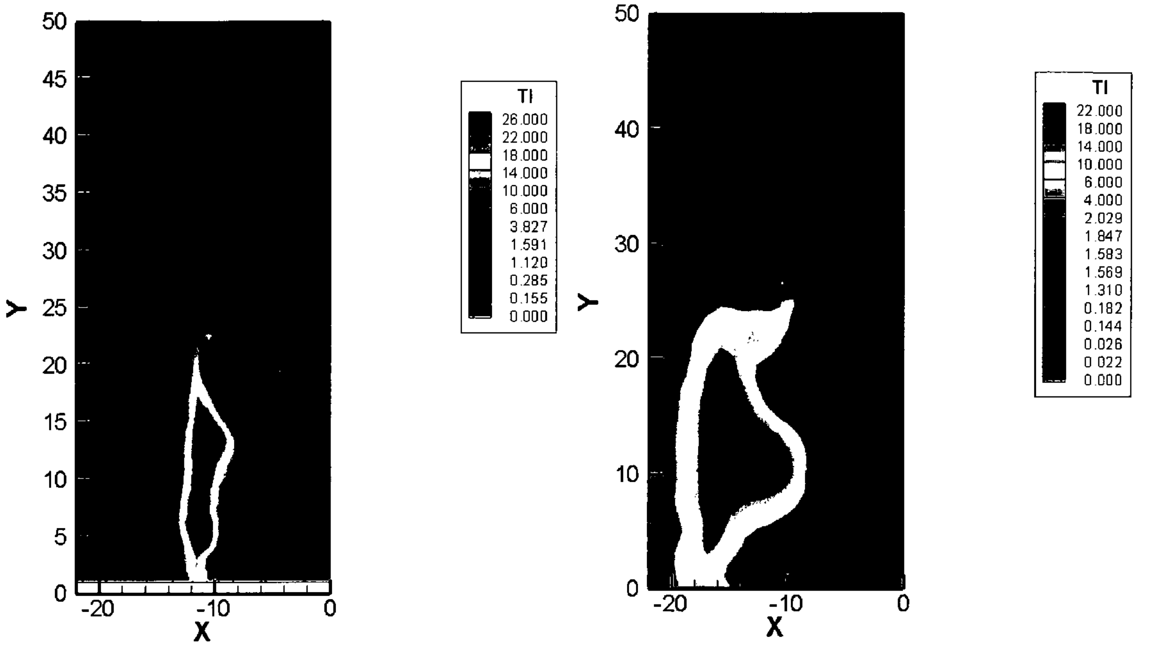

Figure 5.28: Turbulence Intensities (left-case 9 and right-case 10)

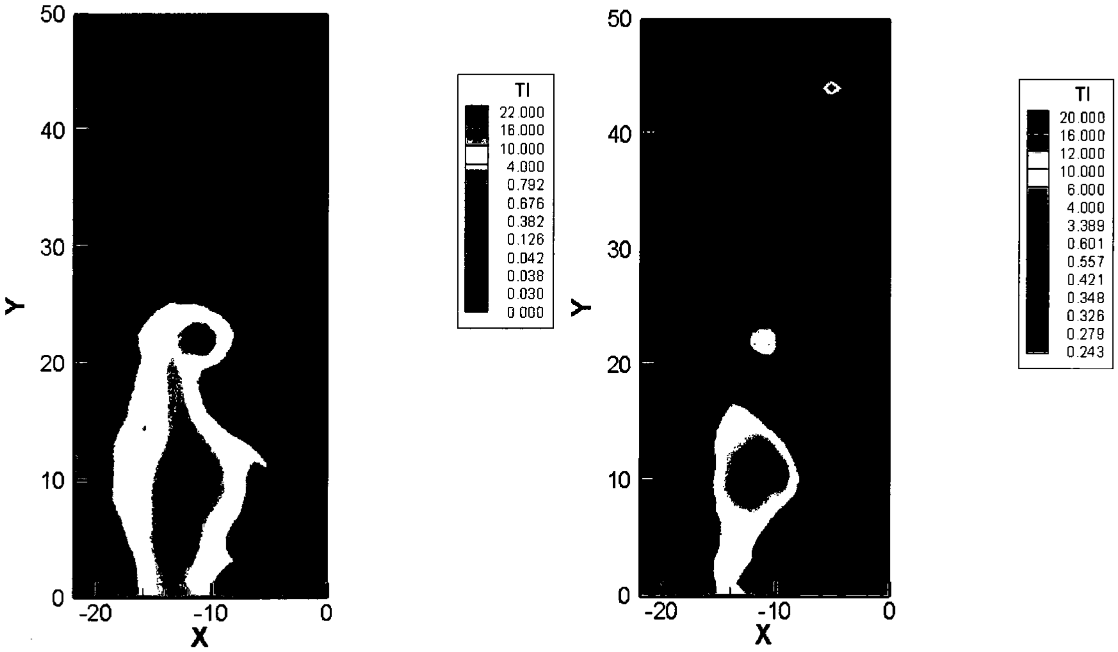

Figure 5.29: Turbulence Intensities (left-case 11 and right-case 12)

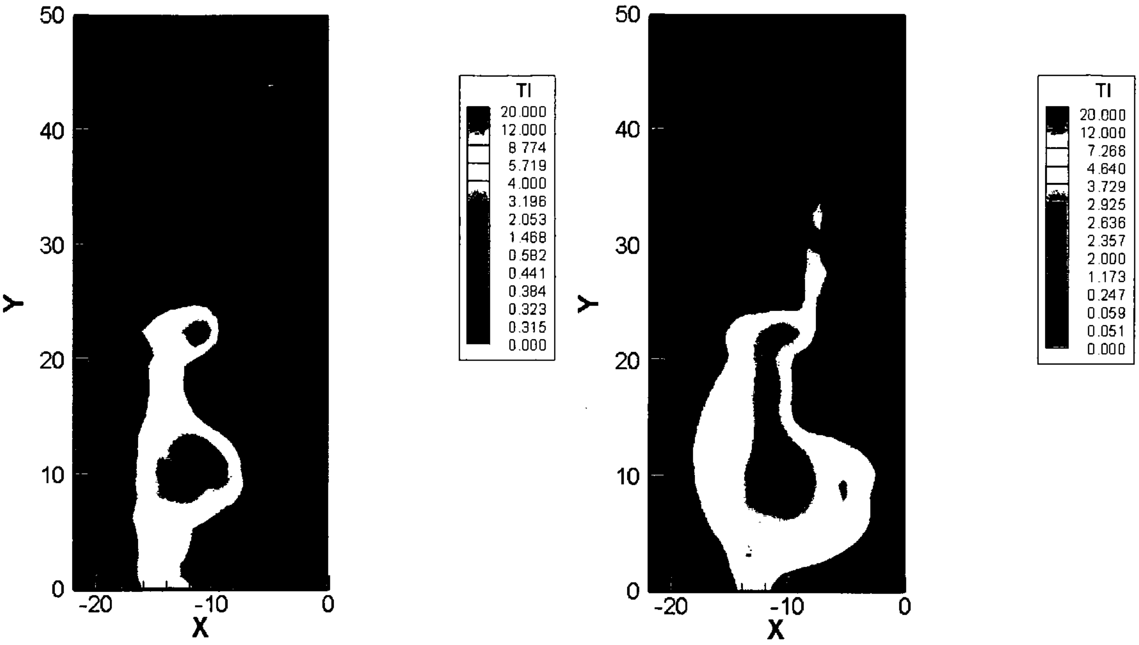

Figure 5.30: Turbulence Intensities (left-case 13 and right-case 14)

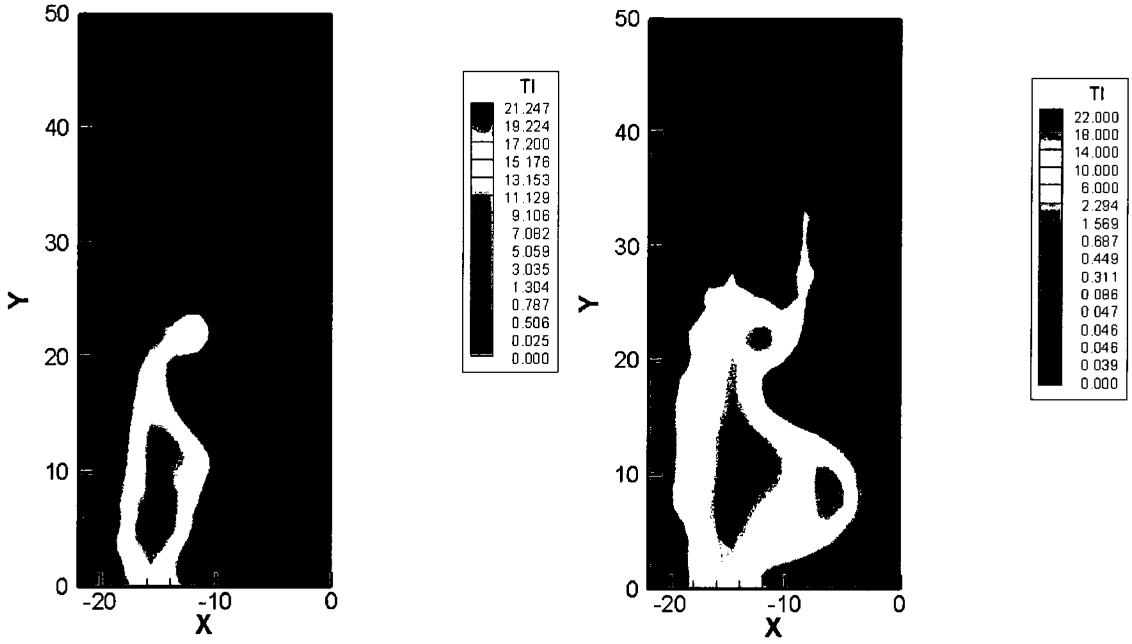

Figure 5.31: Turbulence Intensities (left-case 15 and right-case 16)

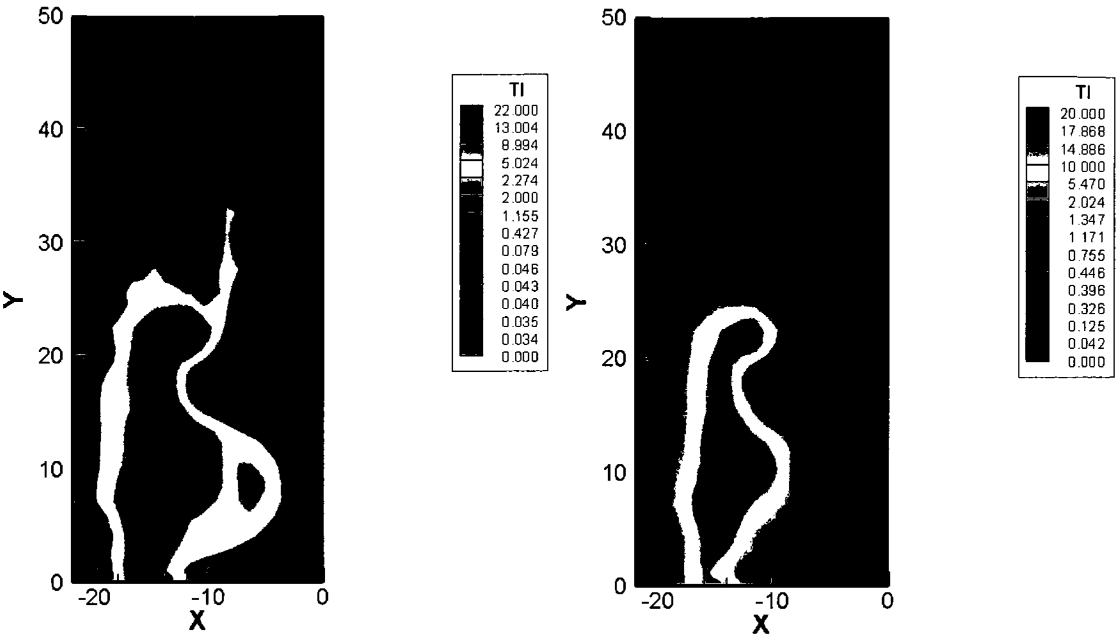

Figure 5.32: Turbulence Intensities (left-case 17 and right-case 18)

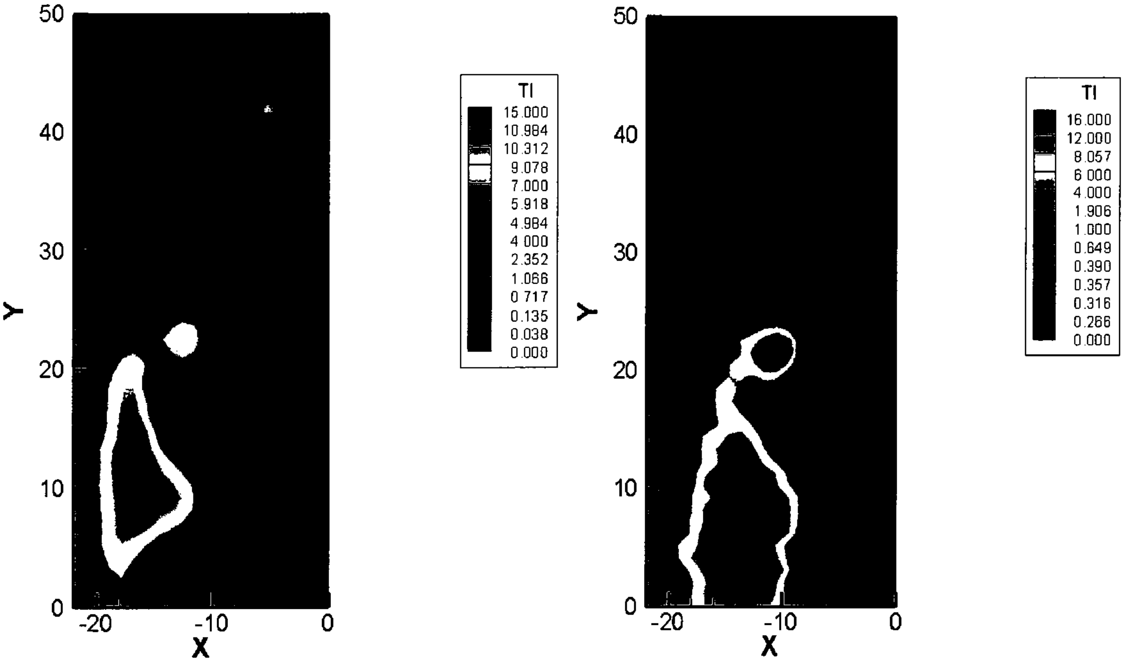

Figure 5.33: Turbulence Intensities (left-case 19 and right-case 20)

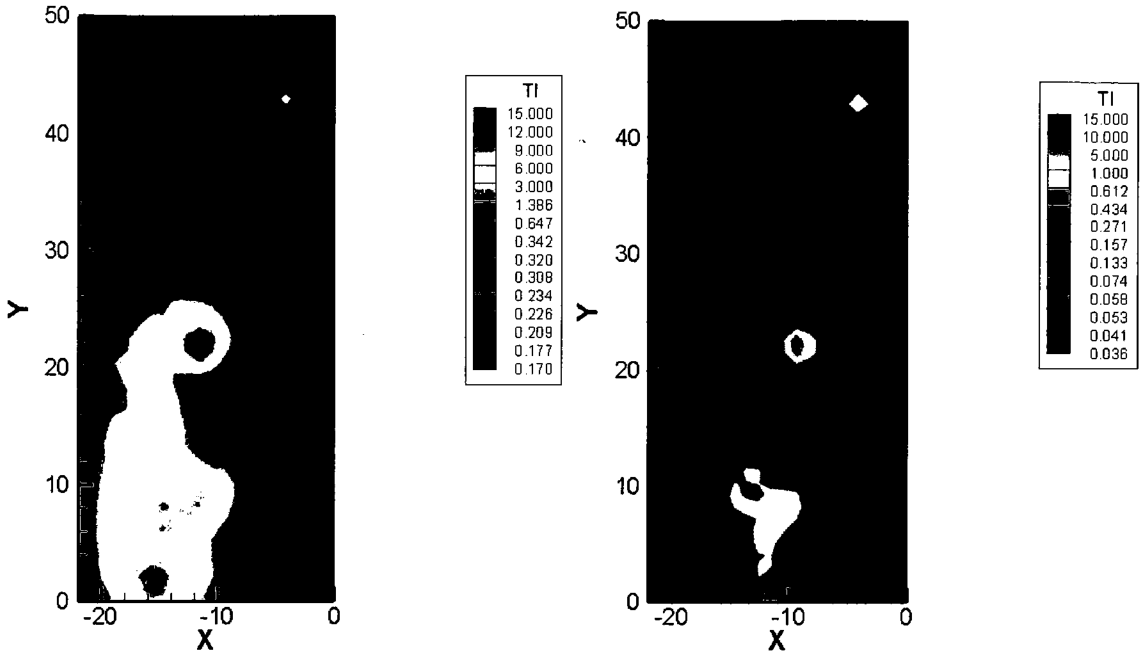

Figure 5.34: Turbulence Intensities (left-case 21 and right-case 22)

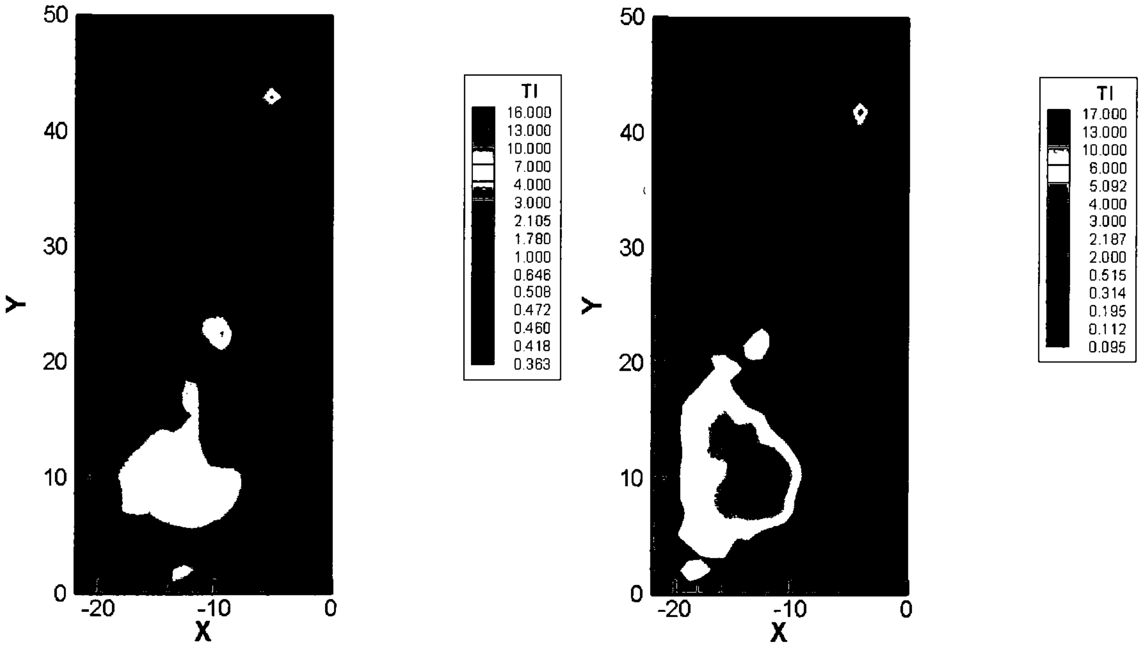

Figure 5.35: Turbulence Intensities (left-case 23 and right-case 24)

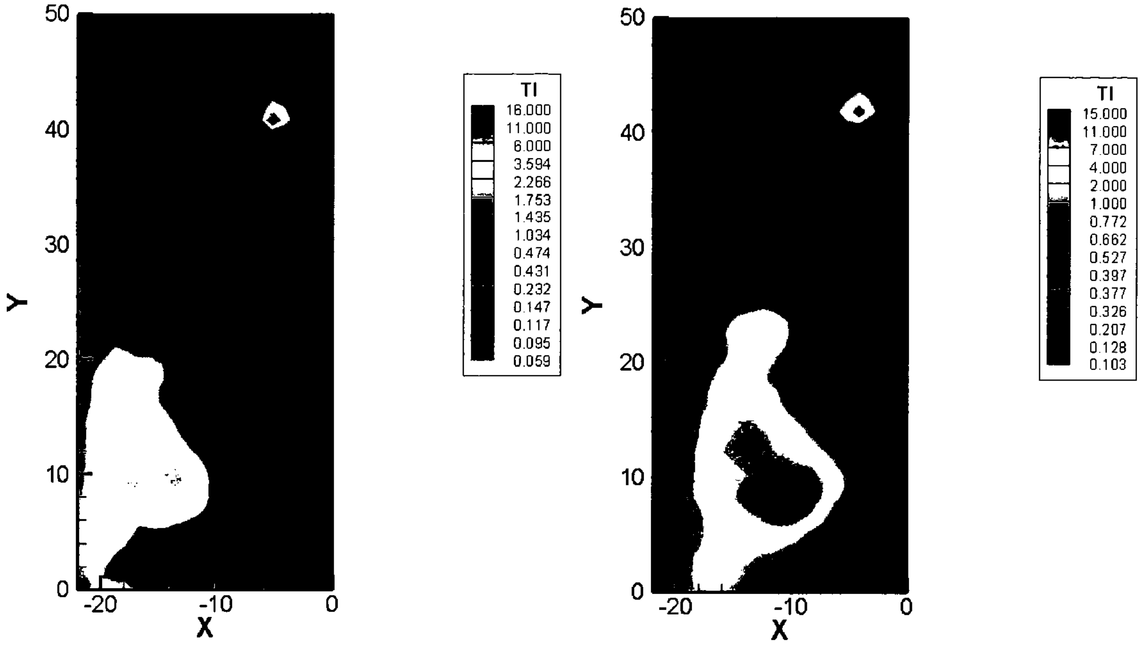

Figure 5.36: Turbulence Intensities (left-case 25 and right-case 26)

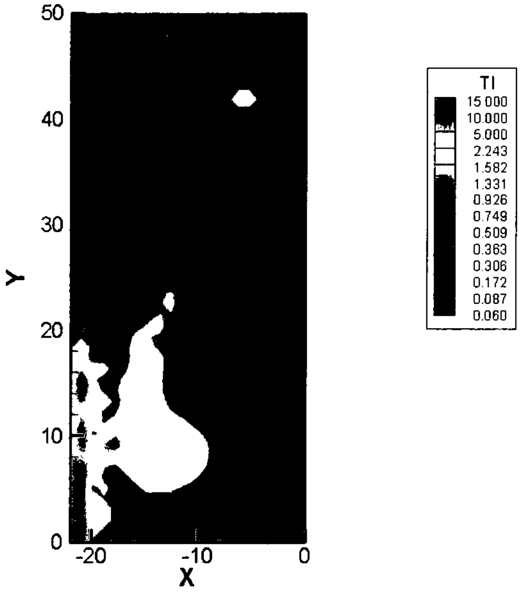

Figure 5.37: Turbulence Intensities (case 27)

5.2.3 Vorticity Magnitude with in-plane Velocity Vectors

The magnitude of the z component of the vorticity gives a measure of vortex strength and is a response to be used in the FCD model. Plotting the distribution of vorticity visualizes the location of both wing tip and flap vortices.

The vorticity graphs (Figures 5.38-5.51) indicate two main structures in the wake with the wing tip vortex exhibiting highest vorticity magnitude while the flap vortex shows a lower vorticity magnitude. As the angle of attack or flap angle increase the strength of both vortices increase as expected. Contrary to the behavior of the wing tip vortex, the decay of the flap vortex is observable with downstream distance and propeller pitch angle. The studies by Huenecke (2002) performed to analyze the lifetime of a vortex from formation to decay and studies by Babie and Nelson (2004) for the interactions and decay of a four vortex system are performed considerably further downstream in the wake compared to the region considered in this study. However, some indications of decay of the vortices are also observed even within the near field. The flap vortex core size is increasing with downstream which can be taken as one indication of decay while no similar indications of decay for the wing tip vortex are observed within the near field wake.

As in the case of turbulence intensities, secondary structures of vorticity are also observable around vortices with the same direction of rotation, reducing in visibility with increasing angle of attack. In the graphs (Figures 5.38-5.51), in addition to the distribution of the magnitude of z vorticity, planar velocity vectors (U and V components of total velocity) were also plotted to highlight the locations of the vortices.

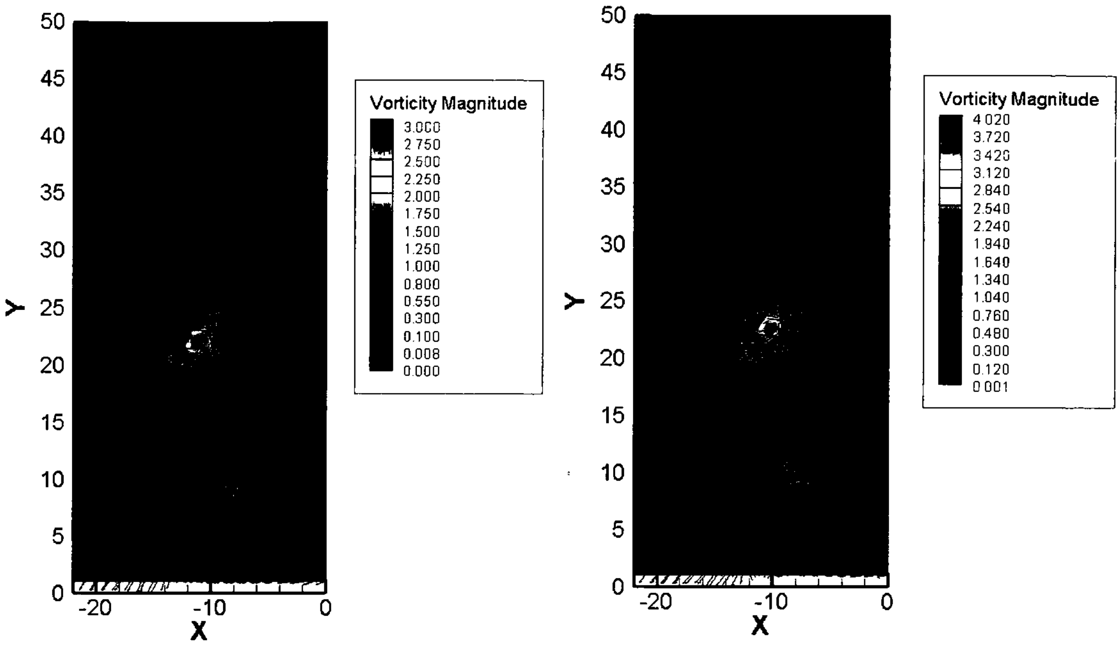

Figure 5.38: Vorticity Magnitude with 2D Vector (left-case 1 and right-case 2)

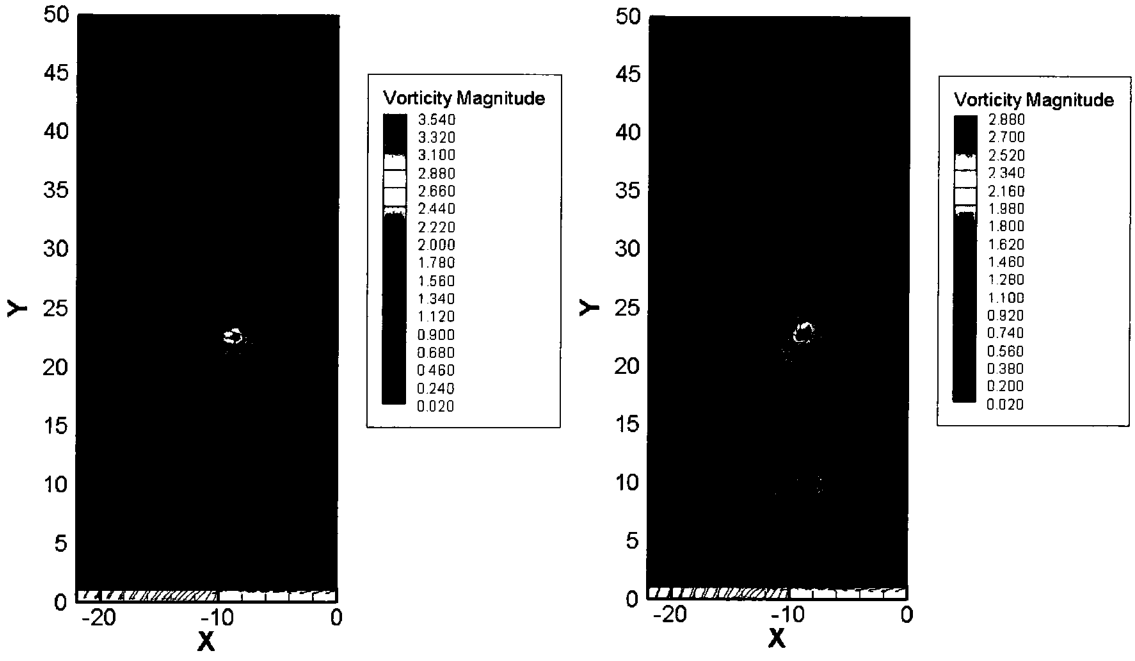

Figure 5.39: Vorticity Magnitude with 2D Vector (left-case 3 and right-case 4)

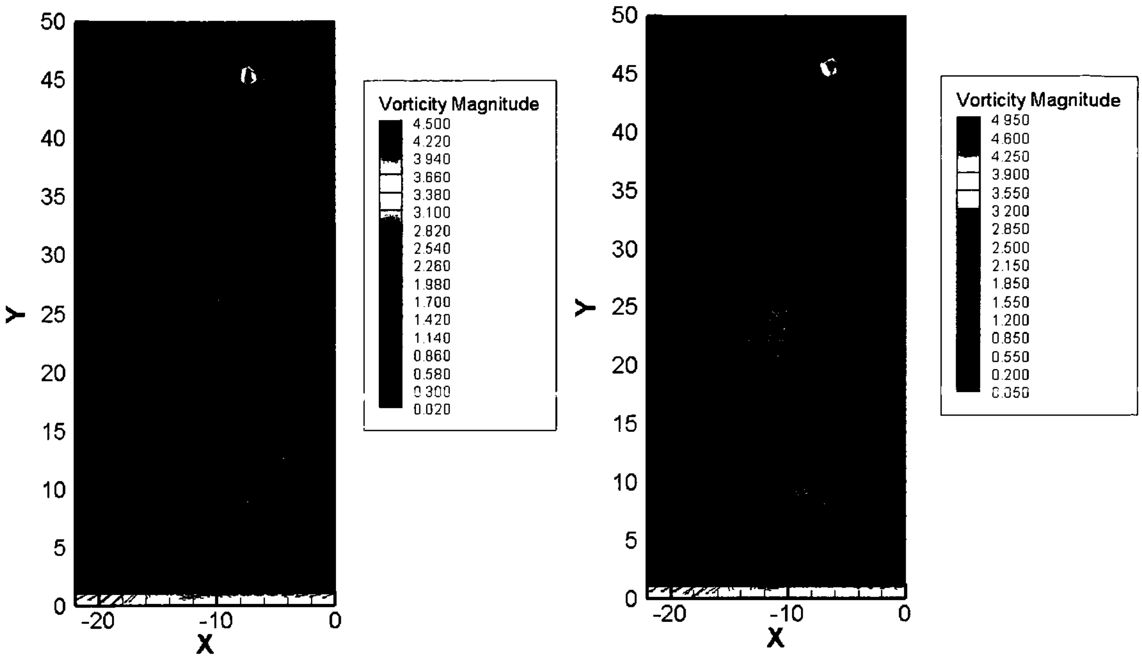

Figure 5.40: Vorticity Magnitude with 2D Vector (left-case 5 and right-case 6)

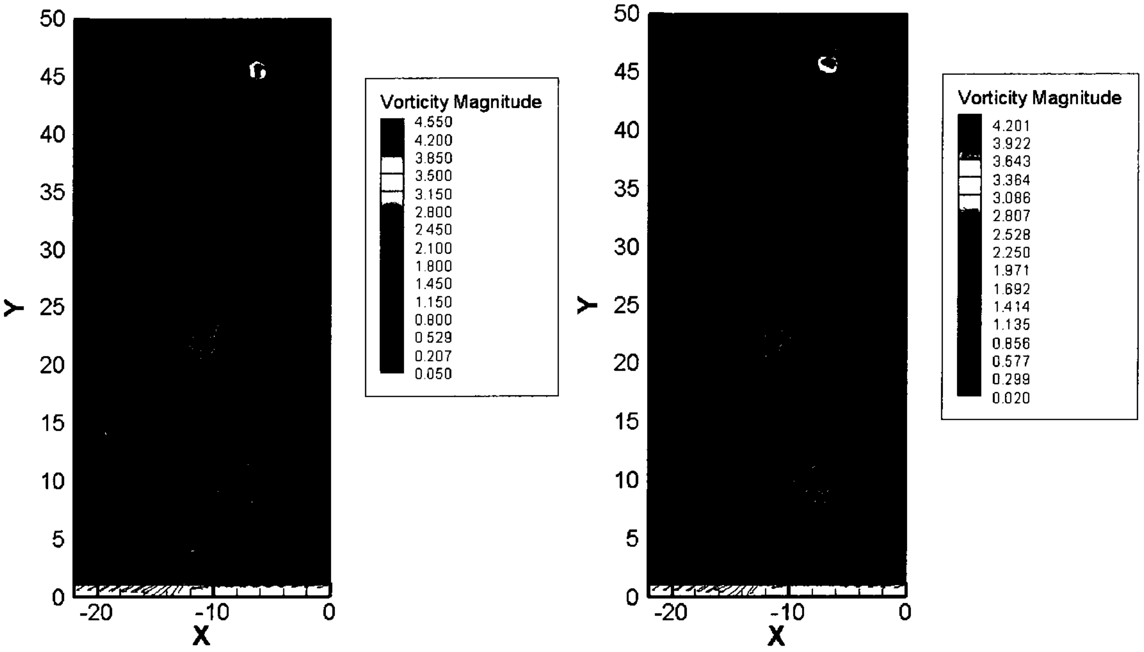

Figure 5.41: Vorticity Magnitude with 2D Vector (left-case 7 and right-case 8)

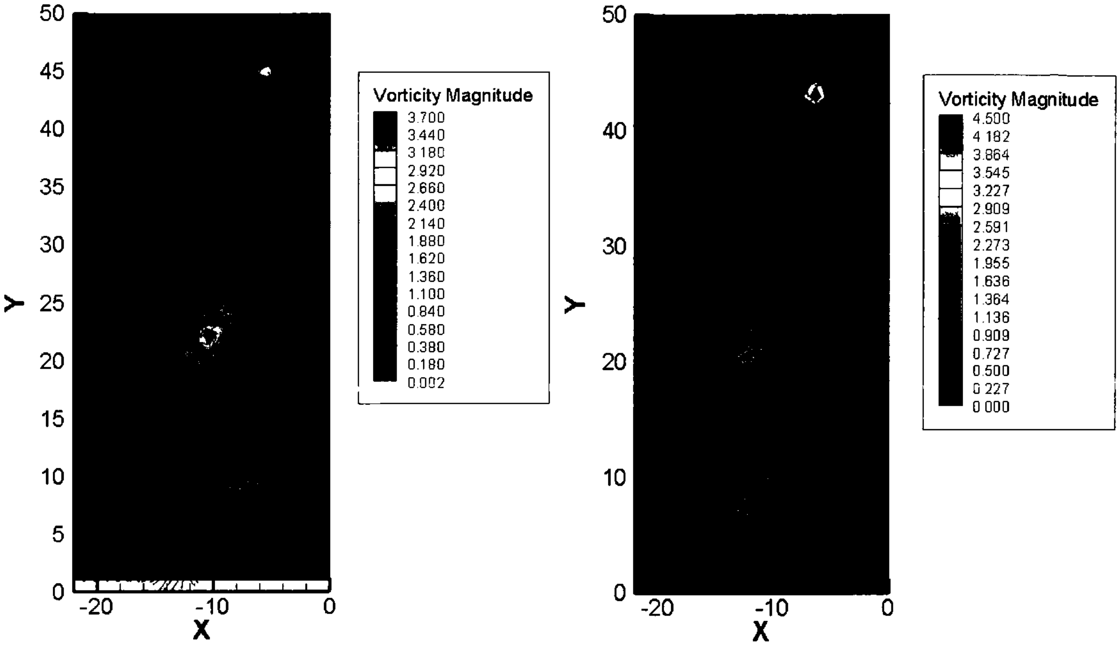

Figure 5.42: Vorticity Magnitude with 2D Vector (left-case 9 and right-case 10)

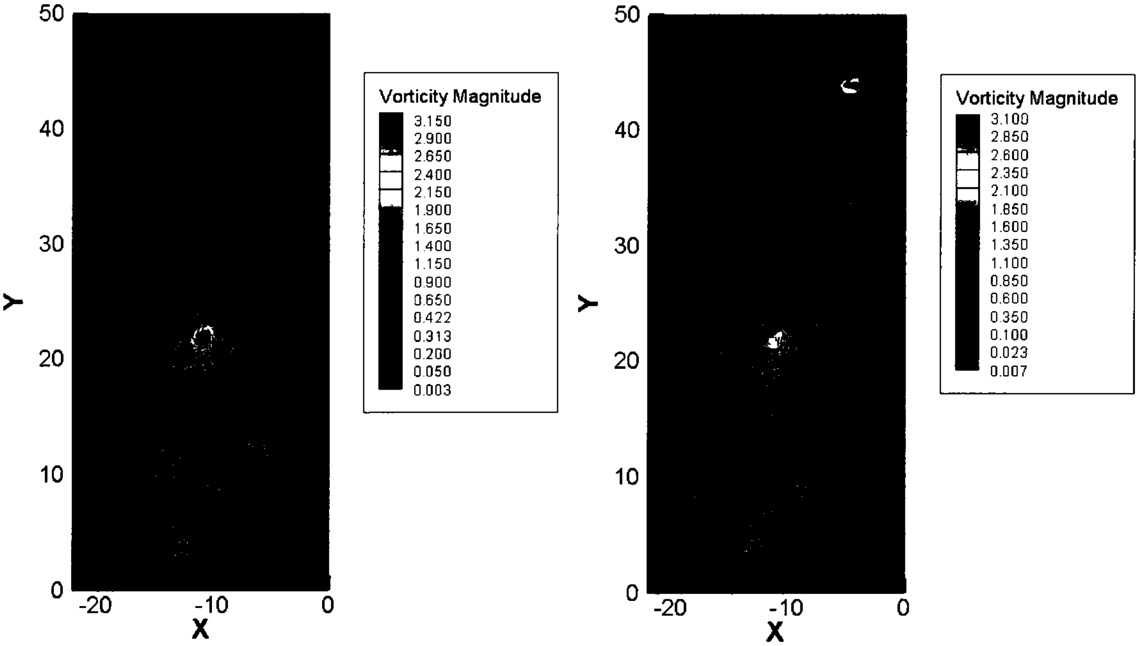

Figure 5.43: Vorticity Magnitude with 2D Vector (left-case 11 and right-case 12)

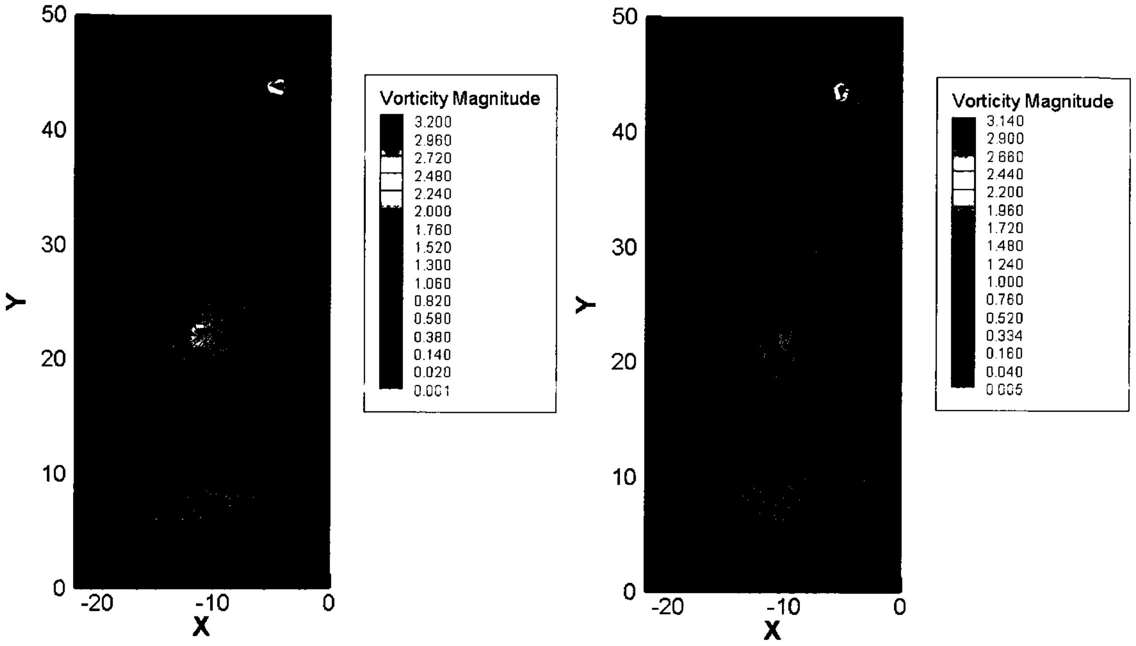

Figure 5.44: Vorticity Magnitude with 2D Vector (left-case 13 and right-case 14)

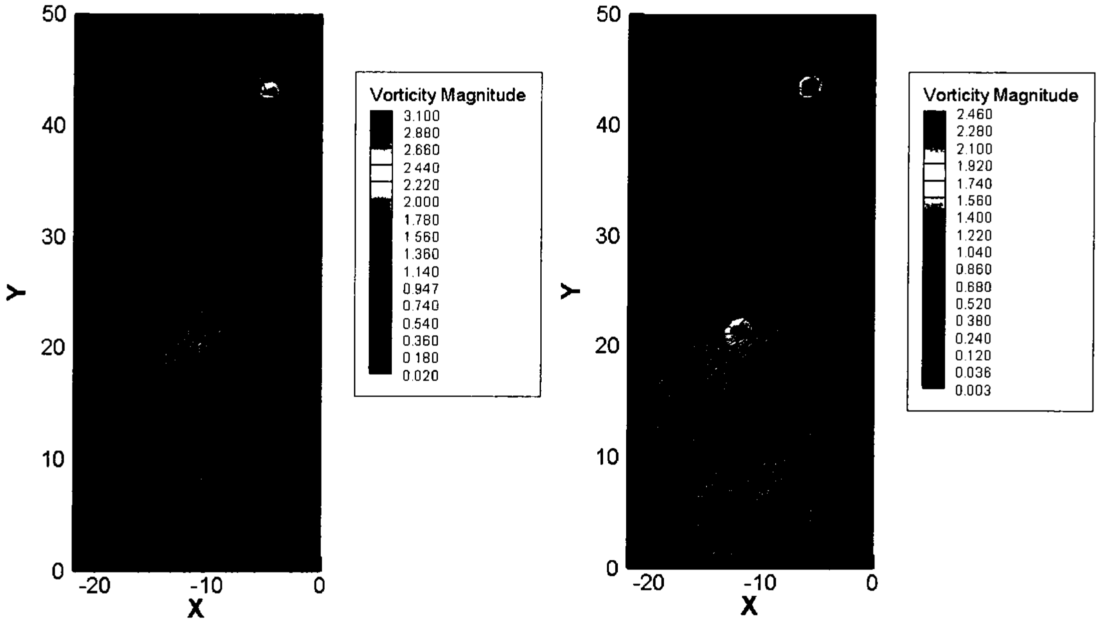

Figure 5.45: Vorticity Magnitude with 2D Vector (left-case 15 and right-case 16)

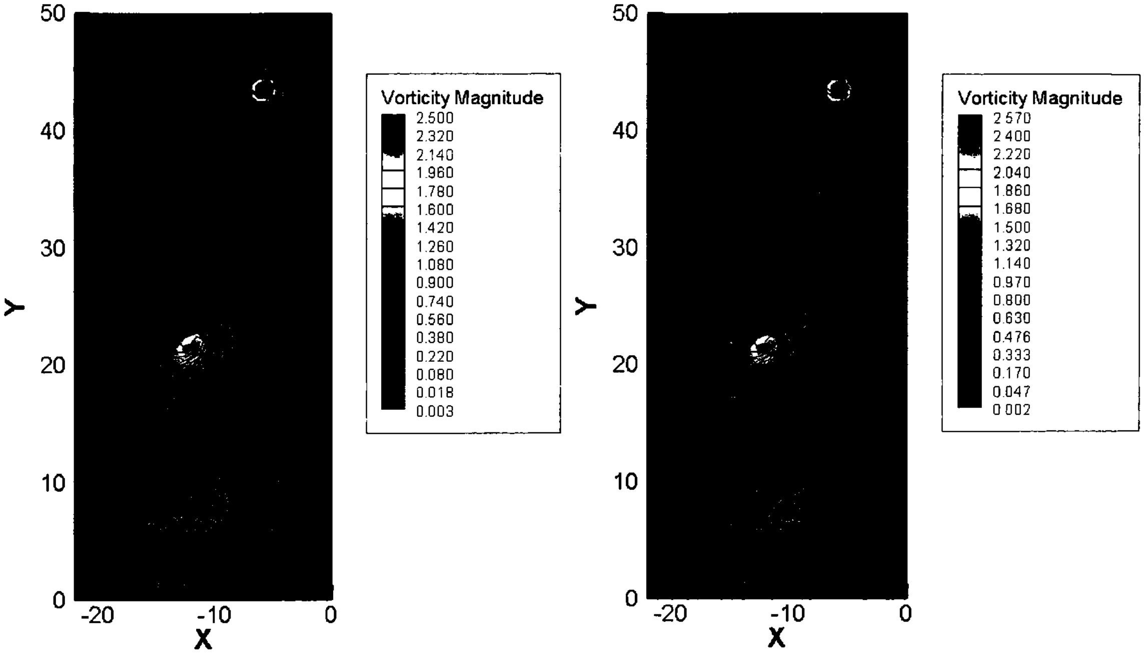

Figure 5.46: Vorticity Magnitude with 2D Vector (left-case 17 and right-case 18)

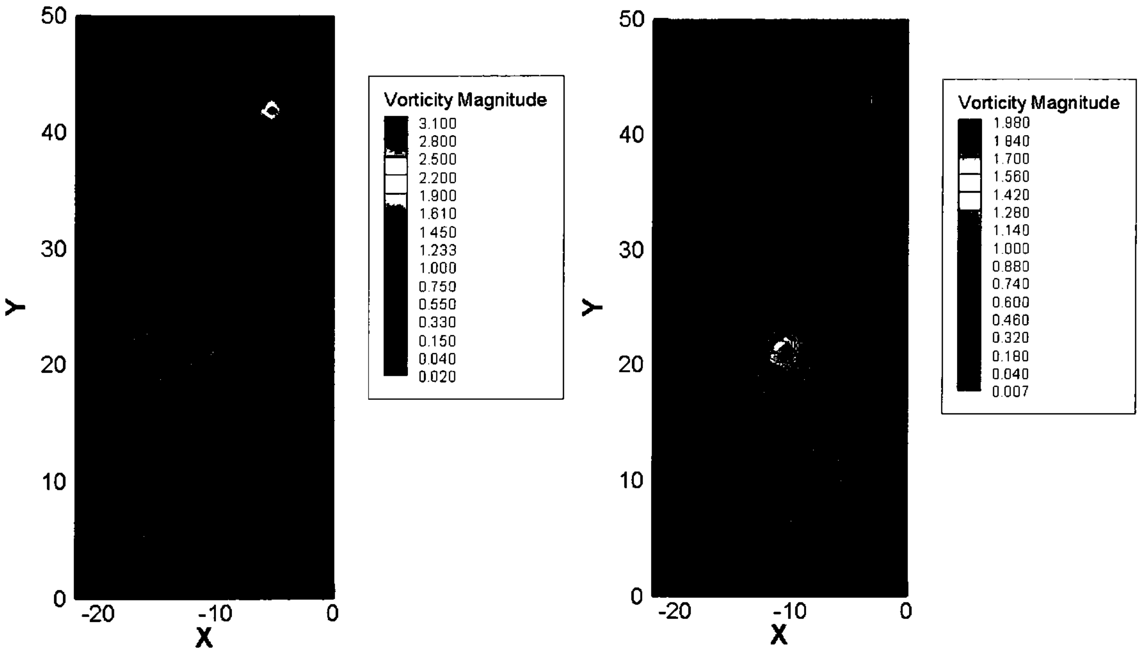

Figure 5.47: Vorticity Magnitude with 2D Vector (left-case 19 and right-case 20)

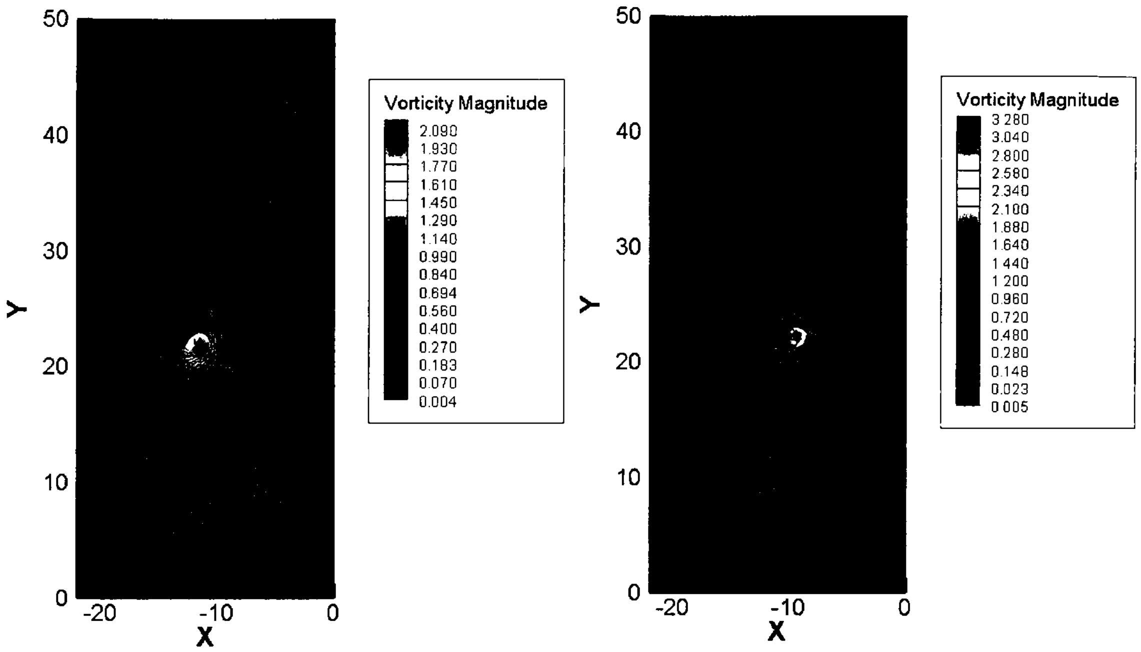

Figure 5.48: Vorticity Magnitude with 2D Vector (left-case 21 and right-case 22)

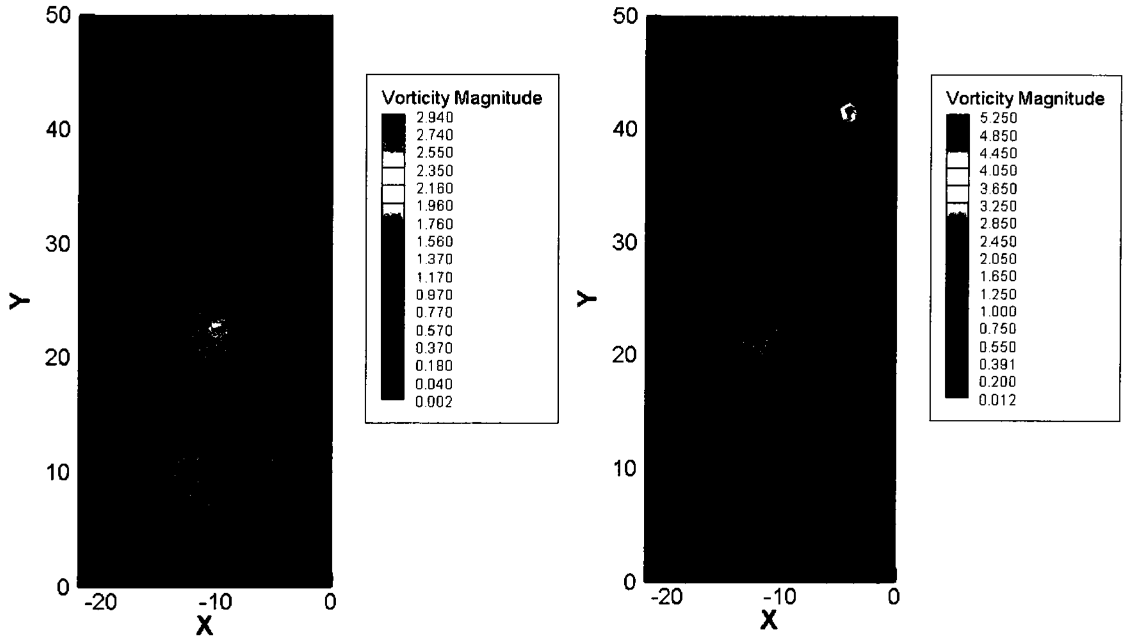

Figure 5.49: Vorticity Magnitude with 2D Vector (left-case 23 and right-case 24)

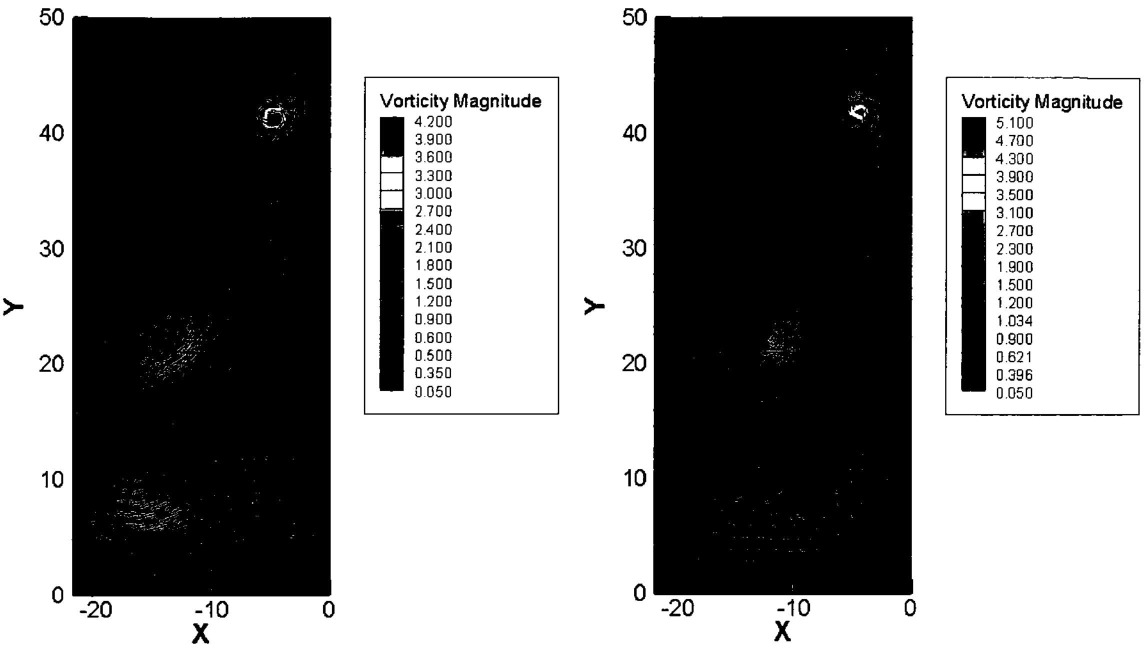

Figure 5.50: Vorticity Magnitude with 2D Vector (left-case 25 and right-case 26)

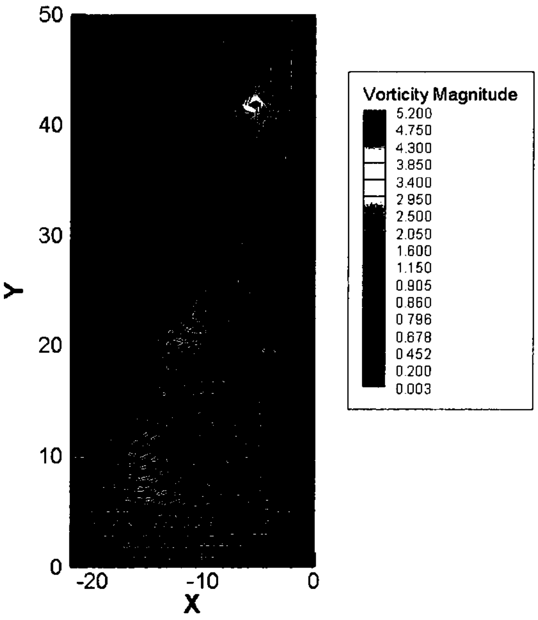

Figure 5.51: Vorticity Magnitude with 2D Vector (case 27)

6 ANALYSIS OF RESULTS

The main objective of the dissertation study was the trajectory analysis of both flap and wing tip vortices, by means of a series of Face Centered Design (FCD) experiments, with the displacements from the trailing edges of both flap and wing tip as the responses. The distances traveled by each vortex were calculated in such a way that the centers of the vortices were measured from the trailing edge of both flap and wing tip for different angle of attack and flap deflection cases. The locations of flap and wing tip trailing edges are given in Table 6.1 for different cases.

Flap deflection (degree)	**Angle of Attack** (degree)	**WING TIP**		**FLAP TIP**	
		X (inches)	**Y** (inches)	**X** (inches)	**Y** (inches)
15	**0**	-6.5	47	-9	23
	5	-7.5		-10	
	10	-8.5		-11	
33	**0**	-6.5		-9.5	
	5	-7.5		-10.5	
	10	-8.5		-11.5	
50	**0**	-6.5		-10	
	5	-7.5		-11	
	10	-8.5		-12	

Table 6.1: Locations of Trailing Edges of Flap and Wing Tip

Two different coordinate systems were defined for both flap and wing tip. The locations of the coordinate systems are shown in Figure 6.1 where each system has different origins (for x and y locations) for different angles of attack and flap deflections as shown in Table 6.1. The motion along the x axis was denoted as the vertical motion of the corresponding vortex while the y axis is taken as the horizontal motion direction. Any vortex motion along the x axis can be classified as either downward or upward due to the direction of the motion (negative means downward and positive means upward). For the horizontal motion, positive motion along the y axis means outward and negative means inward motion.

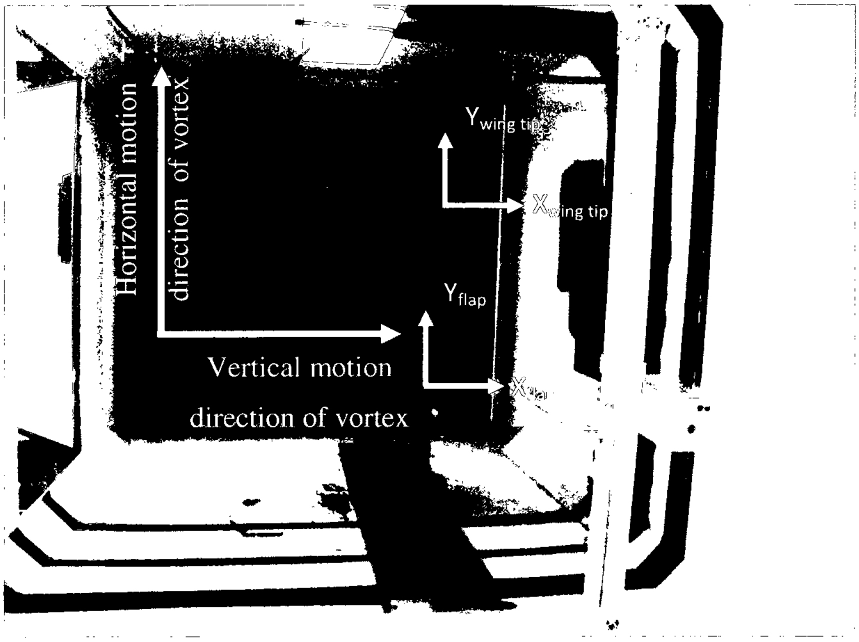

Figure 6.1: Locations of Coordinate Systems for Flap and Wing Tip

6.1 Wake Structure and Features

When analyzing the wake structure of the model, the vortices with a negative value of z vorticity at the outboard edge of the flap and the wing tip were the main vortex structures that can easily be recognized. The other main structure is the propeller wake which evolves with downstream distance and the first indications of merging with flap vortex are recognized at mid distance of near wake region of the wing. Since the distance from wing tip to propeller axis is large compared to the distance from flap edge to propeller axis, no significant indication of merging of wing tip and flap vortices was observed within the near field wake of the wing. The resultant velocity measured by the Hotwire Anemometry around the wing showed that the velocity above the wing is higher for every case compared to the lower region as expected. The highest absolute velocity values are observed at the wake of the propeller due to the induced velocity effect of the propeller and contraction of the propeller wake. Another meaningful term is the turbulence intensity that shows some similar features as does velocity distribution of the wake. The tip and flap vortices are easily recognizable as well as the propeller wake and the turbulence intensity in the propeller wake is higher compared to the turbulence at the vortices due perhaps to separation from the thick blade sections toward the propeller axis.

In addition to these structures, the wake of the whole wing is also recognizable but turbulence intensities are lower.

Figures 5.38 to 5.51, showing the z vorticity magnitude, revealed that the vorticity levels of wing tip are increasing with angle of attack while for the flap vortex the main parameter seems to be the flap deflection as expected. The evolutions of the vorticity magnitude with downstream distance showed that no decrease of vorticity magnitude of the wing tip vortex is observed due to the fact that the near field region is a rather limited region to view such an evolution while the vorticity level of the flap vortex is more affected by other factor settings and interactions thereof.

The trajectory analysis of the vortices showed that the vortices are getting closer to each other with some interaction terms potentially important as main factors. The structure of the flap vortex is much more influenced from the propeller wake compared to the wing tip vortex due to the fact that it is physically closer to propeller. The first indication of the merging of flap and propeller wake is the distortion of the shapes of the propeller wake and flap vortex.

6.2 Regression Model Development

During the experiments data were collected for the displacements of both flap and wing tip vortices in both x and y axes as well as the z vorticity magnitude of both vortices. The shortest distance between the two vortices were also calculated under varying factors to understand whether the vortices are getting physically closer to each other or not. After the regression models are obtained through statistical analysis, the vortex behaviors can be predicted for at least the medium range of the wake. The values of factors and the responses obtained are given in Table 6.2.

It should be noted that all the distance values are normalized with respect to a half wing span to produce analyses with non-dimensional values. The downstream field was divided into three equal regions, with the most downstream point of the wake field was limited to 60% of the half wing span.

NUMBER	ANGLE OF ATTACK	FLAP DEFLECTION	PROPELLER PITCH ANGLE	DOWNSTREAM DISTANCE	FVX	FVY	WTVX	WTVY	FVVS	WTVVS	SDBV
1	0	50	19	0	-1.456	-1.087	0.373	-2.153	-2.947	-1.143	46.346
2	0	50	25	0	-0.905	-1.070	2.443	-2.103	-4.169	-1.447	46.684
3	0	15	19	0	1.150	-1.019	2.421	-2.113	-3.291	-0.931	45.919
4	0	15	25	0	0.243	-0.874	0.753	-2.586	-2.684	-0.804	45.209
5	10	50	19	0	-2.223	-1.194	2.309	-3.843	-1.776	-4.391	45.390
6	10	50	25	0	-1.211	-1.067	4.287	-2.175	-2.809	-4.814	47.127
7	10	15	19	0	1.005	-1.091	4.349	-2.793	-2.774	-4.265	45.642
8	10	15	25	0	0.563	-0.226	4.289	-2.172	-2.474	-4.194	45.472
9	5	32.5	22	0	0.0760	-1.132	4.383	-4.081	-3.822	-3.160	44.813
10	10	32.5	22	30	-2.311	-2.490	4.281	-8.010	-1.526	-4.964	42.918
11	0	32.5	22	30	-1.974	-2.916	2.310	-5.971	-3.280	-1.077	44.704
12	5	32.5	19	30	-0.053	-3.021	6.374	-6.076	-2.529	-3.082	45.238
13	5	32.5	25	30	-0.032	-1.256	6.404	-6.100	-2.874	-3.176	43.520
14	5	15	22	30	0.069	-1.823	4.420	-6.181	-2.011	-3.015	43.235
15	5	50	22	30	-1.289	-3.903	6.374	-8.010	-1.943	-3.096	44.888
16	5	32.5	22	30	-2.092	-3.000	3.285	-6.812	-2.517	-2.334	44.232
17	5	32.5	22	30	-2.071	-2.916	3.335	-7.014	-2.542	-2.353	43.962
18	5	32.5	22	30	-2.092	-2.979	3.495	-6.917	-2.585	-2.398	44.164
19	5	32.5	22	60	-4.046	--3.000	4.386	-10.030	-1.797	-3.099	42.062
20	0	50	19	60	-0.877	-3.504	6.429	-8.094	-1.961	-1.198	44.316
21	0	50	25	60	-2.915	-3.021	4.451	-8.107	-2.307	-1.314	43.865
22	0	15	19	60	-0.780	-1.087	4.874	-7.947	-3.225	-0.801	41.108
23	0	15	25	60	-0.864	-1.024	2.394	-6.833	-2.978	-0.806	41.592
24	10	50	19	60	-1.239	-4.912	8.366	-10.062	-1.056	-5.189	44.580
25	10	50	25	60	-2.054	-2.280	6.656	-11.730	-1.140	-4.068	40.258
26	10	15	19	60	-1.305	-1.818	8.337	-10.048	-1.310	-5.033	41.018
27	10	15	25	60	-2.272	-0.473	6.327	-10.037	-1.121	-5.093	39.406

Table 6.2: Experiment Results

6.2.1 Statistical Analysis

In ANOVA tables presented in this Chapter, an overall summary for the full model (all main effects and interactions), and the model sum of squares is given. According to the data available via ANOVA, the mean square value for the model (MS_{Model}) is calculated as given in Equation 6.1:

$$MS_{Model} = \frac{SS_{Model}}{df} \qquad (6.1)$$

where *SS* denotes the sum of squares and *df* is the degree of freedom.

The statistics for F_0 test the hypothesis as to whether the regression coefficients are all zero or not as follows:

$$H_0: \beta_1 = \beta_2 = \cdots = \beta_{11} = \beta_{12} = \beta_{ij} = 0$$

$$H_1: at\ least\ one\ \beta \neq 0$$

if the F_0 value is large enough it can be concluded that at least one variable has a nonzero effect and then each individual factorial effect should be tested for significance using the F statistic given in Equation 6.2:

$$F_0 = \frac{MS_{model}}{MS_E} \quad (6.2)$$

The P value given in the analyses denotes the probability of observing the F_0 value if the null hypothesis is true. Small probability values call for rejection of the null hypothesis. The probability equals the proportion of the area under the curve of the F-distribution that lies beyond the observed F value.

Several R-squared statistics were presented through the analyses of regression models and these R-squared terms are defined here. The ordinary R-squared term measures the proportion of total variability explained by the model (see Equation 6.3). A potential problem with this statistic is that it always increases as factors are added to the model, even if these factors are not significant:

$$R^2 = \frac{SS_{model}}{SS_{Total}} \quad (6.3)$$

The adjusted R-squared (see Equation 6.4) is a statistic that is adjusted for the size of the model, that is, the number of factors. The adjusted R-squared can actually decrease if nonsignificant terms are added to a model.

$$R^2_{adjusted} = 1 - \frac{SS_E/df_E}{SS_{Total}/df_{Total}} \quad (6.4)$$

The Prediction Error Sum of Squares (PRESS) statistic is a measure of how well the model will predict new data and is computed as the sum of the squared prediction errors obtained by predicting the *i*th data point with a model that includes all observations except the *i*th one. A model with a small value of PRESS indicates that the model is likely to be a good predictor. Related to PRESS, the Prediction R-squared (see Equation 6.5) statistic can be computed as follows which indicates how much the full model explains the variability in new data.

$$R^2_{predicted} = 1 - \frac{PRESS}{SS_{Total}} \quad (6.5)$$

Another test result to be presented through the analyses of experimental data is the lack of fit test for comparing lack of fit variance with pure error variance. If the variances are close to each other it is less likely that lack of fit is significant. Strong lack of fit ($p<0.05$) is an undesirable property, because it indicates that the model does not fit the data well. It is desirable to have an insignificant lack of fit ($p>0.05$). The lack of fit test is performed by using the sum of squares, which is the weighted sum of squared deviations between the mean response at each factor level and the corresponding fitted value.

The regression coefficient for each model term is computed through the analyses and the standard error of each coefficient is defined as given in Equation 6.6:

$$se(\hat{\beta}) = \sqrt{V(\hat{\beta})} = \sqrt{\frac{MS_E}{n2^k}} \quad (6.6)$$

The 95% confidence intervals on each regression coefficient are computed using Equation 6.7:

$$\hat{\beta} - t_{0.025,N-p}se(\hat{\beta}) \leq \beta \leq \hat{\beta} + t_{0.025,N-p}se(\hat{\beta}) \quad (6.7)$$

After the statistical analyses were performed by using ANOVA, some suggestions were made for obtaining better regression models to analyze the behaviors of the vortices. For example "Sequential Model Sum of Squares" analyses suggest the highest order polynomial that is not aliased for fitting the experiment data. The "Lack of fit test" shows whether the selected model has insignificant lack-of-fit or not, and "Model Summary Statistics" are given for the analysis of "Adjusted R-Squared" and the "Predicted R-Squared" values to show how the regression model fits the data in which the higher values of R-squared terms are suggested for better models.

6.2.2 Flap Vortex Vertical Motion (FVX)

The sequential model sum of squares showed us information about the sum of squares and related terms (mean squares, F value and probability value) for different models. If the probability value is less than 0.05, then the model can be attributed as significant with 95% percent confidence. Table 6.3 suggests the use of either a linear or quadratic model to fit the data. Since the cubic model is aliased (number of experiments is not sufficient for a model of cubic order) some terms are confounded and cannot be distinguished, thus it is not suggested.

Source	**Sum of squares**	**df**	**Mean square**	**F value**	**P value Probability>F**	
Mean vs Total	3526	1	3526.192			
Linear vs Mean	803.699	4	200.925	6.622	0.001	Suggested
2FI* vs Linear	215.755	6	35.960	1.274	0.323	-
Quadratic vs 2FI	249.279	4	62.320	3.693	0.035	Suggested
Cubic vs Quadratic	130.650	8	16.331	0.909	0.581	Aliased
Residual	71.840	4	17.960			
Total	4997.414	27	185.089			

Table 6.3: Sequential Model Sum of Squares for FVX

(* 2FI denotes two-factor interaction)

The lack of fit test (see Table 6.4) also suggested a linear or quadratic model to be used as the regression model.

Source	Sum of squares	df	Mean square	F value	P value Probability>F	
Linear	667.520	10	33.380	11948.310	<0.0001	Suggested
2FI	451.760	14	32.270	11551.960	<0.0001	-
Quadratic	202	10	20.250	7248.740	0.0001	Suggested
Cubic	71.830	2	25.920	12857.810	<0.0001	Aliased
Pure error	0.006	2	0.003			

Table 6.4: Lack of Fit Test for FVX

As mentioned before, different R squared terms are defined depending on how well the model fits the data. According to the analysis given in Table 6.5, a quadratic model is preferable since the R squared and the Adjusted R squared terms are relatively higher than is the case with the other models.

Source	Std. Dev.	R-Squared	Adjusted R-Squared	Predicted R-Squared	PRESS	
Linear	5.510	0.546	0.464	0.324	994.430	Suggested
2FI	5.310	0.693	0.501	0.163	1231.600	-
Quadratic	4.110	0.862	0.702	0.219	1149.590	Suggested
Cubic	4.240	0.951	0.683	-7.601	12653.920	Aliased

Table 6.5: Model Summary Statistics for FVX

ANOVA sorts the sum of squares, mean squares, F value and probability values for factors and interaction terms, as given in Table 6.6. The model seems to be significant (with 95% confidence) whereas the factors of flap angle and downstream distance are significant while angle of attack and downstream distance are not significant. However due to hierarchy these two terms are added to the regression model since these two factors have quadratic terms in the model. The only interaction observed is the one obtained from flap angle and downstream distance. As expected vertical motion of the flap vortex is greatly influenced by the propeller wake since the flap edge and the propeller axis are physically close and but an interesting result is obtained such that that the angle of attack has much more influence than the flap angle.

Source	Sum of squares	df	Mean square	F Value	p-value>F	
Model	1209.466	1	172.781	12.542	< 0.0001	significant
A-Angle of attack	13.000	1	13.000	0.944	0.3436	
B-Flap angle	371.557	1	371.557	26.970	< 0.0001	significant
C-Propeller pitch angle	28.776	1	28.776	2.089	0.1647	
D-Downstream distance	390.366	1	390.366	28.335	< 0.0001	significant
BD-Interaction	186.074	1	186.074	13.507	0.0016	significant
A^2	71.365	1	71.365	5.180	0.0346	significant
C^2	216.372	1	216.372	15.706	0.0008	significant
Residual	261.756	19	13.777			
Lack of fit	261.750	17	15.397	5512.029	0.0002	significant
Pure error	0.006	2	0.003			
Cor Total	1471.222	26				

Table 6.6: ANOVA for FVX

The "Lack of fit F-value" of 5512.03 (see Table 6.6) implies the Lack of Fit is significant. There is only a 0.02% chance that a "Lack of fit F-value" this large could occur due to noise.

Std. Dev.	3.712
Mean	11.428
PRESS	489.102
R-Squared	0.822
Adjusted R-Squared	0.757
Predicted R-Squared	0.668

Table 6.7: Model Statistics for FVX

The "Predicted R-Squared" of 0.6676 is in reasonable agreement with the "Adjusted R-Squared" of 0.7565 (see Table 6.7). The coefficient terms to be included in the regression model with their standard errors are given Table 6.8 as well the low and high values for each of them with 95% confidence.

Factor	**Coefficient estimate**	**df**	**Standard error**	**Low (95% CI)**	**High (95% CI)**
Intercept	9.142	1	1.317	6.285	11.898
A-Angle of attack	0.850	1	0.875	-2.681	0.981
B-Flap angle	4.543	1	0.875	-6.374	2.712
C-Propeller pitch angle	-1.264	1	0.875	-3.096	0.567
D-Downstream distance	4.657	1	0.875	-6.488	-2.826
BD-Interaction	3.410	1	0.928	1.468	5.352
A^2	4.627	1	2.033	-8.882	0.372
C^2	8.057	1	2.033	3.802	12.312

Table 6.8: Regression Model Coefficient Estimate for FVX

The regression models for vertical motion for both coded and actual factor settings are given in Equations 6.8 and 6.9 . For the coded settings, the low value corresponds to -1 and high value corresponds to +1, as such it is a useful regression model to use for the comparison of the relative magnitudes of coefficients.

Coded factors

$$(FVX + 4.45)^{1.94} = -4.627 * Angle\ of\ Attack^2 + 8.057 * Propeller\ Pitch\ Angle^2 + 3.410 * Flap\ Angle * Downstream\ Distance - 0.850 * Angle\ of\ Attack - 4.543 * Flap\ Angle - 1.264 * Propeller\ Pitch\ Angle - 4.657 * Downstream\ Distance + 9.142 \qquad (6.8)$$

The greatest effect on the vertical motion of the flap vortex comes from the propeller pitch angle and the second comes from angle of attack. As the propeller pitch angle increases the flap vortex seems to move upward while the vortex moves downward as the angle of attack increases. As expected the flap vortex seems to move downward as it proceeds downstream or the flap angle increases. In both cases due to downwash effects, the interaction of flap angle and downstream distance forces the flap vortex upward as the interaction increases.

Actual factors

$$(FVX + 4.45)^{1.94} = -0.185 * \mathit{Angle\ of\ Attack}^2 + 0.895 * \mathit{Propeller\ Pitch\ Angle}^2 + 0.006 * \mathit{Flap\ Angle} * \mathit{Downstream\ Distance} + 1.681 * \mathit{Angle\ of\ Attack} - 0.455 * \mathit{Flap\ Angle} - 39.810 * \mathit{Propeller\ Pitch\ Angle} - 0.366 * \mathit{Downstream\ Distance} + 467.339 \tag{6.9}$$

The effects of angle of attack squared and propeller pitch angle squared are shown below in Figure 6.2 and 6.3, respectively. While angle of attack has a negative coefficient term, propeller pitch angle has a positive term and their effects can also be viewed in the corresponding figures. Solid lines at the figures show the effect of the factor used at the model while the dashed lines show the confidence bands.

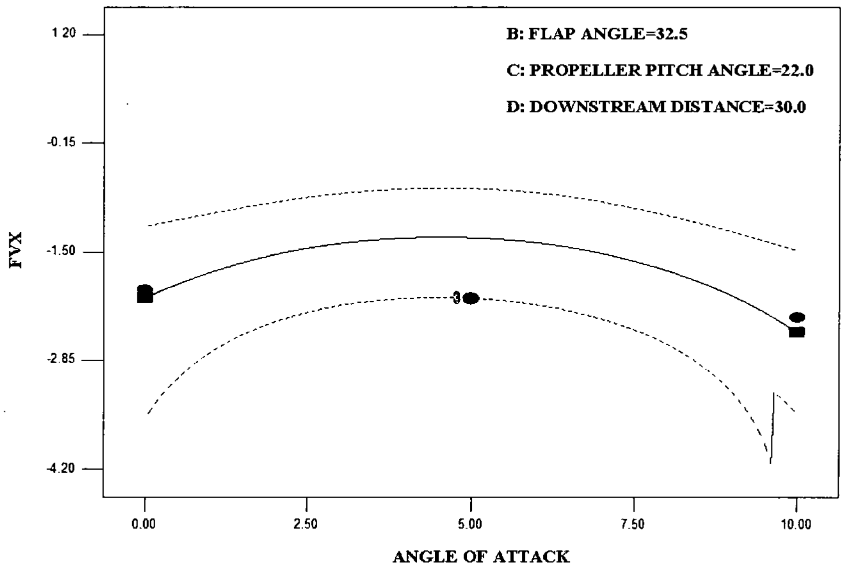

Figure 6.2: Effect of Angle of Attack on FVX

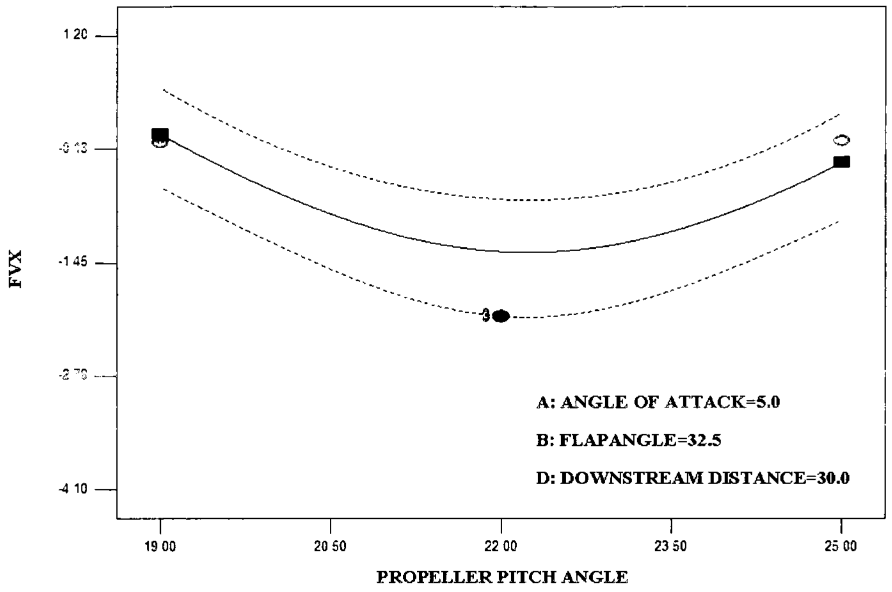

Figure 6.3: Effect of Propeller Pitch Angle on FVX

The interaction effect is shown graphically below in Figure 6.4. As either the flap deflects more or downstream distance increases, the flap vortex is forced to move downward.

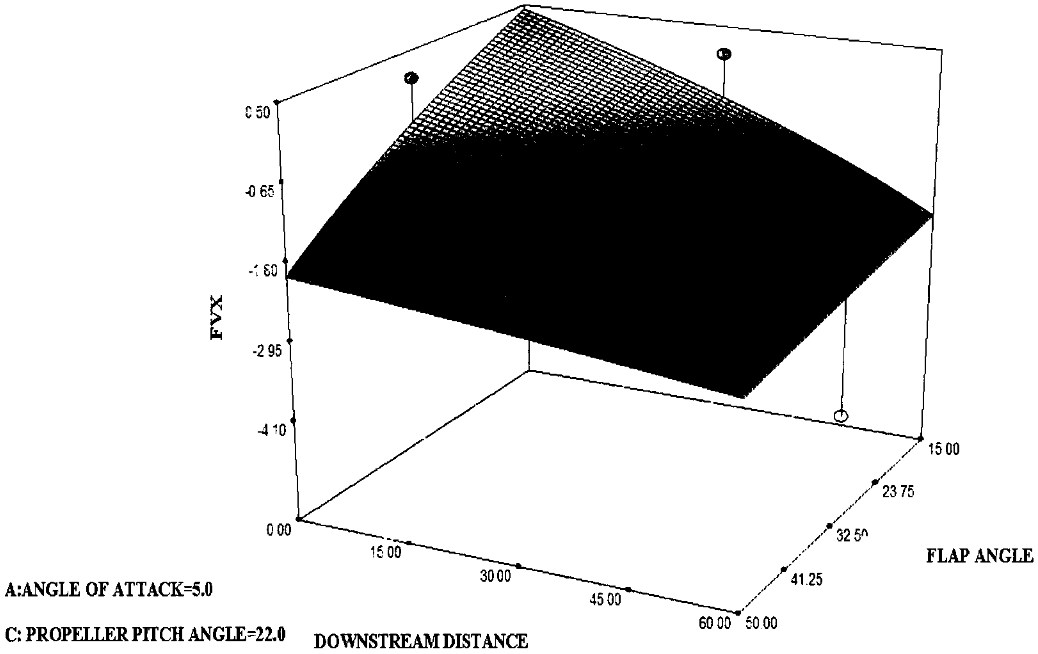

Figure 6.4: Interaction of Flap Angle and Downstream Distance on FVX

6.2.3 Flap Vortex Horizontal Motion (FVY)

The sequential model for sum of squares, given below in Table 6.9, suggests that a quadratic model is the best for fitting the data since probability values are less than 0.05 and F value are the highest among alternatives. Lack of fit tests for FVY applied to the models (See Table 6.10) also suggested using a quadratic model.

Source	**Sum of squares**	**df**	**Mean square**	**F value**	**P value Probability>F**	
Mean vs Total	3229.381	1	3229.381			
Linear vs Mean	521.232	4	130.308	6.716	0.0011	
2FI vs Linear	124.740	6	20.790	1.101	0.4038	
Quadratic vs 2FI	261.677	4	65.419	19.420	<0.0001	Suggested
Cubic vs Quadratic	37.097	8	4.637	5.575	0.0573	Aliased
Residual	3.330	4	0.830			
Total	4177.455	27	154.721			

Table 6.9: Sequential Model Sum of Squares for FVY

Source	**Sum of squares**	**df**	**Mean square**	**F value**	**P value Probability>F**	
Linear	426.777	20	21.339	651.968	0.0015	
2FI	302.036	14	21.574	659.154	0.0015	
Quadratic	40.359	10	4.036	123.310	0.0081	Suggested
Cubic	3.262	2	1.631	49.828	0.0197	Aliased
Pure error	0.066	2	0.033			

Table 6.10: Lack of Fit Test for FVY

Different R-squared terms (see Table 6.11) showed that the quadratic model fits quite well to the data since all the R-squared terms are relatively high compared to other models.

Source	Std. Dev.	R-Squared	Adjusted R-Squared	Predicted R-Squared	PRESS	
Linear	4.405	0.550	0.468	0.319	646.088	
2FI	4.345	0.681	0.482	-0.075	1019.572	
Quadratic	1.835	0.957	0.908	0.753	234.175	Suggested
Cubic	0.912	0.997	0.977	0.395	574.027	Aliased

Table 6.11: Model Summary Statistics for FVY

As shown in the ANOVA (see Table 6.12), the model F-value is 38.43 and the probability value is less than 0.0001 which imply that the model is significant. The significant terms are the flap angle, propeller pitch angle, downstream distance plus some interactions such as angle of attack with propeller pitch angle and flap angle with downstream distance. Further, two factors (propeller pitch angle and downstream distance) are relatively much more effective such that second order of these two factors seem to be significant in the horizontal displacement of the flap vortex. The "Lack-of-Fit F-value" of 100.00 implies the Lack of fit is significant.

The "Predicted R-Squared" of 0.8604 and the "Adjusted R-Squared" of 0.9201 (see Table 6.13) seem to be high enough for fitting the wind tunnel experiment data.

The coefficient estimations with their standard error values are given below in Table 6.14 and the confidence interval for the coefficients are also shown in the right two columns of the table.

Source	Sum of squares	df	Mean square	F Value	p-value>F	
Model	895.640	8	111.955	38.433	<0.0001	significant
A-Angle of attack	1.591	1	1.591	0.546	0.4694	
B-Flap angle	221.952	1	221.952	76.194	<0.0001	significant
C-Propeller pitch angle	77.246	1	77.246	26.518	<0.0001	significant
D-Downstream distance	220.442	1	220.442	75.676	<0.0001	significant
AC-Interaction	28.101	1	28.101	9.647	0.0061	significant
BD-Interaction	84.665	1	84.665	29.065	<0.0001	significant
C^2	38.264	1	38.264	13.136	0.0019	significant
D^2	49.226	1	49.226	16.899	0.0007	significant
Residual	52.434	18	2.913			
Lack of fit	52.368	16	3.273	100.001	0.0099	significant
Pure error	0.066	2	0.033			
Cor Total	948.074	26				

Table 6.12: ANOVA for FVY

Std. Dev.	1.707
Mean	10.937
PRESS	132.362
R-Squared	0.945
Adjusted R-Squared	0.920
Predicted R-Squared	0.860

Table 6.13: Model Statistics for FVY

Factor	Coefficient estimate	df	Standard error	Low (95% CI)	High (95% CI)
Intercept	6.116	1	0.606	4.843	7.388
A-Angle of attack	0.297	1	0.402	-0.548	1.143
B-Flap angle	3.512	1	0.402	-4.357	-2.666
C-Propeller pitch angle	2.072	1	0.402	1.226	2.917
D-Downstream distance	3.500	1	0.402	-4.345	-2.654
AC-Interaction	1.325	1	0.427	0.429	2.222
BD-Interaction	2.300	1	0.427	-3.197	-1.404
C^2	3.388	1	0.935	1.424	5.352
D^2	3.843	1	0.935	1.879	5.807

Table 6.14: Regression Model Coefficient Estimate for FVY

The coded variables used in the regression model (see Equation 6.10) showed that the most influential factors are the downstream distance and the propeller pitch angle since their coefficients are high and these factors have second order terms in the model. In addition, some interaction terms are recognized as significant as seen in the ANOVA, and their coefficients showed that interaction of flap angle and downstream distance is much more effective compared to the interaction of angle of attack and propeller pitch angle. The positive horizontal motion of the flap vortex means that the vortex moves outward and negative motion means that it moves inward. When the propeller pitch angle increases or the flap vortex moves downstream the flap vortex moves outward. These factors enable the wing tip and flap vortices to merge in the far wake of the wing. The other factors influencing the motion of the flap vortex are the flap angle which forces the flap vortex to move inward and the angle of attack to promote the outward motion.

Coded factors

$$(FVY + 5.40)^{1.88} = 3.388 * Propeller\ Pitch\ Angle^2 + 3.843 * Downstream\ Distance^2 + 1.325 * Angle\ of\ Attack * Propeller\ Pitch\ Angle - 2.300 * Flap\ Angle * Downstream\ Distance + 0.297 * Angle\ of\ Attack - 3.512 * Flap\ Angle + 2.072 * Propeller\ Pitch\ Angle - 3.500 * Downstream\ Distance + 6.116 \qquad (6.10)$$

Actual factors

$$(FVY + 5.40)^{1.88} = 0.377 * Propeller\ Pitch\ Angle^2 + 0.004 * Downstream\ Distance^2 + 0.088 * Angle\ of\ Attack * Propeller\ Pitch\ Angle - 0.004 * Flap\ Angle * Downstream\ Distance - 1.884 * Angle\ of\ Attack - 0.069 * Flap\ Angle - 16.315 * Propeller\ Pitch\ Angle - 0.230 * Downstream\ Distance + 192.141 \qquad (6.11)$$

The quadratic effect of propeller pitch angle and downstream distance are shown below in Figures 6.5 and 6.6, respectively.

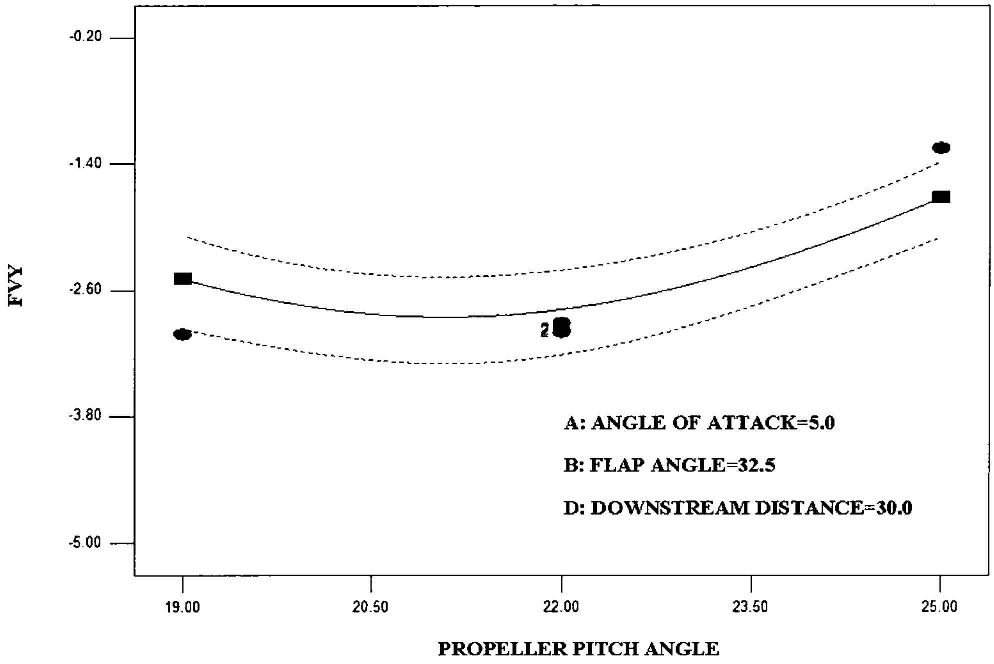

Figure 6.5: Effect of Propeller Pitch Angle on FVY

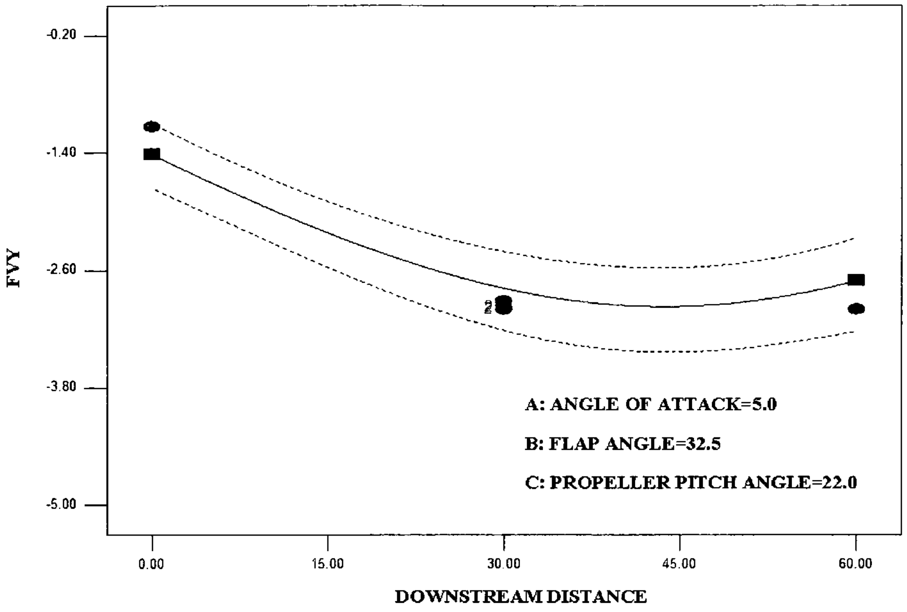

Figure 6.6: Effect of Downstream Distance on FVY

The interactions are shown in Figures 6.7 and 6.8 which show planes like a ridge. In case of interaction of angle of attack and propeller pitch angle, the contribution of interaction on the regression model of the horizontal displacement of flap vortex is relatively less when the propeller pitch angle is around 21° and the displacement is higher when propeller pitch angle is around 25°. The second interaction graphic shown in Figure 6.8 shows that the interaction contribution to the flap vortex displacement is minimum at the farthest downstream point when the flap is fully deployed.

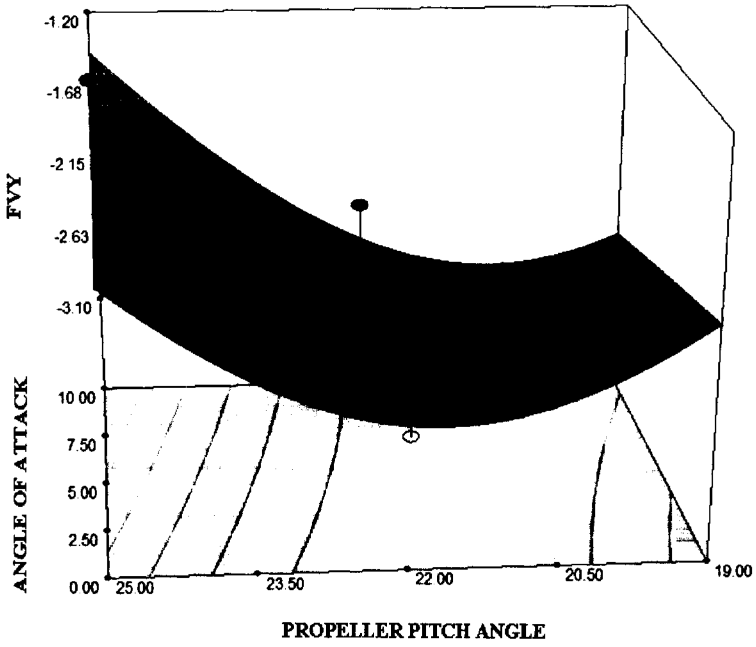

B:FLAP ANGLE=32.5

D: DOWNSTREAM DISTANCE=30.0

Figure 6.7: Interaction of Propeller Pitch Angle and Angle of Attack on FVY

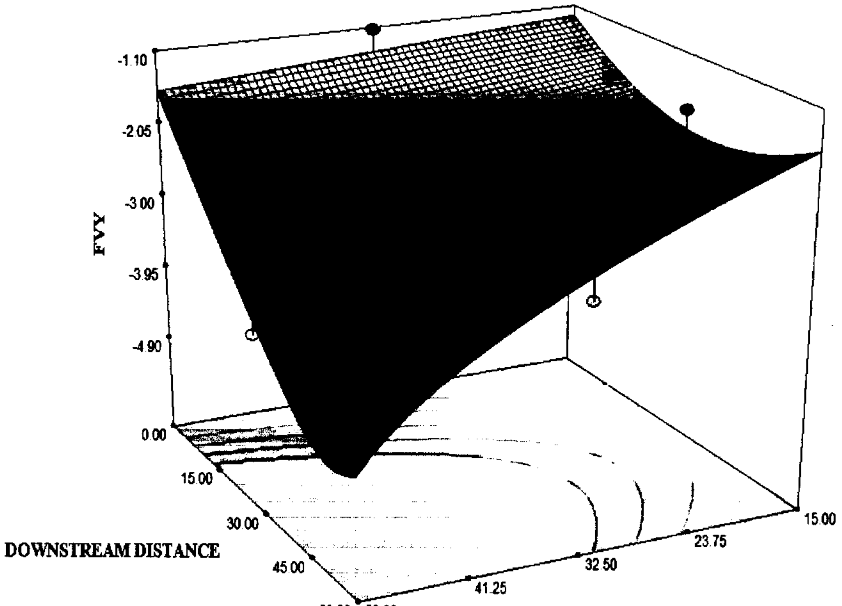

A:ANGLE OF ATTACK=5.0

C: PROPELLER PITCH ANGLE=22.0

Figure 6.8: Interaction of Flap Angle and Downstream Distance on FVY

6.2.4 Wing Tip Vortex Vertical Motion (WTVX)

The motion of the wing tip vortex in the x direction is attributed as vertical motion of the vortex and denoted as WTVX. The sequential model sum of squares and lack of fit analyses for the vertical displacement revealed the values given in Table 6.15 and 6.16 respectively. A linear model is suggested in both analyses.

Source	Sum of squares	df	Mean square	F value	P value Probability>F	
Mean vs Total	516.633	1	516.633			
Linear vs Mean	70.687	4	17.672	10.033	<0.0001	Suggested
2FI vs Linear	14.298	6	2.383	1.559	0.2225	
Quadratic vs 2FI	10.601	4	2.650	2.296	0.119	
Cubic vs Quadratic	8.679	8	1.085	0.839	0.6156	Aliased
Residual	5.172	4	1.293			
Total	626.069	27	23.188			

Table 6.15: Sequential Model Sum of Squares for WTVX

Source	Sum of squares	df	Mean square	F value	P value Probability>F	
Linear	38.726	20	1.936	160.767	0.0062	Suggested
2FI	24.427	14	1.745	144.869	0.0069	
Quadratic	13.826	10	1.383	114.797	0.0087	
Cubic	5.147	2	2.574	213.691	0.0047	Aliased
Pure error	0.024	2	0.012			

Table 6.16: Lack of Fit Test for WTVX

Since the R-squared terms given in Table 6.17 are relatively low (compared to the quadratic model) for linear model, then the quadratic model is used and the ANOVA values are given in Table 6.18.

Source	Std. Dev.	R-Squared	Adjusted R-Squared	Predicted R-Squared	PRESS	
Linear	1.327	0.646	0.582	0.478	57.107	Suggested
2FI	1.236	0.777	0.637	0.566	47.470	
Quadratic	1.074	0.873	0.726	0.437	61.631	
Cubic	1.137	0.953	0.693	6.910	865.651	Aliased

Table 6.17: Model Summary Statistics for WTVX

The ANOVA (see Table 6.18) has shown that model is significant since the F value is 12.54 and the probability value is less than 0.0001. The significant terms are the angle of attack and downstream distance whereas the only interaction term belongs to the propeller pitch angle and downstream distance. Within the regression model the most influential terms are the angle of attack and the propeller pitch angle because their second order terms are located in the model. Propeller pitch angle as a single factor is included in the model due to hierarchy.

Source	Sum of squares	df	Mean square	F Value	p-value>F	
Model	86.455	6	14.409	12.540	<0.0001	significant
A-Angle of attack	28.758	1	28.758	25.028	<0.0001	significant
C-Propeller pitch angle	1.888	1	1.888	1.643	0.2145	
D-Downstream distance	39.350	1	39.350	34.246	<0.0001	significant
CD-Interaction	6.889	1	6.889	5.995	0.0237	significant
A^2	7.969	1	7.969	6.936	0.0159	significant
C^2	7.981	1	7.981	6.946	0.0159	significant
Residual	22.981	20	1.149			
Lack of fit	22.957	18	1.275	105.894	0.0094	significant
Pure error	0.0241	2	0.012			
Cor Total	109.436	26				

Table 6.18: ANOVA for WTVX

The F value of "Lack-of-Fit" which is 105.89 (see Table 6.18) implies the Lack of fit is significant. There is only a 0.94% chance that a F-value of this large could occur due to noise. The "Predicted R-Squared" of 0.6430 (see Table 6.19) is in reasonable agreement with the "Adjusted R-Squared" of 0.7270.

Std. Dev.	1.072
Mean	4.374
PRESS	39.070
R-Squared	0.790
Adjusted R-Squared	0.727
Predicted R-Squared	0.643

Table 6.19: Model Statistics for WTVX

The regression model coefficient estimates are given below in Table 6.20 with their confidence intervals.

Factor	**Coefficient estimate**	**df**	**Standard error**	**Low (95% CI)**	**High (95% CI)**
Intercept	4.374	1	0.380	3.580	5.167
A-Angle of attack	1.264	1	0.253	0.737	1.791
C-Propeller pitch angle	0.324	1	0.253	-0.851	0.203
D-Downstream distance	1.479	1	0.253	0.952	2.006
CD-Interaction	0.656	1	0.268	-1.215	-0.097
A^2	1.546	1	0.587	-2.771	-0.322
C^2	1.547	1	0.587	0.323	2.772

Table 6.20: Regression Model Coefficient Estimates for WTVX

The regression model with coded variables (see Equation 6.12) indicates that the vertical displacement of the wing tip vortex is heavily influenced by both angle of attack and the propeller pitch angle at the same order. The only interaction term that takes a place in the model is the propeller pitch angle and the downstream distance whereas the single factors which are more influential are the angle of attack and the downstream distance. The single factor of propeller pitch angle was actually not significant but was included in the model due to hierarchy.

Coded factors

$$WTVX = -1.546 * Angle\ of\ Attack^2 + 1.547 * Propeller\ Pitch\ Angle^2 - 0.656 * Propeller\ Pitch\ Angle * Downstream\ Distance + 1.264 * Angle\ of\ Attack - 0.324 * Propeller\ Pitch\ Angle + 1.479 * Downstream\ Distance + 4.374 \qquad (6.12)$$

Actual factors

$$WTVX = -0.062 * Angle\ of\ Attack^2 + 0.172 * Propeller\ Pitch\ Angle^2 - 0.007 * Propeller\ Pitch\ Angle * Downstream\ Distance + 0.871 * Angle\ of\ Attack - 7.454 * Propeller\ Pitch\ Angle + 0.210 * Downstream\ Distance + 80.862 \qquad (6.13)$$

The quadratic effects of both the angle of attack and the propeller pitch angle are shown in Figures 6.9 and 6.10, respectively.

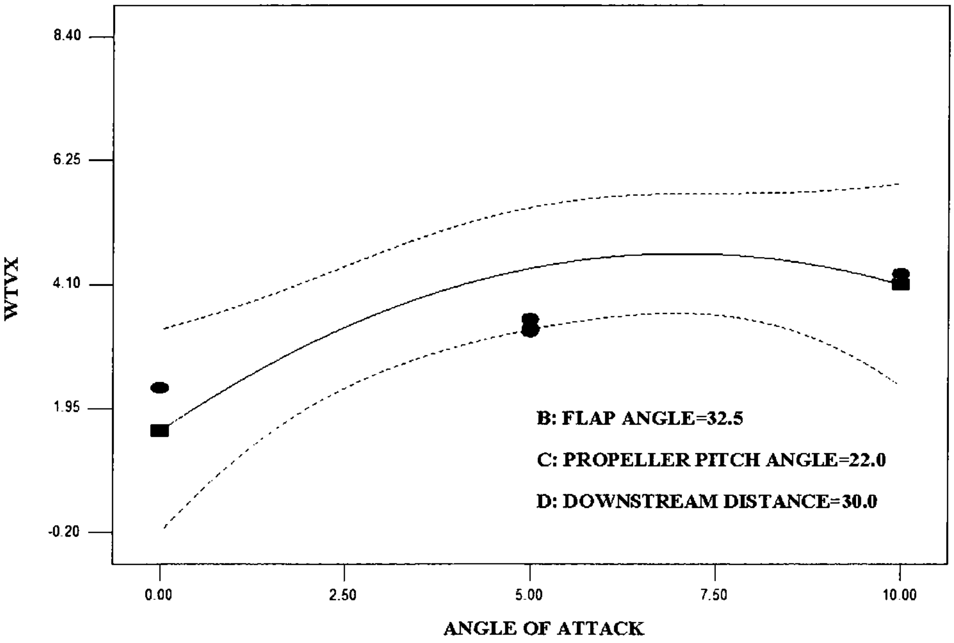

Figure 6.9: Effect of Angle of Attack on WTVX

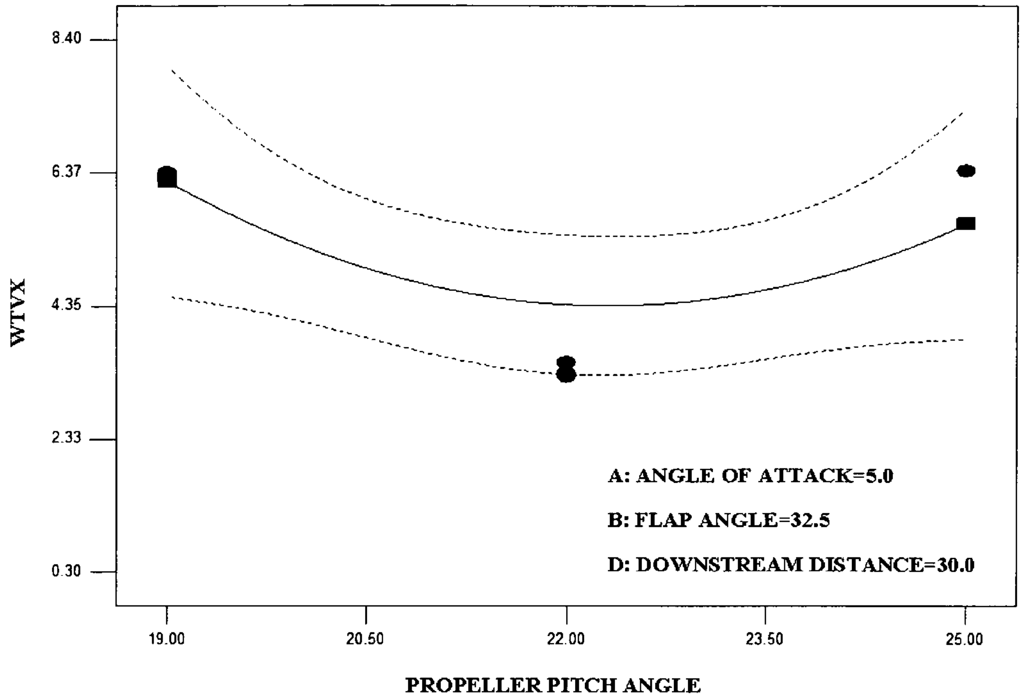

Figure 6.10: Effect of Propeller Pitch Angle on WTVX

The interaction of propeller pitch angle and downstream distance on WTVX is shown in Figure 6.11 in which the contribution of the interaction is a minimum at the trailing edge of the wing and the propeller pitch angle equals to 22°. The maximum contribution of the interaction is obtained at the most downstream distance (downstream distance equal to 60% of the half wing span) when the propeller pitch angle is 19°.

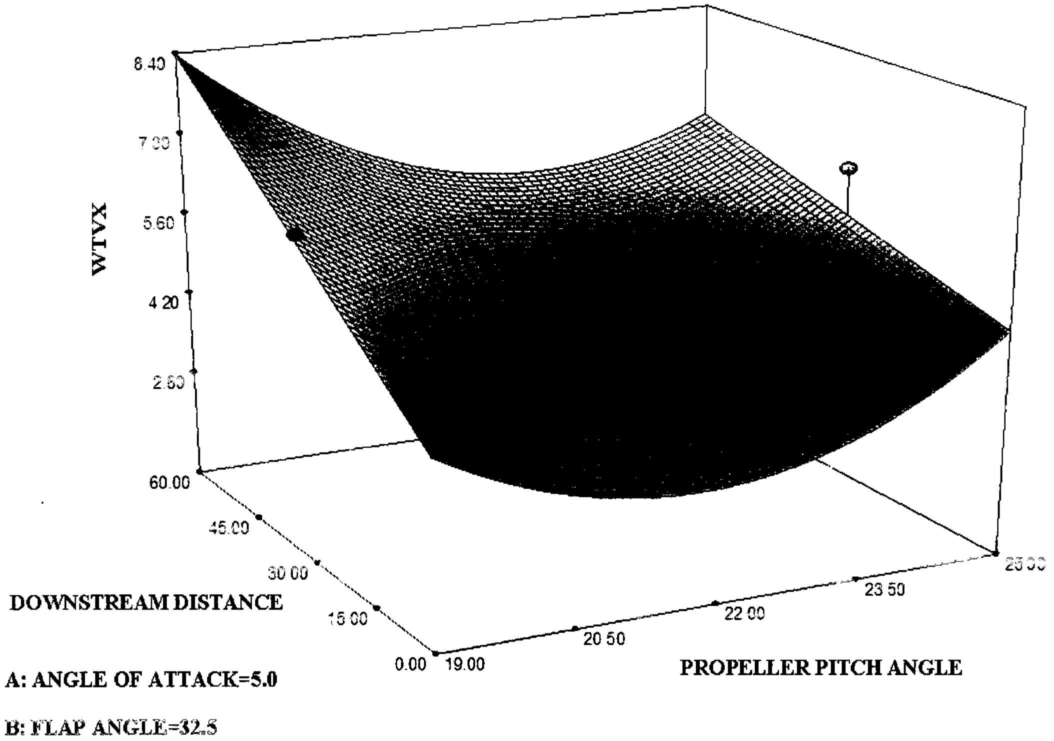

Figure 6.11: Interaction of Propeller Pitch Angle and Downstream Distance on WTVX

6.2.5 Wing Tip Vortex Horizontal Motion (WTVY)

The horizontal motion of the wing tip vortex is in the y direction and denoted by WTVY. The analyses performed for sequential sum of squares, lack of fit, and model summary statistics are given in Tables 6.21, 6.22, and 6.23, respectively. A quadratic model is suggested since the F_0 value is relatively low and values of R-squared are relatively high compared to other models.

Source	Sum of squares	df	Mean square	F value	P value Probability>F	
Mean vs Total	1045.287	1	1045.287			
Linear vs Mean	206.772	4	51.693	60.602	<0.0001	
2FI vs Linear	5.972	6	0.995	1.245	0.3356	
Quadratic vs 2FI	8.332	4	2.083	5.603	0.0088	Suggested
Cubic vs Quadratic	4.276	8	0.534	11.484	0.016	Aliased
Residual	0.186	4	0.047			
Total	1270.826	27	47.068			

Table 6.21: Sequential Model Sum of Squares for WTVY

A cubic model (see Table 6.22) seems to pass lack-of-fit test (insignificant in lack-of-fit test) but since the model is aliased it is not suggested.

Source	Sum of squares	df	Mean square	F value	P value Probability>F	
Linear	18.746	20	0.937	91.536	0.0109	
2FI	12.773	14	0.912	89.104	0.0112	
Quadratic	4.441	10	0.444	43.373	0.0227	Suggested
Cubic	0.166	2	0.083	8.090	0.1100	Aliased
Pure error	0.020	2	0.010			

Table 6.22: Lack of Fit Test for WTVY

R-squared values (see Table 6.23) are very high and seems to fit the model better than two-factor interaction and linear models.

Source	Std. Dev.	R-Squared	Adjusted R-Squared	Predicted R-Squared	PRESS	
Linear	0.924	0.917	0.902	0.867	30.001	
2FI	0.894	0.943	0.908	0.760	54.233	
Quadratic	0.610	0.980	0.957	0.853	33.183	Suggested
Cubic	0.216	0.999	0.995	0.851	33.586	Aliased

Table 6.23: Model Summary Statistics for WTVY

According to the ANOVA (see Table 6.24), the model F-value is 130.46 and implies that the model is significant and that all the single factors except the propeller pitch angle are significant. This term is added to the model due to hierarchy since the square of propeller pitch angle is present in the regression model. The only interaction taking place is the angle of attack and downstream distance. The "Lack-of-Fit F-value" of 30.38 implies the Lack of fit is significant. There is only a 3.23% chance that a "Lack of fit F-value" this large could occur due to noise.

Source	**Sum of squares**	**df**	**Mean square**	**F Value**	**p-value>F**	
Model	219.919	6	36.653	130.462	< 0.0001	significant
A-Angle of attack	12.435	1	12.435	44.261	< 0.0001	significant
B-Flap angle	1.721	1	1.721	6.126	0.0224	significant
C-Propeller pitch angle	0.092	1	0.092	0.327	0.5736	
D-Downstream distance	192.524	1	192.524	685.262	< 0.0001	significant
AD-Interaction	4.916	1	4.916	17.498	0.0005	significant
C^2	8.231	1	8.231	29.296	< 0.0001	significant
Residual	5.619	20	0.281			
Lack of fit	5.599	18	0.311	30.376	0.0323	significant
Pure error	0.021	2	0.010			
Cor Total	225.538	26				

Table 6.24: ANOVA for WTVY

Model statistics given in Table 6.25 show that the predicted R-squared of 0.9474 and adjusted R-squared of 0.9676 are in reasonable agreement and are very high values for wind tunnel experimentation.

Std. Dev.	0.530
Mean	-6.222
PRESS	11.857
R-Squared	0.975
Adjusted R-Squared	0.968
Predicted R-Squared	0.947

Table 6.25: Model Statistics for WTVY

The coefficient estimates are given below in Table 6.26 with their confidence bands.

Factor	**Coefficient estimate**	**df**	**Standard error**	**Low (95% CI)**	**High (95% CI)**
Intercept	-7.003	1	0.177	-7.372	-6.634
A-Angle of attack	-0.831	1	0.125	-1.092	-0.571
B-Flap angle	-0.309	1	0.125	-0.570	-0.049
C-Propeller pitch angle	0.072	1	0.125	-0.189	0.332
D-Downstream distance	-3.270	1	0.125	-3.531	-3.010
AD-Interaction	-0.554	1	0.133	-0.831	-0.278
C^2	1.171	1	0.216	0.720	1.623

Table 6.26: Regression Model Coefficient Estimate

The regression model by using coded variables (see Equation 6.14) indicates that the most important terms in model are the propeller pitch angle and the downstream distance whereas the only interaction is of the angle of attack and downstream distance. As in the case of vertical motion of the wing tip vortex, the second order of the propeller pitch angle is included in the model and has the greatest effect compared to other factors.

Coded factors

$$\mathit{WTVY} = 1.171 * \mathit{Propeller\ Pitch\ Angle}^2 - 0.554 * \mathit{Angle\ of\ Attack} * \mathit{Downstream\ Distance} - 0.831 * \mathit{Angle\ of\ Attack} - 0.309 * \mathit{Flap\ Angle} + 0.072 * \mathit{Propeller\ Pitch\ Angle} - 3.270 * \mathit{Downstream\ Distance} - 7.003 \qquad (6.14)$$

Actual factors

$$\mathit{WTVY} = 0.130 * \mathit{Propeller\ Pitch\ Angle}^2 - 0.004 * \mathit{Angle\ of\ Attack} * \mathit{Downstream\ Distance} - 0.055 * \mathit{Angle\ of\ Attack} - 0.018 * \mathit{Flap\ Angle} - 5.702 * \mathit{Propeller\ Picth\ Angle} - 0.091 * \mathit{Downstream\ Distance} + 59.581 \qquad (6.15)$$

Figure 6.12 shows the quadratic effect of propeller pitch angle on the horizontal motion of wing tip vortex.

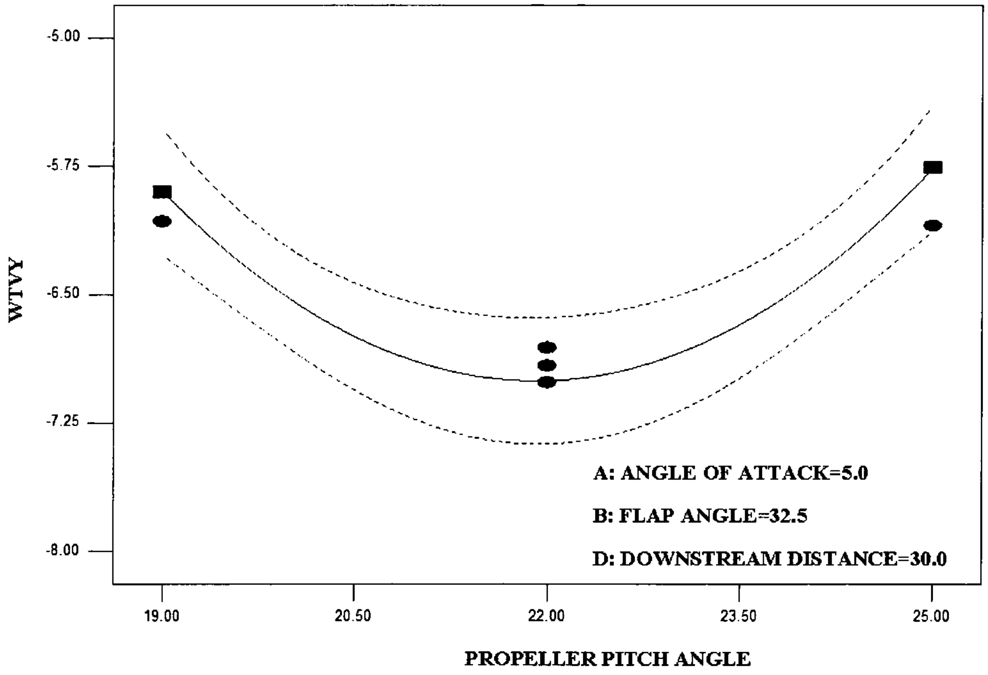

Figure 6.12: Effect of Propeller Pitch Angle on WTVY

The interaction graphic given in Figure 6.13 shows that the surface of interaction seems to be a linear plane in which the minimum interaction contribution is at the most downstream distance and angle of attack is 10° while the maximum value is at the trailing edge of the wing with angle of attack of 0°.

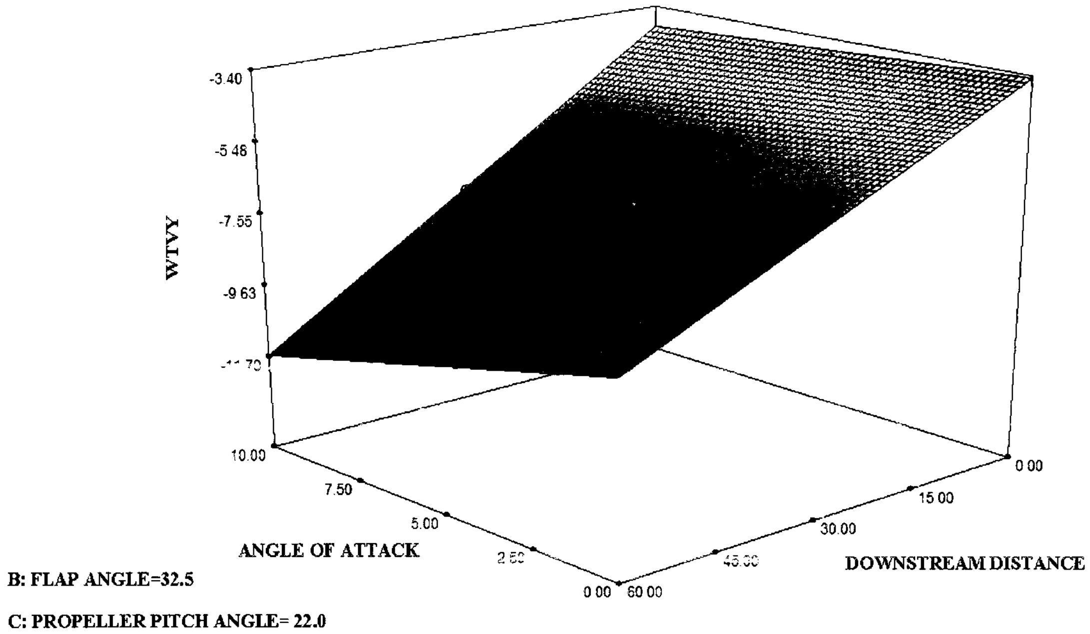

Figure 6.13: Interaction of Angle of Attack and Downstream Distance on WTVY

6.2.6 Shortest Distance Between Vortices (SDBV)

The suggestions of the sequential sum of squares, lack of fit test and model summary (see Tables from 6.27 to 6.29) was to use a linear model for the regression but in case of a linear model the R-squared, adjusted R-squared and predicted R-squared terms (see Table 6.29) are lower compared to the corresponding values of other models. Since its R-squared terms are high and F_0 value is relatively low while not any of the models passed the lack of fit test, a two factor interaction model is used.

Source	Sum of squares	df	Mean square	F value	P value Probability>F	
Mean vs Total	52242.848	1	52242.848			
Linear vs Mean	83.771	4	20.943	24.819	<0.0001	Suggested
2FI vs Linear	8.681	6	1.447	2.343	0.0814	
Quadratic vs 2FI	0.951	4	0.238	0.319	0.8596	
Cubic vs Quadratic	8.373	8	1.047	7.486	0.0345	Aliased
Residual	0.559	4	0.140			
Total	52345.183	27	1938.711			

Table 6.27: Sequential Model Sum of Squares for SDBV

The results of lack of fit test (see Table 6.28) revealed that all the models have similar values of fitting the experimental data.

Source	Sum of squares	df	Mean square	F value	P value Probability>F	
Linear	18.525	20	0.926	47.144	0.0210	Suggested
2FI	9.843	14	0.703	35.787	0.0275	
Quadratic	8.893	10	0.889	45.261	0.0218	
Cubic	0.520	2	0.260	13.232	0.0703	Aliased
Pure error	0.039	2	0.020			

Table 6.28: Lack of Fit Test for SDBV

According to the value of PRESS and predicted R-squared term (see Table 6.29), a linear model would be the best but from the point of view of R-squared and adjusted R-squared terms a two factor interaction model can also be used.

Source	Std. Dev.	R-Squared	Adjusted R-Squared	Predicted R-Squared	PRESS	
Linear	0.919	0.819	0.786	0.685	32.263	Suggested
2FI	0.786	0.903	0.843	0.435	57.825	
Quadratic	0.863	0.913	0.811	0.323	69.293	
Cubic	0.374	0.995	0.965	-0.198	122.610	Aliased

Table 6.29: Model Summary Statistics for SDBV

The ANOVA given in Table 6.30 shows that the model has a F-value of 23.68 which implies that the model is significant, and there is only a 0.01% chance that a "Model F-value" this large could occur due to noise. The angle of attack, flap angle and downstream distance are the single factors that are significant while propeller pitch angle is included in the model because of hierarchy rule. The interaction of propeller pitch angle and downstream distance is barely significant and the plane of the interaction will be given later in the analyses. The "Lack-of-Fit F-value" of 41.193 implies the Lack of fit is significant.

Source	**Sum of squares**	**df**	**Mean square**	**F Value**	**p-value>F**	
Model	86.918	5	17.384	23.680	<0.0001	significant
A-Angle of attack	3.497	1	3.497	4.764	0.0406	significant
B-Flap angle	12.254	1	12.254	16.692	0.0005	significant
C-Propeller pitch angle	2.292	1	2.292	3.122	0.0918	
D-Downstream distance	65.729	1	65.729	89.534	<0.0001	significant
CD-Interaction	3.148	1	3.148	4.288	0.0509	significant
Residual	15.416	21	0.734			
Lack of fit	15.377	19	0.809	41.193	0.024	significant
Pure error	0.039	2	0.020			
Cor Total	102.335	26				

Table 6.30: ANOVA for SDBV

The model statistics given in Table 6.31 shows that Predicted R-Squared of 0.697 and the Adjusted R-Squared of 0.814 are sufficiently high for wind tunnel experimentation.

Std. Dev.	0.857
Mean	43.988
PRESS	31.043
R-Squared	0.849
Adjusted R-Squared	0.814
Predicted R-Squared	0.697

Table 6.31: Model Statistics for SDBV

Regression coefficients estimates are given below in Table 6.32 with their variability in confidence intervals.

Factor	**Coefficient estimate**	**df**	**Standard error**	**Low (95% CI)**	**High (95% CI)**
Intercept	43.988	1	0.165	43.645	44.331
A-Angle of attack	-0.441	1	0.202	-0.861	-0.021
B-Flap angle	0.825	1	0.202	0.405	1.245
C-Propeller pitch angle	-0.357	1	0.202	-0.777	0.063
D-Downstream distance	-1.911	1	0.202	-2.331	-1.491
CD-Interaction	-0.444	1	0.214	-0.889	0.002

Table 6.32: Regression Model Coefficient Estimate for SDBV

Coded variables used in the regression model (see Equation 6.16) of the shortest distance between vortices showed that downstream distance is the most influential single factor in the model, and second comes the flap angle. It can be concluded that with the exception of the flap angle, the vortices get closer to each other as the factors including the interaction term increase.

Coded factors

$$SDBV = -0.444 * Propeller\ Pitch\ Angle * Downstream\ Distance - 0.441 * Angle\ of\ Attack + 0.825 * Flap\ Angle - 0.357 * Propeller\ Pitch\ Angle - 1.911 * Downstream\ Distance + 43.988 \quad (6.16)$$

Actual factors

$$SDBV = -0.005 * Propeller\ Pitch\ Angle * Downstream\ Distance - 0.088 * Angle\ of\ Attack + 0.047 * Flap\ Angle + 0.029 * Propeller\ Pitch\ Angle + 0.029 * Downstream\ Distance + 44.171 \quad (6.17)$$

The interaction of propeller pitch angle and downstream distance is shown in Figure 6.14 and as shown below when the propeller pitch angle is 25° the effect is minimum at the most downstream distance and the effect is maximum at the trailing edge of the wing.

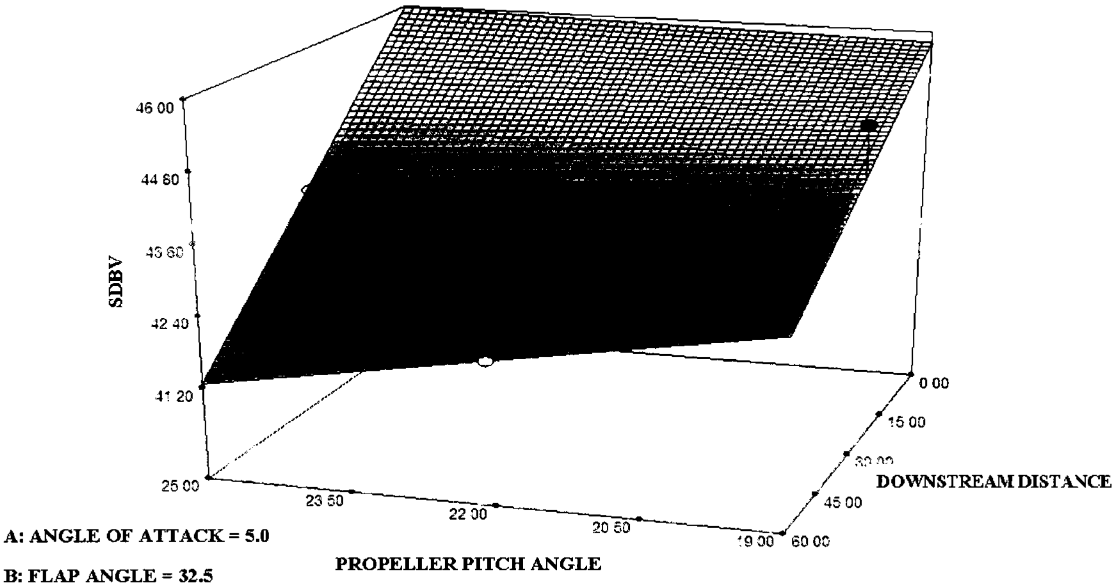

Figure 6.14: Interaction of Propeller Pitch Angle and Downstream Distance on SDBV

6.2.7 Flap Vortex Vorticity Strength (FVVS)

Vorticity levels at the core of the vortices were other responses under investigation and for modeling the maximum vorticity level in the core of flap vortex a quadratic model was suggested from the sequential sum of squares and model statistics given in Tables 6.33 and 6.35, respectively. None of the models is insignificant in the lack of fit test given in Table 6.34.

Source	Sum of squares	df	Mean square	F value	P value Probability>F	
Mean vs Total	1402.035	1	1402.035			
Linear vs Mean	584.100	4	146.025	16.484	<0.0001	
2FI vs Linear	110.333	6	18.389	3.480	0.0214	
Quadratic vs 2FI	44.538	4	11.135	3.339	0.0468	Suggested
Cubic vs Quadratic	36.698	8	4.587	5.525	0.0581	Aliased
Residual	3.321	4	0.830			
Total	2181.025	27	80.779			

Table 6.33: Sequential Model Sum of Squares for FVVS

Source	Sum of squares	df	Mean square	F value	P value Probability>F	
Linear	194.808	20	9.740	236.458	0.0042	
2FI	84.474	14	6.034	146.479	0.0068	
Quadratic	39.936	10	3.994	96.950	0.0103	Suggested
Cubic	3.239	2	1.619	39.309	0.0248	Aliased
Pure error	0.082	2	0.041			

Table 6.34: Lack of Fit Test for FVVS

The R-squared terms (see Table 6.35) are sufficiently high for the quadratic model whereas the PRESS values for all the models are similar except for the cubic model which is not suggested since it is an aliased model.

Source	Std. Dev.	R-Squared	Adjusted R-Squared	Predicted R-Squared	PRESS	
Linear	2.976	0.750	0.704	0.586	322.333	
2FI	2.299	0.892	0.824	0.603	308.932	
Quadratic	1.826	0.949	0.889	0.637	282.830	Suggested
Cubic	0.911	0.996	0.972	0.220	607.329	Aliased

Table 6.35: Model Summary Statistics for FVVS

The ANOVA (see Table 6.36) shows that the model F-value is 30.62 and p-value is less than 0.0001 which means that the model is significant. The test for the significant terms in the model indicates that all the single factors except propeller pitch angle are significant but this term is also included due to hierarchy. Two interaction terms are also significant which are angle of attack and downstream distance interaction, as well as the flap angle and propeller pitch angle interaction. Flap angle greatly influences the flap vortex vorticity as expected since its second order factor takes place in the model. The "Lack-of-Fit F-value" of 90.46 implies that the lack of fit is significant.

Source	**Sum of squares**	**df**	**Mean square**	**F Value**	**p-value>F**	
Model	715.562	7	102.223	30.621	<0.0001	significant
A-Angle of attack	313.137	1	313.137	93.801	<0.0001	significant
B-Flap angle	15.190	1	15.190	4.550	0.0462	significant
C-Propeller pitch angle	3.754	1	3.754	1.124	0.3023	
D-Downstream distance	252.019	1	252.019	75.493	<0.0001	significant
AD-Interaction	71.327	1	71.327	21.366	0.0002	significant
BC-Interaction	28.351	1	28.351	8.493	0.0089	significant
B^2	31.784	1	31.784	9.521	0.0061	significant
Residual	63.428	19	3.338			
Lack of fit	63.346	17	3.726	90.458	0.011	significant
Pure error	0.082	2	0.041			
Cor Total	778.990	26				

Table 6.36: ANOVA for FVVS

The Predicted R-Squared" of 0.817 and the Adjusted R-Squared" of 0.889 (see Table 6.37) seems that quadratic model is adequate to fit the experimental data.

Std. Dev.	1.827
Mean	7.206
PRESS	142.814
R-Squared	0.919
Adjusted R-Squared	0.889
Predicted R-Squared	0.817

Table 6.37: Model Statistics for FVVS

The coefficient estimates are given in Table 6.38 with their standard error values and confidence intervals.

Factor	**Coefficient estimate**	**df**	**Standard error**	**Low (95% CI)**	**High (95% CI)**
Intercept	5.672	1	0.609	4.397	6.946
A-Angle of attack	4.171	1	0.431	3.270	5.072
B-Flap angle	0.919	1	0.431	0.017	1.820
C-Propeller pitch angle	-0.457	1	0.431	-1.358	0.445
D-Downstream distance	3.742	1	0.431	2.840	4.643
AD-Interaction	2.111	1	0.457	1.155	3.067
BC-Interaction	-1.331	1	0.457	-2.287	-0.375
B^2	2.302	1	0.746	0.7404	3.863

Table 6.38: Regression Model Coefficient Estimate for FVVS

The z vorticity level is negative for both flap and wing tip vortices. The negative sign associated with the factors means that the magnitude of the z vorticity increases as the factor increases. When analyzing the regression model (see Equation 6.19) by using actual factor settings it is understood that the only term that increases the z vorticity level in the flap vortex is the flap angle and propeller pitch angle interaction whereas other factors and interaction support the decay of the vorticity level in the flap vortex.

Coded factors

$$(FVVS + 4.59)^{2.32} = 2.302 * Flap\ Angle^2 + 2.111 * Angle\ of\ Attack * Downstream\ Distance - 1.331 * Flap\ Angle * Propeller\ Pitch\ Angle + 4.171 * Angle\ of\ Attack + 0.919 * Flap\ Angle - 0.457 * Propeller\ Pitch\ Angle + 3.742 * Downstream\ Distance + 5.672 \qquad (6.18)$$

Actual factors

$$(FVVS + 4.59)^{2.32} = 0.008 * Flap\ Angle^2 + 0.014 * Angle\ of\ Attack * Downstream\ Distance - 0.025 * Flap\ Angle * Propeller\ Pitch\ Angle + 0.412 * Angle\ of\ Attack + 0.122 * Flap\ Angle + 0.672 * Propeller\ Pitch\ Angle + 0.054 * Downstream\ Distance - 8.678 \qquad (6.19)$$

The effect of flap angle on FVVS is shown in Figure 6.15.

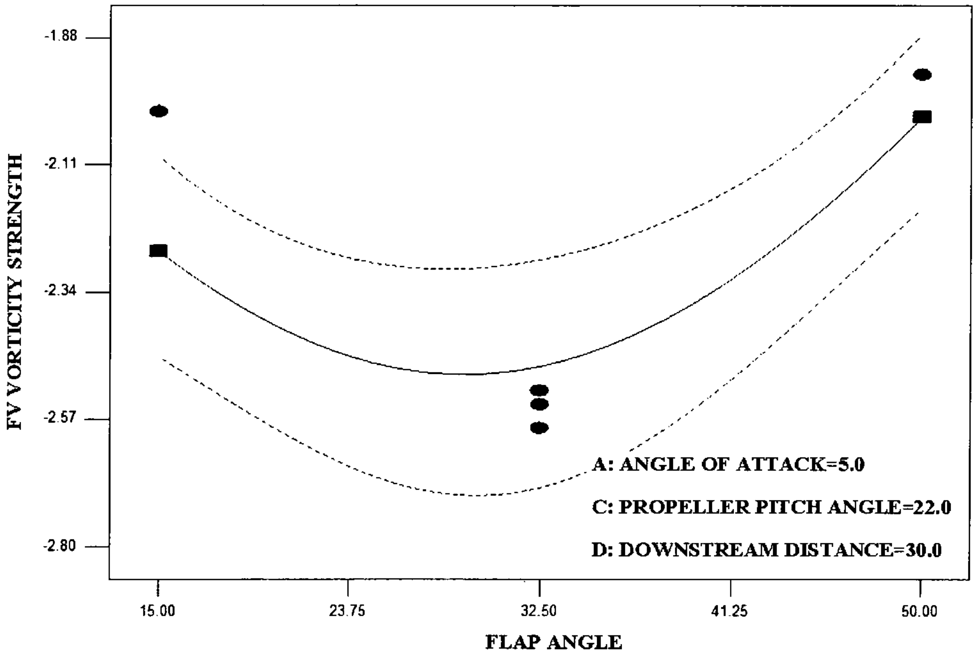

Figure 6.15: Effect of Flap Angle on FVVS

Analysis of the interaction of angle of attack and downstream distance (see Figure 6.16) shows that at the trailing edge of the wing when the angle of attack is 0° the contribution of the interaction to increase the z vorticity level in the flap vortex is maximum, whereas the angle of attack increases or toward the end of downstream region this contribution decreases.

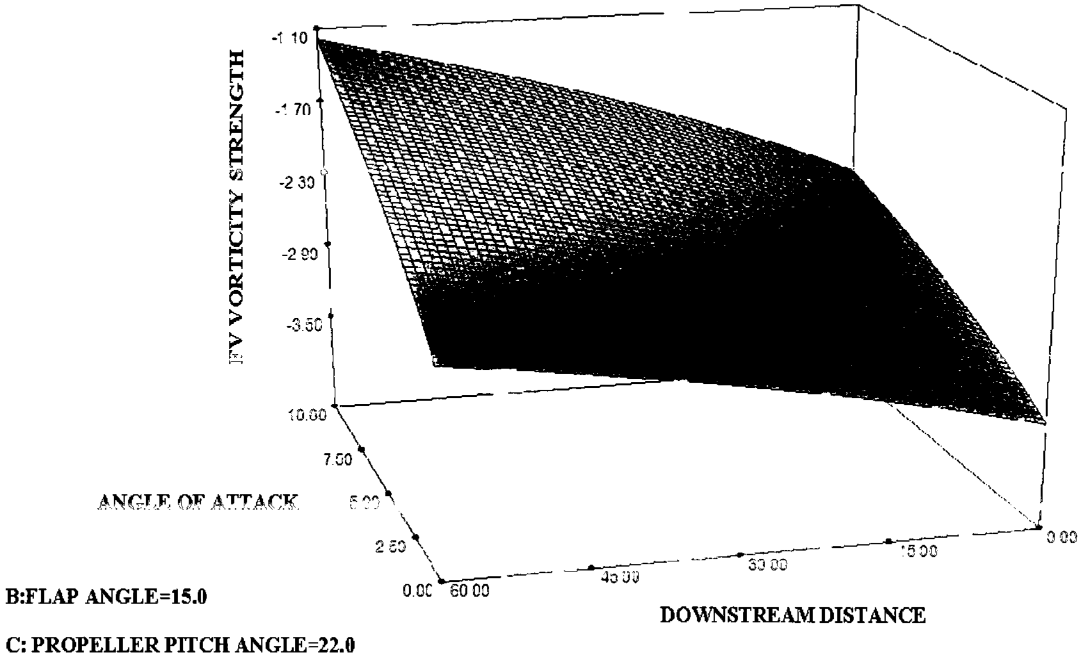

Figure 6.16: Interaction of Angle of Attack and Downstream Distance on FVVS

The analysis of the interaction of flap angle and propeller pitch angle (see Figure 6.17) indicates that the contribution of the interaction is a maximum when the flap is deployed to 50° and propeller pitch angle is 19° while the minimum contribution occurs when the flap is deployed around 30°.

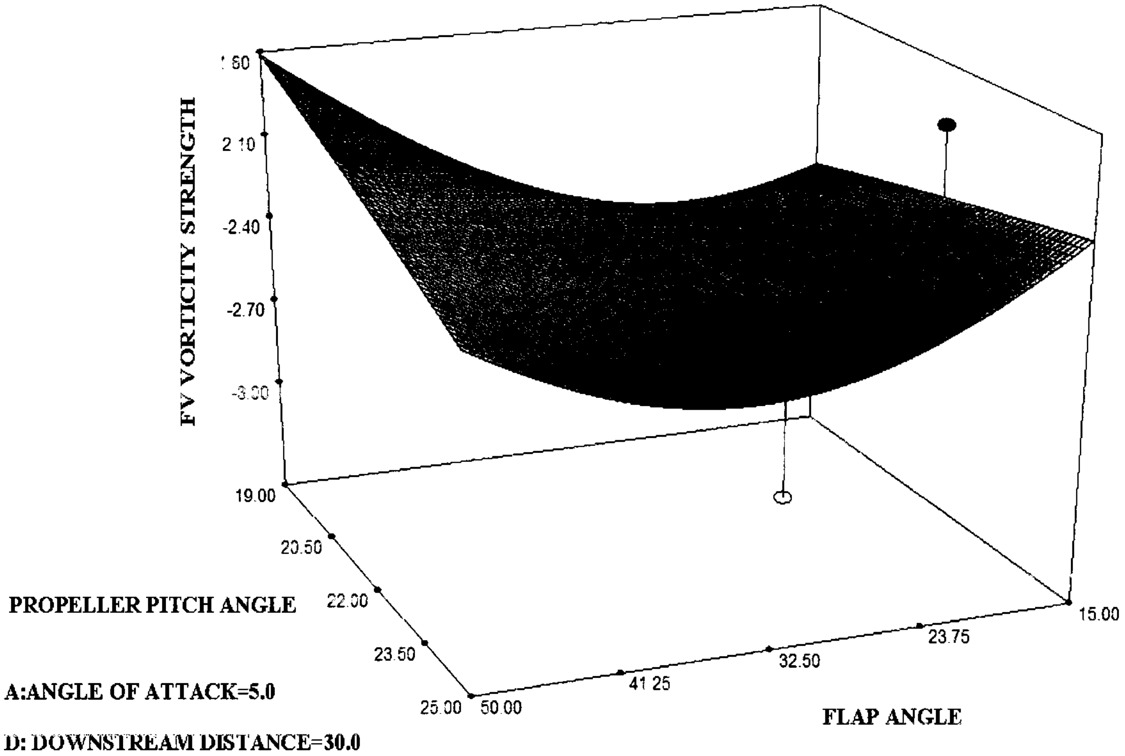

Figure 6.17: Interaction of Flap Angle and Propeller Pitch Angle on FVVS

6.2.8 Wing Tip Vortex Vorticity Strength (WTVVS)

The analyses performed for the sequential sum of squares and model summary statistics is given in Tables 6.39 and 6.41, respectively. Results (see Table 6.41) suggest using a linear model since only the linear model appear significant and R-squared, adjusted R-squared and predicted R-squared values are also very high. Lack of fit test (see Table 6.40) revealed that none of the models are insignificant..

Source	Sum of squares	df	Mean square	F value	P value Probability>F	
Mean vs Total	221.002	1	221.002			
Linear vs Mean	58.931	4	14.733	115.326	<0.0001	Suggested
2FI vs Linear	0.806	6	0.134	1.072	0.4189	
Quadratic vs 2FI	0.024	4	0.006	0.036	0.9972	
Cubic vs Quadratic	0.719	8	0.090	0.285	0.9384	Aliased
Residual	1.262	4	0.316			
Total	282.744	27	10.472			

Table 6.39: Sequential Model Sum of Squares for WTVVS

Source	Sum of squares	df	Mean square	F value	P value Probability>F	
Linear	2.808	20	0.140	127.194	0.0078	Suggested
2FI	2.002	14	0.143	129.564	0.0077	
Quadratic	1.979	10	0.198	179.241	0.0056	
Cubic	1.260	2	0.630	570.514	0.0017	Aliased
Pure error	0.002	2	0.001			

Table 6.40: Lack of Fit Test for WTVVS

The PRESS value (see Table 6.41) for the linear model is relatively low which is desirable while various R-squared terms are very high meaning that the model fits the data well.

Source	Std. Dev.	R-Squared	Adjusted R-Squared	Predicted R-Squared	PRESS	
Linear	0.357	0.955	0.946	0.931	4.264	Suggested
2FI	0.354	0.968	0.947	0.885	7.100	
Quadratic	0.406	0.968	0.931	0.843	9.708	
Cubic	0.562	0.980	0.867	-2.540	218.580	Aliased

Table 6.41: Model Summary Statistics for WTVVS

When the linear model is used it was observed that the model is significant (see Table 6.42) due to the fact that the F_0 value is high and p-value is less than 0.05 whereas the only significant term that takes place in the model is the angle of attack. F_0 value of 121.918, and p-value of 0.0082 (p-value is less than 0.05) for the lack of fit indicate that the lack of fit is significant.

Source	**Sum of squares**	**df**	**Mean square**	**F Value**	**p-value>F**	
Model	58.644	1	58.644	473.277	<0.0001	significant
A-Angle of attack	58.644	1	58.644	473.277	<0.0001	
Residual	3.098	25	0.124			
Lack of fit	3.096	23	0.135	121.918	0.0082	significant
Pure error	0.002	2	0.001			
Cor Total	61.742	26				

Table 6.42: ANOVA for WTVVS

The Predicted R-Squared of 0.942 and Adjusted R-Squared of 0.948 (see Table 6.43) are high enough to show how well the model fits the data.

Std. Dev.	0.352
Mean	-2.861
PRESS	3.609
R-Squared	0.950
Adjusted R-Squared	0.948
Predicted R-Squared	0.942

Table 6.43: Model Statistics for WTVVS

The coefficient estimate for the angle of attack is given below in Table 6.44 with its variability.

Factor	**Coefficient estimate**	**df**	**Standard error**	**Low (95% CI)**	**High (95% CI)**
Intercept	-2.861	1	0.068	-3.001	-2.722
A-Angle of attack	-1.805	1	0.083	-1.976	-1.634

Table 6.44: Regression Model Coefficient Estimate for WTVVS

Since the wake region is limited to 60% of the half wing span, no factor for the decay of the vorticity level is observed for the wing tip vortex. The only mechanism obtained is the effect of angle of attack increasing vorticity levels, as shown in Figure 6.18. Both coded (see Equation 6.20) and actual (see Equation 6.21) factors regression models shows that as the angle of increases the z vorticity level increases. Not any interaction is observed for the wing tip vortex vorticity strength model.

Coded factors

$$WTVVS = -2.861 * Angle\ of\ Attack - 1.805 \qquad (6.20)$$

Actual factors

$$WTVVS = -0.361 * Angle\ of\ Attack - 1.056 \qquad (6.21)$$

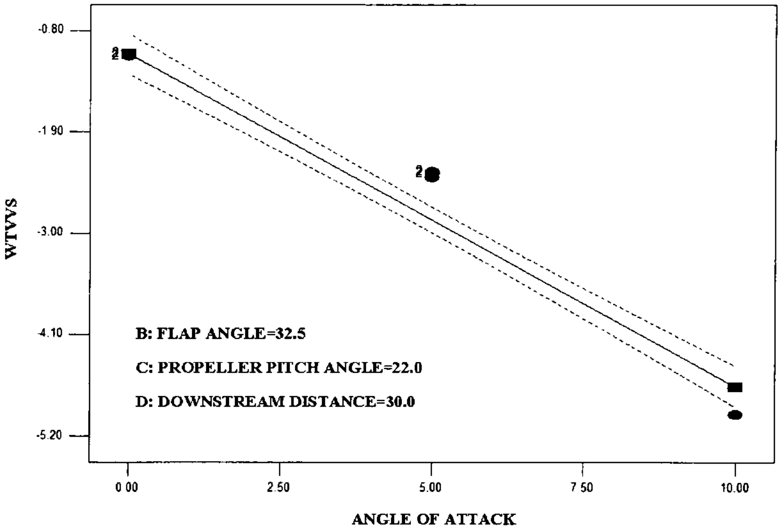

Figure 6.18: Effect of angle of attack on WTVVS

7 DISCUSSION

In this section, the regression models derived will be analyzed statistically whether or not the models are satisfactory. The analyses of the vertical motions of both flap and wing tip vortices are presented in this section while the analyses of the remaining responses are given in Appendix C.

7.1 Analysis of Flap Vortex Vertical Motion (FVX)

As mentioned before the displacement of the flap vortex along the x axis was denoted as FVX, and the regression model showed the influence of factors in both coded and actual variables wherein propeller pitch angle has the greatest effect among others. In this section, the normality analysis for the residuals was performed to see whether this regression model is sufficient to define the relation between the factors as well as interactions with the vertical motion of flap vortex as a response. The residuals mostly lie along the normality line, meaning that the distribution of the residuals looks mostly like a normal (Gaussian) distribution, as seen in Figure 7.1 . It should also be noted that at both ends of the line some of the residuals are located above and below the straight line which means that the tails of the distribution at both sides is a bit thinner than the tails of normal distribution and the residuals at extremes are not as large as expected from a normal distribution.

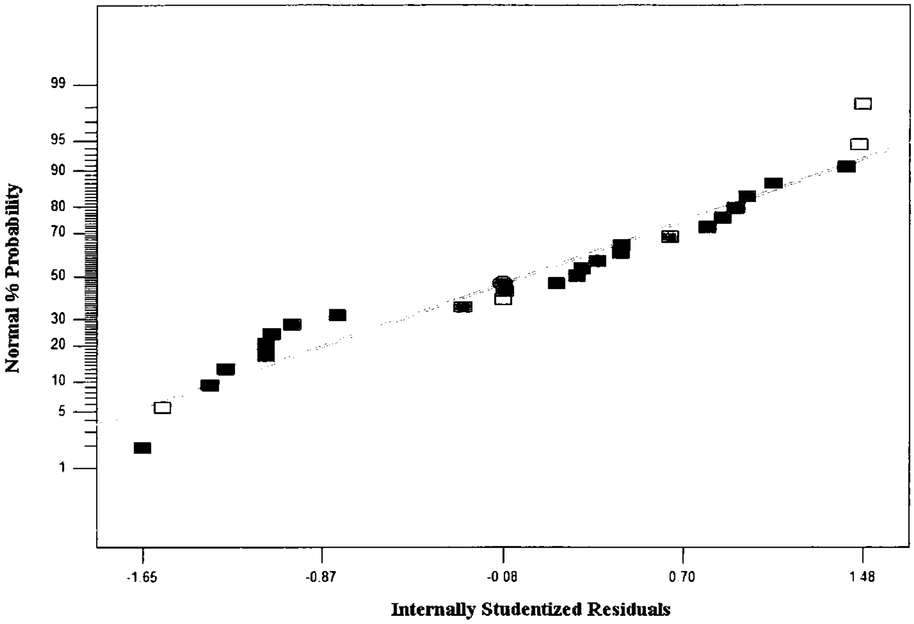

Figure 7.1: Normal Probability Plot of Residuals of FVX

Analysis of the predicted versus actual plot (see Figure 7.2) is performed to show whether the residuals are located along the inclined straight line without any significant structure. If there is any correlation between the residuals and any factor, as well as any significant increase in background noise, the structure of the plots indicates a funnel shape. Also the existence of any outlier is suspected as always and with the plots of predicted versus actual responses the check for any outlier can also be performed. The trend of the residuals indicates that the distribution of the residuals does not indicate a funnel shape, and no outlier is observable which means that FVX passes the test of predicted versus actual.

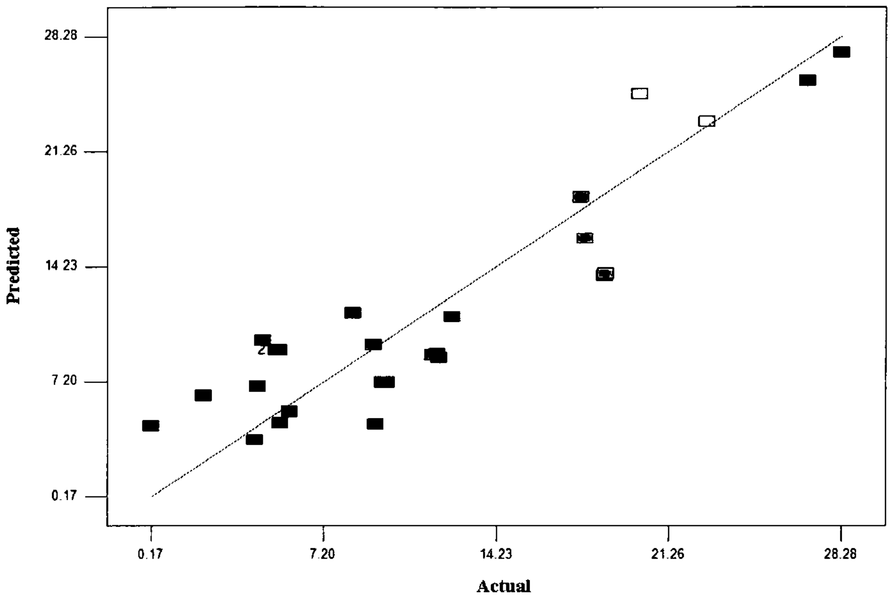

Figure 7.2: Plot of Residuals for Predicted versus Actual FVX

The test for predicted response versus internally studentized residuals is performed to make sure that no outlier exists outside ±3 standard deviations. The residuals shown in Figure 7.3 do not indicate the presence of any outlier.

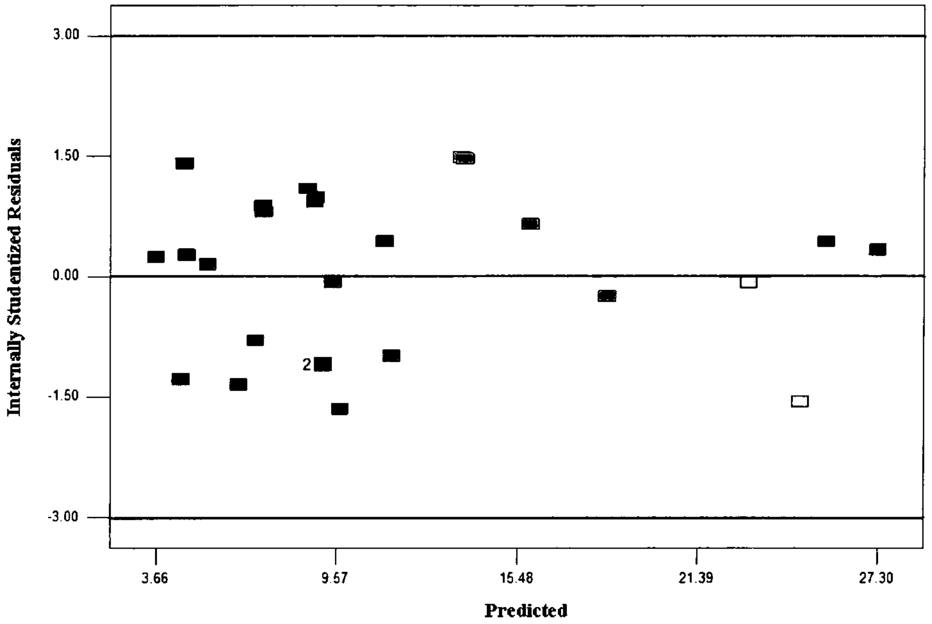

Figure 7.3: Plot of Internally Studentized Residuals versus Predicted FVX

The plot of residuals in time sequence also does not indicate any structure which would imply a correlation between the residuals and any factor. It is understood from the zigzag plots of the residuals that mostly the residuals are independently distributed and no groups of residuals are observed either above or below the line to indicate any correlation between the residuals and any factor. In addition to the analysis given above it is again noted that no outlier is observed in the plot given in Figure 7.4.

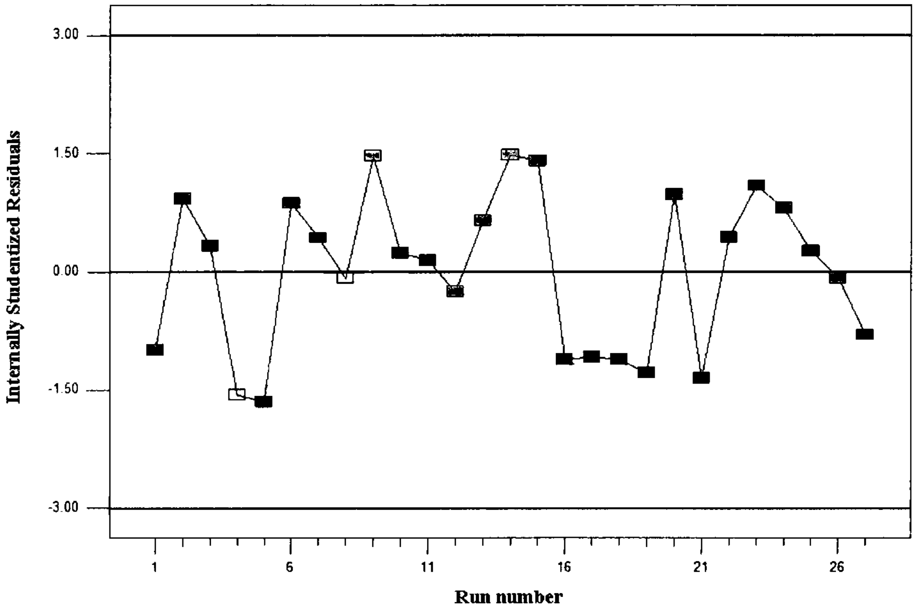

Figure 7.4: Plot of Internally Studentized Residuals versus Run Number for FVX

The analysis of residuals versus factors are performed to check if there is any correlation between the factors. While checking the residuals, any structure in the plot is examined to verify the correlation of residuals with the factor. The structures of the plots can be like a cone, barrel shape, etc.. The graph given in Figure 7.5 shows no structure and it can be concluded that there is no correlation between the residuals and the angle of attack, as well as the variance is constant. Also the existance of any outlier is checked and according to the plots given below no outlier exists.

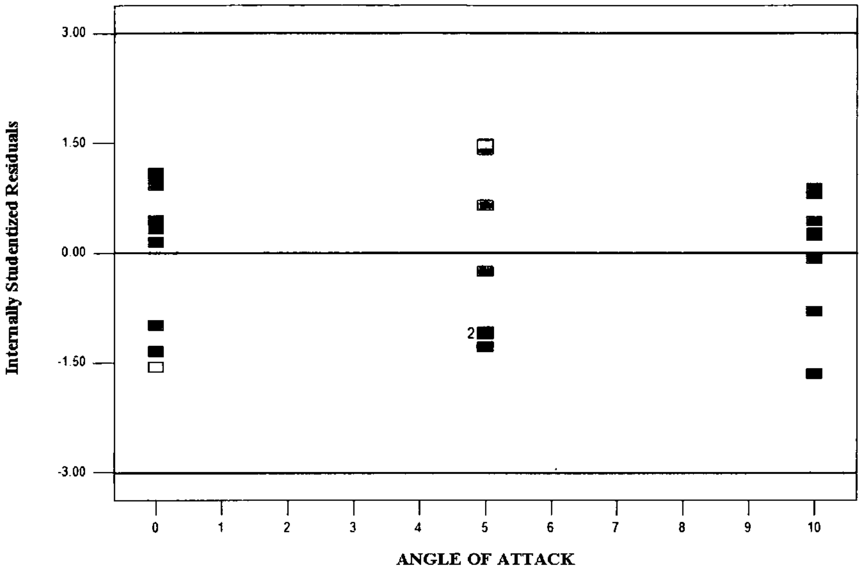

Figure 7.5: Plot of Internally Studentized Residuals versus Angle of Attack for FVX

The flap angle versus internally studentized residuals given in Figure 7.6 also does not show any structure and it can be concluded that the variance is constant as well as that no outlier exists.

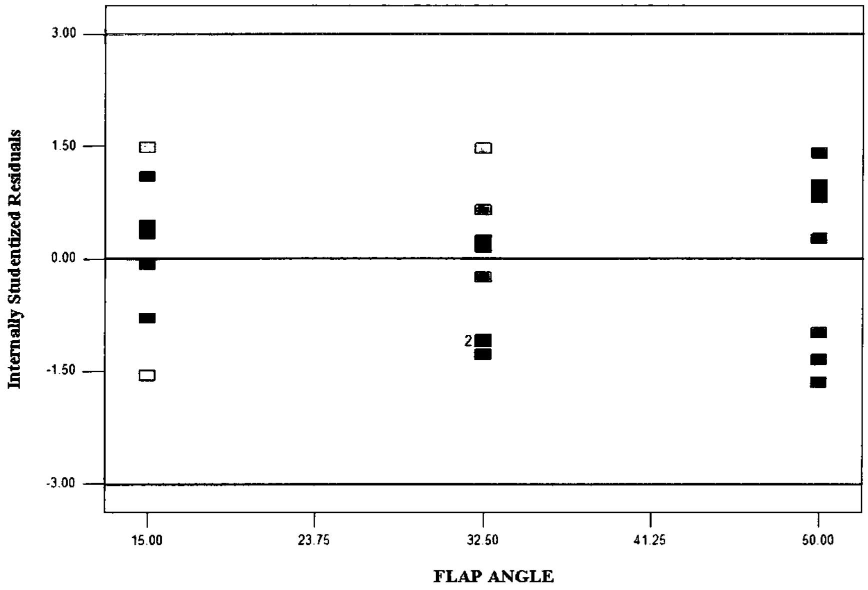

Figure 7.6: Plot of Internally Studentized Residuals versus Flap Angle for FVX

The case of internally studentized residuals versus propeller pitch angle indicates the variance is constant, and there is no structure observed within plots of residuals implying a lack of correlation between the residuals and propeller pitch angle. Also there are no outliers evident in the graph given in Figure 7.7.

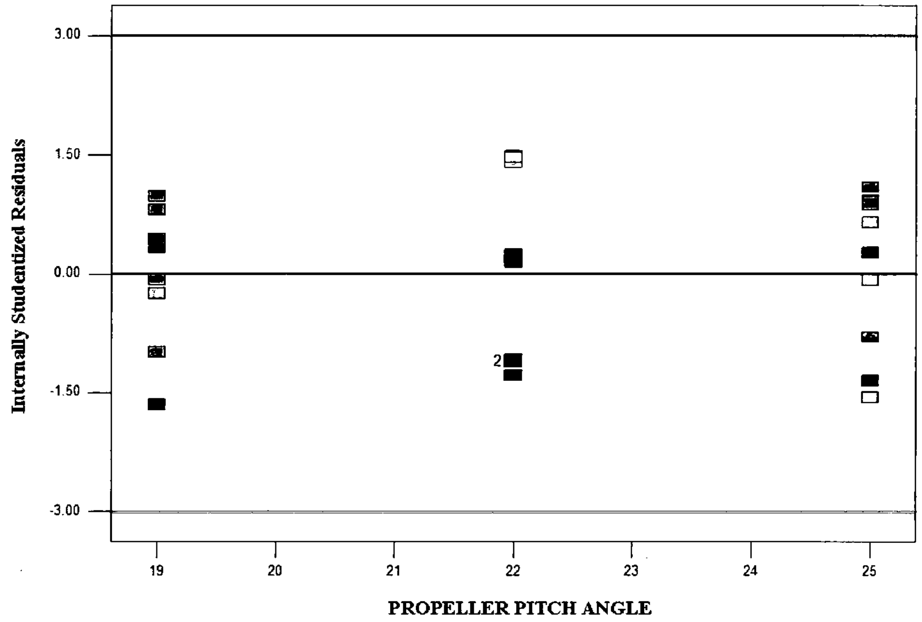

Figure 7.7: Plot of Internally Studentized Residuals versus Propeller Pitch Angle for FVX

The internally studentized residuals versus downstream distance (see Figure 7.8) plot is also the same as plots given for other factors and meaning that there is no outlier or structure in the plots which confirms that the variance is constant and there is no correlation in the plots of residuals related to any factor.

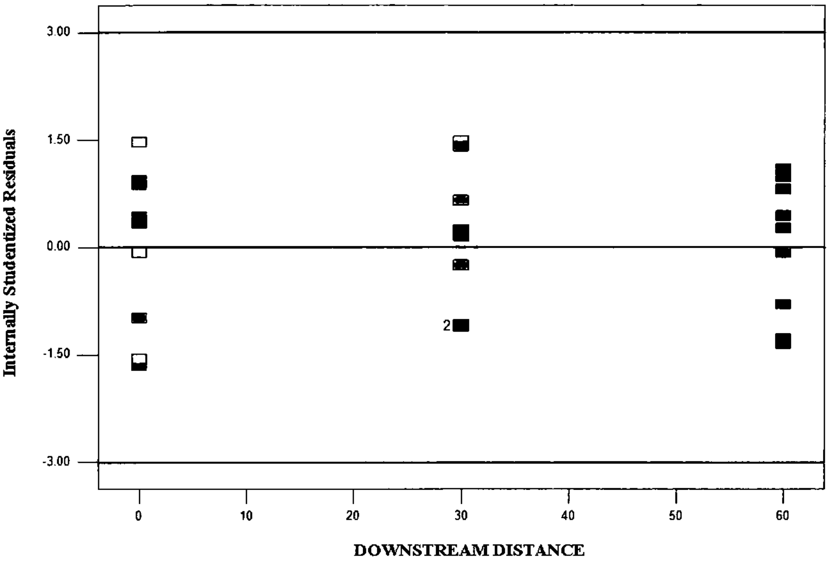

Figure 7.8: Plot of Internally Studentized Residuals versus Downstream Distance for FVX

The Box Cox plot given in Figure 7.9 suggested a transformation to make all the responses positive, to equalize the variances and increase the R-squared terms for better model fitting of the data. The type of the transformation is a power-law where $\lambda=1.94$ and k=4.45083. It should be kept in mind that the regression models predict the responses for the new response as $(FVX+4.45083)^{1.94}$.

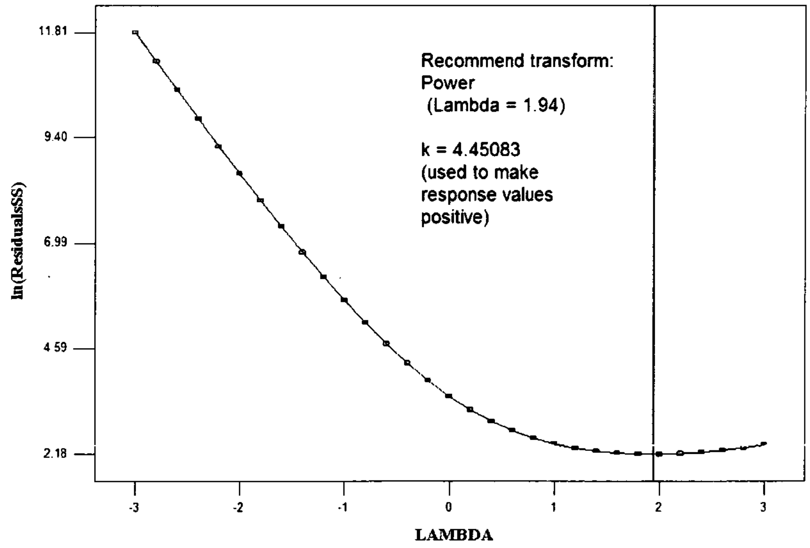

Figure 7.9: Box Cox Plot for FVX

7.2 Analysis of Wing Tip Vortex Vertical Motion (WTVX)

The residual analysis for the vertical motion of the wing tip vortex revealed that the residuals are normally distributed since the normal percentage probability plot versus internally studentized residuals given in Figure 7.10 shows the plots of residuals lying along a straight line. Very slight deflections do not imply any problem for the normality of residuals.

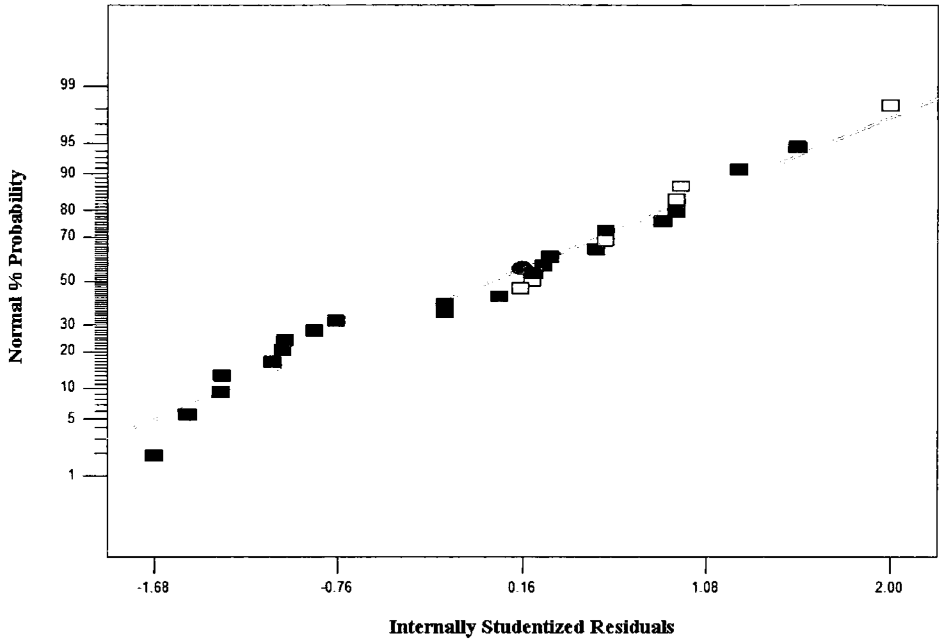

Figure 7.10: Normal Probability Plot of Residuals of WTVX

No structure in the plots of residuals are observed for predicted versus actual given in Figure 7.11 and the plot of internally studentized residuals versus predicted response given in Figure 7.12.

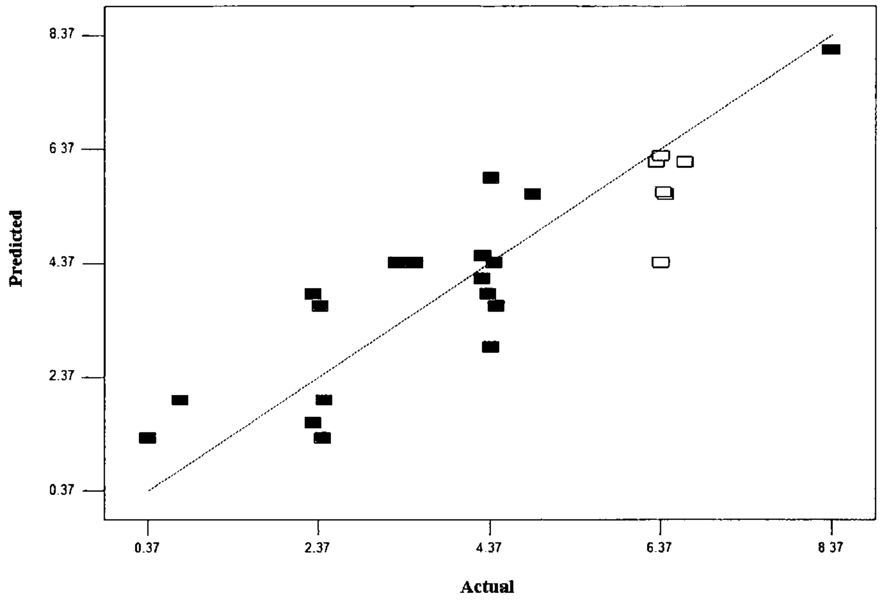

Figure 7.11: Plot of Residuals for Predicted versus Actual WTVX

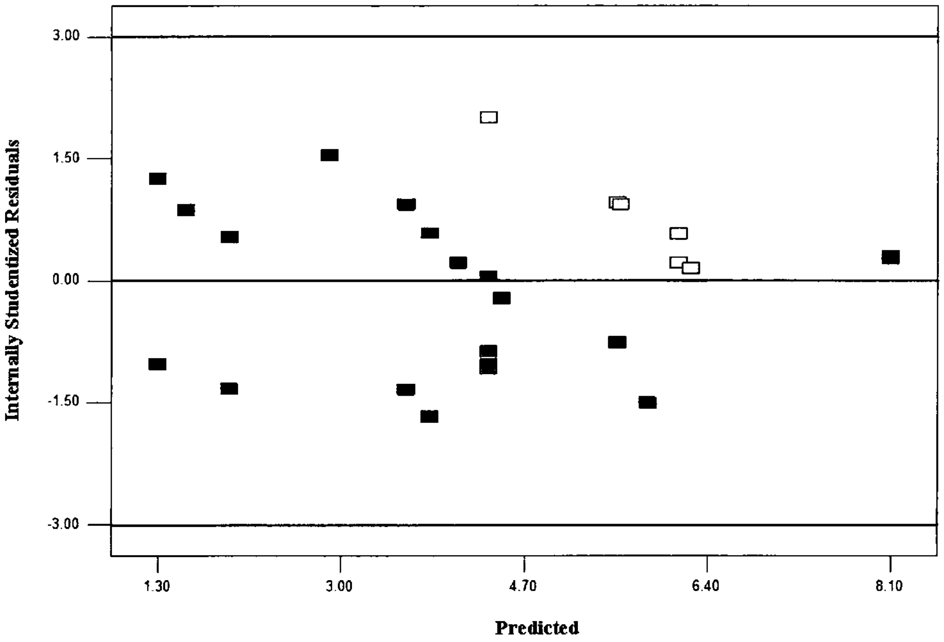

Figure 7.12: Plot of Internally Studentized Residuals versus Predicted WTVX

The graphic showing the internally studentized residuals versus run (see Figure 7.13) indicates that the residuals are independently distributed.

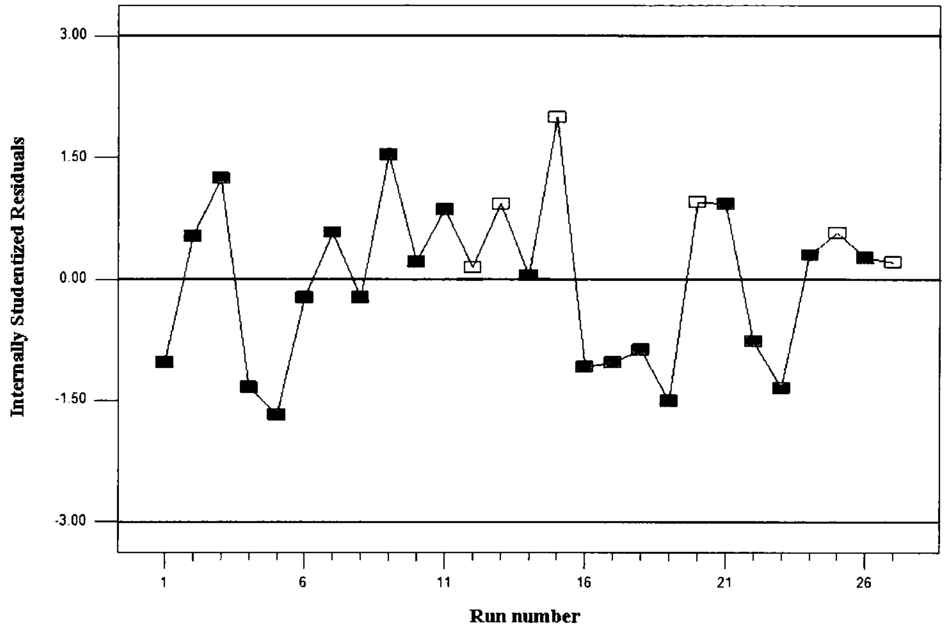

Figure 7.13: Plot of Internally Studentized Residuals versus Run Number for WTVX

The internally studentized residuals versus the four main factors given through Figures 7.14 to 7.17 verify that there is no correlation between the residuals and any factor although some slight barrel shapes are observed at the plots of residuals versus angle of attack and propeller pitch angle.

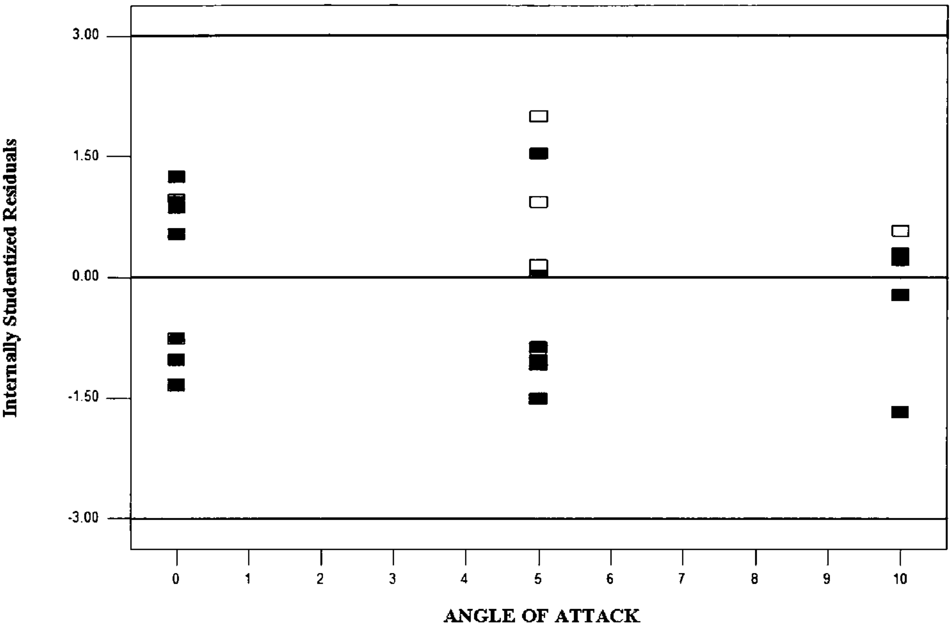

Figure 7.14: Plot of Internally Studentized Residuals versus Angle of Attack for WTVX

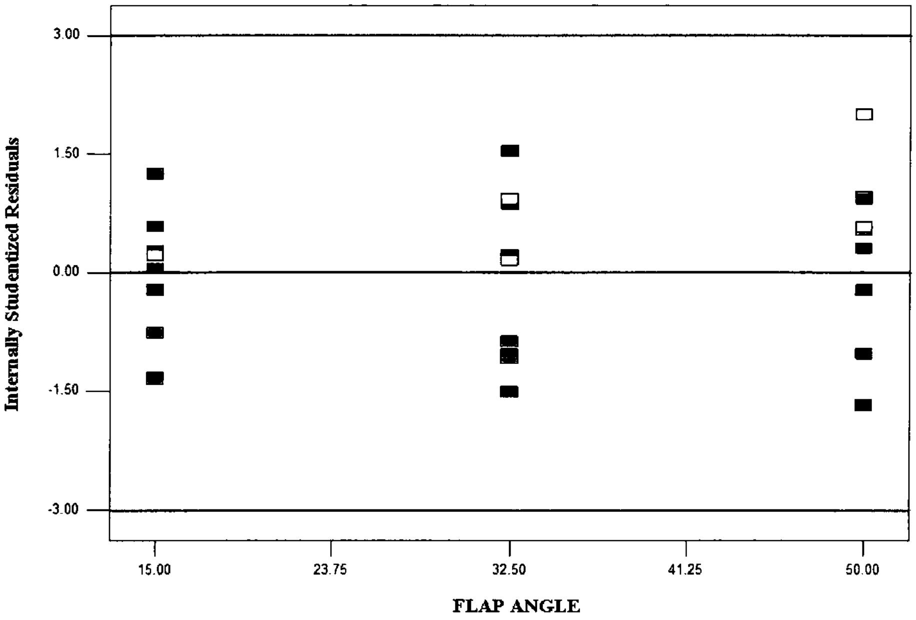

Figure 7.15: Plot of Internally Studentized Residuals versus Flap Angle for WTVX

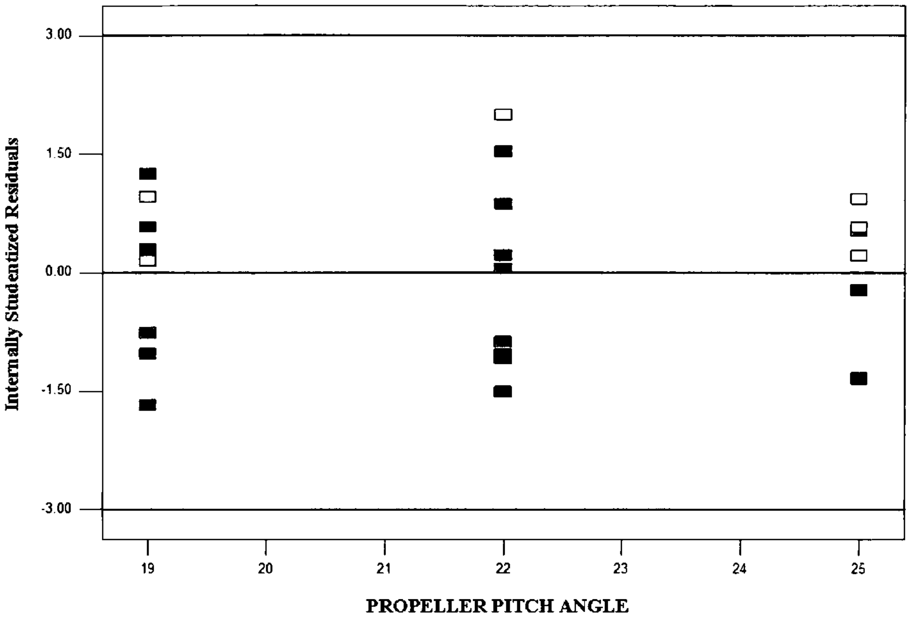

Figure 7.16: Plot of Internally Studentized Residuals versus Propeller Pitch Angle for WTVX

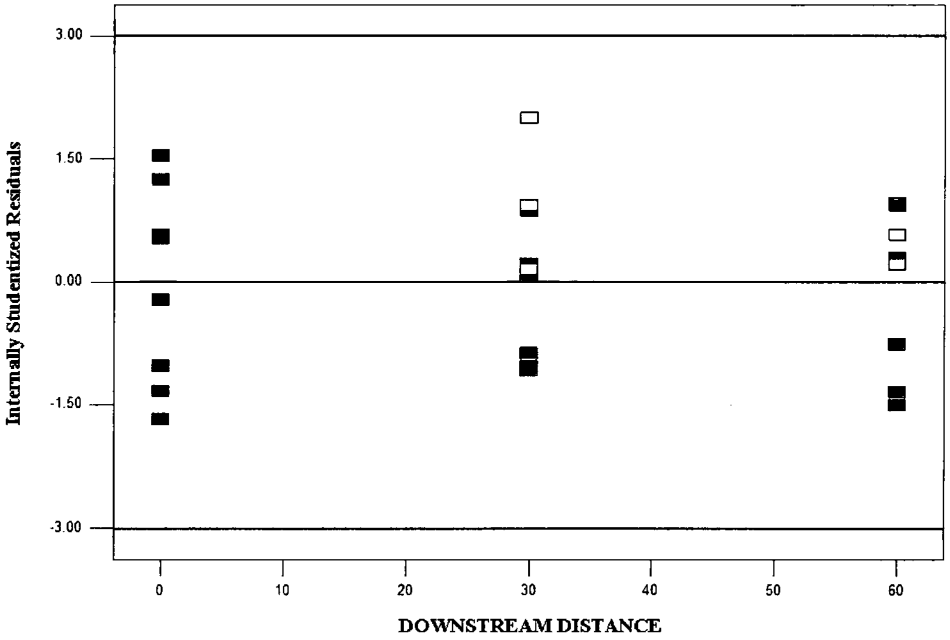

Figure 7.17: Plot of Internally Studentized Residuals versus Downstream Distance for WTVX

In the Box Cox plot given in Figure 7.18 no transformation is recommended.

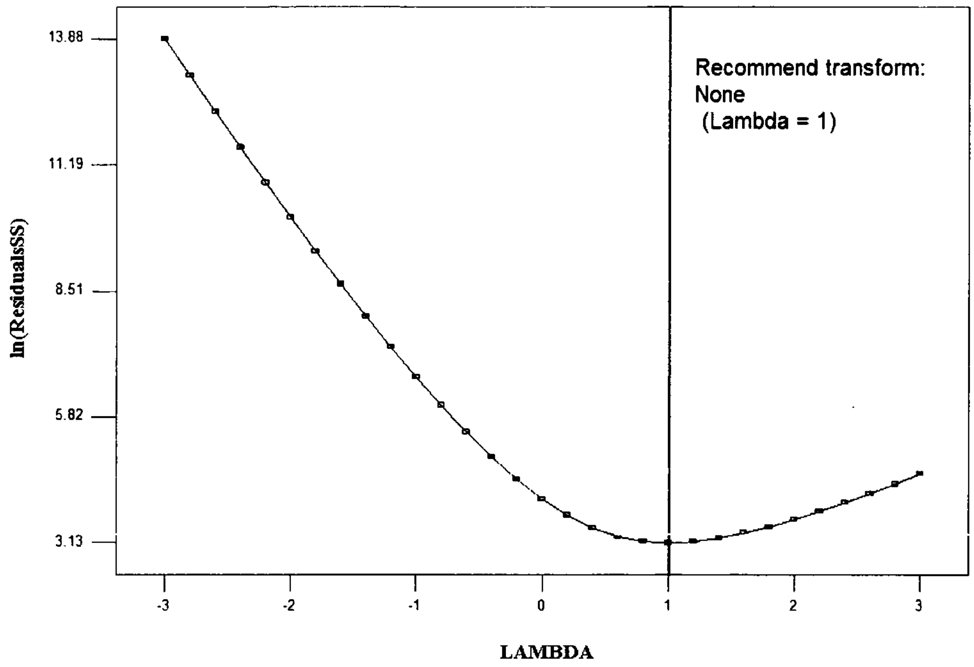

Figure 7.18: Box Cox Plot for WTVX

7.3 Analysis of Other Regression Models

The detailed analyses of the regression models for the responses other than the vertical motions of the wing and flap vortices are given in Appendix C. The brief analyses given in Table 7.1 showed that the regression models satisfied the requirements of the model adequacy checking.

	Normality Check	Independence Check	Constant Variance Check	Residuals for Predicted versus Actual	Any structure in the residuals plots	Outlier
FVY	Passed	Passed	Passed	Passed	None	None
WTVY	Passed	Passed	Passed	Passed	None	None
SDBV	Passed	Passed	Passed	Passed	None	None
FVVS	Passed	Passed	Passed	Passed	None	None
WTVVS	Passed	Passed	Passed	Passed	None	None

Table 7.1: Brief Analysis of Other Responses

(Responses Other than Vertical Motions of the Wing Tip and Flap Vortices)

8 CONCLUSION

8.1 Conclusions

In this dissertation, the near wake field of wing of a medium range and propeller driven twin-engine military cargo aircraft was analyzed using both Particle Image Velocimetry and Hotwire Anemometry systems in a statistical designed experiment.

The main factors that were expected to change the wake field were the angle of attack, flap angle, and propeller pitch angle which are main physical parameters that may alter the magnitudes of wing tip vortex, flap vortex, and propeller wake, respectively. The fourth factor was chosen as the downstream distance which changes all the vortices and propeller wake distribution. It was expected to obtain the quadratic regression models that can define how the vortices evolve with varying factors in a series of experiments designed according to Face Centered Design.

The first experiments were performed using PIV to visualize Reynolds shear stresses and then Hotwire Anemometry to acquire data about wake velocities, turbulence levels, and vorticity levels in the vortices and the propeller wake.

The measurements and statistical analyses of experiments mainly showed that the motion of both vortices in the vertical axis are mainly influenced from the propeller pitch angle as much as angle of attack. Quadratic regression models were obtained in which the angle of attack and the propeller pitch angle are squared and two factor interactions take place as well as single factors. The analyses made for the horizontal measurements of both vortices gave quadratic regression models containing the factor of propeller pitch angle squared (for the horizontal motion of flap vortex, squared of downstream distance also takes place), two factor interactions and single factors. The shortest distance between two vortices indicate if any tendency of merging is present under varying conditions such that all the factors with the exception of flap angle contribute to the merging of vortices as well as the interaction propeller pitch angle and downstream distance. The vorticity strength of both vortices were also under consideration if decay of the vortices are observable within near field wake region. The results showed that within near field wake no decay of wing tip vortex is observed while decay of flap vortex is mainly influenced from the flap angle compared to the other factors. The squared of flap angle is influencing the vorticity of flap vortex as well as the interaction of angle of attack and downstream distance, and the second interaction of flap angle and propeller pitch angle. The near field wake showed that the vortices tend to merge in the medium range wake region and it would be possible to decay and downward motion of wing tip vortex in the extended near field.

The statistical analyses of regression models for the motion and characteristics of both vortices indicate that residuals seem to be independently and normally distributed which are vital for obtaining reliable results. The analyses also revealed that none of the models are insignificant in the lack of fit test and increased replication of design points are strongly recommended for researchers interested in experiments with a similar design and experimental model. Mostly the R-squared and adjusted R-squared values are high for the regression models obtained for the vortex motions and characters. Predicted R-squared values seem to be vary between 64% to 94% for the models of vortex motions and characteristics which can be accepted as satisfactory for the wind tunnel experimentations.

It was concluded that the factors were chosen correctly for the analyses of near field wake region of a propeller mounted wing, such that no insignificant factor was observed at the analyses of the experiments. Some of the interactions were also obtained influencing the regression models of vortex behaviors as expected.

8.2 Prediction of the Trajectories of the Vortices

The trajectories of both wing tip and flap vortices were predicted using the regression models to understand the behaviors of the vortices. In order to plot the trajectories of the vortices, the medium values of the factors were chosen to find the mean values of the trajectories and one standard deviation value was used to show the error bars. As shown in Figures 8.1-8.3, wing tip and flap vortices are approaching each other and they are expected to merge in the medium wake range. Wing tip vortex ascends while the flap vortex seems to descend in the near field wake but it is known from the literature survey that the wing tip vortex descends in the extended near field. Both vortices move inboard within the region starting from the trailing edge of the wing to the edge of near field wake. The flap vortex moves outboard starting from the end of the near field wake and both wing tip and flap vortices move in such a way to create a spiral trajectory.

The flexible hose and the funnel used for transferring the fuel from the tanker aircraft should be located in between the flap outboard edge and the wing tip in order not to vibrate the flexible mechanism extremely during probe and drogue air-refueling operations. The propeller wake is a place for extreme wake hazards and the region between the propeller tip (close to the flap outboard edge) and the flap outboard edge is the place where the merging of the propeller wake and flap vortex takes place. Those regions cannot be used as a safe place for a stable motion of flexible hose of air-refueling mechanism.

During air-drop operations, mainly the rear access ramps are being used for rolling out the large platforms and discharging the parachutists. If it is needed to use the side cargo door, the parachutists will be influenced mainly from the propeller wake starting from the medium wake range but it is not expected to observe any interaction between the discharged logistic supplies or parachutists and the merged vortices.

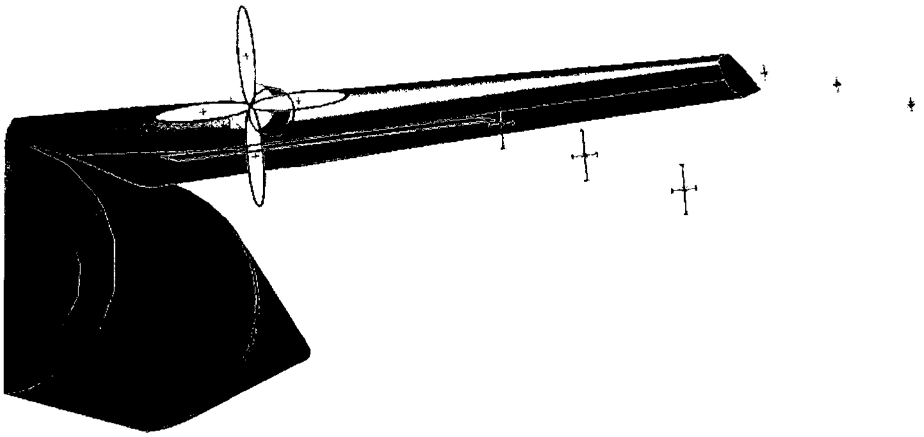

Figure 8.1: Trajectories of the Vortices (Perspective view from upstream)

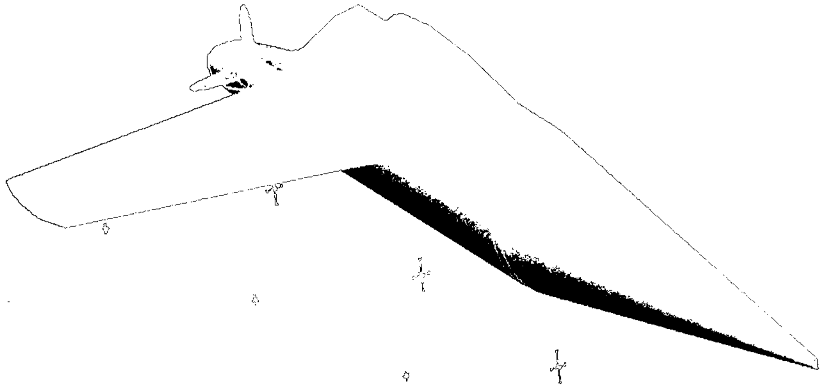

Figure 8.2: Trajectories of the Vortices (Perspective view from downstream)

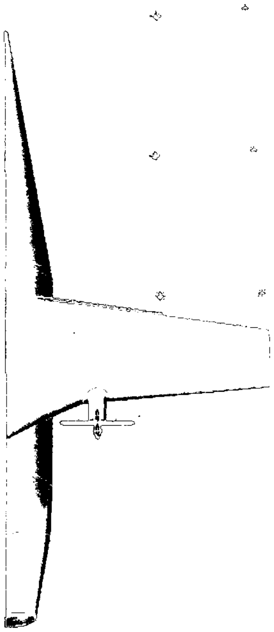

Figure 8.1: Trajectories of the Vortices (Top view)

8.3 Recommendations for Future Work

The air operations such as air-drop and air-refueling needs to be modeled for a larger wake region since the aircraft to be refueled is approaching from far behind the tanker aircraft and should be aware of the oncoming wake hazard effects from the near and extended near fields. The parachutists and logistics units are discharged from the aircraft during air-drop operation flights and those are under the influence of wake hazards up to the extended near field wake region. Then the analyses of trajectories of vortices with varying factors can be performed for the extended near field by enlarging the near field wake region encompassed in the dissertation study.

If the wake region of interest is enlarged to understand the trajectories and properties of vortices up to the extended near field, cubic regression models along with three-factor interactions for modeling the vortex characteristics can be recommended as by increasing the number of experiments such that the new design involves at least five levels of each factor.

REFERENCES

Allen, A., Breitsamter, C., 2009, "Experimental Investigation of Counter-Rotating Four Vortex Aircraft Wake", Aerospace Science and Technology, Vol 13, pp. 114-129.

Babie, B.M., Nelson, R.C., 2004, “Flow Visualization Study of Far Field Wake Vortex Interaction”, 11th International Symposium on Flow Visualization, 9-12 August 2004, University of Norte Dame, Indiana, USA.

Bandyopadhyay, P.R., Stead, D.J., Ash, R.L., 1990, “The Organized Nature of a Turbulent Trailing Vortex”, AIAA Journal, Vol. 29, No. 10, pp. 1627-1633.

Barnes, W.M., 1995, “Aerodynamics Aeronautics and Flight Mechanics-2nd Edition”, John Wiley & Sons Inc., ISBN: 0-471-57506-2.

Batchelor, G.K., 1964, “Axial Flow in Trailing Line Vortices”, Journal of Fluid Mechanics, Vol 20, pp. 645–658.

Biggers, J.C., Orloff, K.L., 1975, “Measurements of the Helicopter Rotor Induced Flow Field”, Journal of American Helicopter Society, Vol 20, No 1.

Birch, D., Lee, T., "Effect of Trailing-Edge Flap on a Tip Vortex", 2005, Journal of Aircraft, Vol 42, pp. 442-447.

Bruun, H.H., 1995, “Hot-wire Anemometry: Principals and Signal Analysis”, Oxford Science Publications, New York.

Box, G.E.P., Wilson, K.B., 1951, “On the Experimental Attainment of Optimum Conditions”, Journal of the Royal Statistical Society, Series B, Vol 13: pp. 1-45.

Cenedese, A., Accardo, L., Milone, R., 1985, “Phase Sampling Techniques in the Analysis of a Propeller Wake”, First International Conference on Laser Anemometry: Advances and Application, BHRA Fluid Engineering, Manchester.

Chiaramonte, J.Y., Favier, D., Maresca, C., Benneceur, S., 1996, “Aerodynamic Interaction Study of the Propeller/Wing Under Different Flow Configurations”, Journal of Aircraft, Vol 33(1), pp. 46-53.

Chigier, N.A., Corsiglia, V.R., 1972, "Wind-Tunnel Studies of Wing Wake Turbulence", Journal of Aircraft, Vol. 9, No. 12, pp. 820-825.

Chigier, N.A., Corsiglia, V.R., 1973, “Tip Vortices-Velocity Distributions”, Proc. American Helicopter Society, 27th Annual Forum.

Chow, J.S., Zilliac, G.G., Bradshaw, P., 1997, "Mean and Turbulence Measurements in the Near Field of a Wingtip Vortex", AIAA Journal, Vol 35, pp. 1561-1567.

Dacles-Mariani, J., Zilliac, G.G., Chow, J.S., Bradshaw, P., 1995, “Numerical/Experimental Study of a Wingtip Vortex in the Near Field”, AIAA Journal, Vol. 33, No. 9, pp. 1561-1568.

Devenport, W.J., Rife, M.C., Liapis, S.I., Follin, G.J., 1995, "Turbulence Structure and Scaling in Trailing Vortices", 33rd Aerospace Sciences Meeting & Exhibit 9-12 January 1995, Reno, NV. (AIAA Paper 95-0588).

Doane, S., 2010, “ODU Wind Tunnel Flow Quality Measurements”, Personal Contact.

Ferreira, G.C., Brunet, S., Garnier, F., 2002, "Numerical Investigation of Turbulent Mixing in a Jet/Wake Vortex Interaction”, AIAA Journal 40, pp. 276–284.

Gerz, T., Holzäfel, F., Darracq, D., 2002, “Commercial Aircraft Wake Vortices”, Progress in Aerospace Sciences, Vol 38, pp. 181-208.

Green, S.I., Acosta, A.J., 1991, "Unsteady Flow in Trailing Vortices", Journal of Fluid Mechanics, Vol. 227, pp. 107-134.

Greenblatt, D., Vey, S., Paschereit, O.C., Meyer, R., 2009, “Flap Vortex Management Using Active Gurney Flaps”, AIAA Journal, Vol 47(12), pp. 2845-2856.

Hoffman, E.R., Joubert, P.N., 1963, "Turbulent Line Vortices", Journal of Fluid Mechanics, Vol 16, pp. 395-411.

Hoshino, T., Oshima, A., 1987, “Measurement of Flow Field Around Propeller by using a 3-Component Laser Doppler Velocimeter”, Mitsubishi Technical Review 24: 46-53 Method, Japan Society of Naval Architects, Japan.

Huenecke, K., 2002, “From Formation to Decay-Extended-Time Wake Vortex Characteristics of Transport-Type Aircraft”, AIAA Paper 2002-3265.

Huppertz, G., Schröder, W., Klaas, M., 2006 “Engine Jet/Vortex Interaction in the Near Wake of an Airfoil”, 36th AIAA Fluid Dynamics Conference and Exhibit, 5 - 8 June 2006, San Francisco, California, AIAA Paper 2006-3747

Jessup, S.D., 1989, “An Experimental Investigation of Viscous Aspects of Propeller Blade Flow”, Ph.D. Thesis, The Catholic University of America, Washington DC.

Kobayashi, S., 1981, “Experimental Methods for the Prediction of the Effects of Viscosity on Propeller Performance”, Department of Ocean Engineering, Rep. 81-7, MIT.

Landgrebe, A.J., Johnson, B.V., 1974, "Measurement of Model Helicopter Rotor Flow Velocities with a Laser Doppler Velocimeter", Journal of American Helicopter Society, Vol 19, No 3, July.

Margaris, P., Marles, D., Gursul, I., 2008, "Experiments on Jet/Vortex Interaction", Experiments in Fluids, Vol 44, pp. 261–278.

McAlister, K.W., Takshashi, R.K., 1991, "NACA 0012 Wing Pressure and Trailing Vortex Measurements", NASA Technical Paper, p. 3151.

McCormick, B.W., Tangler, J.L., Sherrieb, H.E., 1968, "Structure of Trailing Vortices", Journal of Aircraft, Vol. 5, No. 3, pp. 260-267.

Miake-Lye, R.C., Brown, R.C., Kolb, C.E., 1993, "Plume and Wake Dynamics, Mixing and Chemistry Behind a High Speed Civil Transport Aircraft", Journal of Aircraft, Vol 35, pp. 507–660.

Min, K.S., 1978, "Numerical and Experimental Methods for Prediction of Field Point Velocities around Propeller Blades", Department of Ocean Engineering Report 78–12, MIT.

Montgomery, D.C., 2005, "Design and Analysis of Experiments- 6th Edition", John Wiley & Sons Inc, ISBN: 0-471-48735-X.

Moore, D.W., Saffman, P.G., 1973, "Axial Flow in Laminar Trailing Vortices", Proceedings of the Royal Society of London, Vol. 333, pp. 491-508.

Paoli, R., Laporte, F., Cuenot, B., Poinsot, T., "Dynamics and Mixing in Jet/Vortex Interactions", 2003, Physics of Fluids, Vol 15, pp. 1843–1860.

Paoli, R., Helie, J., Poinsot, T., 2004, “Contrail Formation in Aircraft Wakes”, Journal of Fluid Mechanics, Vol 502, pp. 361–373.

Paoli, R., Garnier, F., 2005, “Interaction of Exhaust Jets and Aircraft Wake Vortices: Small-Scale Dynamics and Potential Microphysical-Chemical Transformations”, C.R. Physique, Vol 6, pp. 525-547.

Prandtl, L., Tietjens, O.K.G., 1957, “Applied Hydro- and Aeromechanics: Based on Lectures of L. Prandtl”, Dover Publications, New York.

Raffel, M., Willert, C.E., Wereley, S.T., Kompenhans, J., 2007, "Particle Image Velocimetry: A Practical Guide- 2^{nd} Edition", Springer Berlin Heidelberg New York, ISBN:978-3-540-63683-0.

Rossow, V.J., 1999, “Lift-Generated Vortex Wakes of Subsonic Transport Aircraft”, Progress in Aerospace Sciences, Vol 35, pp. 507-660.

Schell, I., Ozger, E., Jacob, D., 2000, “Influence of Different Flap Settings on the Wake-Vortex Structure of a Rectangular Wing With Flaps and Means of Alleviation with Wing Fins”, Aerospace Science Technologies, Vol 4, pp. 79-90.

Serafini, J.S., Sullivan, J.P., Neumann, H.E., 1981, “Laser Doppler Flow-Field Measurements of an Advanced Turboprop”, 17th Joint Propulsion Conference, AIAA/SAE/ASME, Colorado Springs, Colorado.

Shekarriz, A., Fu, T.C., Katz, J., Huang, T.T., 1993, “Near Field Behavior of a Tip Vortex”, AIAA Journal, Vol 31, No 1.

Sheldrake, C.D., Ainsworth, R.W., 1995, "The Use of Hot Wires Applied to Aerodynamic Measurements in a Model Turbine Stage", VDI Berichte, No 1186, p. 149.

Spalart, P.R., 1998, “Airplane Trailing Vortices”, Annular Reviews of Fluid Mechanics, Vol 30, pp. 107-138.

Stella, A., Guj, G., 1999, "Propeller Wake Evolution Analysis by LDV", Naval Hydrodynamics 22nd Symposium by Office of Naval Research, Carderock Division Naval Surface Warfare Center, Naval Studies Board and National Research Council.

Stella, A., Guj, G., Felice, F.D., 2000, “Propeller Wake Flow Field Analysis by means of LDV Phase Sampling Techniques”, Experiments in Fluids, Vol 28, pp. 1-10.

Veldhuis, L.L.M., Rentema, D.W.E., 1995, “Quantitative Wake Surveys Behind a Tractor Propeller-Wing Configuration”, AIAA Paper 1995-3908.

Wang, F.Y., Proot, M.J., Charbonnier, J.M., Sforza, P.M., 2000, “Near-Field Interaction of a Jet With Leading-Edge Vortices”, Journal of Aircraft, Vol 37, pp. 779–785.

Wang, F.Y., Zaman, K.B.M.Q., 2002, “Aerodynamics of a Jet in the Vortex Wake of a Wing”, AIAA Journal, Vol 40, pp. 401–407.

Westmoreland, W.S., Tramel, R.W., Barber, J., 2008, “Modeling Propeller Flow Fields using CFD”, AIAA Paper 2008, p. 402.

Westphal, R.V., Mehta, R.D., 1989, “Interaction of an Oscillating Vortex with a Turbulent Boundary Layer”, Experiments in Fluids, Vol. 7(6), pp. 405-411.

APPENDICES

APPENDIX A AIR OPERATIONS

A.1 Air-Drop Operations

An air-drop is a type of air-lift and the main idea of this operation is to resupply inaccessible troops (see Figure A-1). When developed during World War II, air-drops were conducted by pushing small crates with parachutes out of an aircraft's side cargo doors. Nowadays, military cargo aircraft are designed with rear access ramps that allow large platforms to be rolled out the back.

There are two types of airdrops and the type of airdrop refers to the method that the airdrop load descends to the ground:

- **Low-Velocity Airdrop (LVAD)** is the delivery method to ensure the impact the ground with minimal force. It is designed to slow down the delicate equipment and larger items (i.e vehicles) as much as possible.
- **High-Velocity Airdrop (HVAD)** is the delivery method to stabilize the fall of the durable items of the payload. The parachute slows the load to some degree but not to the extent of a LVAD.

The parachutes are attached to the load in the LVAD to slow the descent such that the impact velocity should be less than 28.5 ft/sec and the load is extracted from the military cargo aircraft at approximately 140-150 knots (from different types of cargo aircraft such as CN-235, C-160, C-130, etc.) and the parachutes extracted at an altitude of 700 feet or more. According to the limitations of LVAD, the minimum airdrop altitude for heavy equipment is 750 feet. If the airdrop altitude is reduced below the limitations, then the accuracy of the aerial delivery is decreased as well.

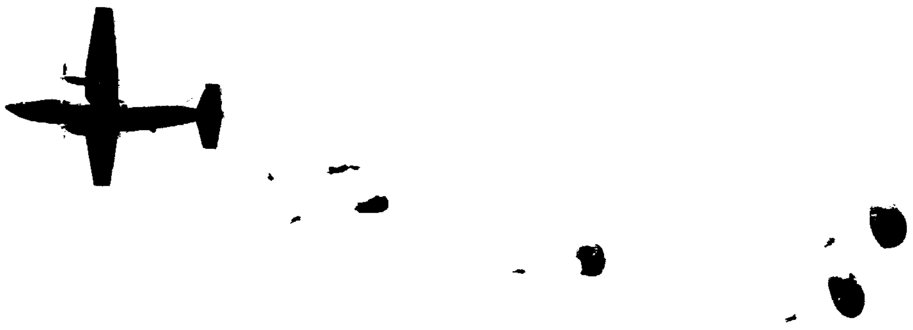

Figure A-1: Air-Drop Operations

A.2 Air-Refueling Operations

Aerial refueling, also called air-refueling, in-flight refueling (IFR), air-to-air refueling (AAR) or tanking, is the process of transferring fuel from the tanker aircraft to the receiver aircraft during flight. This procedure allows the receiving aircraft to remain airborne longer and to extend its range. The two main refueling systems are probe and drogue, which is simpler to adapt to existing aircraft, and the flying boom, which offers greater fuel transfer capacity, but requires a dedicated operator station and specially designed receiving receptacle. There is also a combination "boom drogue adaptor" that combines the first two methods. Usually, the aircraft providing the fuel is specially designed for the task, although refueling pods can be fitted to existing aircraft designs if the "probe and drogue" system is to be used.

A.2.1 Flying Boom Operation

This system uses a rigid, telescoping tube controlled by two small wings that an operator on the tanker aircraft extends and inserts into a receptacle on the receiving aircraft (see Figure A-2). In practice, the pilot of the aircraft being refueled must position the aircraft so that the boom can be engaged, using visual references, including lights used during night refueling. All boom-equipped tankers (i.e. KC-135 Stratotanker, KC-10 Extender), have a single boom, and can refuel one aircraft at a time with this mechanism.

The flying boom is attached to the rear of the tanker aircraft. The attachment is flexible, allowing boom movement up to 25 degrees left or right, and from flush with the bottom of the aircraft up to 50 degrees below horizontal.

A pair of aerodynamic control surfaces which is called "ruddevators" allow precise two dimensional positioning (left/right and up/down) of the boom which is mounted on the outer structural portion of the boom. They are actuated hydraulically and controlled by the system operator using a control stick. Additionally, the system operator may hydraulically extend and retract the inner fuel tube using a lever to position the boom nozzle in the third dimension (fore/aft).

To complete an aerial refueling, the pilot of the receiver aircraft begins by flying formation in the "precontact" position, a position directly below and approximately 50 feet behind the boom nozzle. The boom is flown in the "trail" position at 30 degrees below horizontal, on the tanker's centerline with the nozzle extended 10 feet. The receiver may be slightly left or right of centerline depending on operational guidance or receptacle installation. When cleared, the receiver pilot moves forward aided with either radio or visual commands from the boom operator.

Figure A-2: Air-Refueling Operation (Flying Boom)

A.2.2 Probe and Drogue Operation

This refueling method (see Figure A-3) employs a flexible hose that trails from the tanker aircraft. The drogue (sometimes called a basket) is attached at its narrow end with a valve to a flexible hose. The drogue stabilizes the hose in flight and provides a funnel to aid insertion of the receiver aircraft probe into the hose. The receiver has a probe, which is a rigid arm placed on the aircraft's nose or fuselage. This probe is often retracted when not in use, particularly on high speed aircraft. At the end of the probe is a valve that is closed until it mates with the drogue, after which it opens and allows fuel to pass from tanker to receiver. A standard probe system used by NATO member countries incorporates shear rivets that attach the refueling valve to the end of the probe. If a large side-load or up-and-down load develops while in contact with the drogue, the rivets shear and the fuel valve breaks off rather than the probe or receiver aircraft suffer structural damages. A "broken probe" (actually a broken fuel valve) happen if poor flying technique is used by the receiver pilot, or in turbulence.

Figure A-3: Air-Refueling Operation (Probe and Drogue)

APPENDIX B THEORY OF HOTWIRE AND CALIBRATION DATA

B.1 Theory of Operation

Fundamentally, a hot wire makes use of the principle of heat transfer from a heated surface being dependent upon the flow conditions passing over it. The mode of operation used in this study was Constant Temperature Anemometry (CTA), since it is widely available, is simple to use, and has a high frequency response. To maintain the wire at a constant temperature a feedback circuit is used (see Figure B-1). The hotwire, shown between C and D, forms part of a Wheatstone bridge, such that the wire resistance is kept constant over the bandwidth of the feedback loop. The output voltage is measured since the hotwire voltage is a simple potential division of the output voltage. Since the circuit response is dependent upon the individual hotwire, the feedback circuit must be tuned for each hotwire.

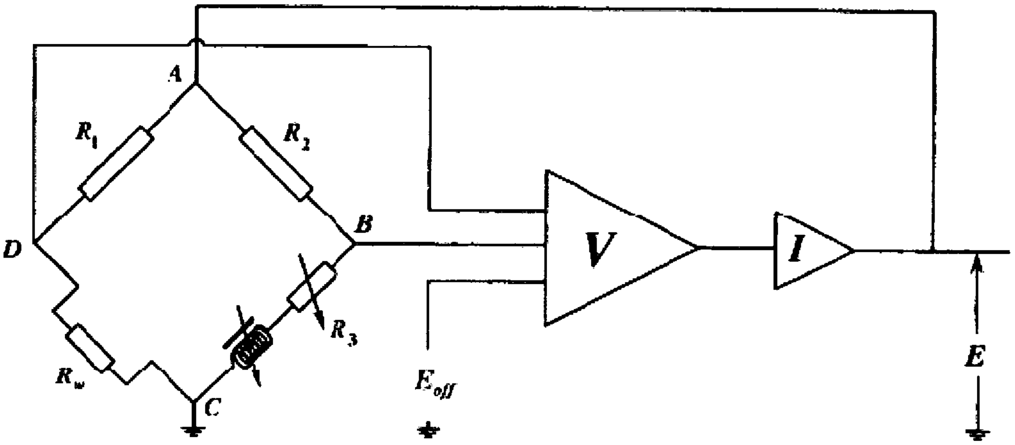

Figure B-1: Schematic of a Constant Temperature Anemometer (Sheldrake, 1995)

B.1.1 Governing Equations

Heat transfer equation for a cylinder is as given in Equation B.1:

$$\varphi = h_c A (T_m - T_a) \qquad \text{(B.1)}$$

Since the wire is basically a cylinder, area of the wire can be calculated using the equation given in Equation B.2:

$$A = \pi d(2L) \quad \text{(B.2)}$$

Defining the Nusselt number as given in Equation B.3:

$$Nu = \frac{h_c d}{k_f} \quad \text{(B.3)}$$

The heat transfer equation becomes (see Equation B.4):

$$\varphi = Nu(2\pi L)k_f(T_m - T_a) \quad \text{(B.4)}$$

Now the heat transfer equation is composed of constants or known parameters except for Nu. The Nusselt number given in Equation B.6 is a function of many parameters (see Equations B.6 and B.7):

$$Nu = f(Re, Pr, \alpha_1, Gr, M, \gamma, a_T \frac{L}{d}, k_m, k_a) \quad \text{(B.5)}$$

where

$$M = f(V, T) \quad \text{(B.6)}$$

$$Re = f(V, \rho, T) \quad \text{(B.7)}$$

The equation for Nusselt number can be simplified (see Equation B.8) by making these assumptions; choosing a fixed geometry, negating natural convection, assuming Pr and γ are constant:

$$Nu = f(Re, \alpha_1, M, a_T) \quad \text{(B.8)}$$

Minimizing the effect of a_T by holding it constant, and using a low Mach number, the Nusselt number becomes (see Equation B.9):

$$Nu = A' + B'\sqrt{Re} \quad \text{(B.9)}$$

This pioneering experimental and theoretical work was done by King (see details in Bruun (1995)). Combining these equations under the assumptions yields Equation B.10:

$$I^2 R_m \propto \left(K + \left(A + \mathrm{B}\sqrt{V}\right)\right)(R_m - R_a) \quad \text{(B.10)}$$

$I, R_m, and\, V$ are the three variables, for a given sensor resistance R_m. This equation is called "King's Law". A and B constants are usually found by calibration (see Equation B.11):

$$I^2 \propto A''' + B'''\sqrt{V} \qquad \text{(B.11)}$$

B.1.2 Hotwire Modes of Operation

There are three modes of operation for hotwire measurements. These are constant current (CC), constant temperature (CT) and constant voltage (CV). During constant current operation mode current is fixed and R_m is allowed to vary with velocity. In the constant voltage mode, voltage is fixed and R_m and current is allowed to vary with velocity. During the experiments constant temperature mode was used. In this mode R_m is fixed and current is allowed to vary with velocity. This mode is the most popular and commercially available system.

B.1.3 Temperature Correction

When the ambient temperature of the fluid changes during the experiments; the voltages acquired from the wires should be corrected using the equation given below:

$$V_{corrected} = \left[\frac{(T_m - T_{a1})}{(T_m - T_{a2})}\right]^2 V_{raw} \quad \text{(B.12)}$$

where

T_m : Constant temperature of the wires for CT operation

T_{a1} : Average ambient temperature during experiment

T_{a2} : Average ambient temperature during calibration

B.2 Calibration of X-Wire

King's Law was used for calibrating the X-wire probes. Measurements made in the free stream for different velocity magnitudes, and constants A and B were calculated using the linear curves. Calibration data for x-wire probes used in the experiments are shown in Figures B-2 and B-3.

An X-wire probe can be used to measure the three components of the velocity (U, V, and W). Since the probe was mounted to the probe holder such that the wires had a 45 degree angle with the horizontal axis of the wind tunnel, the voltages can be used to calculate the U and V components, as shown in Figure B-4. If the probe is rotated 90 degrees so that the wires had a 45 degree angle with the vertical axis, the U and W components can be calculated. Assuming that the "V_A" is the velocity measured from the wire 1, the "V_B" is from the wire 2.

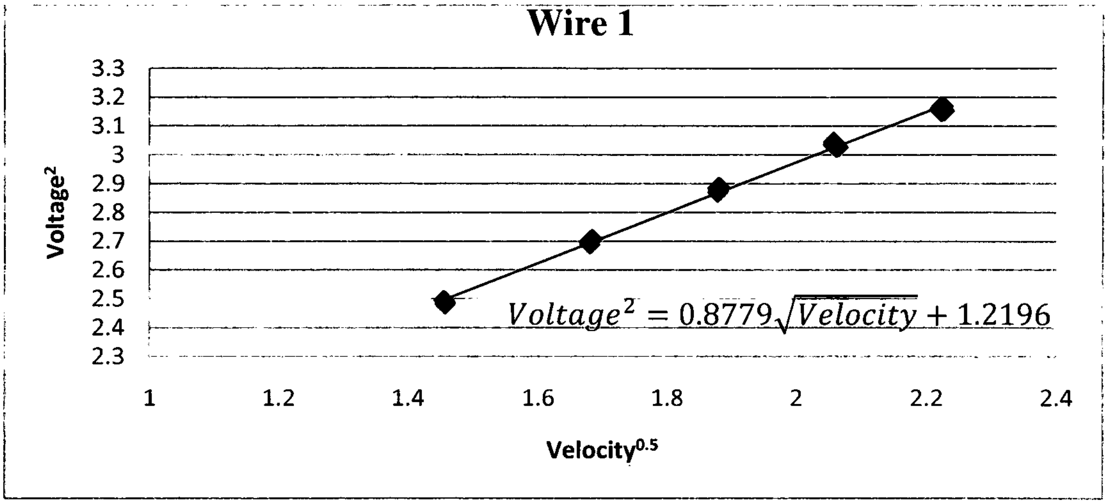

Figure B-2: Calibration Data for Wire 1 (R^2=0.9984)

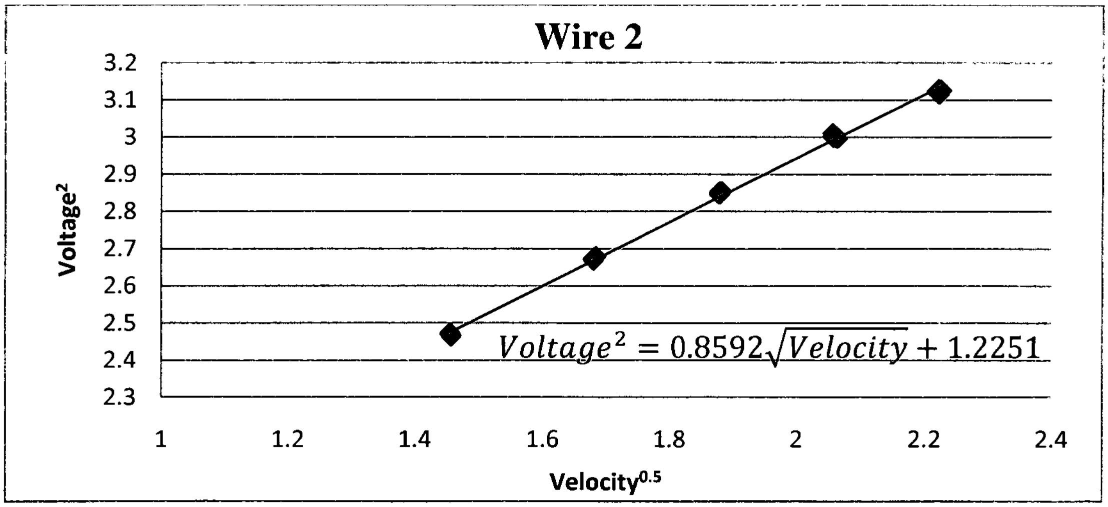

Figure B-3: Calibration Data for Wire 2 (R^2=0.9972)

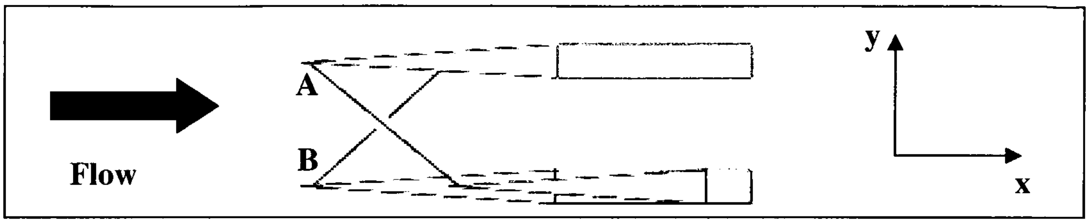

Figure B-4: Schematic Projection of X-Wire

The velocities can be found using Equations B.13 and B.14:

$$\bar{U} = \frac{1}{\sqrt{2}}(\overline{V_A} + \overline{V_B}) \qquad \text{(B.13)}$$

$$\bar{V} = \frac{1}{\sqrt{2}}(\overline{V_B} - \overline{V_A}) \qquad \text{(B.14)}$$

APPENDIX C ANALYSES OF THE OTHER REGRESSION MODELS

C.1 Flap Vortex Horizontal Motion (FVY)

A normal percentage probability plot versus internally studentized residuals given in Figure C-1 shows a trend such that the residuals lie almost along a straight line which means that the distribution residuals is normal while very slight deflections do not create any problem (just that residuals at extremes are not as large as expected from normal distribution). The plot of the residuals for predicted versus actual given in Figure C-2 and the plot of internally studentized residuals versus predicted response given in Figure C-3 do not indicate any structure (i.e funnel shape for the residuals of predicted versus actual). The graphics showing the internally studentized residuals versus run and the four main factors given through Figures C-4 to C-8 verify that the residuals are independently distributed, while no outlier or any correlation between the residuals and any factor exist. The Box Cox plot given in Figure C-9 has recommended a power-law transformation to equalize the variance and increase the R-squared terms for better fitting of the model. The transformation is as $(FVY+5.40367)^{1.88}$ and it should be noted that the new transformed response will be used in regression models.

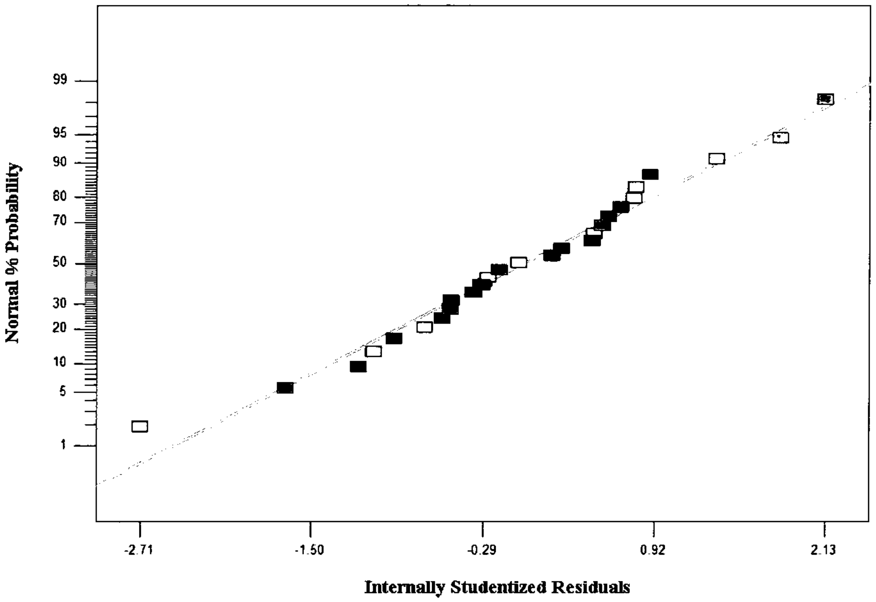

Figure C-1:Normal Probability Plot of Residuals of FVY

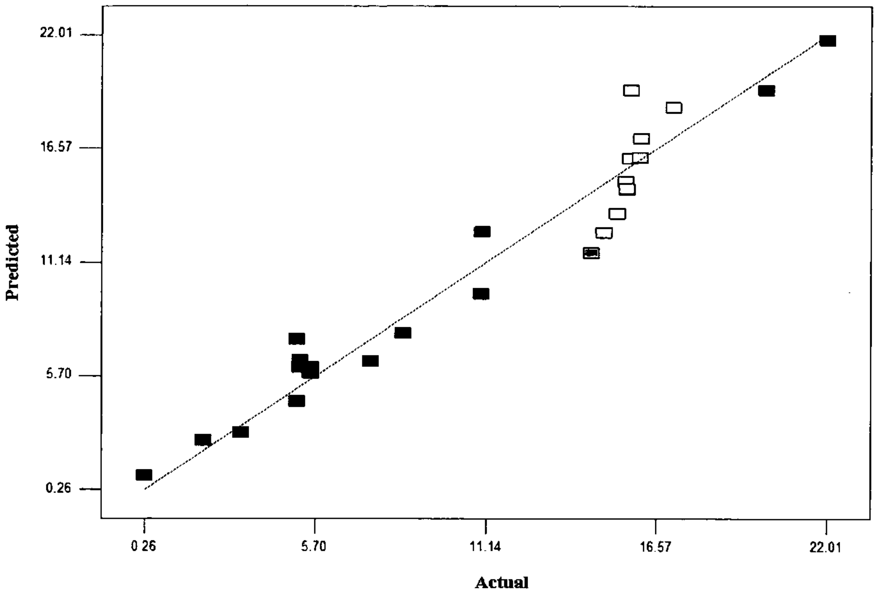

Figure C-2: Plot of Residuals for Predicted versus Actual FVY

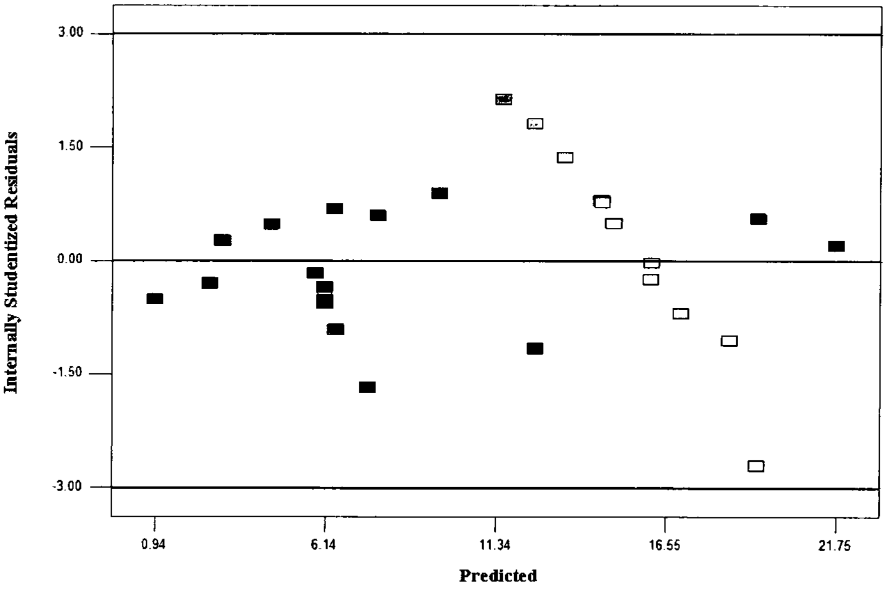

Figure C-3: Plot of Internally Studentized Residuals versus Predicted FVY

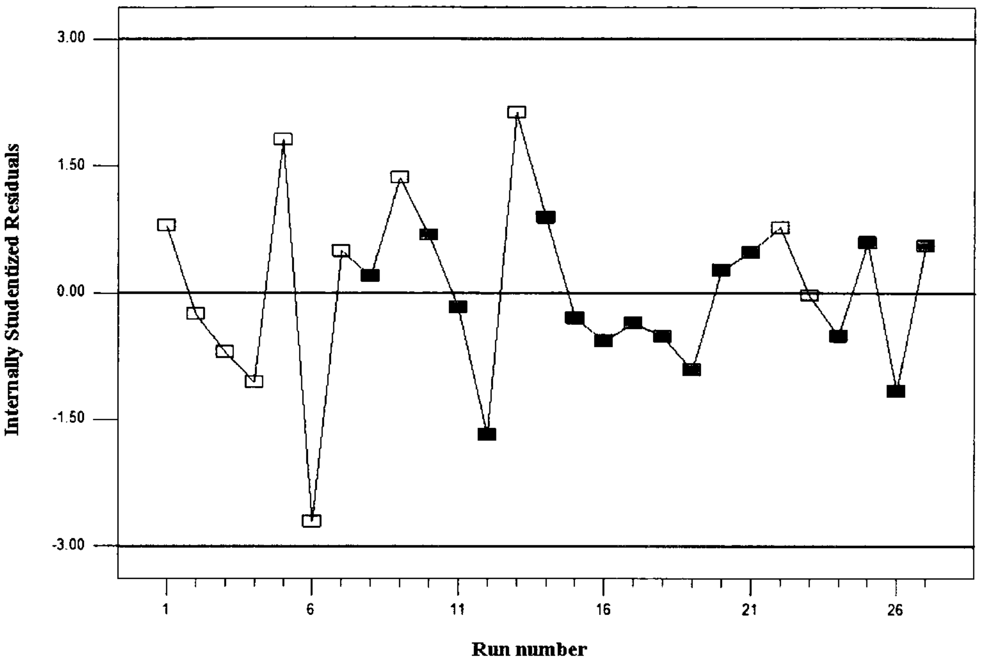

Figure C-4: Plot of Internally Studentized Residuals versus Run Number for FVY

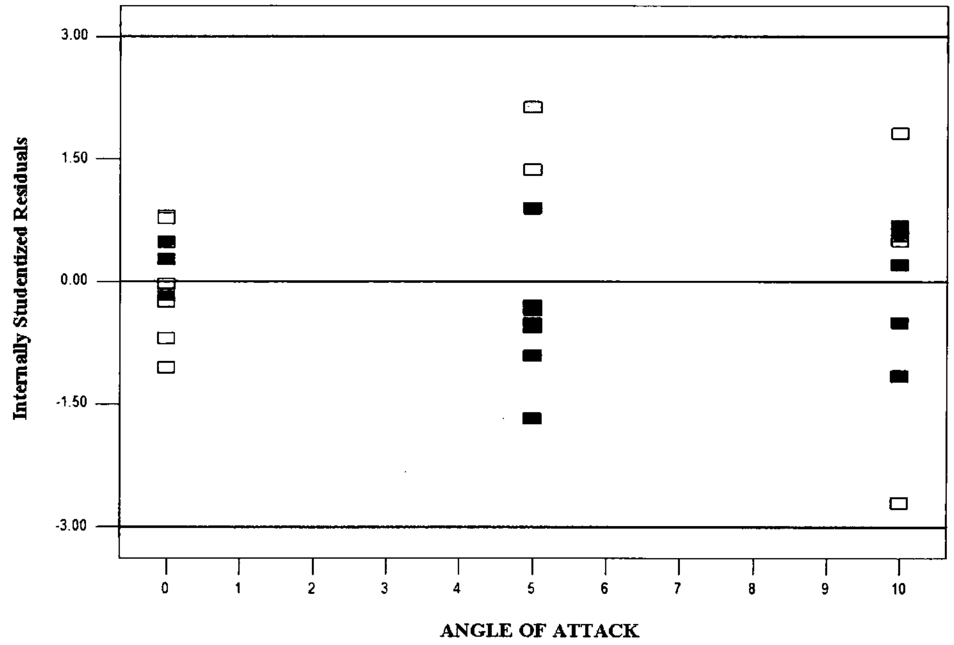

Figure C-5: Plot of Internally Studentized Residuals versus Angle of Attack for FVY

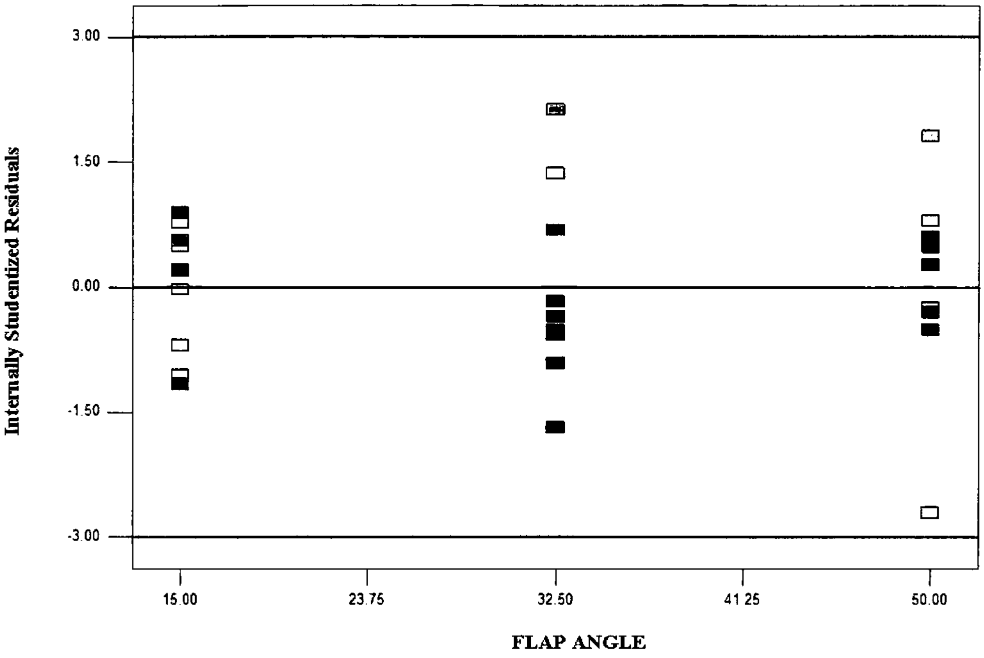

Figure C-6: Plot of Internally Studentized Residuals versus Flap Angle for FVY

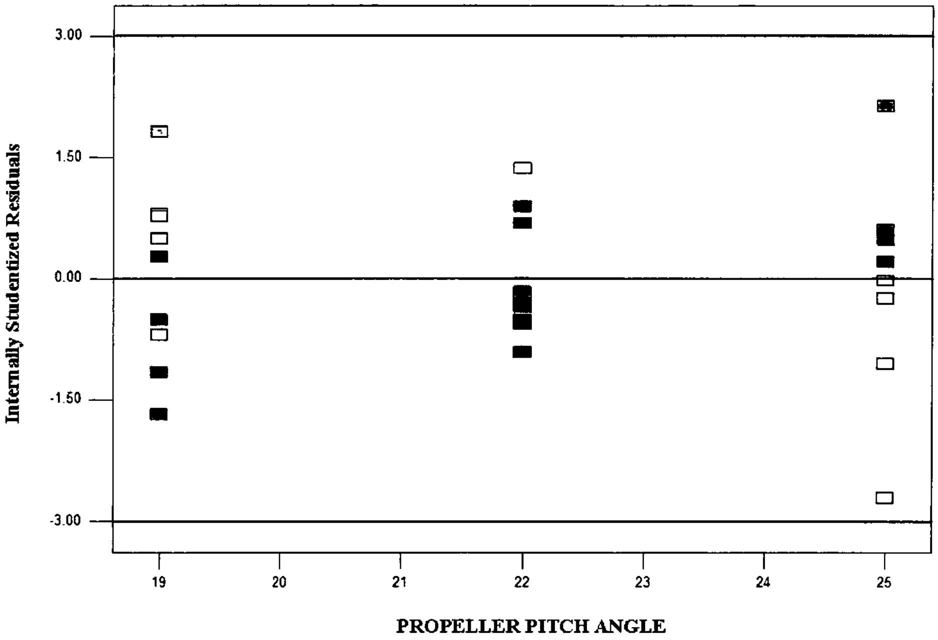

Figure C-7: Plot of Internally Studentized Residuals versus Propeller Pitch Angle for FVY

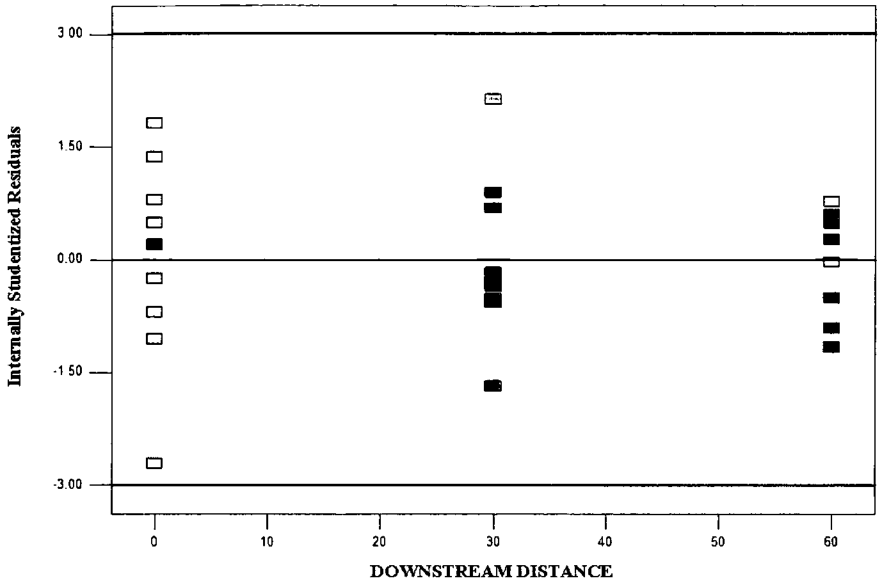

Figure C-8: Plot of Internally Studentized Residuals versus Downstream Distance for FVY

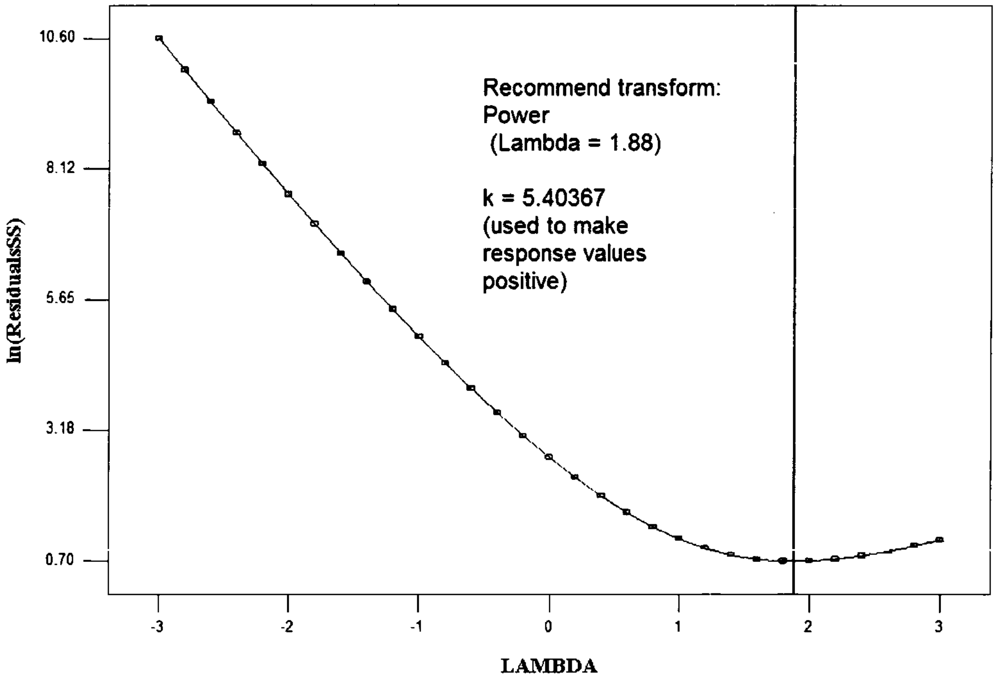

Figure C-9: Box Cox Plot for FVY

C.2 Wing Tip Vortex Horizontal Motion (WTVY)

Through the analyses made for checking the distribution of residuals (whether or not they are normally and independently distributed) the normality check is the first that should be applied by plotting normal percentage probability versus internally studentized residuals, as given in Figure C-10. This graph shows that the scattering of the residuals are in such that the residuals are lying along a straight line which indicates that residuals are normally distributed. The plot of the residuals for predicted versus actual is given in Figure C-11 and the plot of internally studentized residuals versus predicted response given in Figure C-12 are structureless. The graphics given in Figure C-13 for the internally studentized residuals versus run shows that the residuals are independently distributed which is favorable while the plots of residuals versus four main factors given through Figures C-14 to C-17 verify that there is no outlier or correlation between the residuals and any factor under estimation. In addition to these analyses, the Box Cox plot given in Figure C-18 plot does not recommend any transformation.

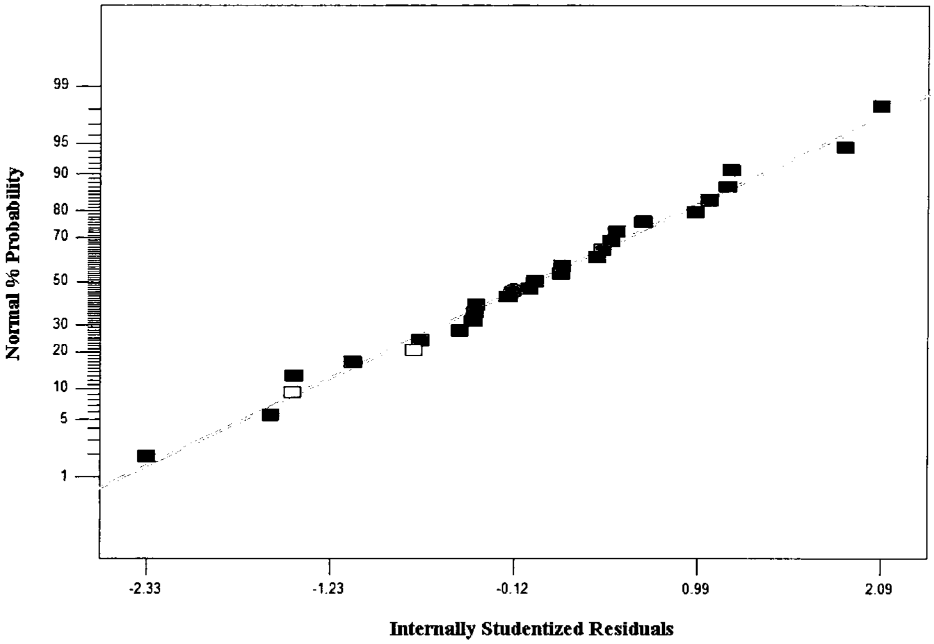

Figure C-10: Normal Probability Plot of Residuals of WTVY

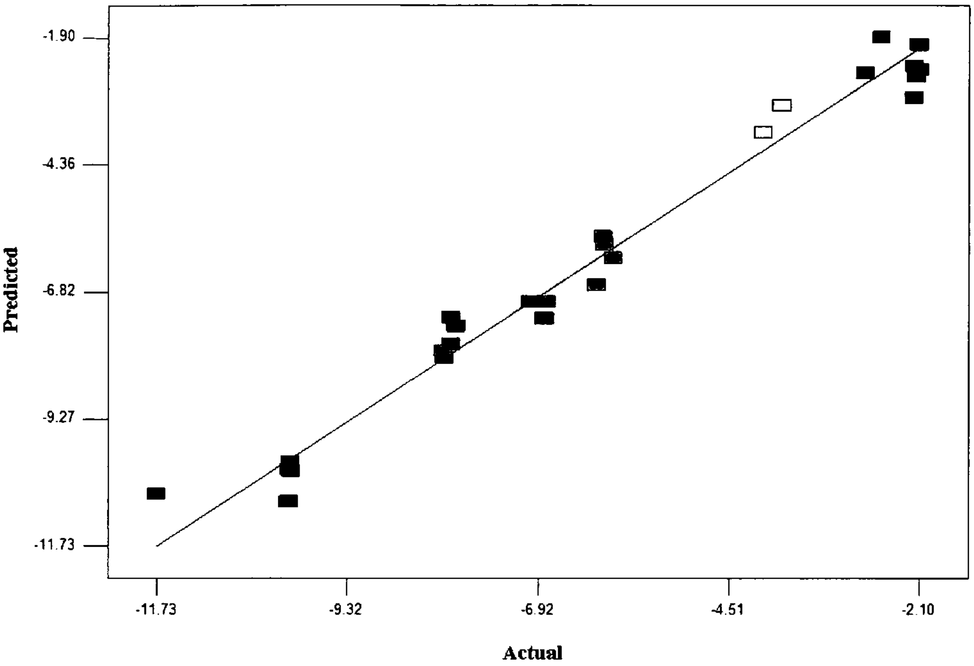

Figure C-11: Plot of Residuals for Predicted versus Actual WTVY

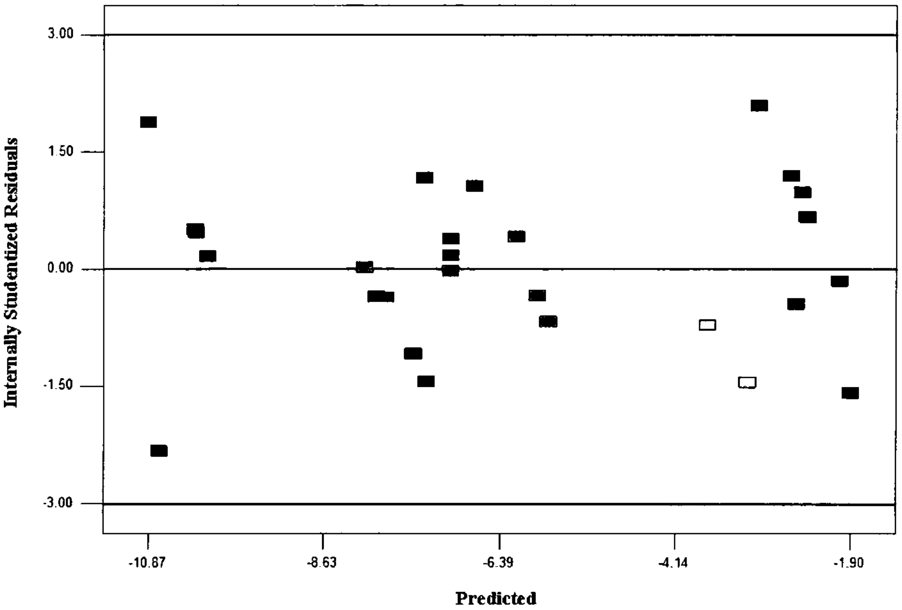

Figure C-12: Plot of Internally Studentized Residuals versus Predicted WTVY

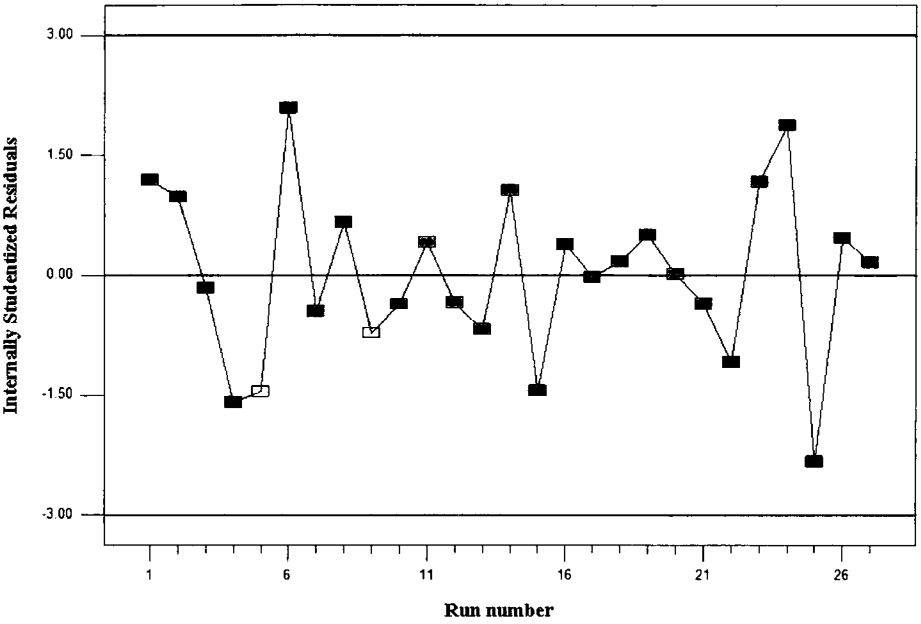

Figure C-13: Plot of Internally Studentized Residuals versus Run Number for WTVY

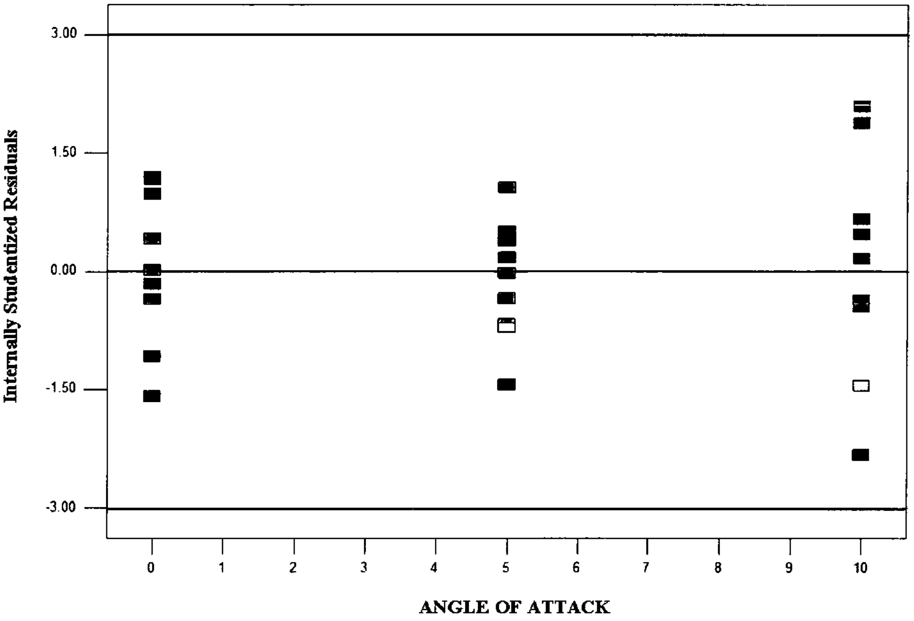

Figure C-14: Plot of Internally Studentized Residuals versus Angle of Attack for WTVY

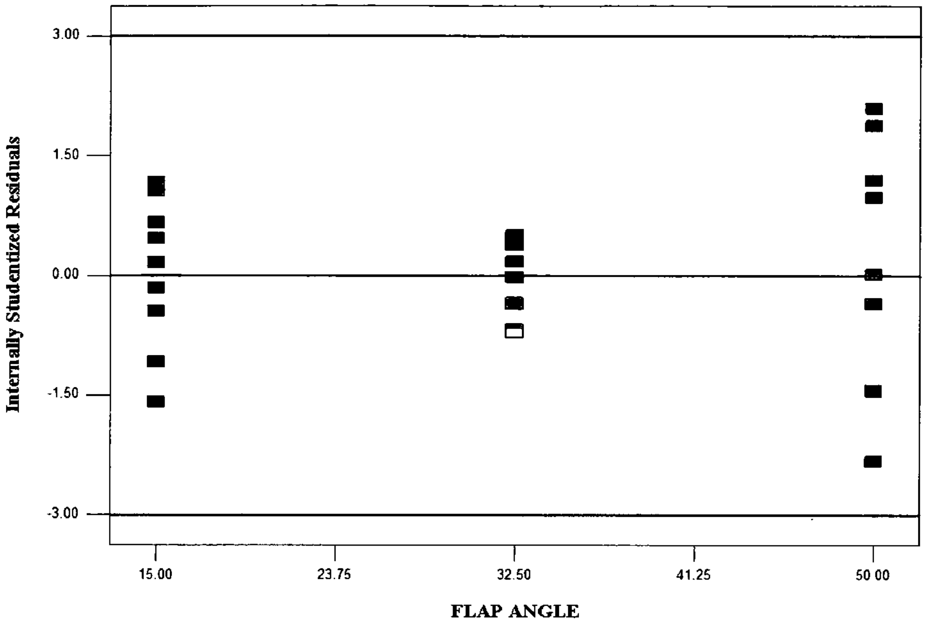

Figure C-15: Plot of Internally Studentized Residuals versus Flap Angle for WTVY

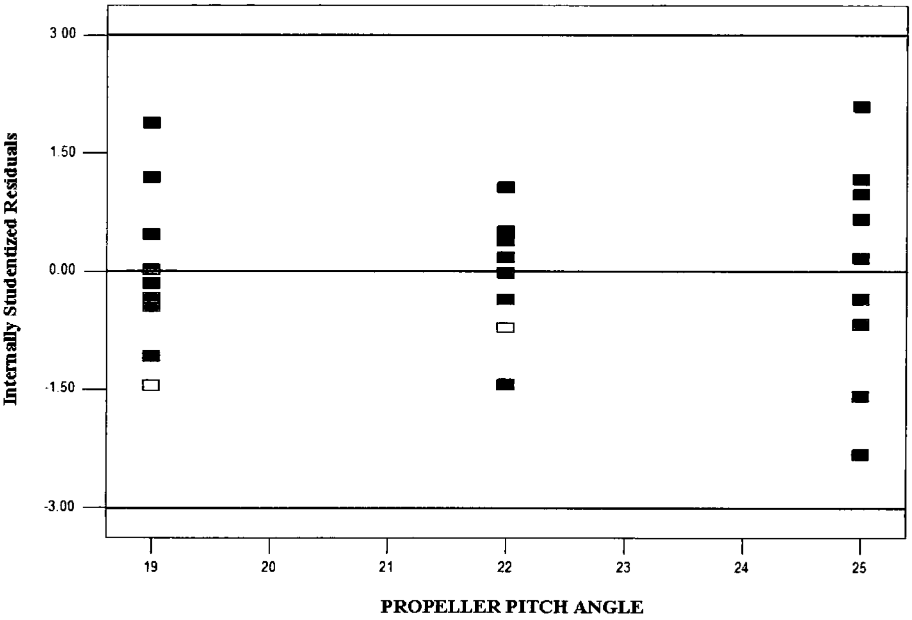

Figure C-16: Plot of Internally Studentized Residuals versus Propeller Pitch Angle for WTVY

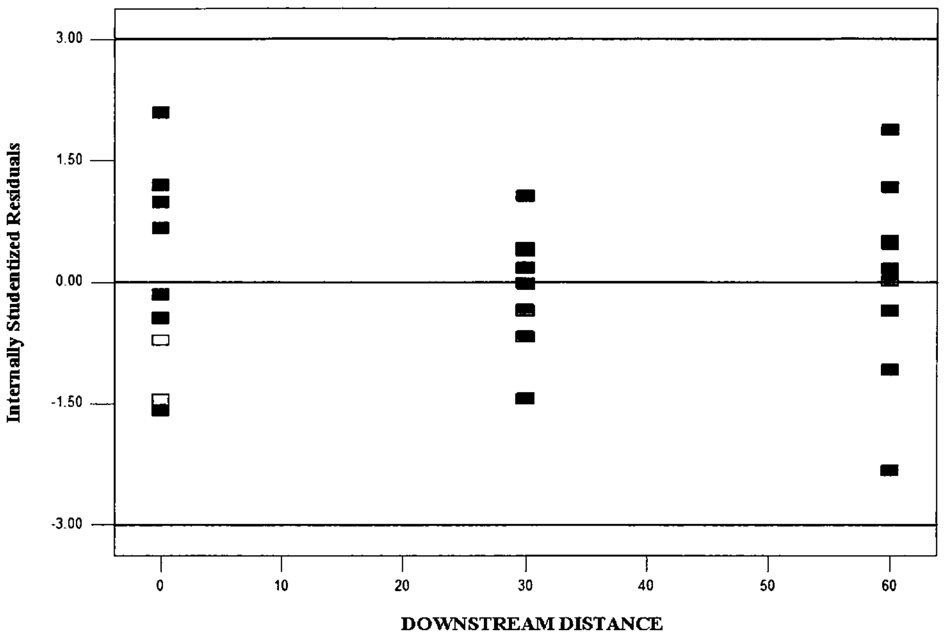

Figure C-17: Plot of Internally Studentized Residuals versus Downstream Distance for WTVY

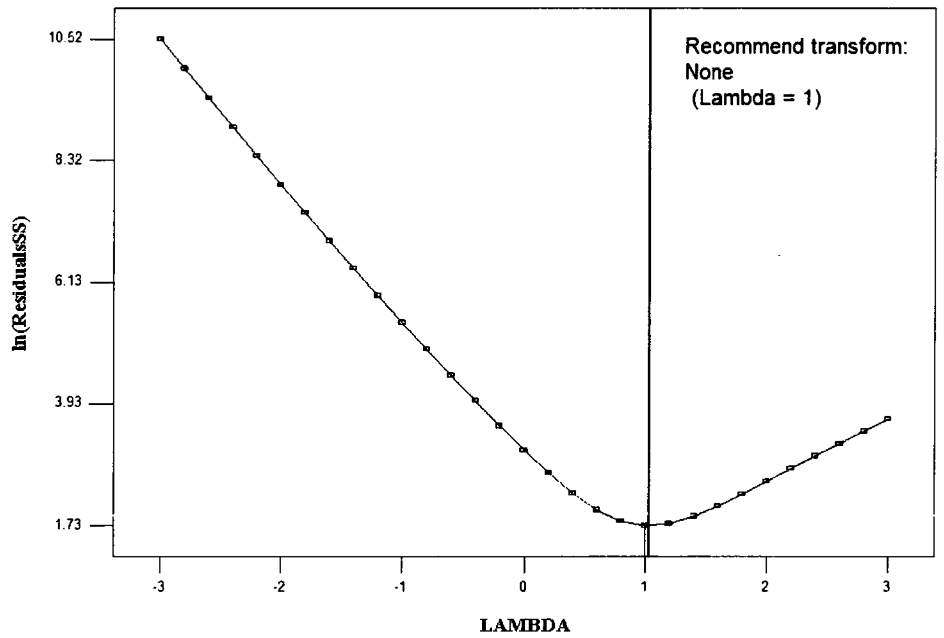

Figure C-18: Box Cox Plot for WTVY

C.3 Shortest Distance Between Vortices (SDBV)

The model adequacy check performed by normality check revealed that mostly the residuals are normally distributed although very slight deflections at both central and tail parts of the plots are observed in Figure C-19. Actually, the scattering at the central part of the plot is important compared to the tails as the deflection at tails means that residuals at extremes are not as large as expected (the value of large residuals are not as expected from a normal distribution) while the slight deflection at the central part means that the shape of distribution of residuals indicate a distribution similar to normal distribution but a broader and shallower one. The plot of the residuals for predicted versus actual given in Figure C-20 and the plot of internally studentized residuals versus predicted response given in Figure C-21 do not indicate any structure. The graphics in Figure C-22 showing the internally studentized residuals versus run verifies that the residual distribution independent and the plots of residuals versus four main factors given through Figures C-23 to C-26 indicate slight coning but this structure does not create a serious concern, and it can be concluded that no outlier or any correlation between the residuals and any factor exist. Figure C-27 showing the Box Cox plot does not recommend any transformation since the variance seems to be constant.

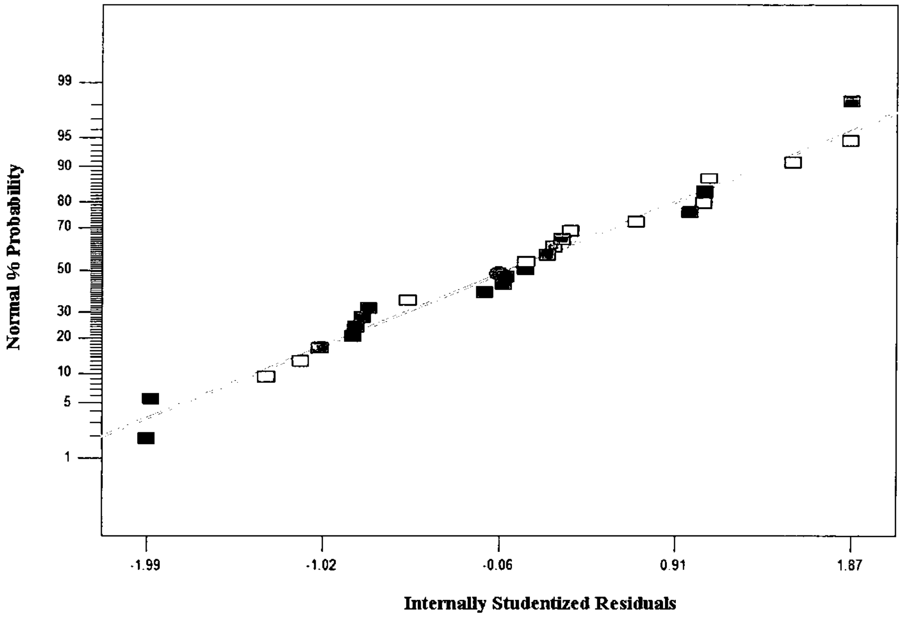

Figure C-19: Normal Probability Plot of Residuals of SDBV

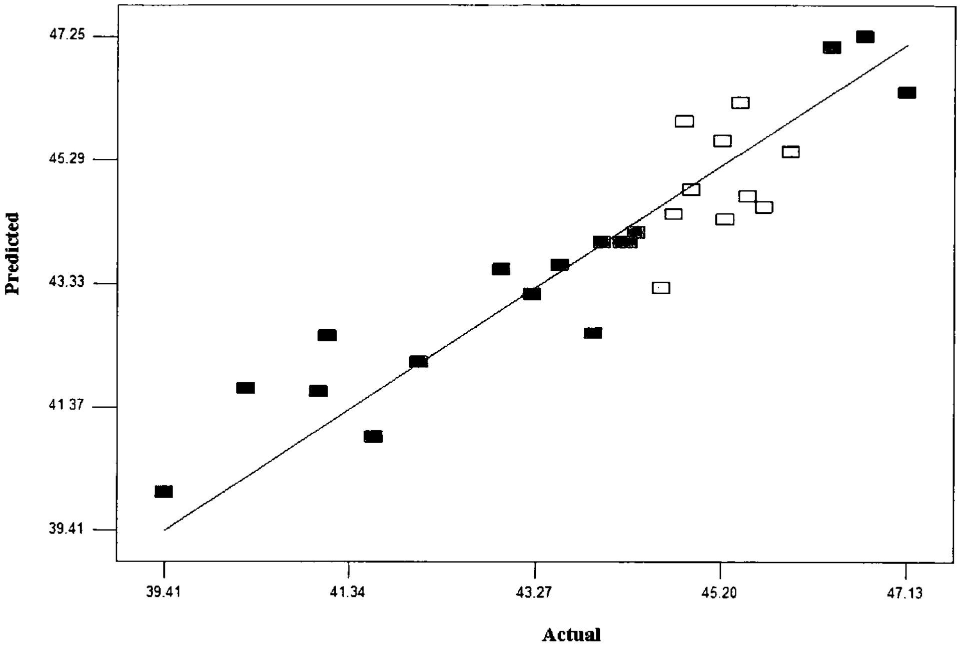

Figure C-20: Plot of Residuals for Predicted versus Actual SDBV

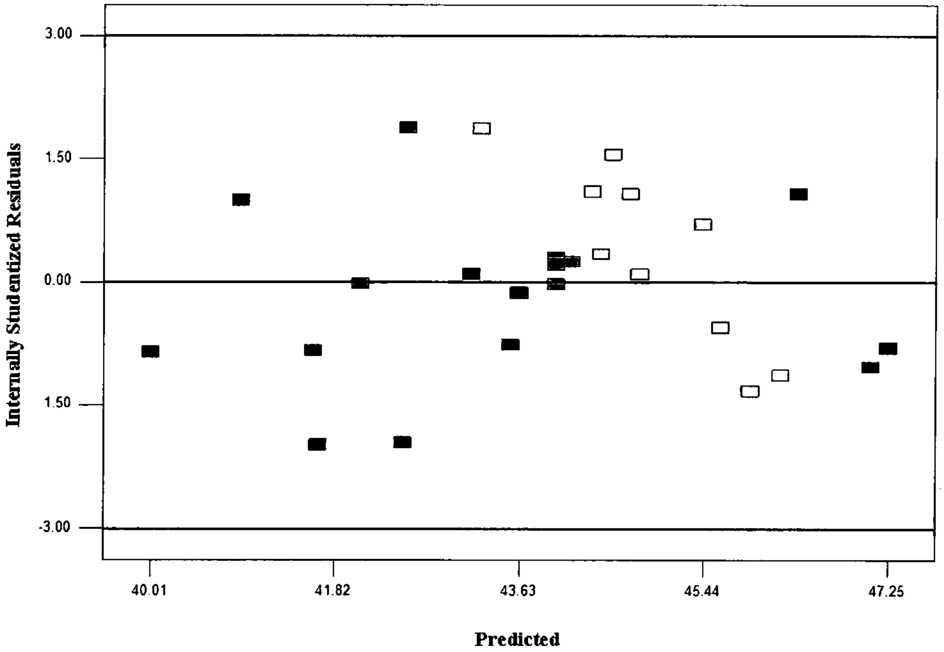

Figure C-21: Plot of Internally Studentized Residuals versus Predicted SDBV

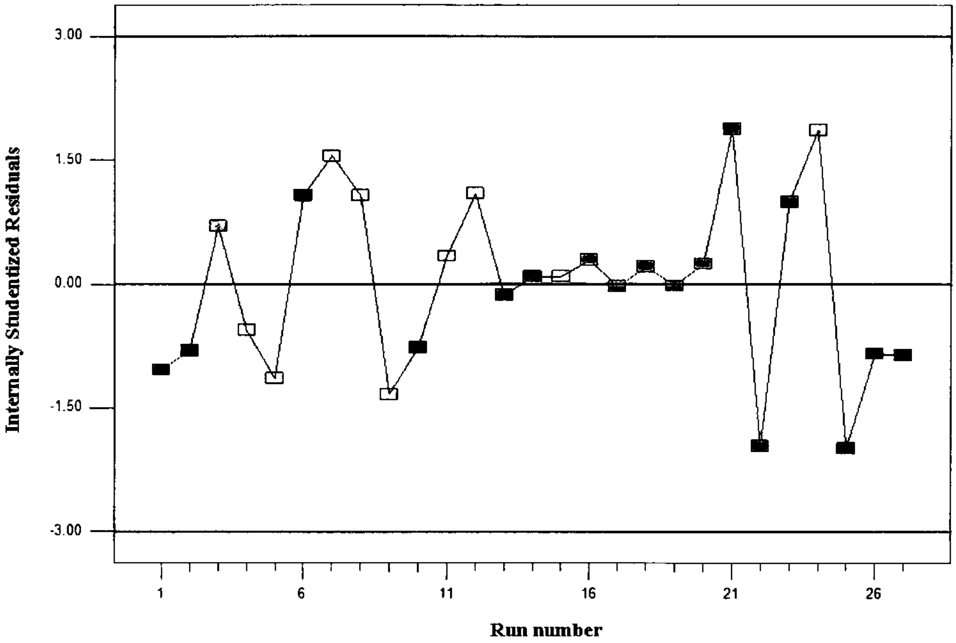

Figure C-22: Plot of Internally Studentized Residuals versus Run Number for SDBV

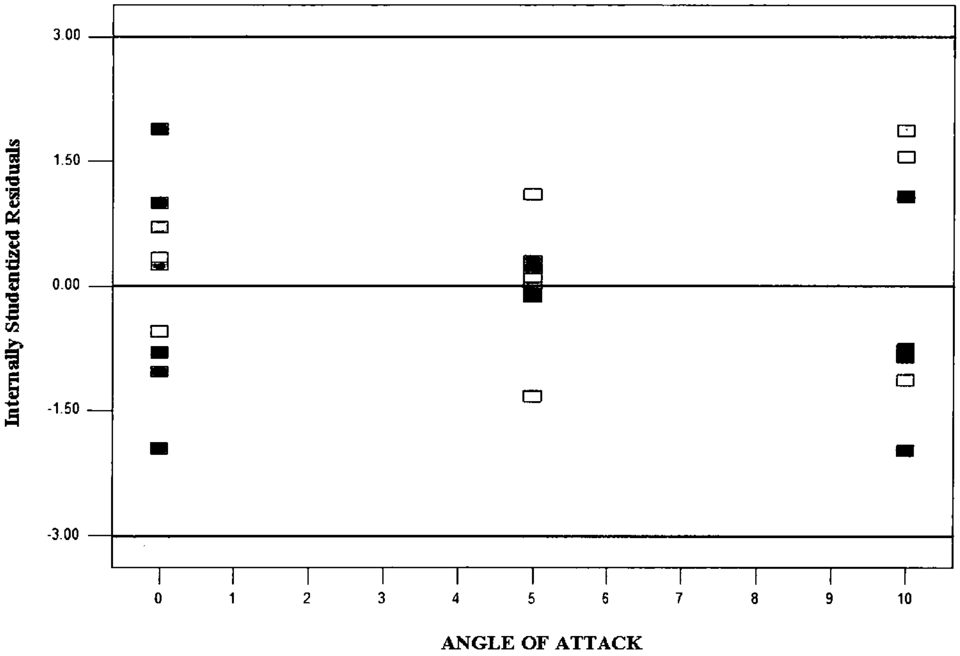

Figure C-23: Plot of Internally Studentized Residuals versus Angle of Attack for SDBV

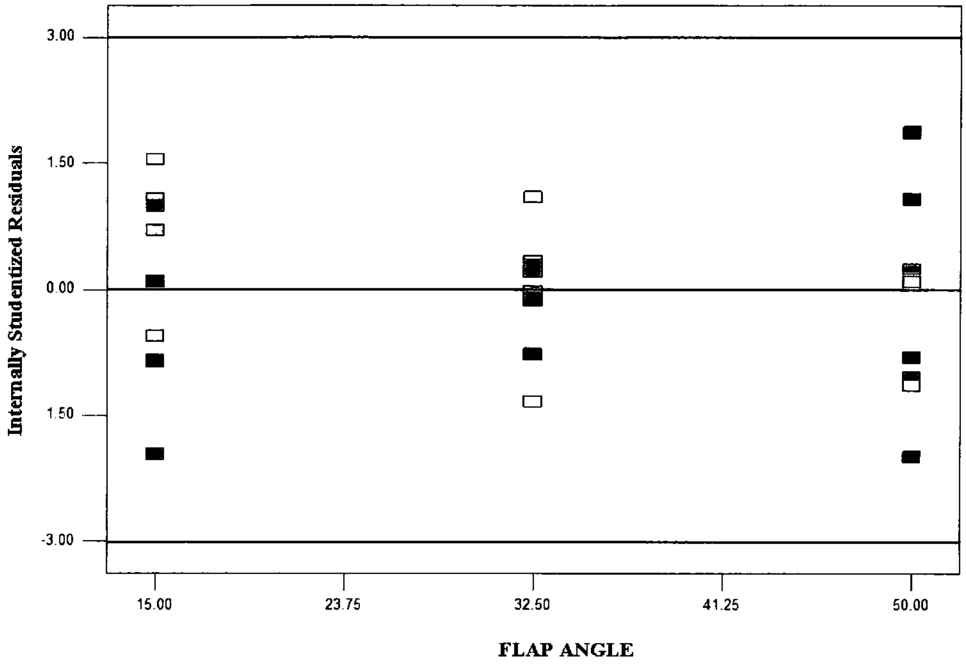

Figure C-24: Plot of Internally Studentized Residuals versus Flap Angle for SDBV

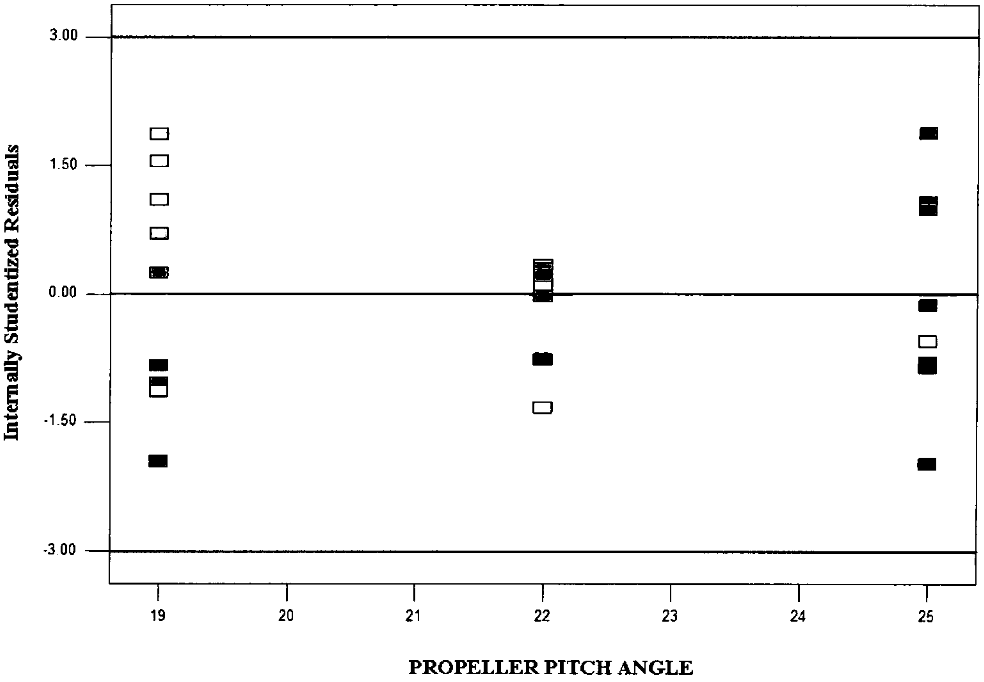

Figure C-25: Plot of Internally Studentized Residuals versus Propeller Pitch Angle for SDBV

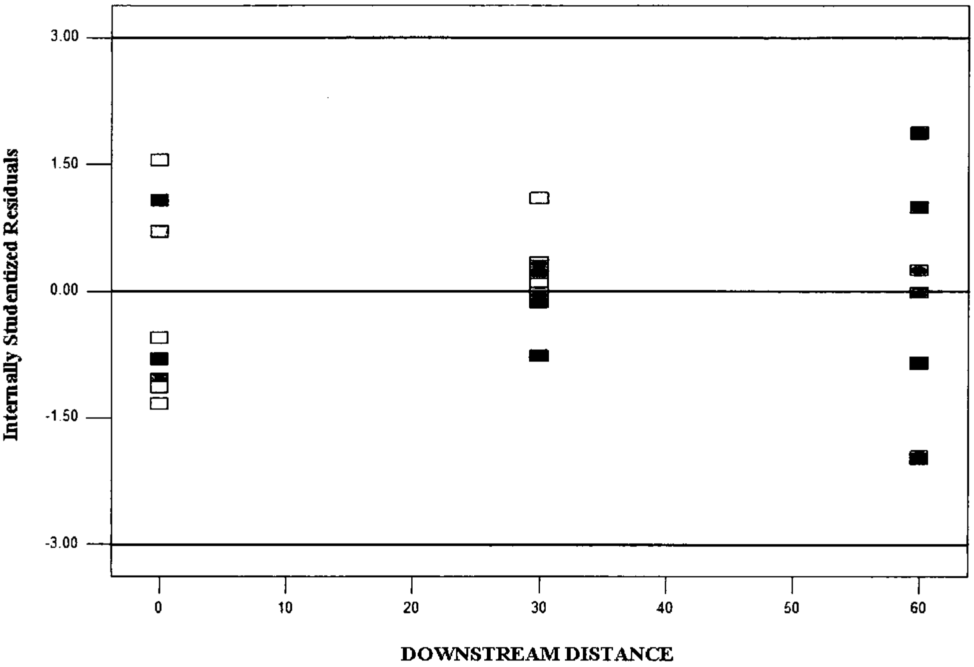

Figure C-26: Plot of Internally Studentized Residuals versus Downstream Distance for SDBV

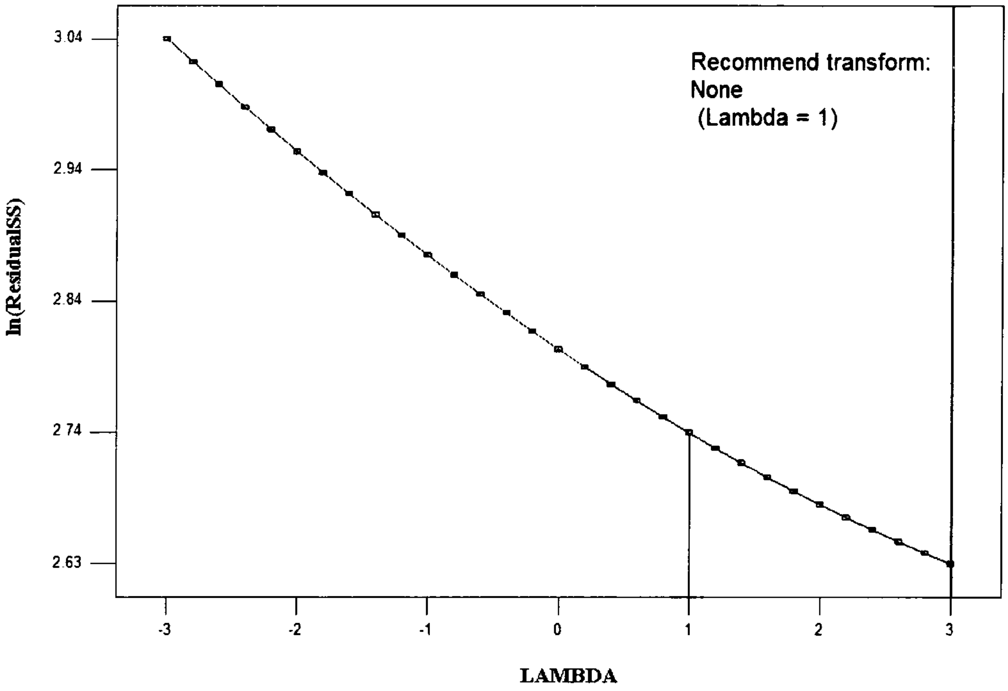

Figure C-27: Box Cox Plot for SDBV

C.4 Flap Vortex Vorticity Strength (FVVS)

Figure C-28 given below shows the normal percentage probability plot versus internally studentized residuals. The scattering of the residuals along the line shows a slight snaking trend around the central part and the left tail which means that the residuals distribution looks quite similar to the normal distribution while the shape is a bit broader and shallower since the smallest residuals are not as small as expected from the normal distribution. The general plot shows that there is no serious problem with the normality check of the residuals. The plot of the residuals for predicted versus actual given in Figure C-29 and the plot of internally studentized residuals versus predicted response given in Figure C-30 do not indicate any structure. The graphics showing the internally studentized residuals versus run in Figure C- 31 and the four main factors given through Figures C-32 to C-35 verify that the residuals are independently distributed, while no outlier or any correlation between the residuals and any factor exist, although a very slight coning is observed in the residuals versus angle of attack graph. The Box Cox plot in Figure C-36 recommends a power-law transformation to equalize the variance and increase the R-squared terms for better fitting of the model. The new response in the regression models is the transformed response $(FVY+4.5859)^{2.32}$.

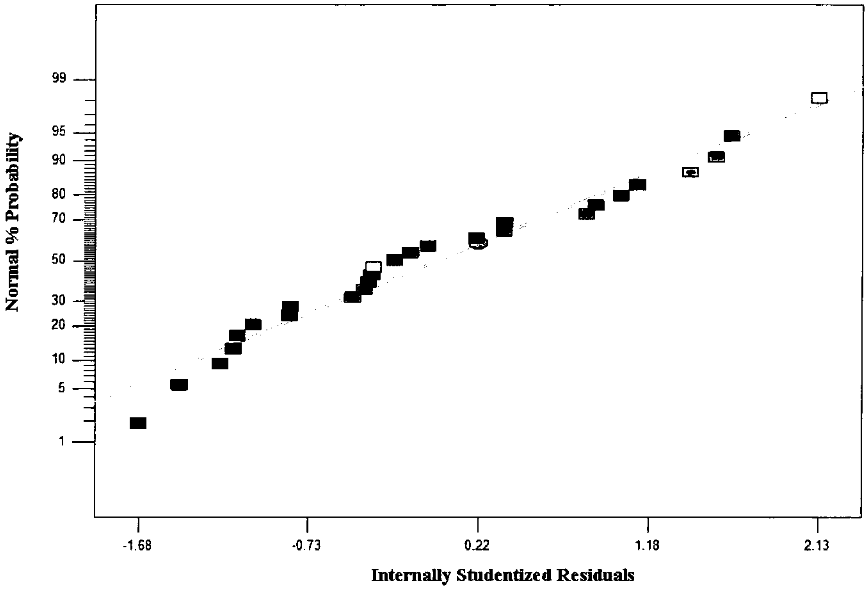

Figure C-28: Normal Probability Plot of Residuals of FVVS

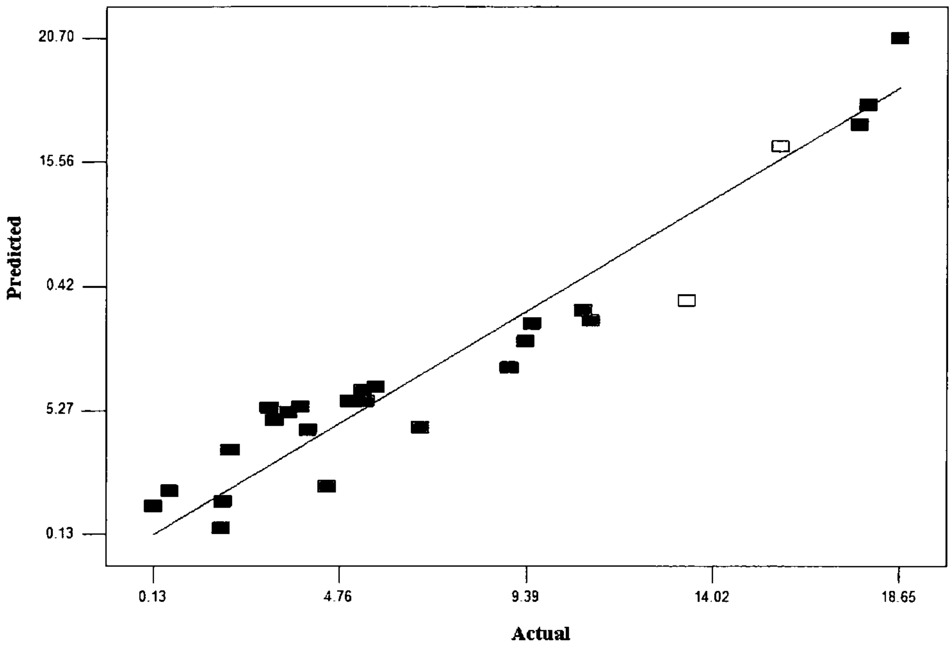

Figure C-29: Plot of Residuals for Predicted versus Actual FVVS

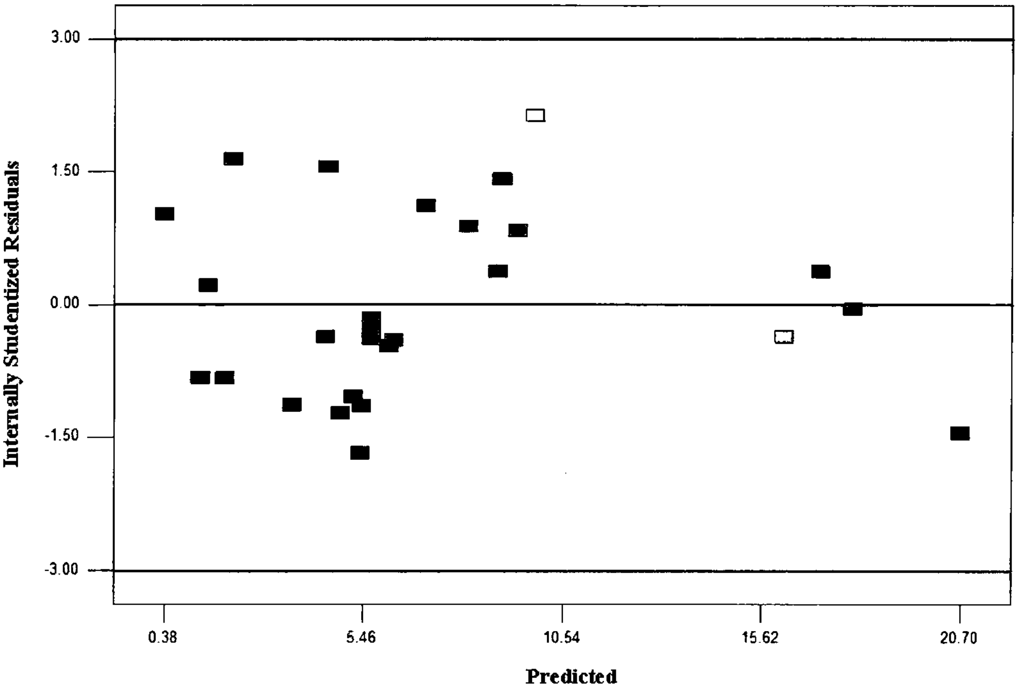

Figure C-30: Plot of Internally Studentized Residuals versus Predicted FVVS

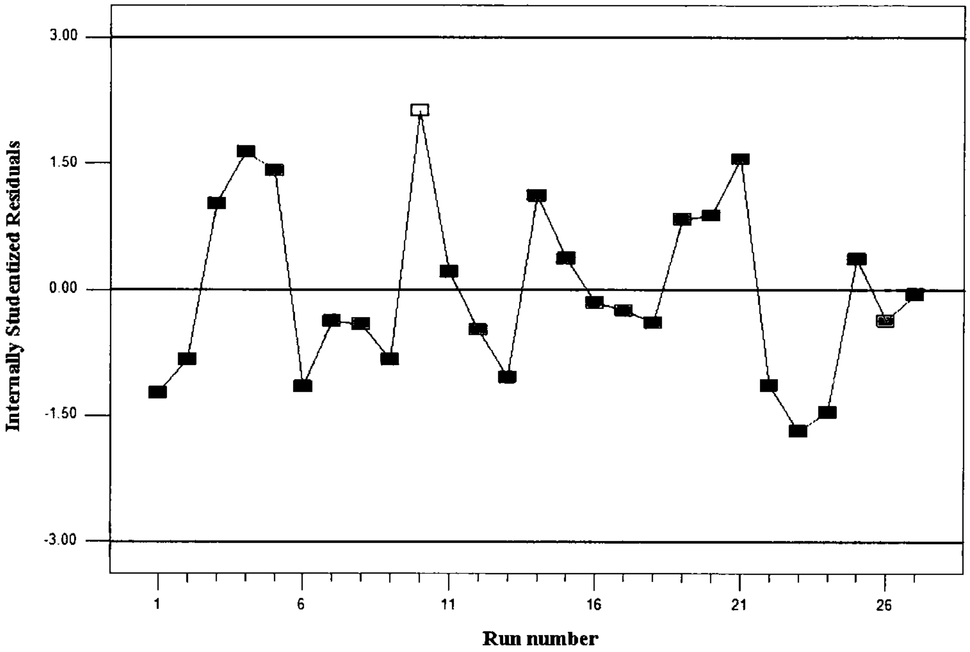

Figure C-31: Plot of Internally Studentized Residuals versus Run Number for FVVS

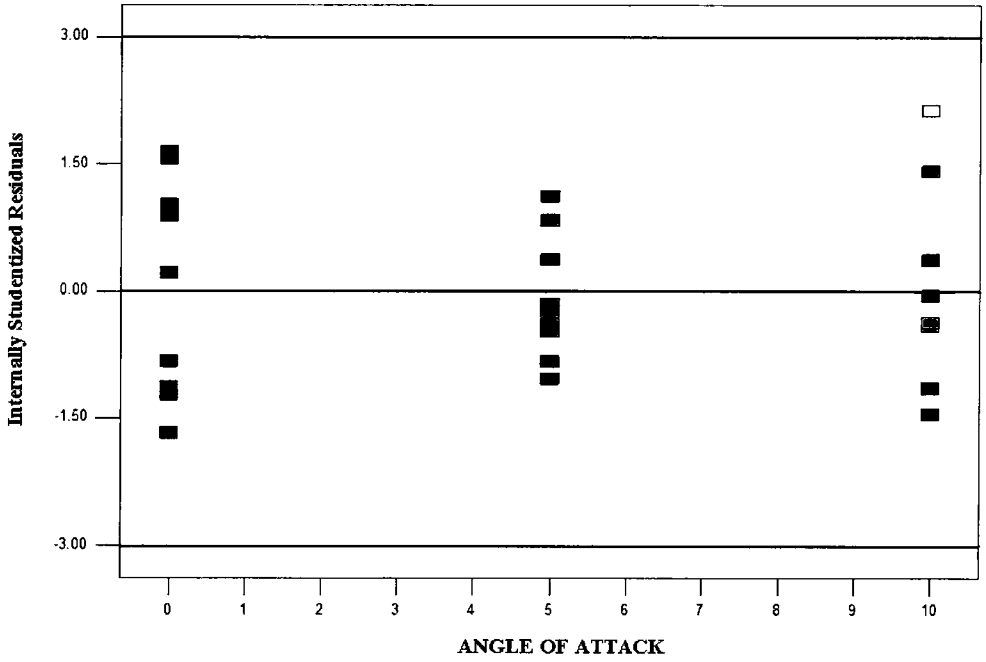

Figure C-32: Plot of Internally Studentized Residuals versus Angle of Attack for FVVS

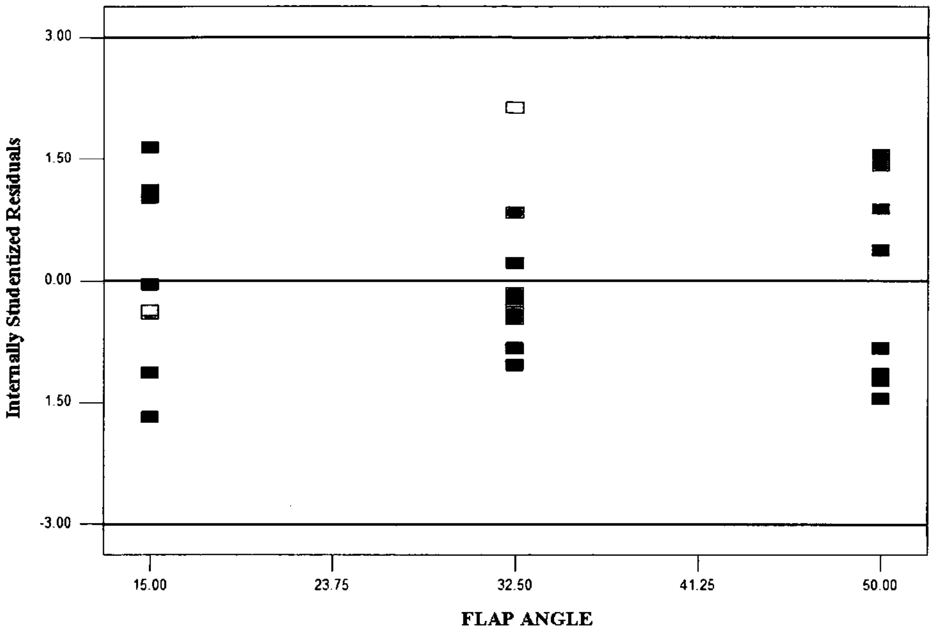

Figure C-33: Plot of Internally Studentized Residuals versus Flap Angle for FVVS

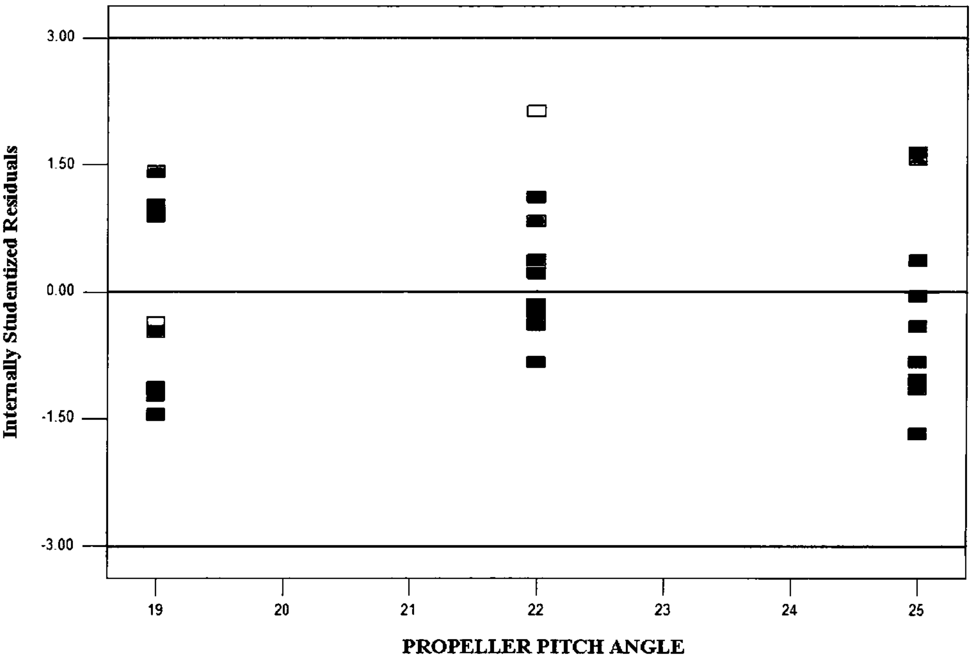

Figure C-34: Plot of Internally Studentized Residuals versus Propeller Pitch Angle for FVVS

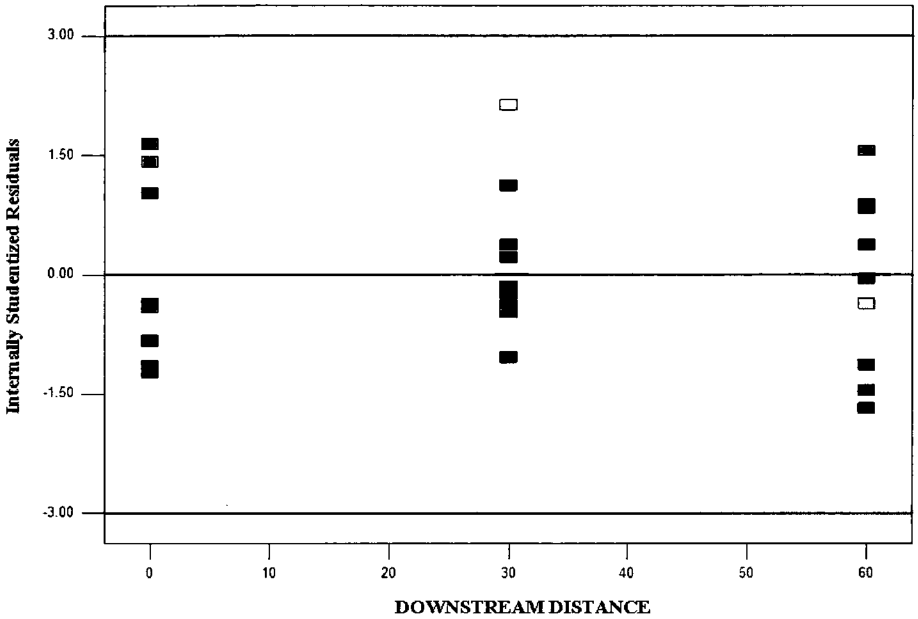

Figure C-35: Plot of Internally Studentized Residuals versus Downstream Distance for FVVS

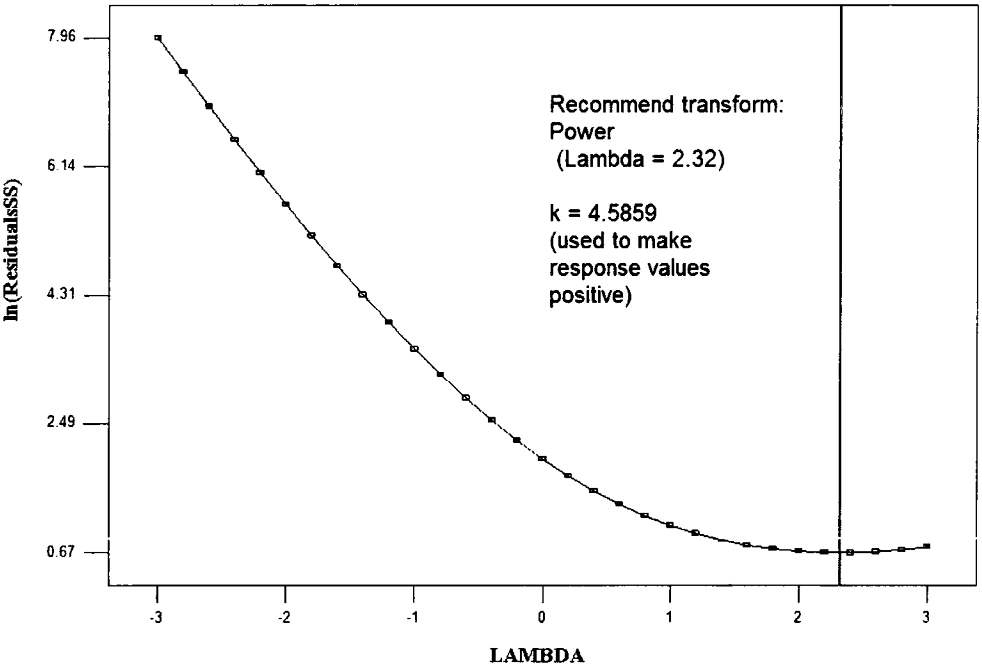

Figure C-36: Box Cox Plot for FVVS

C.5 Wing Tip Vortex Vorticity Strength (WTVVS)

The regression model for the vorticity strength of the wing tip vortex is obtained such that only the angle of attack influences the response. The residuals were checked as to whether or not the residuals are normally distributed by plotting the normal percentage probability versus internally studentized residuals given in Figure C-37 showing that a broader and shallower distribution unlike normal distribution exists. Actually the deflections are remarkable but do not result in a serious problem for the normality check. The plot of the residuals for predicted versus actual given in Figure C-38 does not indicate any significant shape while the plot of internally studentized residuals versus predicted response given in Figure C-39 indicates a slight coning which does not mean a significant problem. The graphics showing the internally studentized residuals versus run in Figure C-40 and the four main factors (for angle of attack a slight coning is observed) given through Figures C-41 to C-44 verify that the residuals are independently distributed, while no outlier or any correlation between the residuals and any factor exist. The Box Cox plot given in Figure C-45 does not recommend any transformation.

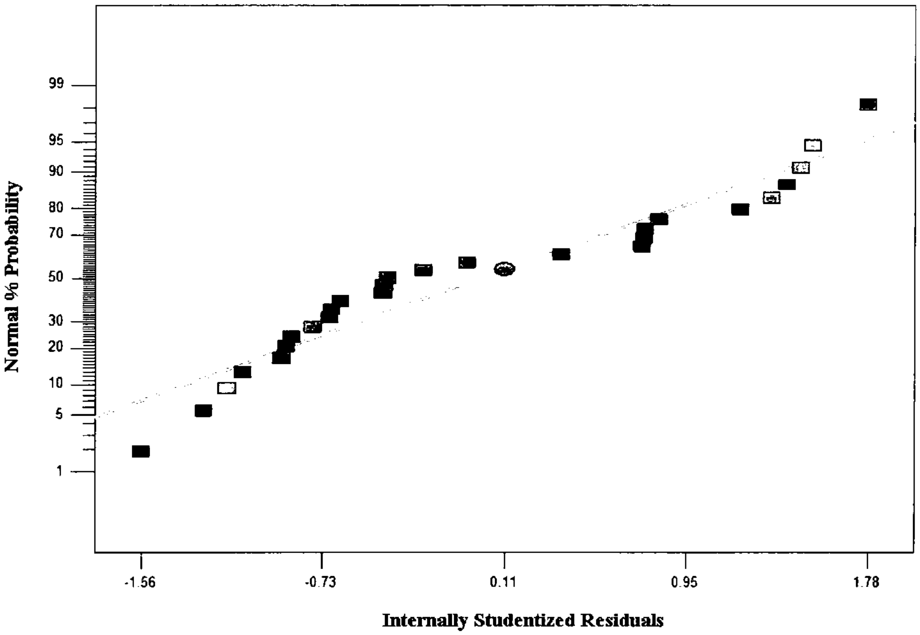

Figure C-37: Normal Probability Plot of Residuals of WTVVS

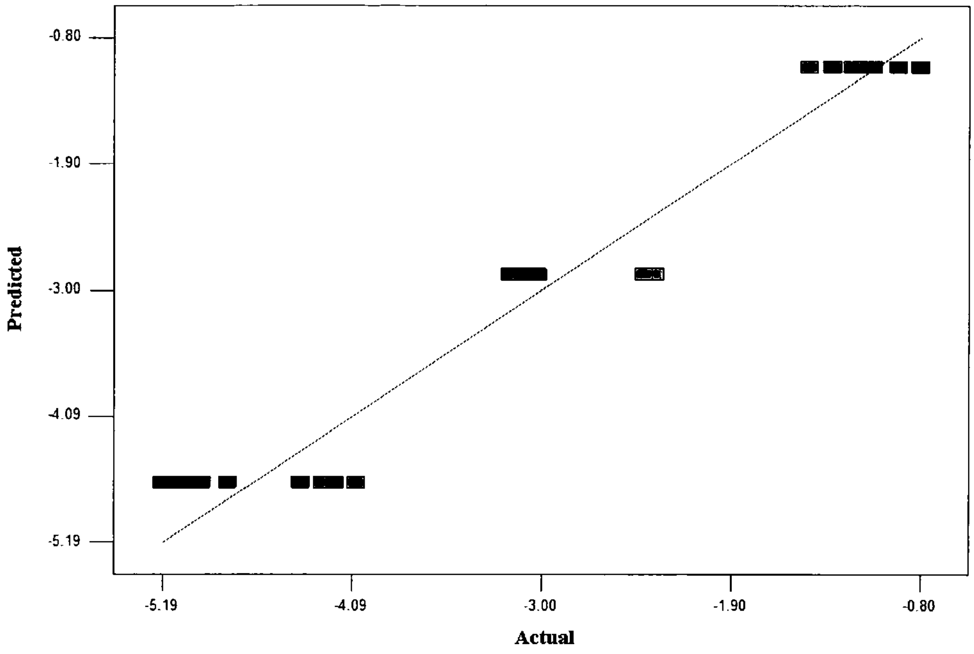

Figure C-38: Plot of Residuals for Predicted versus Actual WTVVS

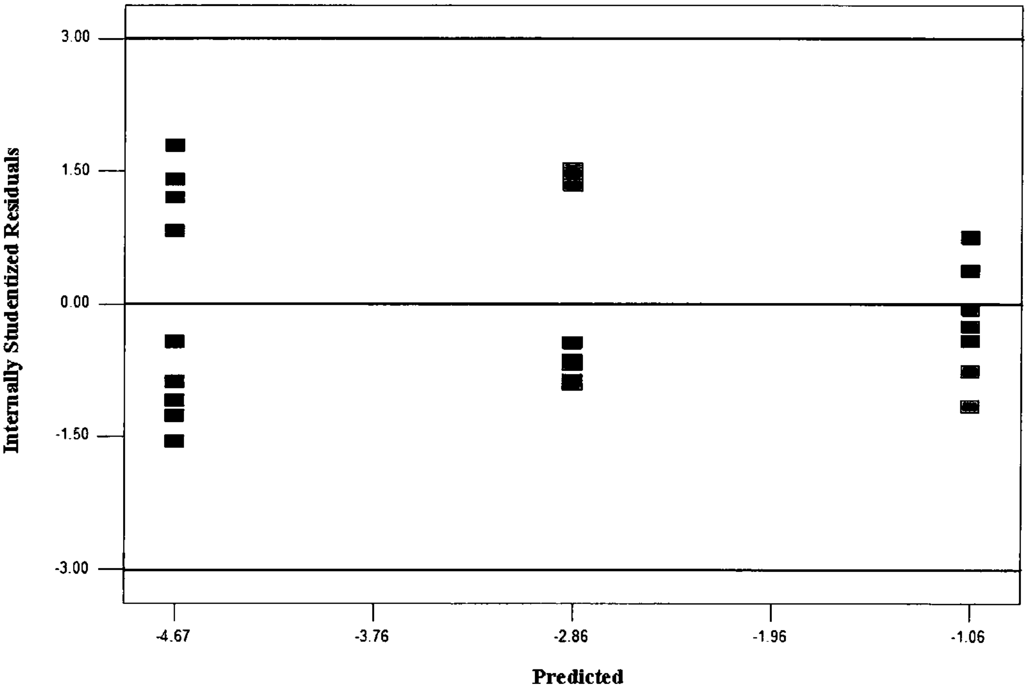

Figure C-39: Plot of Internally Studentized Residuals versus Predicted WTVVS

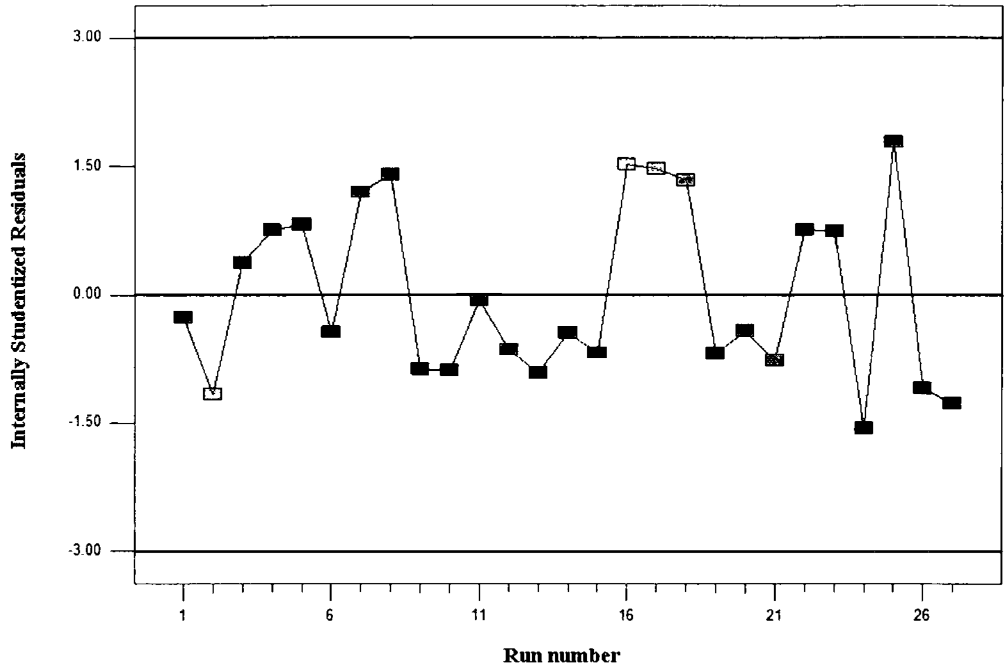

Figure C-40: Plot of Internally Studentized Residuals versus Run Number for WTVVS

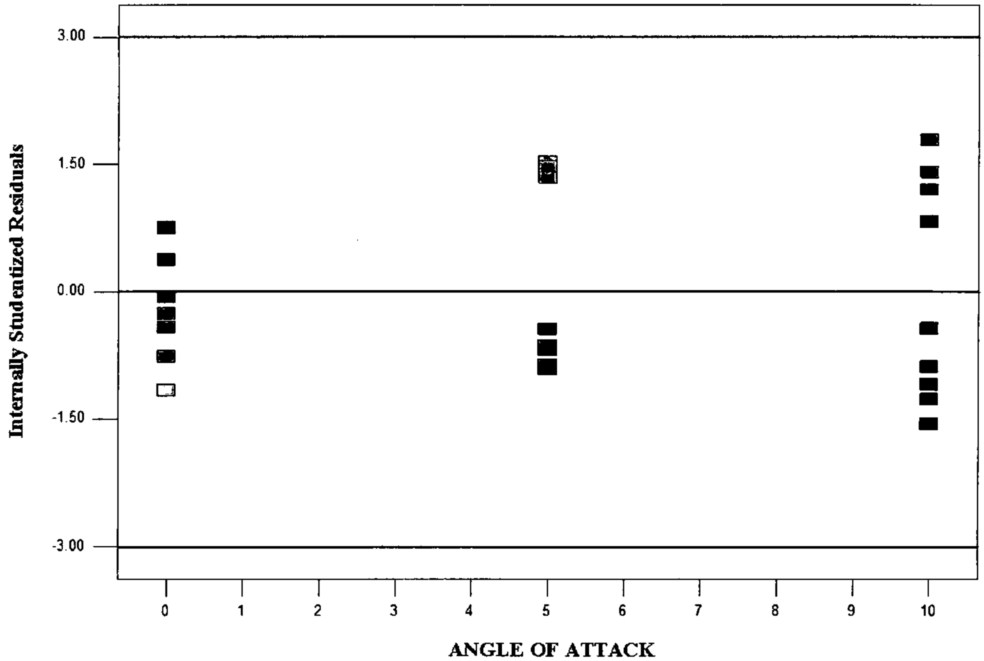

Figure C-41: Plot of Internally Studentized Residuals versus Angle of Attack for WTVVS

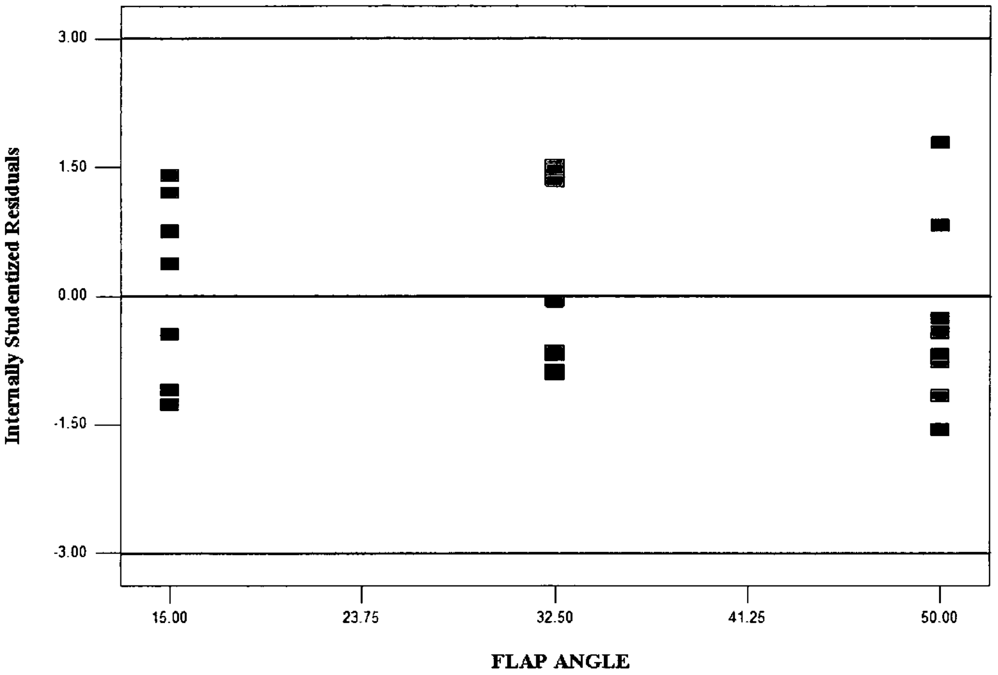

Figure C-42: Plot of Internally Studentized Residuals versus Flap Angle for WTVVS

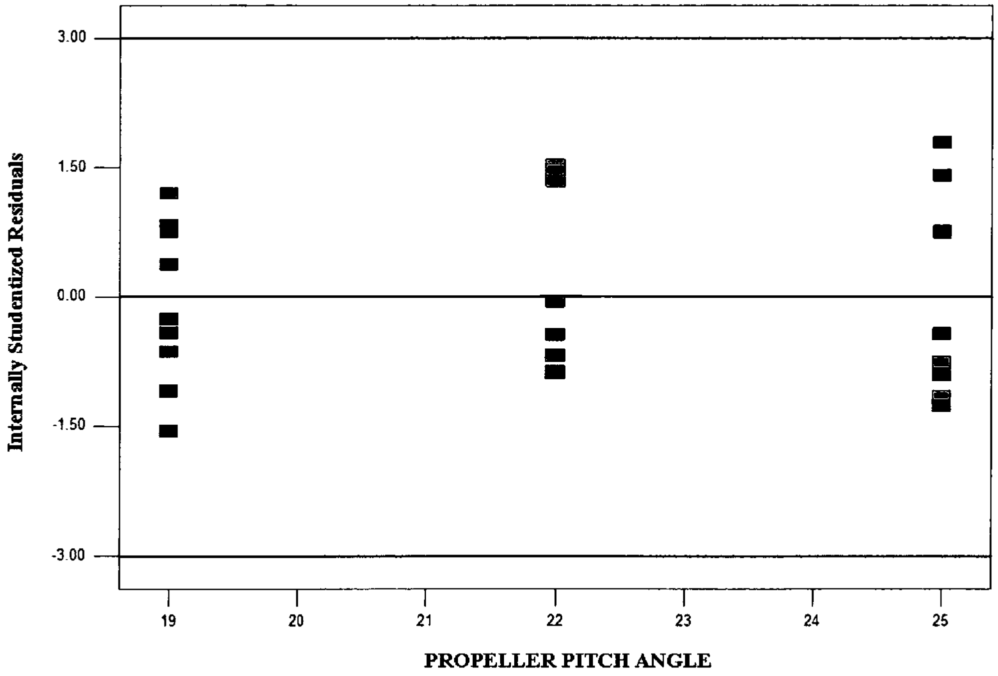

Figure C-43: Plot of Internally Studentized Residuals versus Propeller Pitch Angle for WTVVS

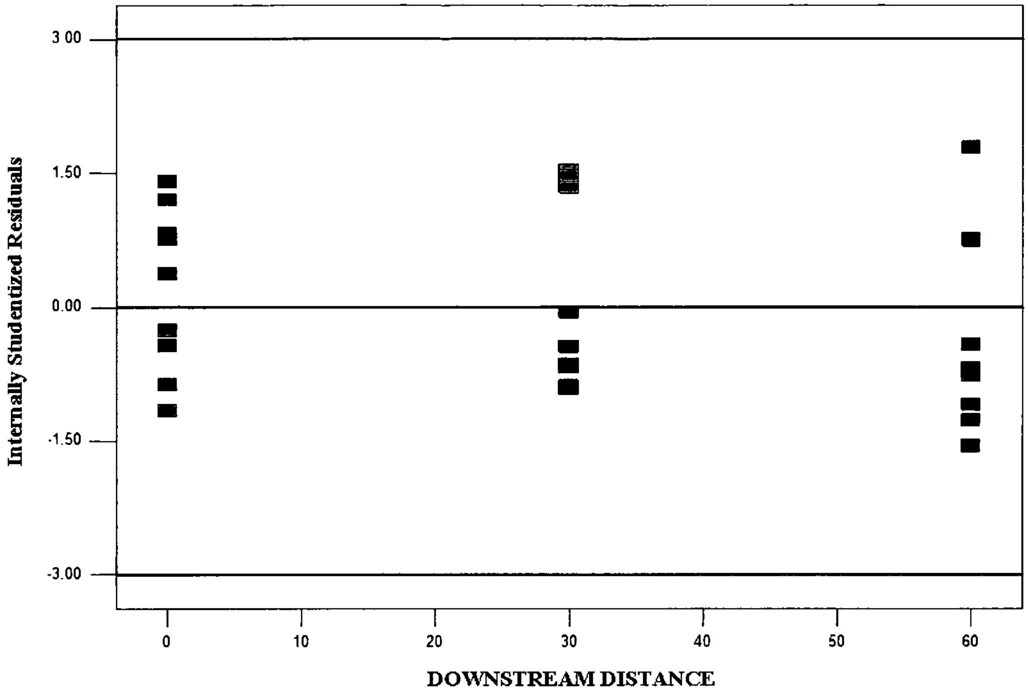

Figure C-44: Plot of Internally Studentized Residuals versus Downstream Distance for WTVVS

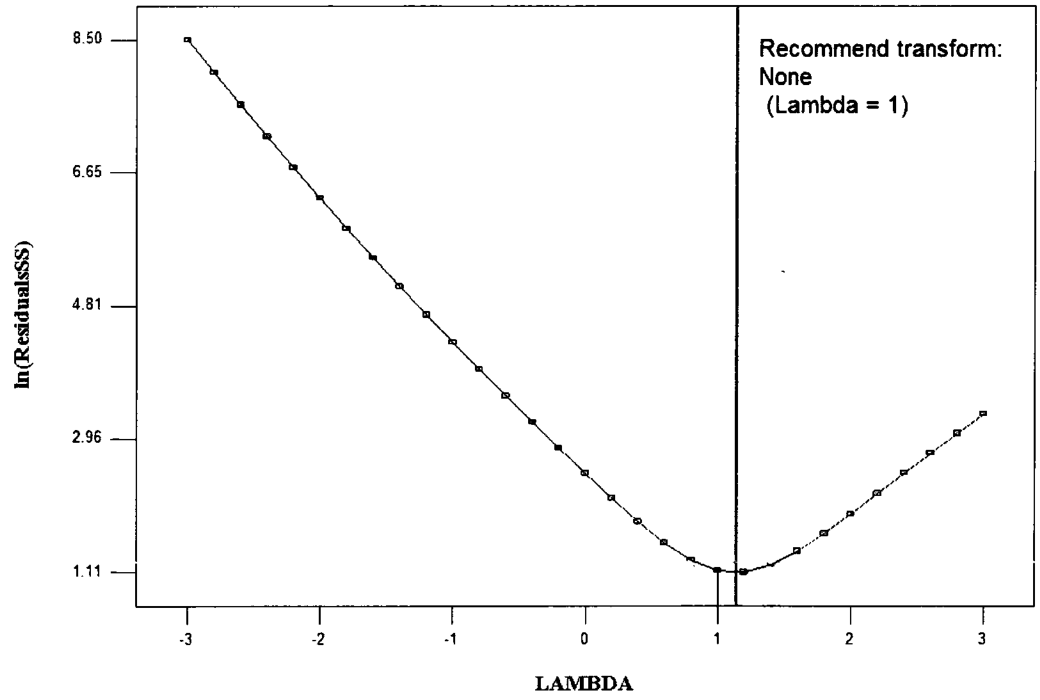

Figure C-45: Box Cox Plot for WTVVS

VITA

DEGREES

- **Master of Science Aerospace Engineering**
  Middle East Technical University, Ankara, July 1998
- **Bachelor of Science Aerospace Engineering**
  Turkish Air Force Academy, Istanbul, August 1992

PROFESSIONAL CHRONOLOGY

- Combat Aircraft Maintenance School, Izmir, Officer Training, October 1992-July 1993,
- 5th Main Jet Base, Merzifon/Amasya, Aircraft Maintenance Officer, September 1993-May 1994,
- Aeronautical Engineering Department of Middle East Technical University, Ankara, M.Sc. Student, May 1994-July 1998,
- Aeronautical Engineering Department of Turkish Air Force Academy, Istanbul, Lecturer, September 1998-August 2006,
- Military Academy of Georgia, Tbilisi/Georgia, Military Consultant, September 2004-September 2005,
- Planning and Principles Department of Turkish General Staff, Ankara, Project Officer, August 2006-August 2007,
- Aeronautics and Space Technologies Institute (ASTIN) of Turkish Air Force Academy, Istanbul- Aerospace Engineering Department of Old Dominion University (ODU), Norfolk (VA), Ph.D. Student, September 2007-September 2010.

SCHOLARSHIP WON

- Scholarship of the Scientific and Technological Research Council of Turkey (TUBITAK) for the support of M.Sc. thesis project,
- Scholarship of Canadian Ministry of Defense for Aerospace Research at National Research Council of Canada.